The longitudinal cascade development of cosmic-ray showers from observations of atmospheric Cerenkov radiation

M. P. Chantler

THE LONGITUDINAL CASCADE DEVELOPMENT OF COSMIC-RAY SHOWERS FROM OBSERVATIONS OF ATMOSPHERIC CERENKOV RADIATION

by

M.P. CHANTLER B.Sc.

A thesis submitted to the University of Durham in accordance with the regulations for admittance to the degree of Doctor of Philosophy

Department of Physics,
University of Durham.

July 1982

ABSTRACT

This thesis is concerned with the measurement of the longitudinal cascade development of large cosmic-ray showers from observations of atmospheric Cerenkov radiation. The purpose of the measurements is to obtain information on the mass composition of the primary cosmic rays and on the gross features of the high-energy hadronic interactions.

The characteristics of the Cerenkov light signal which are strongly coupled to the longitudinal shower development are described with reference to computer simulation results. An experiment designed to measure these characteristics was deployed in Dugway, Utah, U.S.A. between October 1977 and March 1980. Measurements were made in showers of primary energy 10^{15} - 10^{18} eV.

Existing data anslysis techniques have been refined and new procedures developed in order to optimise the reduction of the digital data. A detailed analysis is given of two aspects of the time structure of the Cerenkov light signal in showers of mean primary energy $\sim 2 \times 10^{17}$ eV. The measurements are interpreted in terms of the mean depth of electron cascade maximum and the fluctuations occurring between showers.

The many results on the cascade development currently available from the Dugway data are summarised. Interpretation of the results is found to be possible in the framework of scaling-based models of the high energy hadronic interactions which incorporate an enhancement of the central-region multiplicity. This allows certain inferences to be made concerning the primary mass composition. Specifically, primaries of energy $\sim 10^{16}$ eV appear to be predominently heavy nuclei, and the mass composition becomes lighter with increasing primary energy until at least $\sim 2 \times 10^{17}$ eV. While no other single experiment has yet been in a position to corroborate these results, broad consistency is found between the Dugway results and the combined results from a number of other experiments.

TABLE OF CONTENTS

Page

Page

CHAPTER 1

INTRODUCTION

1.1 THE COSMIC RADIATION

Bombarding the Earth's atmosphere from all directions in space are a variety of particles and photons. The high-energy component of this flux, from about 10^6eV to the highest recorded energy in excess of 10^{20}eV, is termed cosmic radiation. Since the discovery of this extra-terrestrial ionising radiation with a balloon-borne experiment (Hess (1912)), studies of cosmic rays have contributed to our understanding of the structure of the universe both on an astrophysical scale and on the smallest scale of the elementary particles.

Cosmic rays are the only sample of matter reaching us from outside the solar system, and they can be expected to contain information on their sources, the regions where they were accelerated to such high energies, and processes occurring in the interstellar (and possibly intergalactic) medium through which they have propagated. Apart from the sun, which is known to accelerate particles up to GeV energies during flares, no other sources of cosmic-ray particles have been unambiguously identified.

Important advances in particle physics achieved through cosmic-ray experiments have included the discovery of the positron (Anderson (1932)) and the discovery of the muon by several independent groups in 1937. Particle accelerators have now replaced cosmic rays as an investigative probe into the nature of particle interaction at energies up to $\sim 10^{12}$eV, with immediate prospects for studies to $\sim 10^{15}$eV. However, cosmic rays are expected to be the only source of particles with energies $> 10^{15}$eV for a considerable time into the future.

This thesis is concerned with the study of high-energy cosmic rays within the energy band 10^{15} - 10^{18}eV, with particular emphasis on those with energies near to 10^{17}eV. The underlying question to which this work

is addressed is 'What is the nature of the cosmic-ray particles at these energies?'. The solution to this problem has important astrophysical significance particularly in its bearing on theories of the origins of cosmic rays. However, the low flux of primary cosmic rays at high energies ($\sim 10^{-2}m^{-1}yr^{-1}sr^{-1}$ at $10^{17}eV$) dictates that they be observed indirectly via the widely spread showers of secondary particles which they produce in the atmosphere (extensive air showers). Owing to the complex structure of extensive air showers (EAS) the interpretation of experimental measurements must rely on detailed shower simulations which incorporate models of the high-energy particle interactions. The uncertainty in the nature of the high-energy interactions requires that the astrophysical and particle physics aspects of the present investigation are necessarily interdependent.

1.2 STUDIES CONCERNING THE ORIGINS OF COSMIC RAYS

Much current enquiry is focussed on the question of whether high-energy cosmic rays are predominantly galactic or extragalactic in origin. The locally observed cosmic-ray energy density ($\sim 1eV.cm^{-3}$) is close to other galactic energy densities : those of starlight, the kinetic energy of ionised interstellar gas and the interstellar magnetic fields. It can be argued that if cosmic rays are extragalactic in origin, then the frequency of the objects producing them must be several orders of magnitude higher, in relation to the matter density, in extragalactic space then in the Galaxy. In this case the enormous total energy content of the cosmic-ray flux would be second only to that contained in the rest-mass energy of matter in the universe. Models incorporating a predominantly galactic production and containment of cosmic rays, or enhanced production and trapping within the local supercluster of galaxies, yield a more acceptable total energy content of the cosmic-ray flux.

Studies of high-energy cosmic rays can be divided into three broad categories : the energy spectrum, the arrival directions and the mass composition. These are complementary areas of investigation which provide constraints for theoretical models of cosmic-ray sources, acceleration and propagation mechanisms.

1.2.1 The Energy Spectrum

The integral energy spectrum is illustrated in figure 1.1. The measurements suggest a complicated shape which may be reflecting the dominance of different source types in different energy bands. Features in the energy spectrum might also be expected from propagation effects in the interstellar and intergalactic media.

Two features in the energy spectrum are of particular interest : the increase in slope (or 'knee') at $\sim 3 \times 10^{15}$eV, and the decrease in slope (or 'ankle') at $\sim 10^{19}$eV. One mechanism proposed to account for the knee is a cut-off in magnetic rigidity above which cosmic rays leak out of the Galaxy (Peters (1961) , Bell et al. (1974), Cowsik et al. (1981)). Such a cut-off would affect light nuclei at lower energies than heavy nuclei, so that an enrichment of heavy nuclei would become evident with increasing energy. However, some doubt has been expressed that the shape of the knee can be explained by magnetic trapping effects alone (Hillas (1979)). A further proposal is that cosmic rays produced by galactic pulsars may dominate the spectrum between 10^{14} and 10^{16}eV (Karakula et al. (1974)). One development of this idea considers an extragalactic component taking over at higher energies (Strong et al. (1974)). Supernova explosions are also considered to be candidates for the acceleration of galactic cosmic rays up to energies of perhaps 10^{15}eV (see Volk (1981) for a review).

It can be argued that cosmic rays of very high energies ($> 10^{17}$eV) are only produced in very exceptional violent events, and that there

FIGURE 1.1 The flux of primary cosmic rays at the top of the atmosphere. Experimental uncertainties are represented by cross-hatching. (From Gaisser and Yodh (1980)).

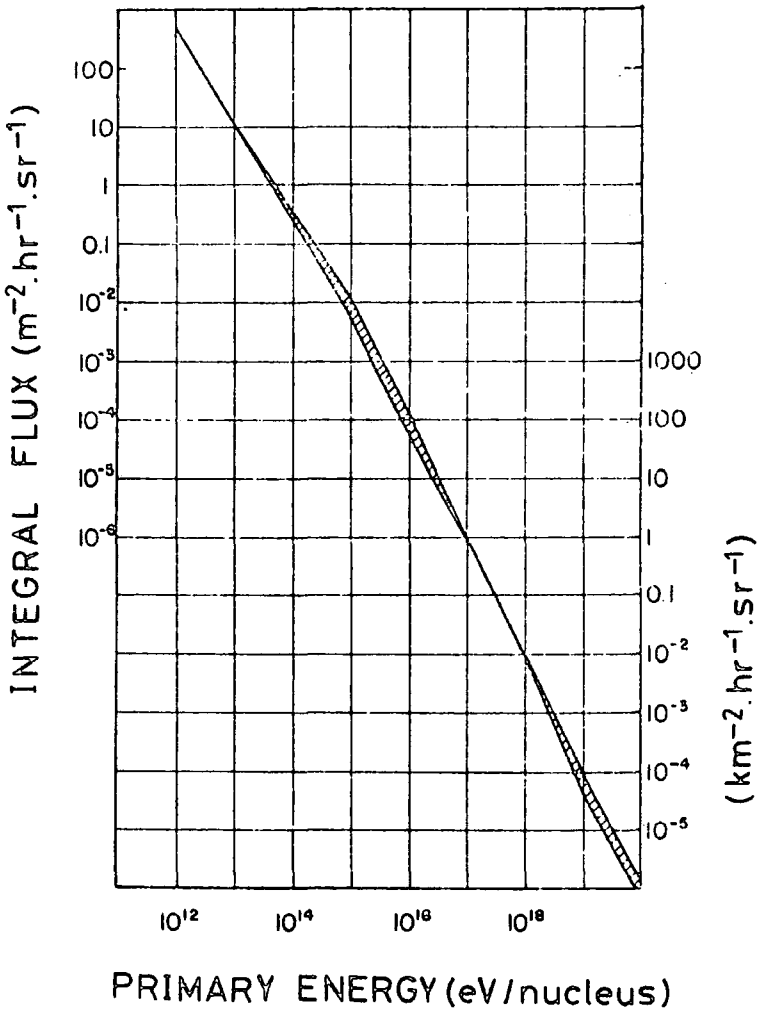

have probably been no such events in the Galaxy within the lifetime of the cosmic-ray particles (estimated at 2×10^7yr for cosmic rays with energies $\sim 10^9$eV). If this were the case then cosmic rays with energies $\gtrsim 10^{17}$eV may well originate outside the Galaxy. Possible extragalactic sources include radio galaxies, Seyfert galaxies, quasars and rich clusters of galaxies.

The presence of the ankle in the primary energy spectrum at $\sim 10^{19}$eV (Bower et al. (1981)) is perhaps not as firmly established as the knee at $\sim 3 \times 10^{15}$eV, but if confirmed will have important implications. It was first noted by Greisen (1966) and Zatsepin and Kuzmin (1966) that protons with energies $\gtrsim 10^{19}$eV would suffer rapid loss of energy due to photoproduction of pions in collisions with the 2.7K black-body photons. If the cosmic-ray flux was universal in origin at this energy a steepening of the spectrum should be observed. One possible solution to this problem is that cosmic rays, even at these ultra-high energies, are produced and confined within the Galaxy. This would require fairly heavy primary particles and the existence of an ordered magnetic field extending far outside the galactic disc (Hillas and Ouldridge (1975), Hillas (1981a)). Alternatively, models with enhanced production of cosmic rays in galactic clusters, and in particular the local super-cluster centred on Virgo (15 Mpc away), can produced satisfactory agreement with the observations (Giler et al. (1980)).

1.2.2 The Arrival Directions

The angular distribution of charged cosmic-ray particles arriving in the vicinity of the solar system depends in a complicated way on the distribution of their sources and on the structure of the interstellar magnetic fields. It is known that large-scale magnetic fields of 2 - 3μG are present in the Galaxy, although there is much uncertainty on the detailed structure of these fields. At energies $\gtrsim 10^{12}$eV the effects of solar and interplanetary magnetic fields are not significant, and

anisotropies in the arrival directions could, if established, yield useful information on the origins and propagation mechanisms of the cosmic-ray primaries.

Until comparatively recently the apparent high degree of isotropy of the cosmic-ray flux was interpreted as evidence against a galactic origin, since preferred directions should emerge at sufficiently high energies when the magnetic deflections become small. However, there is now evidence for the existence of complicated anisotropies over a wide range of energies (see Kiraly et al. (1979) for a review). For example, there are indications that an anisotropy sets in at $\sim 10^{14}$eV which has an amplitude increasing with energy. At $\sim 10^{17}$eV observations suggest that a significant anisotropy is present (Coy et al. (1981a)). No firm conclusions have yet been drawn for these results. Any interpretation will remain largely speculative without a knowledge of the mass composition of the primaries, upon which estimates of the gyromagnetic radii and hence the efficiency of magnetic containment depend.

In the energy band 10^{19} - 10^{20}eV a correlation has been found between galactic latitude and primary energy (Lloyd-Evans et al. (1979)), indicating that the more energetic particles come from higher latitudes. A survey of the arrival direction of 58 cosmic-ray primaries with assigned energies $> 5 \times 10^{19}$eV showed notable concentrations from outside the galactic plane (Krasilnikov (1979)). Since the Larmor radius of a 10^{20}eV proton is 30Kpc in a magnetic field of 3μG, it seems unlikely that these results could be accounted for with a model of galactic production and confinement; although a galactic origin may just be conceivable for heavier primary particles (Hillas and Ouldridge (1975)).

1.2.3 The Mass Composition

At energies $\lesssim 10^{14}$eV the primary cosmic-ray flux is sufficient for direct measurement of the mass number of cosmic-ray nuclei from balloon

and satellite experiments. Below about 10^{12}eV the mass spectrum is known fairly accurately and comparison with solar system abundances can provide information on cosmic-ray sources and propagation mechanisms. Table 1.1 shows the mean observed distribution of low-energy cosmic-ray nuclei, and the inferred relative abundances at the source after allowing for fragmentation of the nuclei in collisions with interstellar gas (spallation). The presence of certain light elements is thought to be due almost entirely to spallation, and this has been used to provide an indication of the mean amount of matter traversed in the Galaxy. For example, Shapiro et al. (1975) estimated the mean free path of C,N and O nuclei as 4.5 g.cm^{-2} of hydrogen-like material. Observations indicate that the ratio of secondary to parent nuclei is a decreasing function of energy. One possible interpretation of this is that there is an energy-dependent leakage from the source region which results in less matter being traversed by the cosmic-ray parent nuclei of higher energies (Cowsik and Wilson (1973)). Spallation also gives rise to unstable isotopes some of which have been used as 'cosmic-ray clocks' to estimate the mean lifetime of cosmic rays in the Galaxy. Results on the ratio of the unstable isotope ^{10}Be to ^{9}Be and ^{7}Be have been used to infer a lifetime of $\sim 2 \times 10^{7}$yr (Garcia-Munoz et al. (1975)) for cosmic rays of energy $\sim 10^{9}$eV.

Measurements of the energy spectra of individual nuclei, or groups of nuclei, in the energy band 10^{10} - 10^{13}eV provide strong evidence that the spectral slope for iron-group nuclei is flatter than for light nuclei (see Gaisser and Yodh (1980) and Hillas (1975) for reviews). This effect might be attributable to a variety of mechanisms including, for example, the presence of sources rich in heavy elements with a flatter than average production spectrum (Juliusson (1975)), or the fragmentation of heavy nuclei with an energy-dependent leakage from the source regions

TABLE 1.1

The observed mass distribution of low energy cosmic rays, normalised to Z = 6 (from Hillas (1975)).

Z	OBSERVED MEAN	EXTRAPOLATED PRE-SPALLATION COMPOSITION
1	7×10^5	$2\text{-}5 \times 10^5$
2	37500	26000
3	141	-
4	89	-
5	249	-
6	1000	1000
7	246	110±20
8	895	1070±20
9	17	-
10	162	160±20
11	26	8±4
12	187	230±20
13	29	20±10
14	143	204±30
15	6	0-6
16	33	30±6
17	6	
18	14	7±5
19	8	
20	22	22±8
21	5	
22	14	
23	7	
24	16	3±3
25	6	0-6
26	96	205±30
27	3	
28	4	8±2

(Cowsik and Wilson (1973)). Certain indirect observations, based on measurements of EAS, provide evidence that the proportion of heavy nuclei increases further at higher energies. For example, measurements of the arrival-time distribution of hadrons in EAS are interpreted as indicating an increasing abundance of heavy nuclei at energies 10^{14} - 10^{15}eV due to a rigidity-dependent failure of galactic containment (Cowsik et al. (1981)).

At energies >> 10^{14}eV the cosmic-ray flux is so low that information on the primaries must be obtained indirectly by making measurements of EAS. Although considerable progress has been achieved in the measurement and understanding of many characteristics of EAS, there is at present no consensus on the primary mass composition at these energies. The difficulty arises in reliably extrapolating from ground-based observations of EAS (which record gross features of the way in which the energy is dissipated to the numerous secondary particles) to the properties of the primary particles. EAS parameters which retain information on the mass of the primary particle require careful identification and detailed shower simulations with which to interpret the observations.

The determination of the primary composition at EAS energies remains one of the most important goals in cosmic-ray physics. A knowledge of the mass composition of the primary beam would provide an invaluable complement to observations of the energy spectrum and arrival directions, and thus help to elucidate the origins, acceleration and propagation mechanisms of high-energy cosmic rays.

1.3 EXTENSIVE AIR SHOWERS (EAS)

Direct observation of cosmic-ray primaries of energy >> 10^{14}eV would require detectors near the top of the atmosphere either having exceptionally large dimensions or operating for inordinately long periods. Observations of the secondary radiation in the atmosphere, following the interactions

between the primary and air nuclei, can however yield information on the nature of the cosmic-ray primary. There follows a short description of EAS and the models of the high-energy particle interactions which are central to the interpretation of the experimental data. This leads to a brief discussion of those aspects of EAS to which the present investigation is directed, and which are considered especially valuable in elucidating the primary mass composition and the gross features of the high-energy particle interactions.

1.3.1 The Structure of EAS

When a primary cosmic-ray nucleon (or nucleus) collides with an air nucleus high in the atmosphere, secondary mesons (principally pions) are produced and a fragment nucleon (or nucleons). The charged mesons and the nucleons interact again to sustain the hadronic core of the cascade. Other charged pions decay to muons and neutrinos. The muons produced have a significant probability of surviving to sea level. At the highest energies the charged pions tend to interact rather than decay because of relativistic time-dilation. The neutral pions decay almost instantaneously into two gamma-photons which initiate the electromagnetic component of the cascade. The muonic and electromagnetic components are continuously replenished by the hadronic core.

The most numerous particles in an EAS are the electrons and positrons. These are produced when a gamma-photon undergoes pair production, transforming its energy into an electron-positron pair. Electrons and positrons in turn radiate gamma-photons via the bremsstrahlung process, and so the electromagnetic component grows with increasing depth into the atmosphere. This growth continues until, at the critical energy in air ($\sim 10^8$eV), energy losses due to Compton scattering and ionisation become competitive with the production processes, and the cascade begins to decay. The electromagnetic cascade also obtains a lateral spread owing to multiple Coulomb scattering of the shower electrons. At sea

level, in a large EAS, the electromagnetic component extends to a radius of $\lesssim$ 1km from the axis of symmetry of the shower. The hadronic core extends to a few metres, and the muonic component extends to $\gtrsim$ 1km owing to the angular distribution of the parent pions and the altitude of production.

Optical Cerenkov photons are produced by the shower electrons at all stages of the cascade development. Observations of the Cerenkov-photon flux penetrating to ground level provide information on the structure of the longitudinal cascade which in turn can be related to the mass of the primary particle. A study of this topic will be presented in the following chapters of this thesis.

1.3.2 Models of the High-Energy Particle Interactions

Models of the high-energy particle interactions are required for the detailed simulation of EAS, which in turn plays an essential role in the interpretation of experimental measurements. However, the high energy hadron-hadron collisions are several orders of magnitude greater in energy than those studied with particle accelerators. It is therefore necessary to extrapolate the inclusive cross-sections, the secondary particle multiplicities and momentum distributions from accelerator data up to EAS energies. A widely used theoretical framework for extrapolating data on hadronic interactions is the Feynman scaling model (Feynman (1969)). According to this model the momentum distribution of the secondaries simply scales with energy. This gives rise to a secondary particle multiplicity (n_s) increasing as log E (where E is that part of the incident hadron energy available for particle production).

It is useful at this stage to introduce the Feynman variable 'x', defined as $x = P_{11}^{*} / P_{0}^{*}$, where P_{11}^{*} and P_{0}^{*} are the longitudinal momentum and the maximum possible longitudinal momentum of a secondary particle in the centre of mass system. The consensus view in recent reviews of EAS data is that there is little evidence for a violation of scaling

in the 'fragmentation region' ($x \sim 1$): the domain in which a leading particle is believed to proceed with a significant fraction of the incident energy. However, there are indications (Gaisser et al. (1978), Gaisser and Yodh (1980), Tonwar (1981)) that the secondary particle multiplicity may increase with energy more rapidly than predicted by the scaling model in the 'central region' ($x \sim 0$) : the domain in which the majority of the secondaries are produced. For this reason the calculations of the Durham group (Gaisser et al. (1978)) have been carried out for a range of central-region multiplicities which are consistent with accelerator data at lower energies. These are $n_s \propto \log E$, $n_s \propto E^{1/4}$ (as predicted by the Landau model (Landau (1953)) and $n_s \propto E^{1/3}$.

Both cosmic ray (Yodh et al. (1972)) and accelerator measurements (Amaldi et al. (1977)) suggest that the proton-proton cross-section (σ_{pp}) increases over the range 10^{11} - 5 x 10^{13}eV. The extrapolations of the pp and πp cross-sections to EAS energies which are considered in the model calculations are : σ = constant, $\sigma \propto \log s$ and $\sigma \propto \log^2 s$ (where s is the centre of momentum-energy squared).

The sets of assumptions described above have been incorporated into the Durham group's computer simulations of EAS, the results of which are referred to throughout this thesis. The effects of the choice of interaction model on the longitudinal cascade development of EAS are discussed in the following section.

1.3.3 The Longitudinal Cascade Development

The growth of the electron cascade is a fundamental characteristic of an EAS. The computed average cascade curves for two (extreme) model assumptions and for proton and iron nucleus primaries are shown in figure 1.2. A useful parameterisation of electron cascade curves is the depth in the atmosphere of the cascade maximum (t_{max}). For a given primary energy an early-developing cascade, i.e. one with a small value

FIGURE 1.2 Electron cascade development curves for average showers of primary energy 10^{17} eV. The calculations are for two interaction models and for iron nucleus and proton primaries.

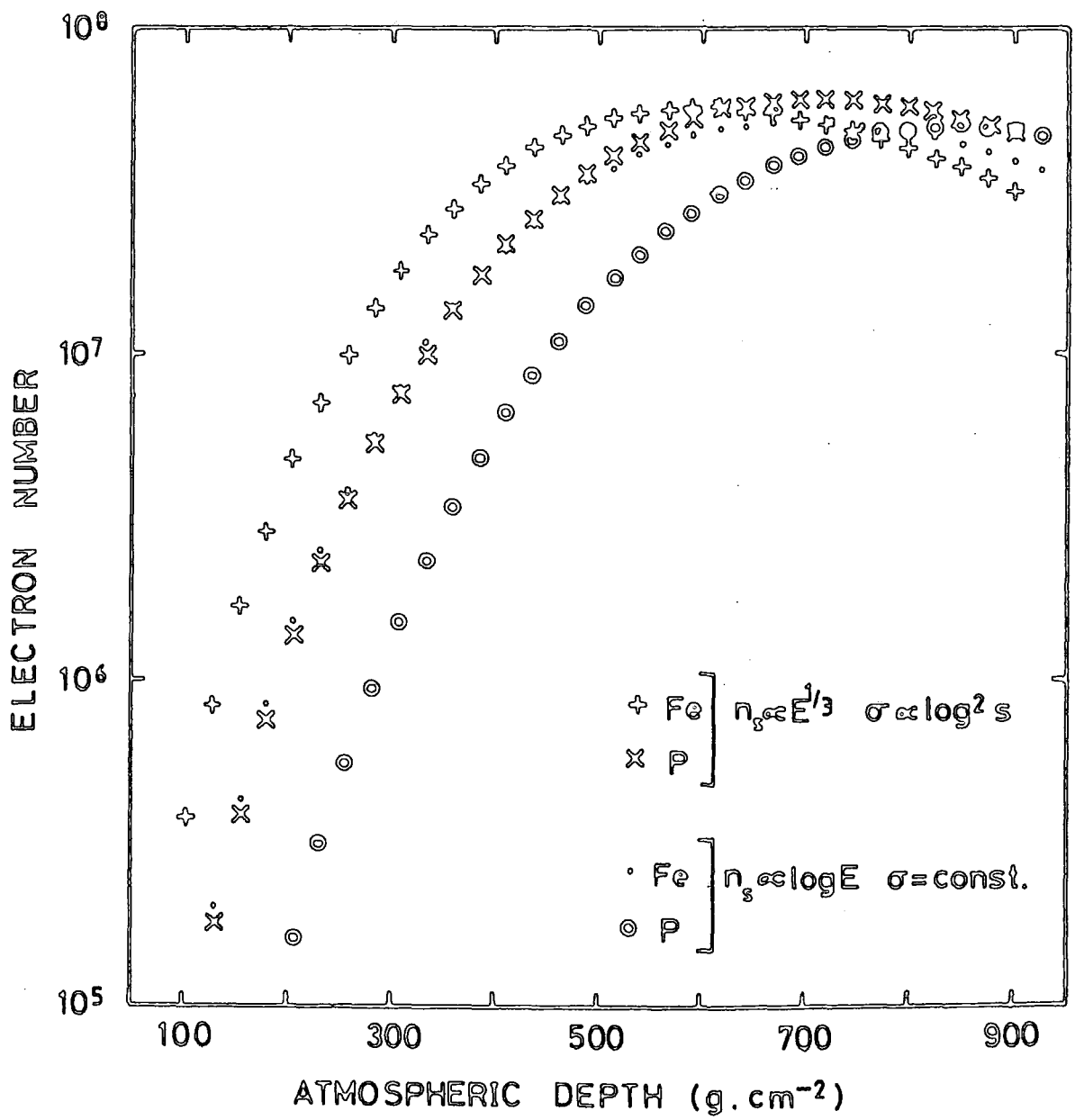

of t_{max}, can be the result of a heavy primary nucleus, a large interaction cross-section (σ), a high secondary particle multiplicity (n_s) or any combination of these factors. The curves shown in figure 1.2 illustrate the interdependence between the determination of the primary mass and the characteristics of the high-energy interactions.

Stochastic variations in the height of the first interaction and subsequent interactions result in an intrinsic fluctuation in t_{max}. The extent of this fluctuation is to some extent dependent on the interaction model but more strongly dependent on the primary mass composition. A heavy primary nucleus fragments gradually, nucleons being freed in successive interactions. The superposition of the many sub-showers generated tends to smooth out the effects of large statistical fluctuations in individual interactions. Much larger fluctuations are therefore expected from proton primaries than from heavy nucleus primaries.

Observations of both the mean ($\overline{t_{max}}$) and the standard deviation ($\sigma(t_{max})$) of the distribution in t_{max} can provide constraints for the possible combinations of interaction model and primary mass composition. In addition, $\overline{t_{max}}$ increases with primary energy (E_p) at a rate which is relatively weakly dependent on the interaction model for a fixed primary composition. The 'elongation rate' ($d(\overline{t_{max}})/d(\log E_p)$), as it is termed, could be expected to show significant deviations from the model predictions if the mass composition were changing rapidly with primary energy. A non-zero value for the quantity $d(\sigma(t_{max}))/d(\log E_p)$ might also be indicative of a mass composition changing with primary energy. While these are not the only EAS parameters containing information on the primary mass composition, their measurement is potentially of great value and is the subject of both world-wide endeavours and of the present investigation.

1.3.4 Scope of this Thesis

The aim of this work is to obtain measurements of the longitudinal

development of EAS from observations of atmospheric Cerenkov radiation, and to relate these to the broad characteristics of both the primary mass composition and the high-energy hadronic interactions.

In chapter 2 consideration is given to the basic theoretical aspects of Cerenkov light in EAS. Cerenkov light observables which are strongly coupled with the cascade development are described with reference to computer simulation results. The observational background to the present experimental work is outlined.

Chapter 3 contains a description of the experimental apparatus, which was located at Dugway, Utah, U.S.A. The periods of operation, details of the datasets recorded and preliminary analysis procedures are described.

Chapter 4 examines in detail the data reduction and error analysis techniques which have been developed to determine parameters, sensitive to the cascade development, to a known accuracy.

Chapters 5 and 6 provide detailed descriptions of the data analysis of two aspects of the Cerenkov-light time-structure in EAS. The measurements are interpreted in terms of the mean and standard deviation of the underlying distribution in t_{max}.

Chapter 7 summarises the available results from the Dugway experiment. Comparison with computer simulation predictions enables certain inferences to be made concerning the possible interaction models and the behaviour of the primary mass composition. The Dugway results on the cascade development are compared with those from other experiments.

Finally, in chapter 8, the interpretation of the Dugway results is summarised and discussed in the context of other work. The astrophysical implications are briefly examined. The priorities for further data analyses are indicated, followed by some suggestions for future experimental work.

CHAPTER 2

CERENKOV RADIATION IN EXTENSIVE AIR SHOWERS

2.1 INTRODUCTION

Cerenkov radiation is produced when a charged particle traverses a dielectric medium at a velocity in excess of the phase velocity of light in the medium. The first experimental studies were made by Cerenkov (1934, 1937), and a satisfactory theoretical interpretation in terms of classical electromagnetic theory was given by Frank and Tamm (1937). A simplified account of the phenomenon follows in section 2.2.

Blackett (1948) proposed that Cerenkov radiation at optical wavelengths, produced in the atmosphere by cosmic-ray particles, may contribute a small part ($\sim 10^{-4}$ of the total) of the night sky brightness. Measurements of the radiation produced by single particles in dense gases were first made by Ascoli et al. (1953) and in air at S.T.P. by Barclay and Jelley (1955).

Jelley and Galbraith (1953) suggested that the Cerenkov radiation produced in the atmosphere by extensive air showers ($\sim 10^{15}$eV) should be detectable at ground level. This proposal was tested with an experiment based on the idea that since a large number of electrons arrive at ground level in an EAS within a very short time interval $\sim 10^{-8}$s, this would result in a temporary enhancement of the Cerenkov component above the background brightness level. Provided that the time constant of the recording equipment is sufficiently small, the Cerenkov light signal should be resolvable from the general night sky background. In their experiment (Galbraith and Jelley (1953)), the authors used a phototube at the focus of a parabolic mirror situated at the centre of an EAS array of Geiger-Muller tubes. A coincidence between the photomultiplier signal and the discharge of one or two of the

Geiger-Muller tubes was observed in 22 out of 50 occasions. There followed a series of exploratory experiments by the same authors at the Pic du Midi observatory (1955), in which it was established that the radiation was a penetrating component of EAS, was partially polarised and that the spectrum was consistent with Cerenkov light. The discovery was consolidated by further experiments by Nesterova and Chudakov (1955) in the U.S.S.R. and by Boley et al. (1961) in the U.S.A. Measurements were subsequently extended to larger showers ($\gtrsim 10^{17}$eV) by Krieger and Bradt (1969) at mountain altitudes and Egorov et al. (1971) at sea level.

Most of the earlier observations of Cerenkov light were concerned with the lateral distribution of light at the observation level; and indeed studies of this aspect of the radiation have continued to the present day, providing accurate primary energy estimations and valuable information on the cascade development. The information on the longitudinal cascade contained in the light pulse shape was noted by Boley (1964), and measurements of the pulse shape in large showers began at the Yakutsk array in the early 1970's (Efimov et al. (1973)). More recently a powerful technique involving synchronised measurements of the arrival time of the light front at widely spaced detectors has been developed (Orford and Turver (1976)), enabling the construction of a 3-dimensional image of the cascade development in Cerenkov light.

The sensitivity of the various aspects of Cerenkov light in EAS to the cascade development is considered in a discussion of computer simulation results (section 2.3), which play an essential role in the interpretation of current measurements. This is followed by a brief description of some recent measurements (section 2.4).

2.2 THEORETICAL CONSIDERATIONS

A simplified treatment of the Cerenkov effect is presented here, followed by a summary of basic properties of the radiation with respect to its production in EAS and its propagation through the atmosphere. The material is based largely on the reviews by Jelley (1958, 1967) and Boley (1964).

2.2.1 Cerenkov Radiation from a Single Particle

A charged particle traversing a dielectric medium sets up a transient polarisation in the medium; the depolarisation results in the emission of electromagnetic radiation from regions around the track of the particle. In the general case, the radiated wavelets from all parts of the track will interfere destructively at a distant point giving a resultant field of zero intensity. However, if the phase velocity (v), is greater than the phase velocity of light in the medium ($^{c}/_{n}$) (where n is the refractive index of the medium), the wavelets can interfere constructively to produce a conical wavefront travelling at an angle θ_c to the particle track. The phenomenon is illustrated by the Huygen's construction in figure 2.1. From this treatment, the fundamental Cerenkov relation is easily obtained:

$$\cos \theta_c = \frac{^{c}/_{n}}{v} = \frac{1}{\beta n} . \qquad 2.1$$

Three conditions follow from this:

(i) Only particles for which $\beta n > 1$ can produce Cerenkov light. Therefore, for a given refractive index there is a minimum threshold velocity:

$$\beta_{MIN} = \frac{1}{n} . \qquad 2.2$$

(ii) For an ultra-relativistic particle with $\beta = 1$, there is a maximum angle of emission:

$$\theta_{MAX} = \cos^{-1} (\frac{1}{n}). \qquad 2.3$$

FIGURE 2.1 The Huygen's construction for Cerenkov light from a particle with velocity v in a medium with refractive index n.

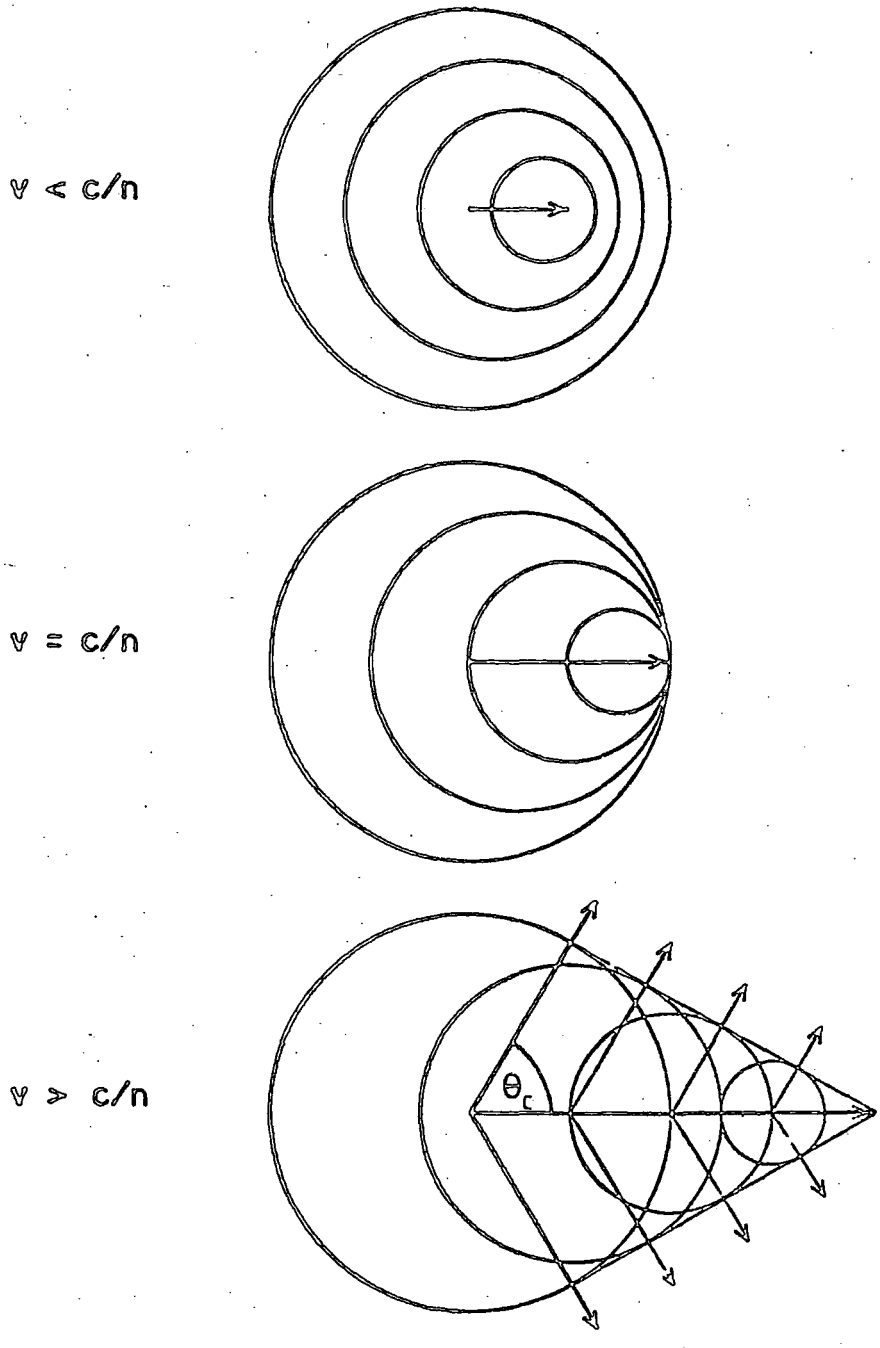

(iii) Cerenkov radiation can be produced only at those frequencies for which $n > 1$; thus excluding the x-ray and γ-ray regions of the spectrum.

Frank and Tamm (1937) calculated the energy (dE) given to the production of Cerenkov photons of wavelengths between λ_1 and λ_2 by a particle of charge Ze in traversing a path dL as:

$$\frac{dE}{dL} = 4\pi^2 Z^2 e^2 \int_{\lambda_1}^{\lambda_2} \left(1 - \frac{1}{\beta^2 n^2}\right) \frac{d\lambda}{\lambda^3} . \qquad 2.4$$

Two points of interest arise from this:

(i) The production of Cerenkov photons is inversely proportional to the square of the wavelength. The emission spectrum will therefore be enriched in the U.V. and blue regions.

(ii) The production is proportional to the square of the charge of the radiating particle.

2.2.2 Cerenkov Radiation in EAS

In air at S.T.P., the refractive index (n) is 1.00029. This implies, using equation 2.3, that the maximum angle of emission of Cerenkov light (θ_{MAX}) is 1.3° (for a particle with $\beta = 1$). The radiated light is, therefore, strongly directionally related to the path of the radiating particle. The threshold energies for the production of Cerenkov light can be calculated from equation 2.2, and at sea level these are 21 MeV for electrons, 4.3 GeV for muons, and 390 GeV for protons. The production rate of Cerenkov photons for an electron in air at S.T.P., for example, can be calculated from equation 2.4. For emission in the wavelength range 3500-5500 Å (a typical response for a photomultiplier tube) this is $\sim$ 30 photons m^{-1}. While the above results apply at sea level, at higher altitudes the refractive index will of course be smaller, leading to higher threshold energies, lower production rates and smaller emission angles.

The directional aspect of Cerenkov light mentioned above is largely masked in air by the effects of multiple Coulomb scattering of the particles producing the radiation. Protheroe (1977) calculates that for 30 MeV electrons, typical of those in an EAS, the r.m.s. scattering angle is ~ 0.3 rad. One advantage accrues from this Coulomb scattering: since Cerenkov light is produced at all levels of development in an EAS by electrons scattered over a wide angular distribution with respect to the core direction, the Cerenkov light reaching the ground has a broad lateral distribution, thus facilitating easy shower detection.

In EAS the majority of Cerenkov light production is by the electrons, these being by far the most numerous particles in the cascade, and having the lowest threshold energy. Of the electrons arriving at sea level, 85% have an energy above the 21 MeV threshold for Cerenkov production. Boley (1964) calculates that for each electron reaching sea level, there are $\sim 4.1 \times 10^5$ Cerenkov photons produced. This numerical advantage of photons over electrons enables the detection and measurement of the Cerenkov light signal without the statistical limitations inherent in particle measurements.

The most desirable and unique aspect of Cerenkov light measurements is that they offer information concerning the longitudinal history of the shower electrons. The Cerenkov signal recorded at ground level is the sum of the contributions from all those electrons throughout the cascade which have radiated light into the acceptance solid angle of the detector. In particular, the time dependence of the Cerenkov signal retains information on the longitudinal electron cascade development. For example, the light arriving at ground level first is produced early in the shower development, while the arrival time of the light produced later in the cascade is delayed owing to geometrical path-length effects. This is in contrast to particle detector measurements which mainly offer

information on the local particle density at one state of development in the history of the air shower.

The main features of the Cerenkov light signal observed at ground level are modified to a certain extent by a number of processes. The absorption of light on propagation through the atmosphere varies approximately as the secant of the zenith angle (strictly for a source outside the atmosphere). Allen (1955) gives the absolute transmission of light through the atmosphere which increases from 63% at 4000 Å (in the vertical) to 83% at 5000 Å, indicating that absorption does not present a serious problem to experimental measurements. A detailed description of the atmospheric attenuation by the processes of Rayleigh scattering, aerosol scattering and ozone absorption is given by Elterman (1968); these effects being sufficient to warrant inclusion in any simulation of Cerenkov radiation EAS. The effects of dispersion, refraction and diffraction in EAS are considered by Jelley (1967), and found to be negligible.

Having considered the copious production of Cerenkov photons in air showers and the factors influencing the propagation through the atmosphere, some comment should be made on what other forms of light might affect the observations. Firstly, the background continuum radiation from the night sky rises steadily by a factor of about six between 3600 Å and 6500 Å. This is fortunate, since the Cerenkov spectrum is peaked towards the violet. Absolute sky brightness does, of course, depend greatly on the site and local conditions; an important factor in the choice of observation site being freedom from extraneous lighting such as the diffuse light from a large town. Secondly, there is the possibility of contamination of the Cerenkov signal by light produced from other mechanisms. Table 2.1 shows that Cerenkov light production dominates over other mechanisms. The one exception to this

TABLE 2.1

Radiation processes for air at S.T.P. and radiation in the region 4000-6000 Å (from Jelley (1967)).

PROCESS	ASSUMPTIONS	ANGULAR DISTRIBUTION	ENERGY LOSS dE/dL ($eV.cm^{-1}$)
Cerenkov	E_e = 100 MeV	$\sim 1.3^{o}$	≈ 0.8
ionization + recombination	lifetime of the states $< 5.10^{-8}$ sec	isotropic	8.10^{-3}
synchrotron	$E_e \approx 3.10^{10}$	in vacuo(Mc^2/E)	1.3×10^{-7}
	$E_e \approx 10^{9}$ eV	in air 1.3^{o}	$\approx e^{-50}$
bremsstrahlung	Z = 9 E_e = 100 MeV	same as for synchrotron radiation	$< 4.10^{-5}$

is recombination light, which provides one method of observing EAS at the highest energies, and is utilised in the 'Fly's Eye' experiment (Bergeson et al. (1977)).

A prime disadvantage associated with Cerenkov radiation might be said to be its removal by one additional process from the principal workings of the shower. This complicates the interpretation of the observations in terms of the fundamental aspects of the primary cosmic rays and the particle interactions. The best approach to this problem is through the use of detailed Monte Carlo simulations of Cerenkov light in EAS, and these are discussed in the following section.

2.3 COMPUTER SIMULATIONS OF CERENKOV LIGHT IN EAS

2.3.1 Introduction

The inadequacy of simple analytic treatments of Cerenkov light in EAS was clearly indicated when Barclay and Jelley (1956) observed a substantial proportion of the light at core distances greater than 126m, which was the expected cut-off distance from calculations (Jelley and Galbraith (1955)) in which no account was taken of the lateral spread and angular distribution of the shower electrons. Detailed computer simulations have since enabled accurate predictions of many characteristics of the Cerenkov light in EAS, incorporating the effects of Coulomb scattering of electrons and other important factors such as the atmospheric attenuation of light.

The role of computer simulations of Cerenkov light is twofold. Firstly, they can provide information at the design stage of the experiment, indicating which observational parameters are expected to show the greatest sensitivity to the cascade development. Secondly, by tailoring the simulations specifically to the measured quantities, the observations can be interpretated without the ambiguities associated with interpretations based on more general treatments of EAS.

Although computer simulations of Cerenkov light in EAS have been carried out by many groups, consideration is restricted here to the results of the Durham group (e.g. Protheroe (1977) , Protheroe and Turver (1979), McComb and Turver (1981a, 1981b and 1982a)) which are directly relevant to the measurements analysed in this thesis.

2.3.2 The Calculation

A series of computer simulations of Cerenkov light in EAS have been carried out for the range of primary energy 10^{15} - 10^{18}eV, and for several models of the hadronic interactions based on the Feynman scaling hypothesis (Feynman (1969)). While scaling in the fragmentation region is preserved in each of the model calculations, the model for the pion multiplities in the central region is taken from : scaling ($n_s \propto \log E$) , $n_s \propto E^{1/4}$ or $n_s \propto E^{1/3}$. The calculations have also been performed for three different extrapolations from accelerator measurements of the pp and πp cross sections, i.e. σ = const., $\sigma \propto \log s$ and $\sigma \propto \log^2 s$. Primary particles of atomic mass number from A = 1 to A = 56 have been employed; calculations were made for observation levels at sea level and higher altitudes, encompassing a range of zenith angles from 0^o to 60^o.

The simulation technique has been described in detail by Protheroe (1977). The hadron cascade is treated in one dimension, and the pion production spectrum is calculated at 40 levels in the atmosphere. The electron-photon and Cerenkov-light components of the shower are then calculated from the pion spectrum. The high energy part of the electromagnetic cascade, for which the effect of Coulomb scattering is small, is described analytically using 'Approximation A' of cascade theory. At lower energies, the development of the cascade is followed in 4 dimensions by Monte Carlo methods. The Cerenkov radiation produced by the electromagnetic cascade is followed to the observation level through a realistic

atmosphere incorporating the wavelength dependent effects due to ozone absorption, aerosol attenuation and Rayleigh scattering. The detailed effects of the geomagnetic field on the lateral development of the electron cascade are also included. At the observation level the Cerenkov radiation can be folded with the spectral and temporal response of the detecting systems, allowing for detailed and direct comparison between observations and simulations.

2.3.3 The Lateral Distribution of Cerenkov Light

Figure 2.2 illustrates the expected average lateral distributions of Cerenkov light at sea level and at an atmospheric depth of 834 $g.cm^{-2}$ for three different primary masses and three decades of primary energy. The lateral distribution becomes broader when:

(i) the primary mass increases,

(ii) the primary energy decreases, and

(iii) the observation depth increases.

In each of these cases the cascade is developing further from the observation plane, which is the principal factor in determining the broadness of the lateral distribution. The total amount of light at the observation level depends on the primary energy, and this point is considered in more detail in section 4.3.2.

For core distances (r) in the range 100 - 500m the lateral distribution can be represented by a power law of the form:

$$\Phi(r) \propto r^{-\gamma} . \qquad 2.5$$

The steepness of the lateral distribution, i.e. the power law exponent (γ), is a strong measure of shower development: this is illustrated in figure 2.3 where it is plotted against depth of electron cascade maximum irrespective of assumptions of primary energy and primary mass.

The calculated lateral distributions for the Dugway altitude at an atmospheric depth of 862 $g.cm^{-2}$ in the core distance range 50 - 350m

FIGURE 2.2 The lateral distribution of photon density for average showers at two atmospheric depths. The calculations employed the scaling model with constant interaction cross-section. (From Protheroe and Turver (1977)).

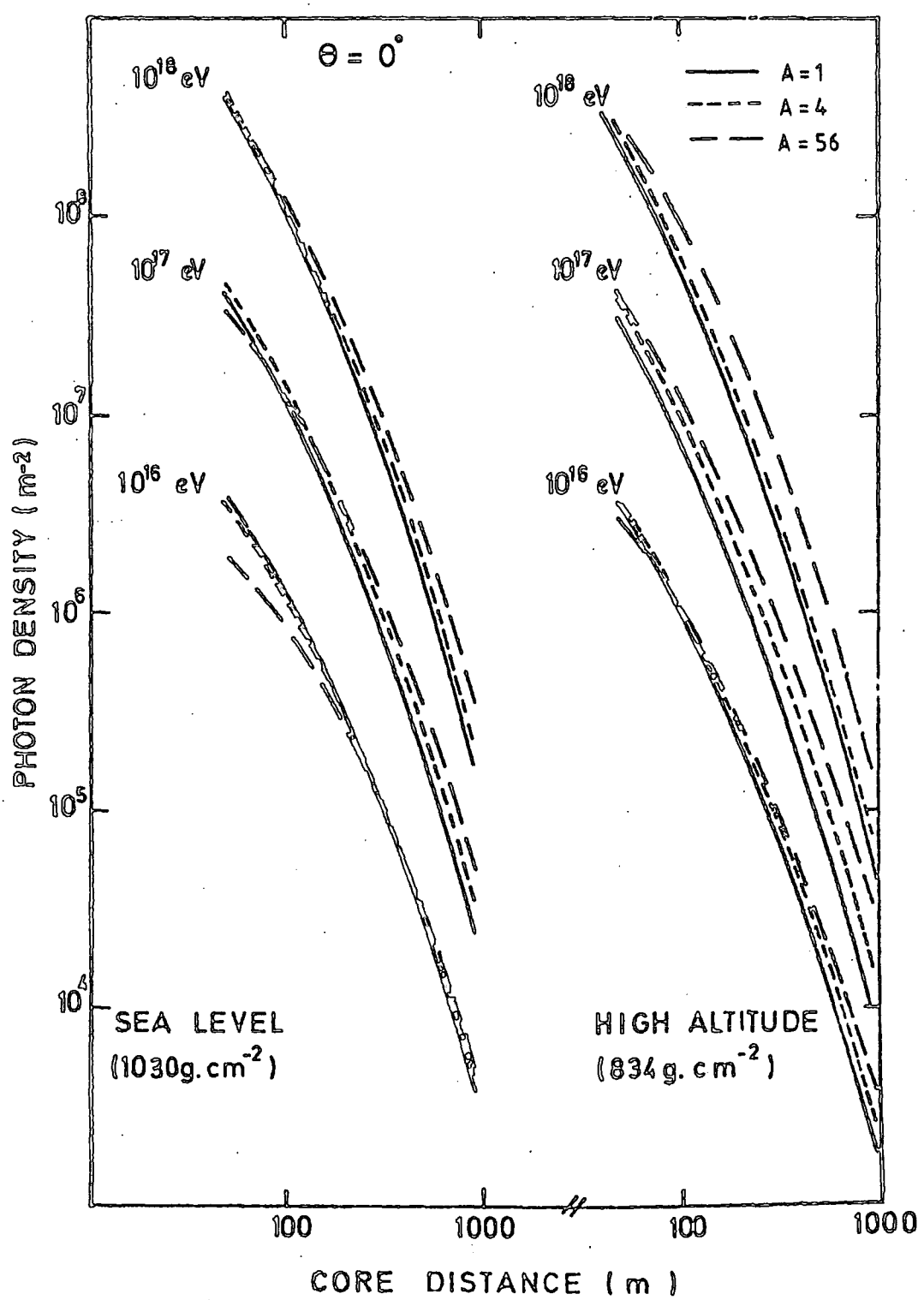

FIGURE 2.3 The lateral structure function exponent at sea level (γ) plotted against depth of cascade maximum irrespective of primary mass or primary energy. The calculations employed the scaling model with constant interaction cross-section. (From Protheroe (1977)).

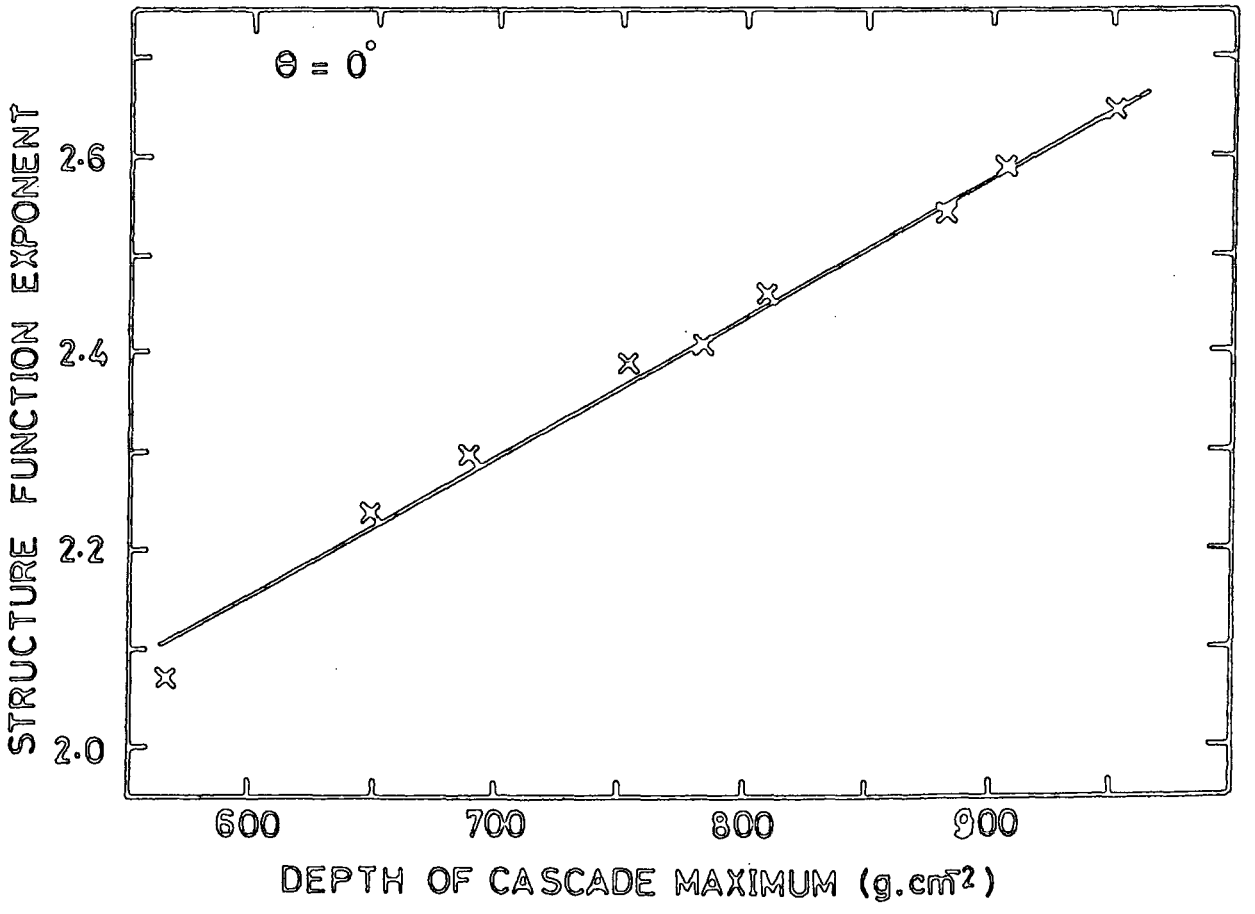

can be represented by a modified power law of the form:

$$\Phi(r) \propto (r + 50)^{-\eta} \quad . \qquad 2.6$$

In figure 2.4, the exponent (η) is plotted against depth of electron maximum for a range of models and for a range of zenith angles. It can be seen that, at least for the range of models considered here, the exponent (η) relates to the depth of cascade maximum with no significant model dependence. An increase in zenith angle produces a broadening of the lateral distribution as the cascade maximum develops at a constant depth but further away from the observation plane. However, it should be noted that the shape of the lateral distribution cannot be uniquely described in terms of distance (in $g.cm^{-2}$) to the cascade maximum independent of zenith angle, as might be expected from simple arguments, and has been assumed in many previous treatments of experimental data.

To summarise, the lateral structure function exponent can be related directly to depth of electron cascade maximum. This transformation is expected to be independent of primary mass, primary energy and model of hadronic interactions, but is specific to the particular zenith angle of the EAS.

2.3.4 The Cerenkov Light Pulse Profile

The time structure of the Cerenkov light pulse depends on path length differences from various levels in the cascade development, which result in time delays at the observation level. The dependence is complicated by other factors, in particular the Coulomb scattering of the shower electrons and refractive index effects. The detailed arrival-time distribution of Cerenkov light at the observation level is predicted from the simulations over a wide range of core distances.

The pulse profiles can be parameterised in a number of ways. The two most useful of these are the full width at half the maximum height (FWHM), and the rise-time, i.e. the time from the 10% to the 90% levels

FIGURE 2.4 The lateral structure function exponent at an atmospheric depth of 862 g.cm^{-2} (η) plotted against depth of cascade maximum irrespective of primary energy. The calculations are for average showers initiated by iron nucleus and proton primaries. Results for a range of interaction models and zenith angles are shown.

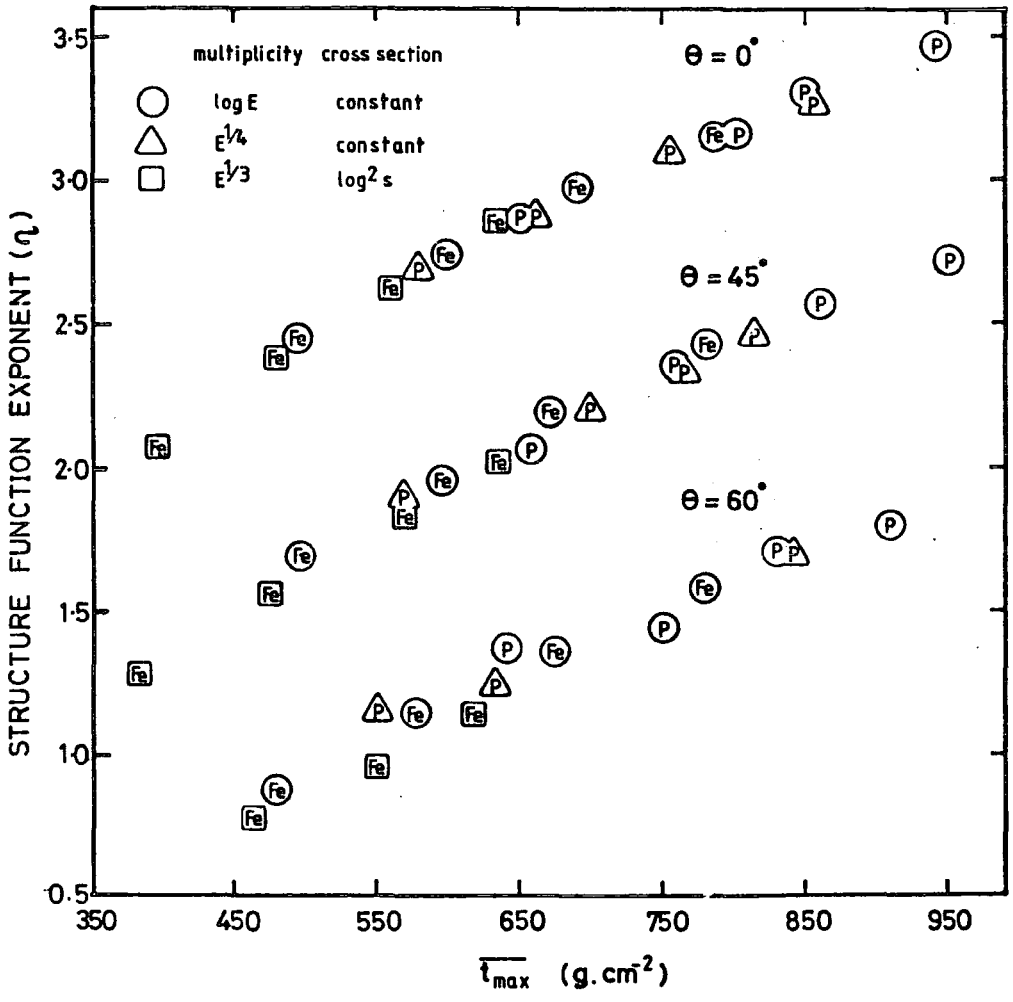

on the leading edge of the pulse. At large core distances ($\gtrsim$ 150m) both of these parameters increase monotonically with core distance and with increasing depth of electron cascade maximum. Figure 2.5 shows the dependence of FWHM at 300m from the core on the depth of electron maximum and zenith angle for the case of an infinite bandwidth system located at an atmospheric depth of 862 g.cm^{-2}. As in the case of the lateral structure function exponent, both the FWHM and the rise-time can be related directly to depth of shower maximum, independently of the primary mass, primary energy and model of hadronic interactions. The transformation to depth of maximum must again rely on the computer simulation result specific to the shower zenith angle. This is illustrated in figure 2.6, which shows that changes in the zenith angle introduce discontinuities into an otherwise smooth relation between distance to shower maximum and the FWHM at 300 m.

2.3.5 The Height of Origin of Cerenkov Light in EAS

It was first suggested by Fomin and Khristiansen (1971) and Efimov et al. (1973) that the FWHM of Cerenkov pulse depends on the longitudinal development of showers, and the dependence of pulse shapes on 'shower age' was investigated by Bosia et al. (1972). Later, Protheroe et al. (1975) indicated that other measures of the pulse time structure are also sensitive to the cascade development. In particular, they showed that the expected radii of curvature corresponding to the light arriving at successive percentage levels in the light pulse (e.g. 10%, 50%, and 95% levels on the leading edge and the 10% level on the falling edge) decreased monotonically with this sequence of percentage levels, and correlated strongly with depth of cascade maximum.

These developments stimulated an interest in identifying the origin of the light arriving at a given time in the pulse. A relation between

FIGURE 2.5 The FWHM (300 m) for an infinite bandwidth system, located at an atmospheric depth of 862 g.cm^{-2}, plotted against depth of cascade maximum irrespective of primary energy. The calculations are for average showers initiated by iron nucleus and proton primaries. Results for a range of interaction models and zenith angles are shown.

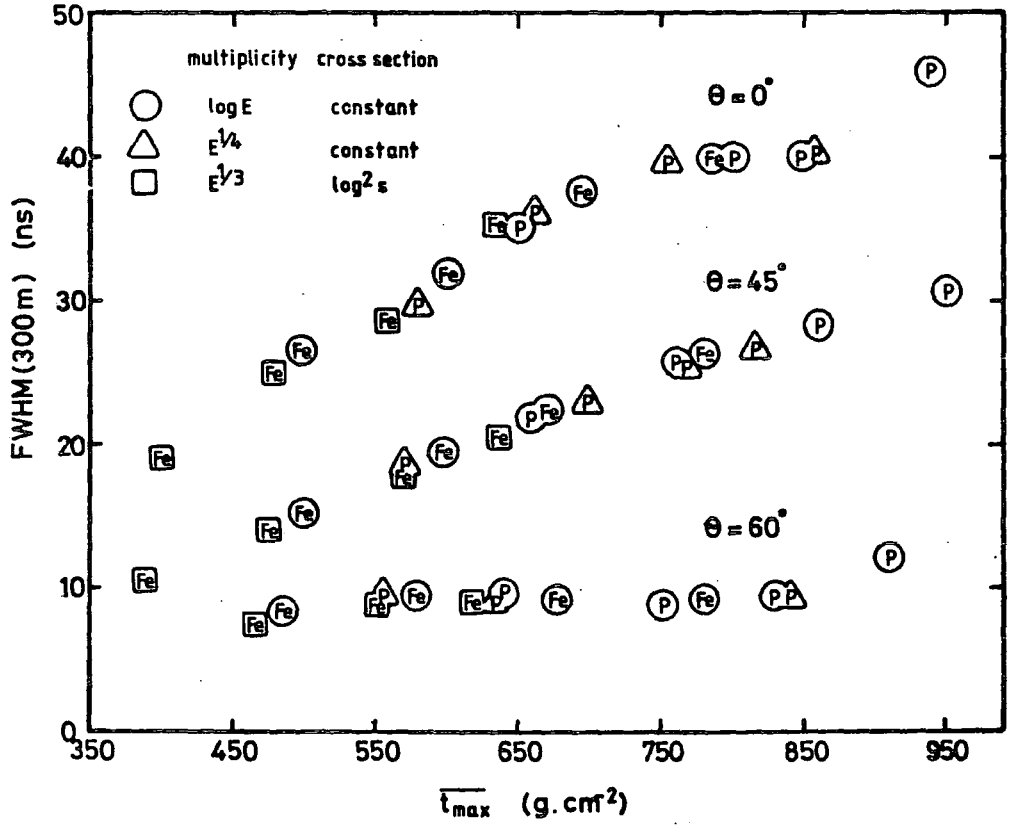

FIGURE 2.6 The dependence of the FWHM (300 m) at an atmospheric depth of 862 g.cm^{-2} on distance to shower maximum (in g.cm^{-2}) and zenith angle.

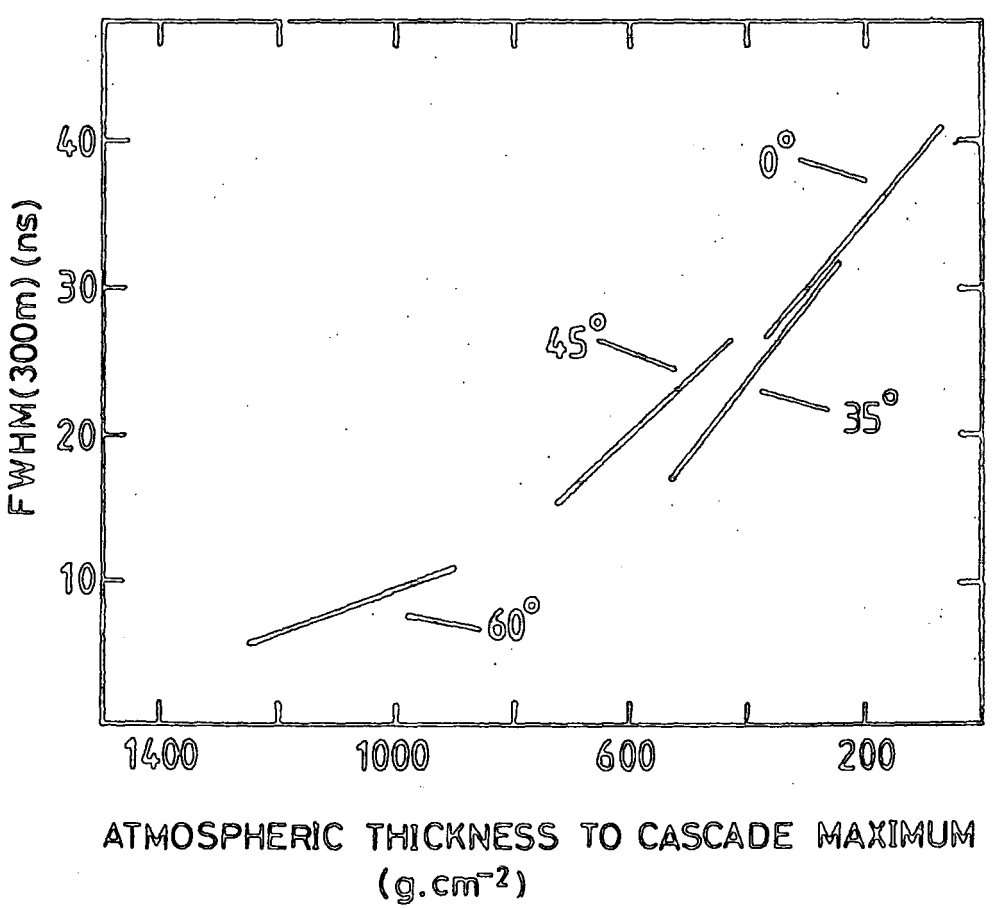

the height of origin of Cerenkov photons and their arrival time is suggested by a simple treatment of the delays due to path length and refractive index effects. A photon emitted from the core region of a vertical shower at an altitude h, will reach the ground at a distance r from the core at a time:

$$t\,(h,r) \simeq \frac{\sqrt{(h^2 + r^2)}}{c} \left\{ 1 + \frac{H}{h}\,(n - 1)(1-\exp\,(^{-h}/H)) \right\} \qquad 2.7$$

where H is the atmospheric scale height and n is the refractive index of air. Figure 2.7 shows the time delay { t(1km, r) -t(h,r) } using the approximation that the shower particles propagate at the velocity of light (c). It can be seen that for $r \gtrsim 100$ m the light reaches the observation level first from the highest altitudes, and that the arrival times show a direct relation to the altitude of origin of the light.

Computer simulations make possible the identification of those regions of the electron cascade which give rise to the Cerenkov photons at various times in the light pulse. An average 10^{17}eV proton initiated shower (scaling model) has been segmented by considering separately the electron cascades and the Cerenkov light resulting from the neutral pions produced in eight equal sections of atmospheric depth. Figure 2.8 shows the eight subshowers that make up the total electron cascade, and figures 2.9 and 2.10 show the contributions of each subshower to the total photon density and the pulse time structure respectively. It is clear from figure 2.9 that most of the light close to the shower core originates from low in the atmosphere; whereas at larger core distances the pulse shape follows the electron cascade development with the earliest detected light originating high in the atmosphere.

The link between the electron cascade development and the phase of the Cerenkov light pulse suggests the possibility of inferring the shape of a substantial part of the electron cascade from high resolution pulse shape measurements. Detailed information on the shape of the

FIGURE 2.7 The time delay of light originating at an altitude of 1 km with respect to that originating at h km as a function of h. (From Hammond et al. (1978)).

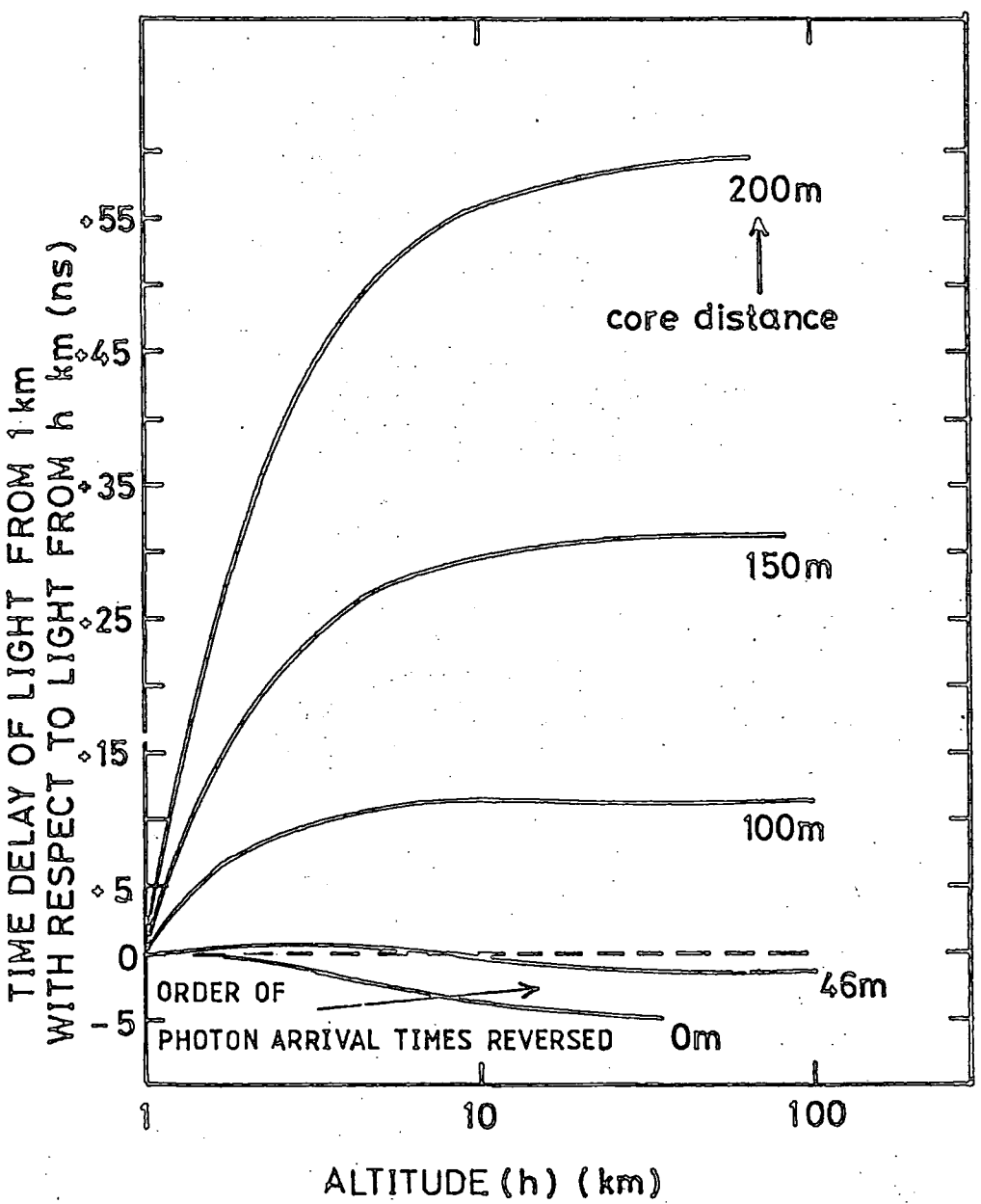

FIGURE 2.8 The electron cascade of an average 10^{17} eV proton initiated shower shown segmented into subshowers. The calculation employed the scaling model with constant interaction cross-section. (From Hammond et al. (1978)).

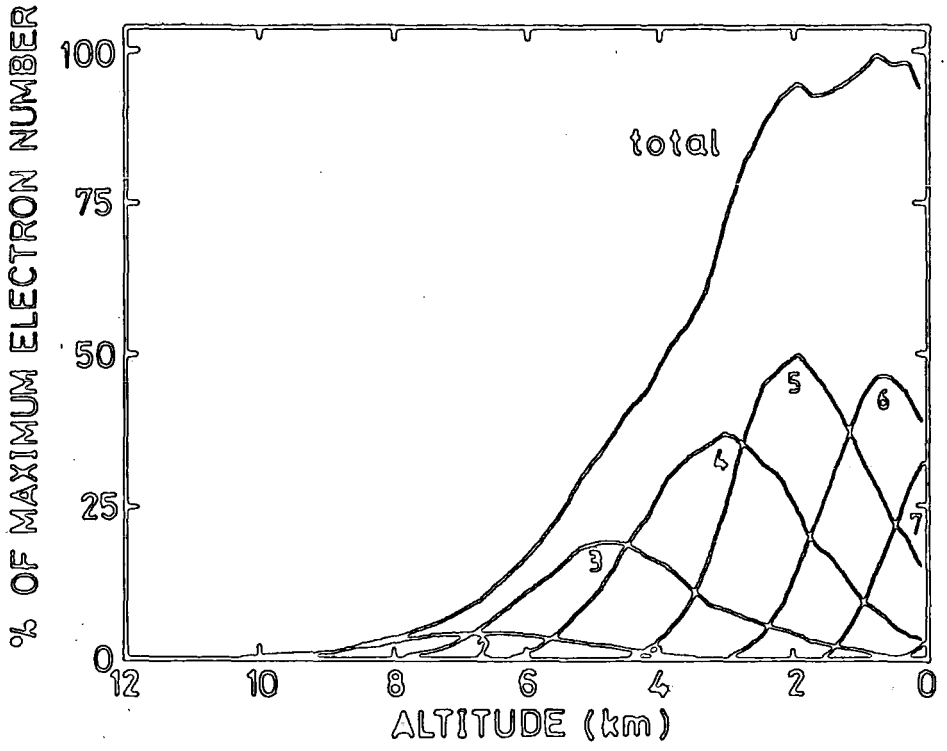

FIGURE 2.9 The lateral distribution of photon density at sea level showing the contributions from each of the subshowers of figure 2.8.

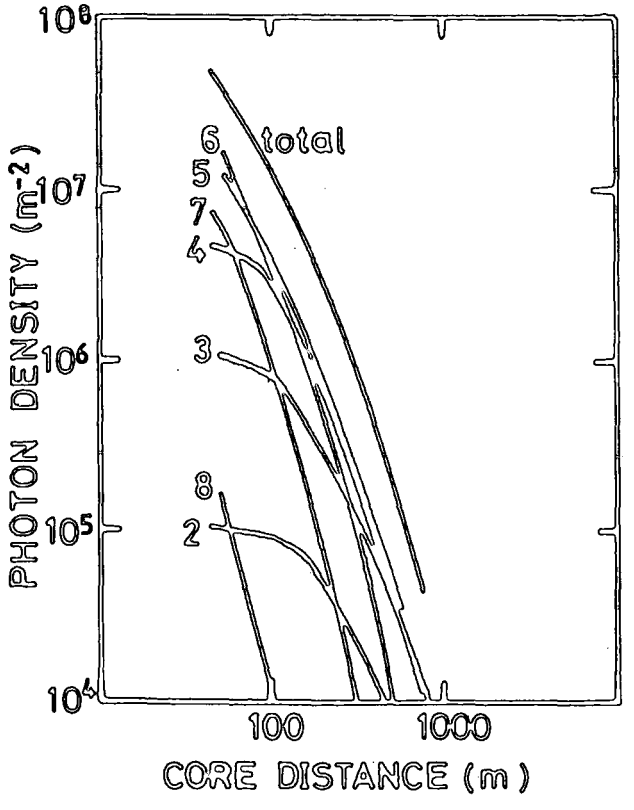

FIGURE 2.10 The contributions to the light pulse at sea level from each of the subshowers of figure 2.8 are shown at various core distances.

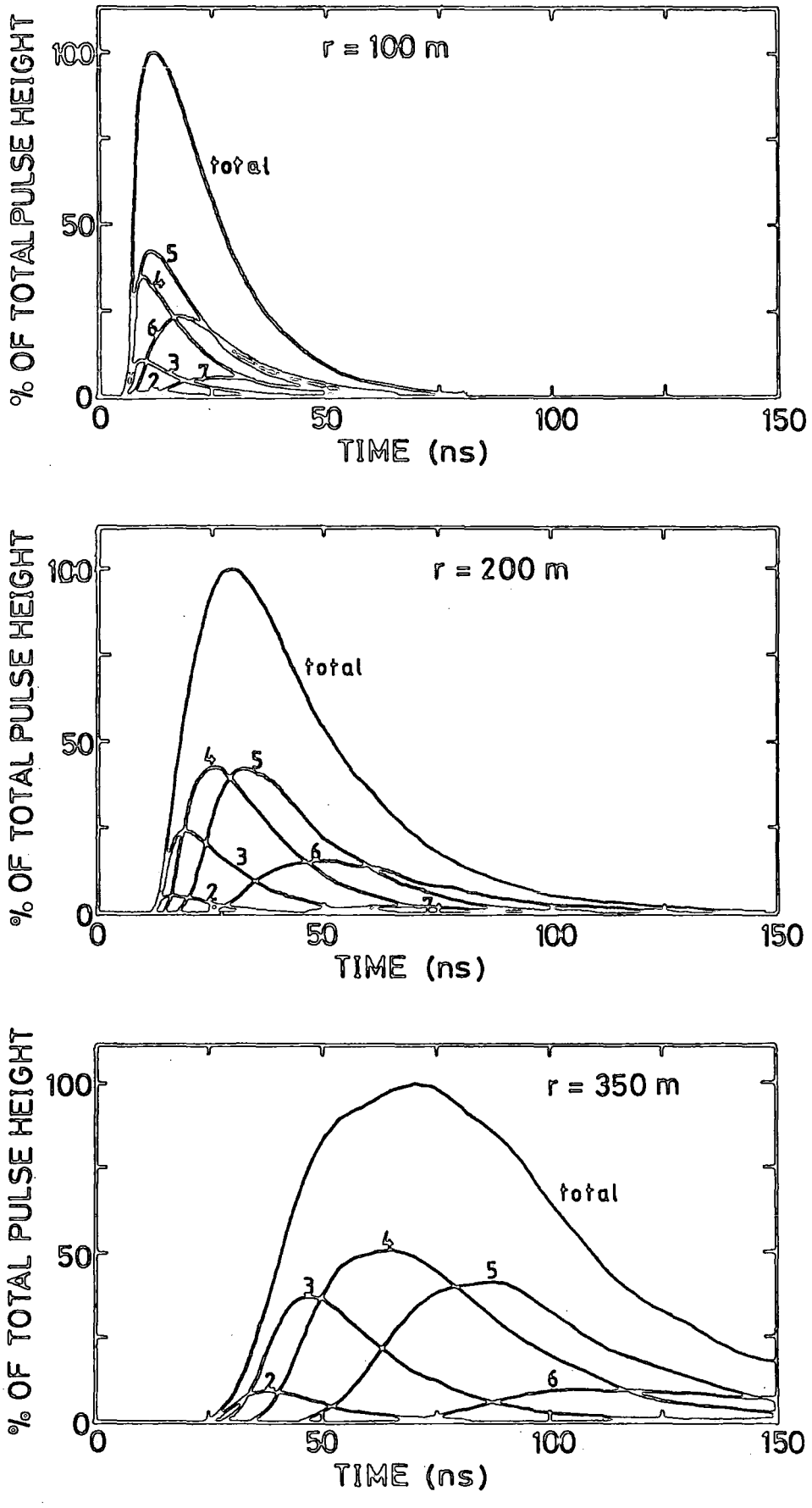

cascade (especially the important rising edge) would provide an additional constraint in the interpretation of air shower data in terms of the model of hadronic interactions and primary mass composition. In addition, the absolute arrival time of the light (or the curvature of the light front) relates to the depth of development of the cascade, and this forms the basis of a direct mapping of the cascade development described in the following section.

2.3.6 Imaging the Cascade from the Curvature of the Light Front

Whereas only slight differences in the shape of the electron cascade are found from simulations of showers initiated by different primary particles or generated using different models, more significant and more easily measurable differences in the depth of cascade development are apparent. Considerable importance is therefore attached to the measurement of this quantity. The lateral distribution of the light intensity and the pulse shape have already been shown to be sensitive to the depth of cascade development, parameterised for convenience by the depth of electron maximum. The mapping between the height of origin of the Cerenkov photons and their arrival time has led to the development of a technique to reconstruct both the shape of the cascade and its position in absolute terms directly from the timing information (Orford and Turver (1976)).

Figure 2.11 shows the arrival time of the light (with respect to the tangent plane) at specified percentages of maximum intensity as a function of core distance. The time delays at $r \gtrsim 150$ m are well represented by the form $a + br^2$, which is the dependence produced by a spherical light front. This provides the basis for the method of analysis in which the Cerenkov photons arriving at a certain percentage level in the light pulse are considered to have originated from a point source and propagated as a spherical front. This is justifiable since the light arriving at large core distances originates high above the array and is

FIGURE 2.11 The simulated time delay behind the tangent plane at sea level for various percentage levels of the pulse height as a function of core distance. The solid lines are fits to the form $a + br^2$ over the core distance range 100 - 500 m. The calculations incorporate the Haverah Park system response. (From Hammond et al.(1978)).

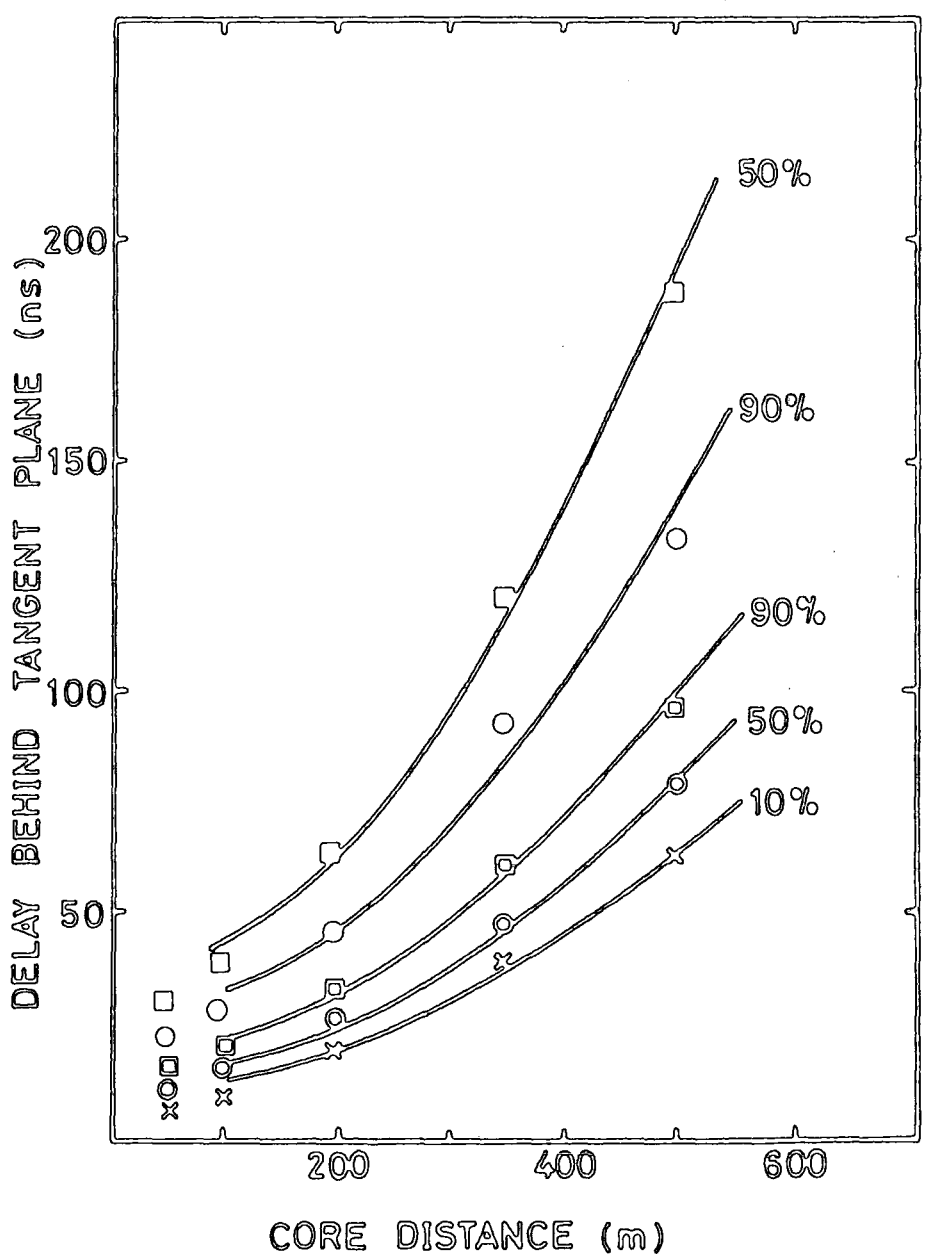

produced quasi-isotropically, i.e. the light is produced by widely scattered electrons in a volume which is small relative to the extent of the array.

The analysis technique requires the fitting of spherical fronts to the synchronised arrival times of the light at specified percentage levels in pulses at large core distances. The origins of the spheres obtained in this procedure are collinear and lie along the shower trajectory. Further, they provide an image in space and time of the build up and decay of the cascade as perceived in Cerenkov light. An immediate advantage of this procedure is that the sequence of centres of emission of Cerenkov light provide the shower arrival direction, and by extrapolation the shower core at the observation level. Figure 2.12 summarises schematically the information available for individual showers using this technique.

The observed depth of the cascade in Cerenkov light can, if required, be related to the more conventional parameterisation of longitudinal development, the depth of electron maximum. Calculated depths of the various percentage levels of the perceived Cerenkov image are found to correlate well with depth of electron maximum; this is illustrated in figure 2.13 for average cascades observed at sea level with the Haverah Park system bandwidth. It is seen that the Cerenkov image maximum occurs at systematically higher altitudes than the electron maximum; this is because the Cerenkov light is produced only by those electrons above the threshold energy. Also, the broadening of the observed light pulse due to the finite system bandwidth will cause a small displacement between the perceived image centre and the actual centre of Cerenkov light emission.

Figure 2.14 illustrates the relation between the perceived depth of Cerenkov maximum and the depth of electron maximum at the Dugway altitude

FIGURE 2.12 A summary of the information available from measurements of the synchronised time structure of the light pulse at widely spaced detectors.

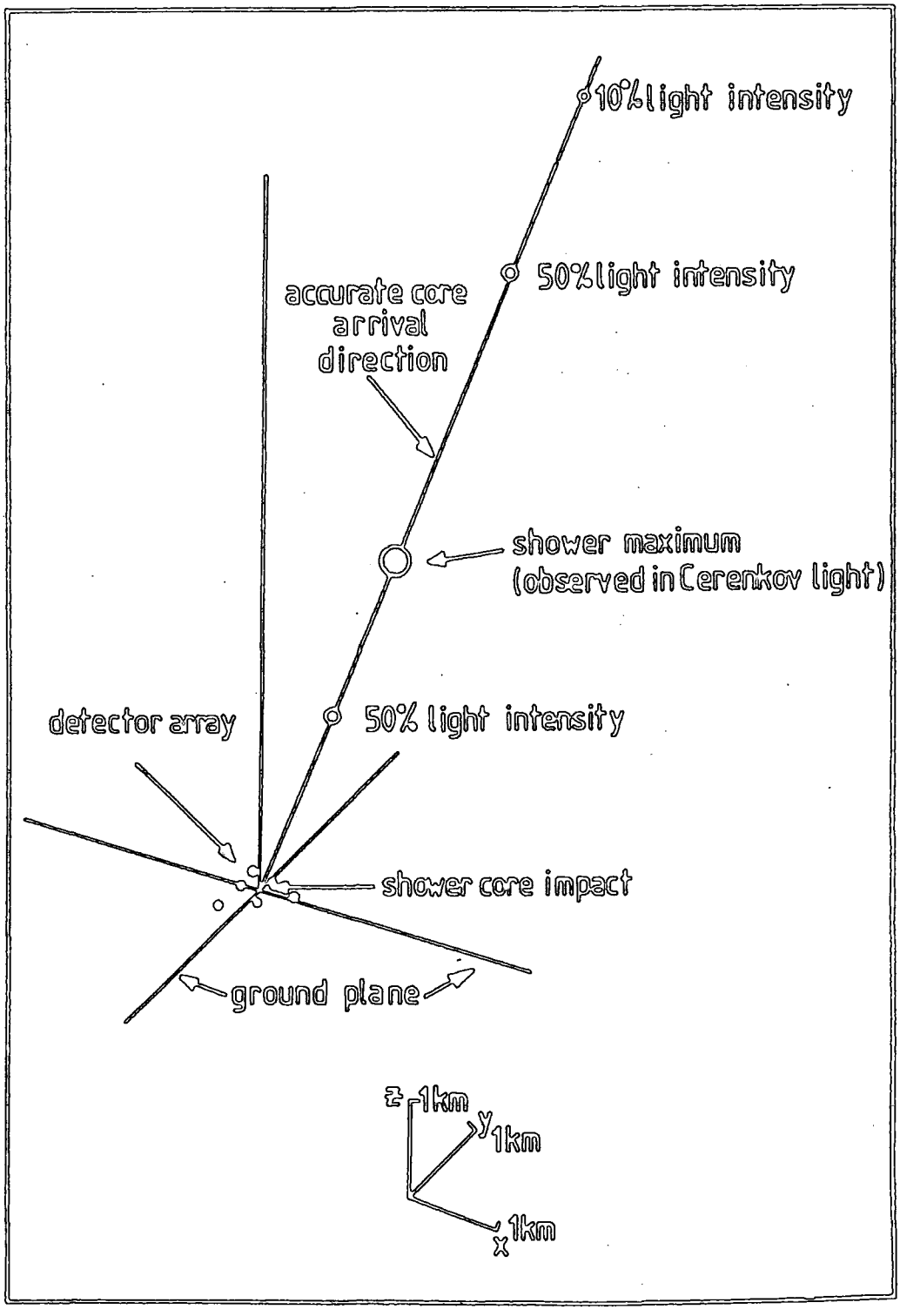

FIGURE 2.13 The depth of Cerenkov light origin corresponding to the 10% and 90% levels on the rising edge of the pulse and the 90% and 50% levels on the falling edge plotted against depth of cascade maximum. The calculations are for average showers observed at sea level with the Haverah Park system response. (From Protheroe and Turver (1979)).

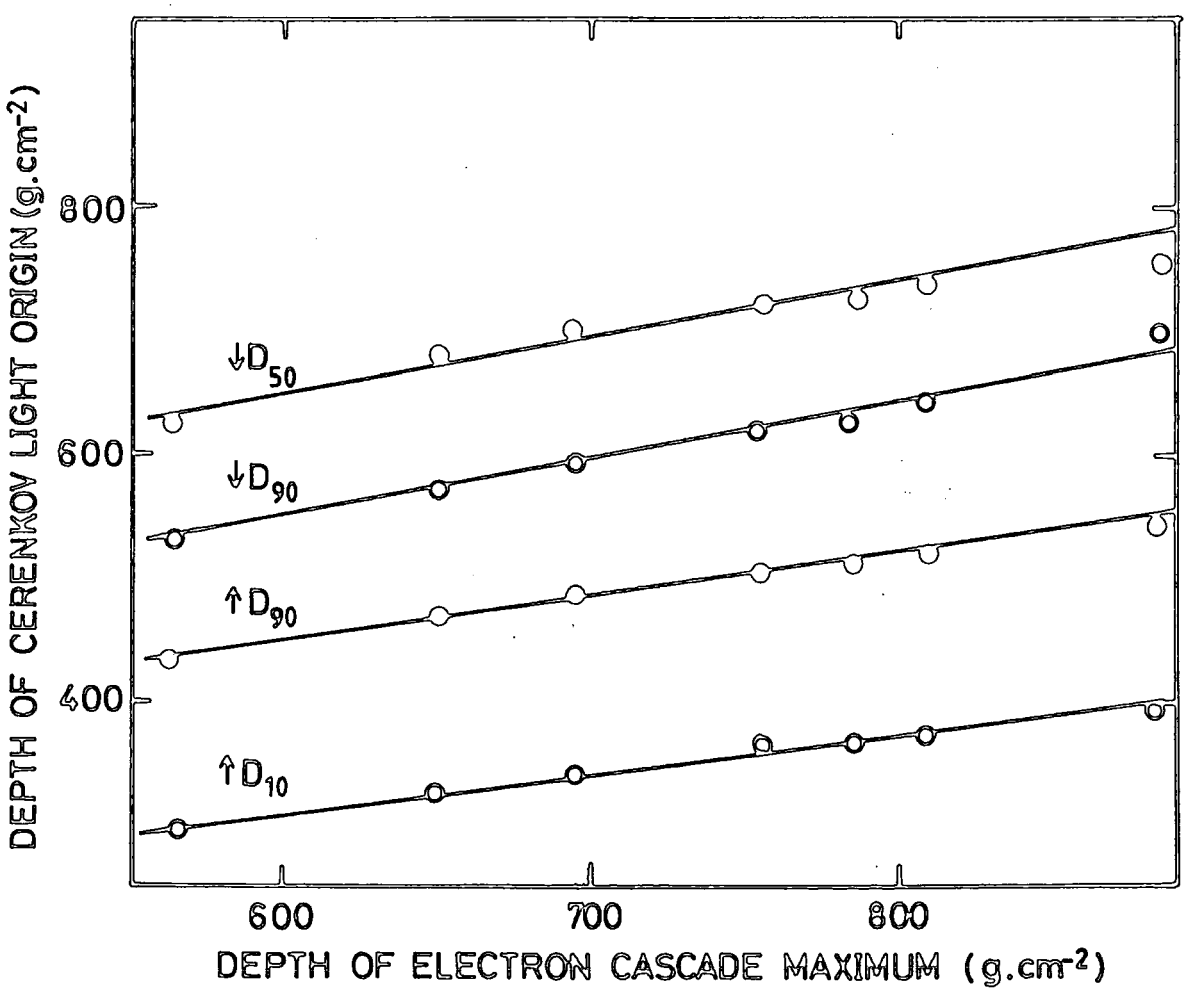

FIGURE 2.14 The depth of Cerenkov light maximum (D_{100}) for an infinite bandwidth system at an observation depth of 862 $g.cm^{-2}$ plotted against depth of cascade maximum irrespective of primary energy. The calculations are for average showers initiated by iron nucleus and proton primaries. Results for a range of interaction models and for two zenith angles are shown.

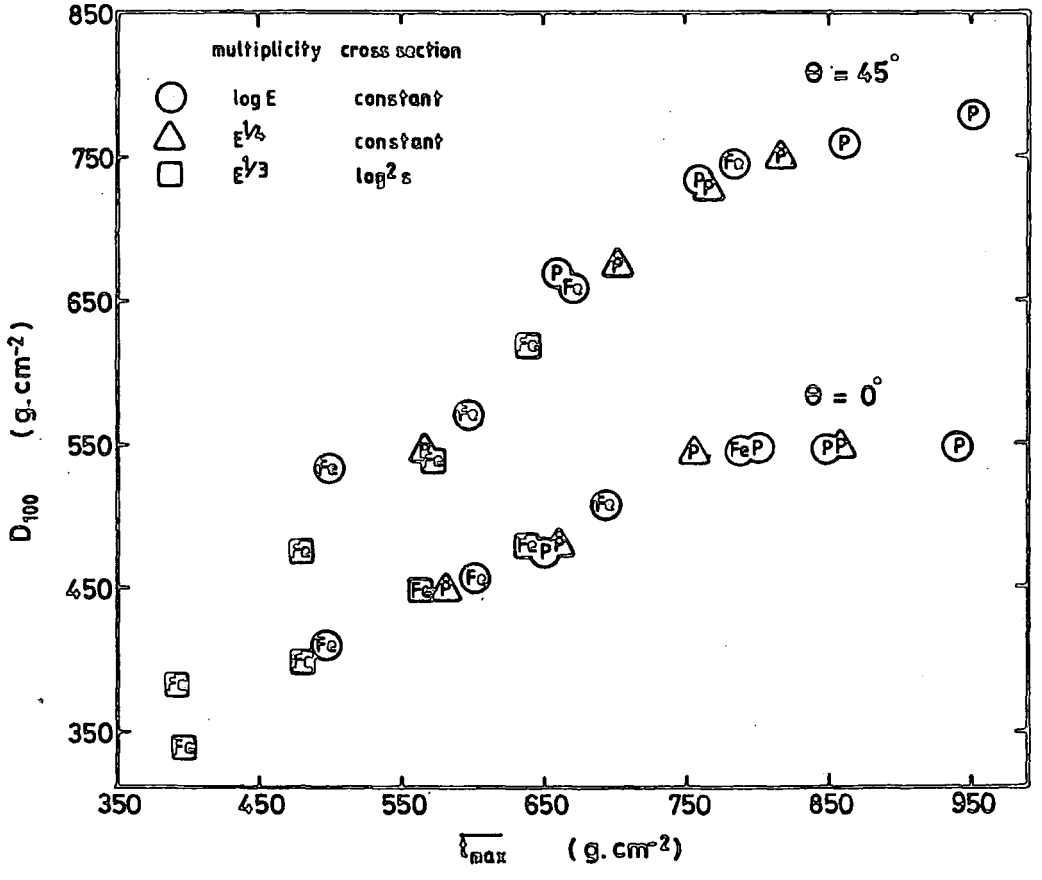

for several model calculations and for two zenith angles. A number of points of interest arise from this diagram. Firstly, it is clear that the transformation from depth of Cerenkov maximum to depth of electron maximum can be made with no significant model dependence. Secondly, the increase in altitude (from Haverah Park to Dugway) causes a severe reduction in sensitivity for the deeper developing vertical showers. This is thought to be a geometric effect due to the detectors not receiving the light from the low altitude part of the cascade. Thirdly, an increase in zenith angle produces an increase in the apparent depth of Cerenkov maximum due to more of the latter part of the cascade being imaged.

Despite the effects of these processes on the perceived Cerenkov image, the technique is expected to show good sensitivity to the longitudinal cascade development at the Dugway altitude for non-vertical showers of energy > 10^{17}eV. For example, the time delay behind the tangent plane of the peak of the light pulse at r = 350 m changes by about ± 5ns for a ± 100 g.cm^{-2} change in depth of electron maximum (for a 45^{o} shower). This compares to a change in the FWHM of the pulse of ± 4 ns. Calculations by other workers have confirmed both the feasibility of reconstructing the cascade curve from synchronised measurements of the arrival time (Ivanenko and Makarov (1977)), and the greater sensitivity of the absolute arrival times over the pulse widths to height of cascade development (Hillas (1982)).

2.3.7 Cerenkov Light from Fluctuating Showers

Measurements of the average characteristics of EAS based on observational parameters described in sections 2.3.3 to 2.3.6 are expected to provide some constraints on the range of possibilities for the primary mass composition and nuclear interaction models. However, an interpretation of the measured average depth of cascade maximum in

terms of the primary mass composition would be strongly model-dependent. The most promising source of additional information on the mass composition is, as explained in chapter 1, the extent of the shower to shower fluctuations in the cascade development. The fluctuations in the electron cascade are mirrored by fluctuations in the development-sensitive Cerenkov light parameters. For example, figure 2.15 illustrates the expected correlation between the depth of electron maximum and the lateral structure function exponent (γ) at sea level for 20 proton and 10 iron nucleus initiated showers of energy 5×10^{17}eV. Similar correlations are obtained for other development-sensitive Cerenkov light parameters. The iron nucleus initiated showers clearly produce a much smaller range of fluctuations in the Cerenkov light parameters than the proton initiated showers. The fluctuations between cascades, measured by the variations in development-sensitive Cerenkov light parameters, would provide a less model-dependent source of information on the primary mass composition.

2.3.8 Conclusions

The Cerenkov light signal can be described in detail by three independent facets, each of which has been shown to be sensitive to the longitudinal cascade development:

(i) the lateral distribution of Cerenkov light intensity,

(ii) the pulse time structure as parameterised by the FWHM or the rise-time, and

(iii) the origin of light derived from the curvature of the light front.

In each of these cases the measured Cerenkov parameter can be related to the depth of electron cascade maximum (a useful parameter for inter-comparison between many differing EAS measurements). The transformation from Cerenkov light parameter to depth of electron cascade maximum can

FIGURE 2.15 The sea level lateral structure function exponent (γ) in individual proton and iron nucleus initiated showers plotted against the depth of cascade maximum. (From Protheroe and Turver (1979)).

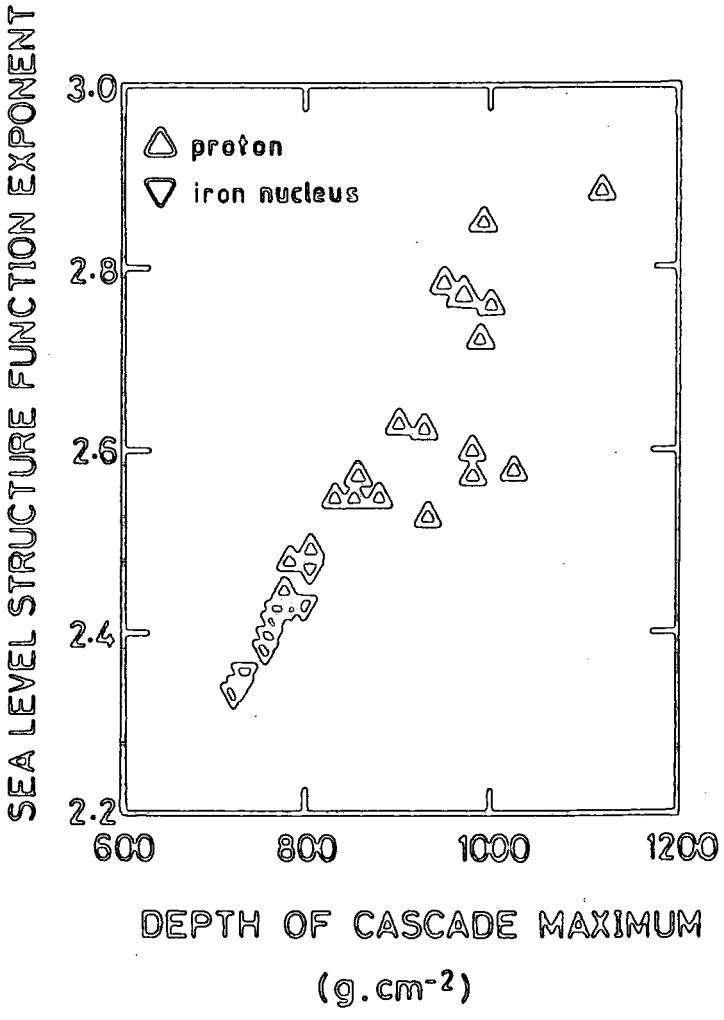

be made virtually independently from the choice of primary mass, primary energy, or model of hadronic interactions employed in the calculation. This is a consequence of the complete dependence of the Cerenkov light signal on the electron-photon cascade. The transformation is, however, specific to the shower zenith angle. The recent availability of simulations of Cerenkov light from inclined showers is therefore expected to permit more detailed interpretations of current measurements.

The accurate experimental determination of the average shower development, and comparison with simulation predictions, is expected to provide some constraints on the question of primary mass composition and the model of hadronic interactions. Valuable additional constraints can be expected from observations of the fluctuations in Cerenkov light parameters which reflect the intrinsic fluctuations in the cascade development.

2.4 OBSERVATIONAL BACKGROUND TO THE PRESENT WORK

2.4.1 Introduction

In recent years observations of Cerenkov light in EAS have been made at many locations and at several altitudes. Table 2.2 lists some of the arrays which are currently operating (a few of which have only recently been established) or which have been operating within the past decade. An indication is given for each array as to which aspects of the Cerenkov signal have been investigated and the range of primary energy considered. Where relevant data are available, results from these experiments will be compared with results from the Dugway array in chapter 7.

Attention is focussed here on results from the Durham group's pilot experiment at Haverah Park (e.g. Hammond et al. (1978), Protheroe and Turver (1979)). Measurements of Cerenkov light in EAS were made

TABLE 2.2

Recent experiments to observe Cerenkov light in EAS.

	APPROXIMATE ENERGY RANGE (eV)	ATMOSPHERIC DEPTH	LATERAL DISTRIBUTION	PULSE SHAPE	LIGHT FRONT CURVATURE
Yakutsk (U.S.S.R.) Kalmykov et al. (1977)	2×10^{16} - 3×10^{18}	sea level	√	√	
Samarkand (U.S.S.R.) Khristiansen et al. (1977)	3×10^{15} - 3×10^{16}	940 $g.cm^{-2}$	√	√	
Buckland Park (Australia) Thornton et al. (1979)	5×10^{15} - 10^{17}	sea level	√	√	
Bowie (U.S.A.) Tornabene (1979)	10^{13} - 10^{15}	sea level	√		√
Akeno (Japan) Inoue et al. (1981)	3×10^{15} - 10^{18}	935 $g.cm^{-2}$	√	√	
Haverah Park (U.K.) Hammond et al. (1978)	2×10^{17} - 2×10^{18}	1016 $g.cm^{-2}$	√	√	√
Volcano Ranch (U.S.A.) Orford et al. (1976)	10^{17} - 10^{18}	834 $g.cm^{-2}$	√	√	
Dugway (U.S.A.) Chantler et al. (1979a)	3×10^{15} - 10^{18}	862 $g.cm^{-2}$	√	√	√

with an array of eight widely spaced detectors operating in conjunction with the deep water Cerenkov detectors of the EAS particle array. The measurements, recorded with an analogue system, included the lateral distribution, the pulse shape and the curvature of the light front.

2.4.2 The Lateral Distribution of Pulse Areas

Figure 2.16 shows the measured average lateral distributions of Cerenkov light intensities for showers of primary energy estimator $\rho\ (500)_{ve}$ = 2.0 and 0.2 m^{-2} (the Haverah Park primary energy estimator, indicating the particle density at 500 m from the core). These results were compared with computer simulation predictions, and interpreted (Wellby (1977)) as indicating depths of shower maximum at 610 ± 98 $g.cm^{-2}$ and 810 ± 98 $g.cm^{-2}$ respectively. The radial dependence of light intensities (in the range 100 - 500 m) was found to be satisfactorily described by a simple power with exponent (γ) (as in equation 2.5).

The lateral structure function exponent (γ) was shown by multiple regression to exhibit the following variation with primary energy estimator and zenith angle (θ):

$$\gamma = 1.20 - 3.55 \cos\theta - 0.29 \log_{10} \rho(500)_{ve} \quad . \qquad 2.8$$

This result is consistent with the broadening of the lateral distribution as the showers develop further from the observation plane.

2.4.3 The Pulse Profiles

Figures 2.17 and 2.18 show the variation of the pulse FWHM and rise-time with core distance for showers of energy $\sim 2 \times 10^{17}$eV. These data are compared with the computer simulation predictions for an average, scaling model, iron nucleus initiated shower. Also shown are results from the Yakutsk array (Kalmykov et al. (1976)), which have had the effects of instrumental broadening removed by the authors. The results are consistent with the simulation expectation for a cascade with a depth of maximum of $\sim$ 700 $g.cm^{-2}$. The radial dependence of the

FIGURE 2.16 Average lateral distributions of Cerenkov light densities recorded with the Haverah Park system.

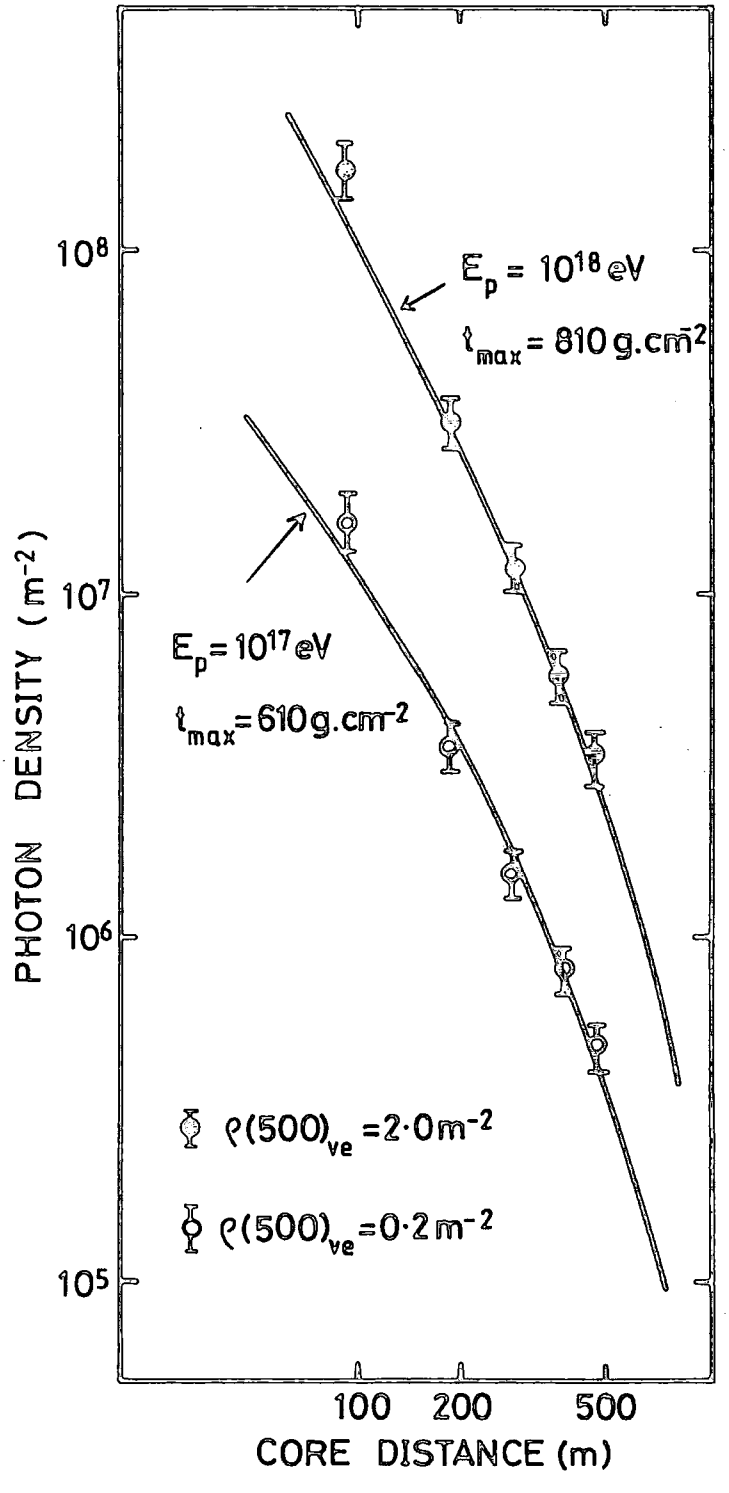

FIGURE 2.17 The average variation of the FWHM with core distance recorded with the Haverah Park and Yakutsk systems. (From Protheroe and Turver (1979)).

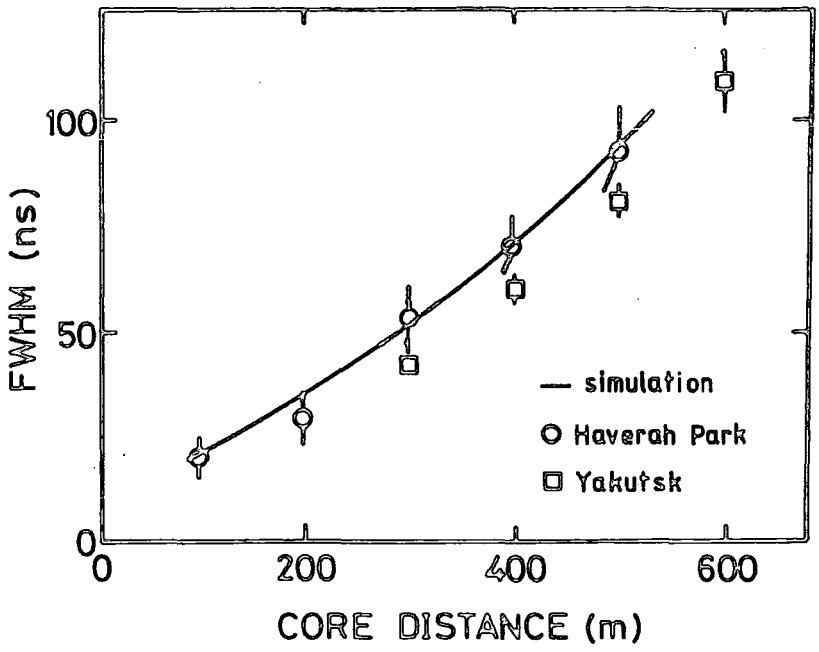

FIGURE 2.18 The average variation of the rise-time with core distance recorded with the Haverah Park system. (From Protheroe and Turver (1979)).

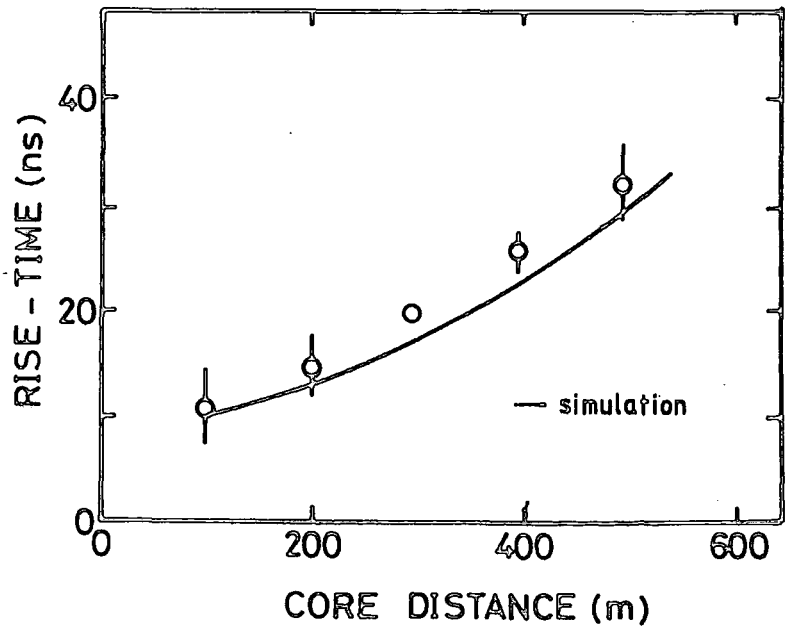

FWHM and rise-time (in the range 100 - 500 m) was found to be consistent with the form $a + br^2$, which is the dependence suggested by the near sphericity of the light fronts (see section 2.3.6).

Zenith angle and energy variations were also observed in the pulse shape measurements. For example, the FWHM at 400 m from the core was found, by multiple regression, to show the following dependence:

$$\text{FWHM}(400\text{ m}) = -45.14 + 120.3 \cos\theta + 9.92 \log_{10} \rho(500)_{ve} . \quad 2.9$$

This result is consistent with the expected narrowing of the pulse as the depth of shower maximum occurs further from the observation plane.

2.4.4 Imaging the Cascade from Curvature Measurements

The early measurements of the curvature of the light front were made in small showers ($\lesssim 10^{15}$ eV), close to the shower core. At such distances most of the results showed that the origin of the light was low in the atmosphere: 3 km according to Malos et al. (1962) and $\gtrsim$ 2 km according to Boley et al. (1961). As discussed in section 2.3.5, this is to be expected for measurements close to the shower core, but at larger core distances the majority of the light will be received from higher altitudes.

Synchronised measurements of the arrival time of the light front made at Haverah Park (Orford and Turver (1976)) enabled the estimation of the radii of curvature of the light arriving at various percentage levels in the light pulse. Spherical fits to the 10% level on the rising edge, for example, produced radii of curvature ranging from 5 to 12 km, with residual deviations from perfect spheres of only a few ns. No systematic deviations from sphericity were observed in the data. Figure 2.19 shows the average Cerenkov image for showers of primary energy $\sim 2 \times 10^{17}$ eV obtained by making spherical fits to the timing data in individual showers recorded with zenith angles up to 40°. Also shown are the computer simulation predictions for average vertical showers

FIGURE 2.19 The average Cerenkov image obtained from synchronised measurements of the time structure of the Cerenkov light signal. (From Orford and Turver (1976)).

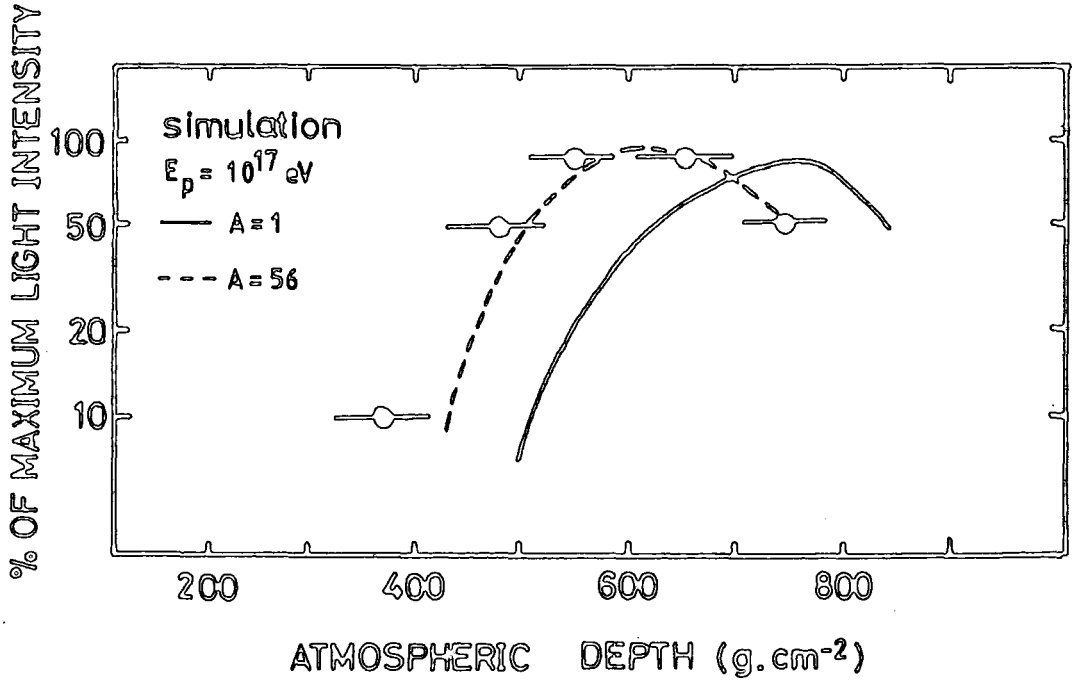

having two different depths of electron cascade maximum. This work showed the potential of this technique to provide useful information on the longitudinal cascade development in individual showers.

2.4.5 Fluctuations in the Cascade Development

A preliminary investigation of the fluctuations in the cascade development was carried out by Wellby (1977). Removal of the systematic variations in the Cerenkov light parameters due to the finite zenith angle and energy ranges leaves residual variations due both to fluctuations in shower development and to measurement errors. Correlations between the residual variations in independent parameters were established, confirming that genuine cascade fluctuations were being observed. However, the data sample was not large enough to permit a detailed quantitative analysis of the measurement errors. The estimate of the fluctuations in depth of cascade maximum was 111 $g.cm^{-2}$. This represented an upper limit, containing an unresolved component due to measurement errors.

2.4.6 Conclusions

The observations of Cerenkov light carried out at Haverah Park were found to be in satisfactory overall agreement with computer simulation predictions. The combination of results from the different techniques implied that the average characteristics of showers of primary energy $\sim 2 \times 10^{17}$ to $\sim 2 \times 10^{18}$ eV were consistent with cascades having depths of maximum from ~ 680 to ~ 770 $g.cm^{-2}$. The sensitivity of the observational parameters to cascade development in individual showers was demonstrated; and although significant fluctuations between showers were observed, the data sample was insufficient for the estimation of the primary mass composition.

This work provided the motivation for a new atmospheric Cerenkov light experiment at Dugway, U.S.A. The new site was chosen for its

considerably more favourable climate, offering long periods of clear skies and the possibility of recording a significantly larger data sample. In addition, the experience gained at Haverah Park could be employed in the construction of Cerenkov light detectors of improved design specification. With these advantages, the aim of the new experiment was to provide a more detailed determination of the average characteristics of showers and an estimation of the size of fluctuations in the cascade development. Accurate measurements of these quantities could be expected to provide a worthwhile contribution to the studies of the primary mass composition.

CHAPTER 3

THE DUGWAY ATMOSPHERIC CERENKOV LIGHT EXPERIMENT

3.1 INTRODUCTION

An EAS array of Cerenkov light detectors was established at Dugway Proving Grounds in the Great Salt Lake desert, Utah, U.S.A. (longitude 112^{o} 49'W, latitude 40^{o} 12'N), during the summer of 1977. The site was located at an altitude of 1451 m above sea level, with a mean vertical depth into the atmosphere of 862 $g.cm^{-2}$. Data were taken during three seasons of operation from September 1977 until March 1980 when the array was dismantled. In this chapter a description is given of the recording equipment and its calibration, the running periods, and the procedures developed to process the data into a convenient form for future more detailed analyses. Figure 3.1 shows the array layout (of 400 m radius) employed to record large showers of primary energy $\sim 10^{17}$eV.

3.2 THE RECORDING EQUIPMENT

3.2.1 Design Considerations

The Haverah Park Cerenkov detector array utilised an analogue recording system,whereby the Cerenkov pulse received by each photo-multiplier was amplified and passed down a high quality coaxial cable to a central recording station. Here the signals were displayed on oscilloscopes and photographed on fast film. The response of this system to a 2 ns wide light pulse (from a NE 130 light pulser) was a pulse with a FWHM of 18 ns and a rise-time of 9 ns. In order to obtain increased sensitivity to the longitudinal cascade development, the new experiment required an improved system response. This was to be achieved by digitising appropriate information on the Cerenkov light signal at each detector. In this way the information could be transmitted in digital format to the central recording station, avoiding the degradation of the signal associated with the transmission of an analogue pulse through

FIGURE 3.1 The layout of the Dugway atmospheric Cerenkov light array adopted for recording large showers of primary energy $\sim 10^{17}$ eV.

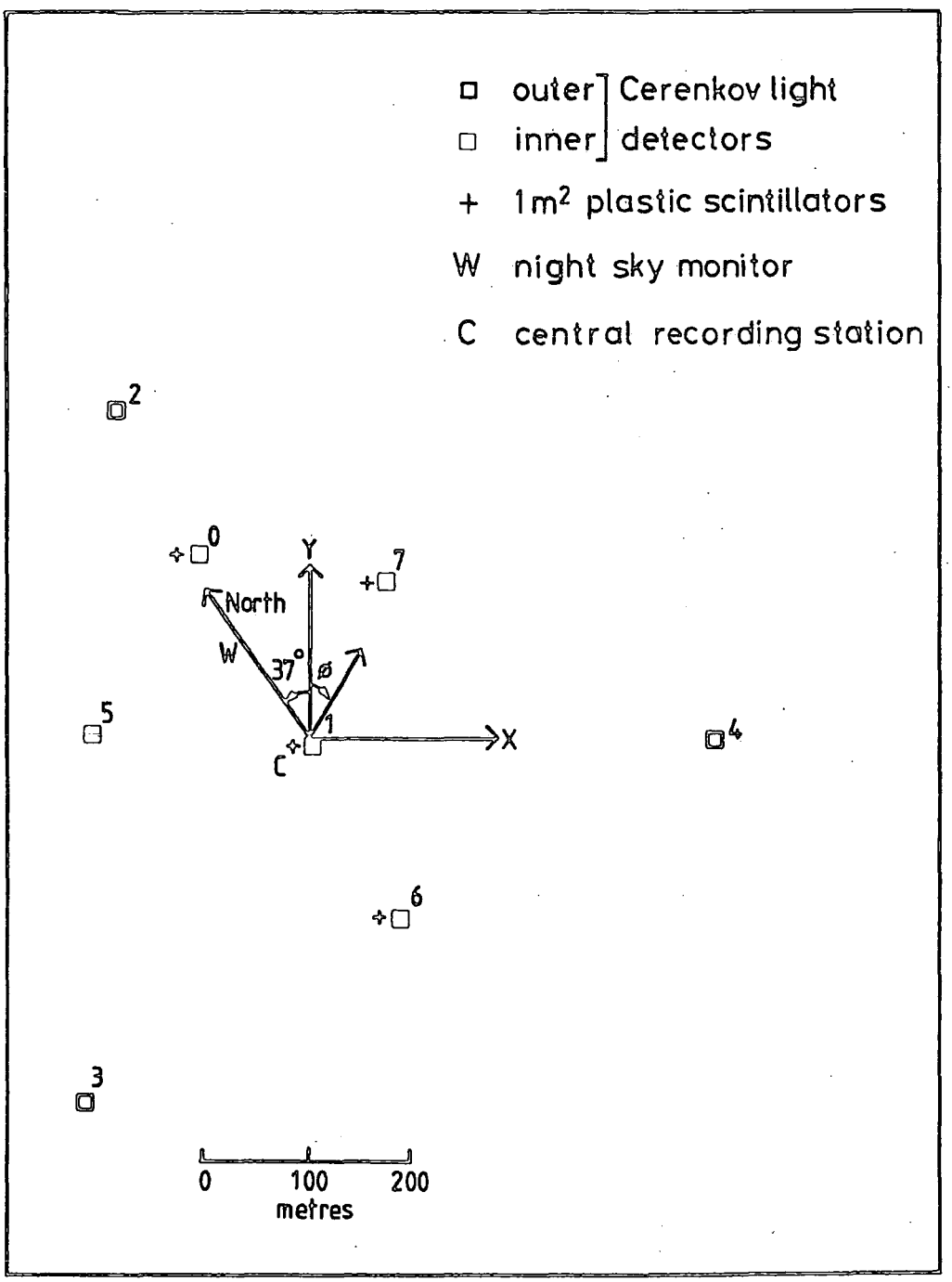

several hundred metres of cable.

The information to be digitised was the pulse area, the time of arrival of the pulse and the pulse shape. In order to avoid an 'a priori' decision on which pulse shape parameters would contain the most information (e.g. the rise-time) and digitising these, a more flexible system was adopted. The charge would be measured sequentially through the pulse in narrow time intervals, after which the pulse shape could be reconstructed using fitting procedures. Further details of the digitisation process are given in section 3.2.3.

The photomultiplier tubes and the housing of the new detectors were tested in April 1976 in conjunction with the Volcano Ranch array at Albuquerque, New Mexico, at an atmospheric depth of 834 $g.cm^{-2}$.

The description of the recording equipment in the following sections is applicable to the second and third seasons of operation of the Dugway array (from September 1978), during which the majority of the data was recorded. Some minor modifications to the equipment were made following the first season of operation which have been described by Shearer (1980).

3.2.2 The Cerenkov Light Detectors

The array comprised of eight Cerenkov light detectors each of which contained a fast response, 12 cm diameter, photomultiplier (R.C.A. type 4522), viewing the night sky through a perspex window, together with its associated electronics. The response of this type of photomultiplier to a light flux has been described by Orford et al. (1977). During daylight hours the photocathode was protected from the bleaching effect of the sunlight by a blind which was automatically drawn above the photomultiplier face. Surrounding the photomultiplier tube was a mumetal shield to minimise the effect of the geomagnetic and local magnetic fields on its performance. Each detector contained a thermostatically

controlled heating element which could maintain the internal detector temperature at approximately 20°C during the cold desert winters when the air temperature often dropped to < -10°C. During the hot summers, when daytime air temperatures rose to > 35°C, fans circulated air and helped to maintain the electronics at the ambient temperature.

When exposed to moonless clear night sky, each photomultiplier was operated with a photocathode potential such that the anode current was normally only 1% of the maximum rating. In the event of the current of any tube exceeding 10% of this maximum, the high voltage was turned off automatically. The signal was taken from the 11th dynode of the photomultiplier tube (which has a total of 14 dynodes) to allow the voltage per stage to remain high with a consequent fast response time. Further amplification of the signal (x 100) was obtained by two LeCroy VV100 amplifiers, yielding a total photomultiplier amplifier gain of 60,000. After amplification the signal was split, one channel going to a discriminator, and the other to an 8-way fanout. The purpose of the fanout was to feed the signal to the digitising electronics which would simultaneously sample various aspects of the pulse. Figure 3.2 shows the analogue paths within a detector.

The detectors were small (60 x 55 x 90 cm) and portable. This allowed them to be quickly relocated to form arrays of radii 200 m and 100 m in addition to the main array format of 400 m radius.

3.2.3 The Digitisation System

When the amplified signal exceeded a threshold of 20 mV, the discrimination unit generated a set of command pulses. Some of these were sent to initiate 10 ns wide gates to measure the charge sequentially through the pulse; another pulse was used to start a time stretcher (all timing occurred relative to the time at which the discrimination

FIGURE 3.2 The analogue paths within a detector.

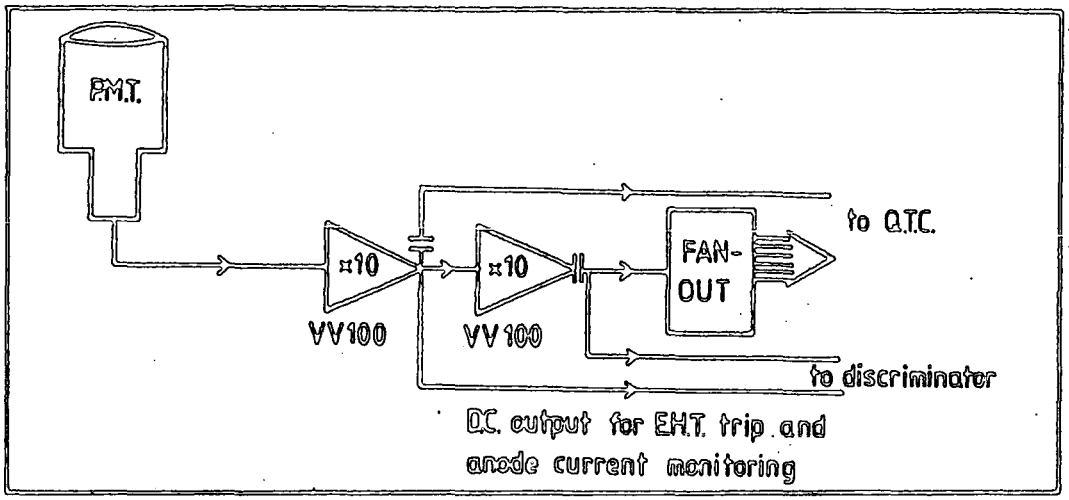

FIGURE 3.3 The pulse shape and arrival-time digitisation system.

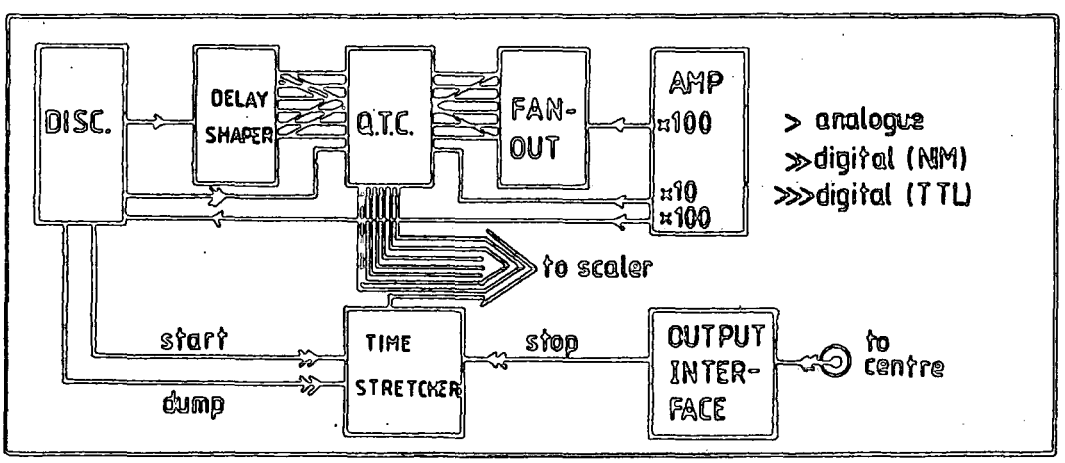

FIGURE 3.4 The data acquisition system.

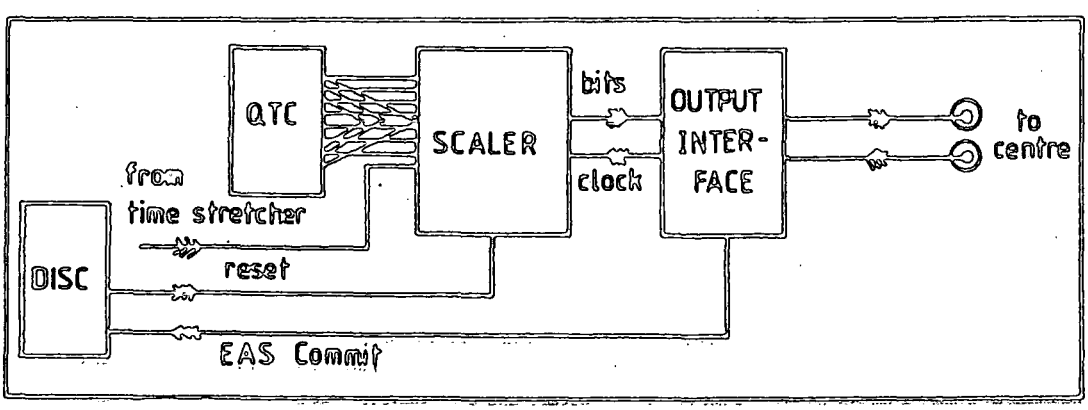

level was exceeded); and a pulse was sent to the EAS coincidence unit in the central recording station. If an EAS coincidence was not generated in the 5μs following a detector trigger, the discrimination unit initiated the clearance of the digitisation system in readiness for another light pulse. The propagation time through the discriminator was 20 ns with a jitter of < 1 ns, and a positive feedback system was employed to ensure the same delay for large and small pulses.

A seven channel gated charge-to-time converter (Q.T.C.) (see Stubbs and Waddoup (1977)), was used to sample the charge sequentially through the pulse, and to integrate the total charge. The gating pulses were arranged to provide the optimum sampling of typical pulses, and the analogue signal was delayed so that the gates occurred relative to the time at which the pulse height exceeded 20 mV. Figure 3.5 illustrates the nominal sampling (slicing) times adopted for the inner ring (0,1,5,6,7) and outer ring (2,3,4) detectors. Since the outer ring detectors would be sampling wider and smaller pulses on average than the inner ring detectors, this demanded a slightly expanded sampling time including the 10 ns prior to the discrimination time.

The time of arrival of the Cerenkov light pulse at each detector (relative to the other detectors) was recorded using a time stretcher with a stretching ratio of 75 : 1 (see Waddoup and Stubbs (1976)). This, combined with a scaling rate of 20 MHz, provided a sensitivity of 0.7 ns per bit. The time stretcher was started by the Cerenkov pulse if it exceeded the discrimination level, and was stopped at an arbitrary time later by the EAS coincidence pulse from the central control system. The relative time of arrival of the time stretcher stop pulse at each detector was accurately known from calibrations.

The information from the Q.T.C. and the time stretcher was then passed on to a 64 bit fast scaler. To summarise, the information comprised:

FIGURE 3.5 The nominal pulse shape sampling times adopted for the inner and outer ring detectors. Also shown are schematic representations of typical Cerenkov light pulses.

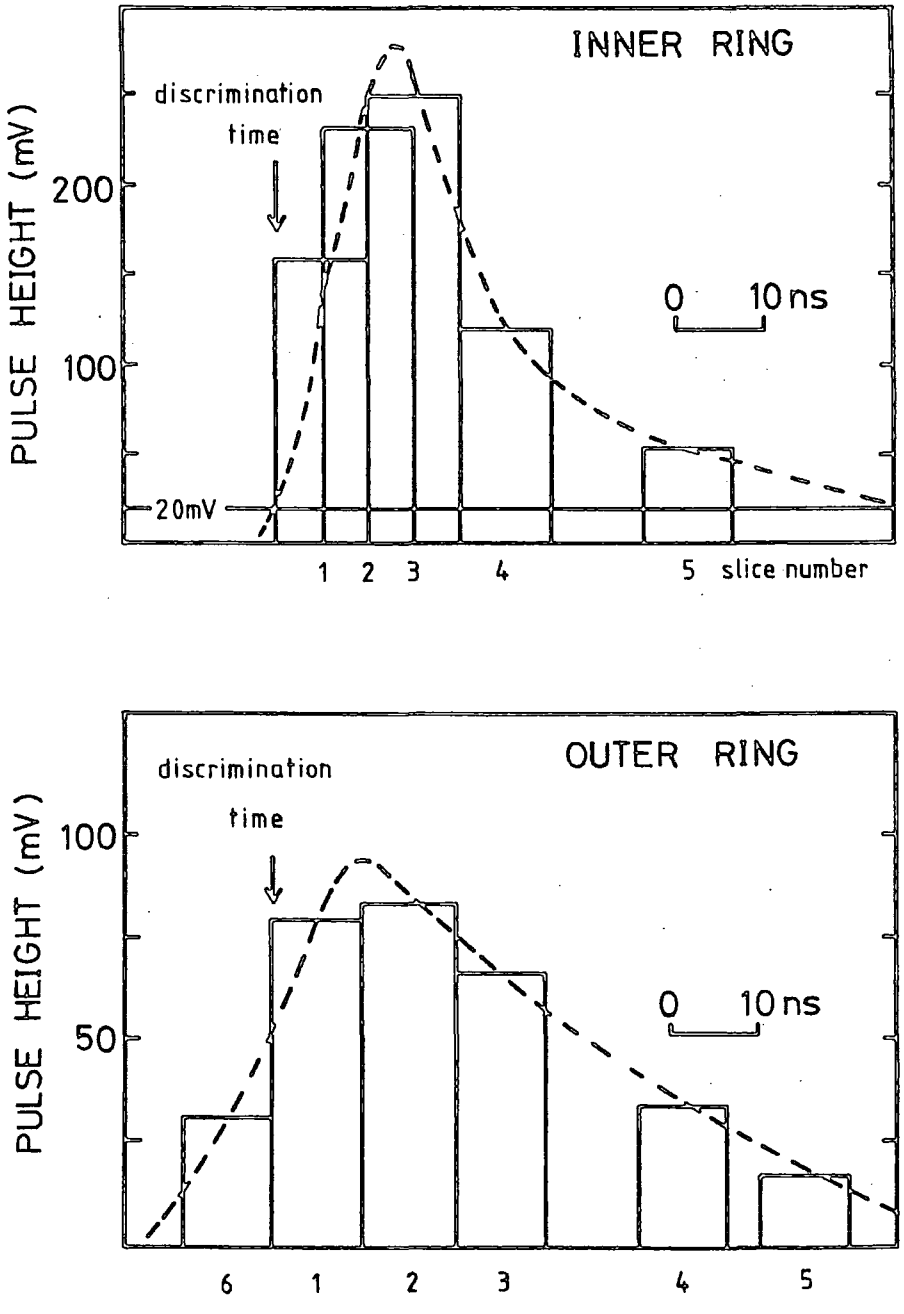

(i) the total pulse area,

(ii) five sequential samples of the pulse area in an inner ring detector, or six in an outer ring detector, and

(iii) a time interval, which was the time at which the light pulse exceeded the discrimination level relative to the EAS coincidence.

The scaler unit (described by Waddoup and Stubbs (1977)), was an eight channel parallel input, serial output scaler, with a maximum clock frequency of 20 MHz. The basic design was modified to provide one 16-bit word for the time interval, 8-bit words for all the slices except slices 5 and 6 in the outer ring detectors, which were assigned 4-bit words (see figure 3.5 for slice nomenclature), and an 8-bit word for the pulse area. A schematic representation of the pulse shape and arrival-time digitisation system is shown in figure 3.3

3.2.4 The Central Control System and Data Logging

The array was controlled by a Tektronix 4051 mini-computer located in the central station. The computer, programmed in BASIC, was used to command the array on and off, record the data, calibration information and various environmental parameters. Each detector was connected to the central station with a power supply cable, a cable from the detector to the EAS coincidence unit, a cable down which the synchronising pulse was passed to the detector, a cable for the transmission of the digital data and a multiway cable for d.c. monitoring levels. The 'status' of each detector was monitored at the central station. This included information such as whether the E.H.T. supply and the phototube were switched on and whether the blind was drawn. This 'housekeeping' information was converted from d.c. voltage levels to digital form and read into the computer.

An EAS coincidence was generated if a response from any three of the detectors 2,3,4,5,6,7 was received within a 'window' of 3.6 μs. This coincidence window allowed for showers to be recorded from any zenith angle. The majority of EAS triggers were formed by a shower impact in one of the four equilateral triangles: 2,5,7; 3,5,6; 4,6,7; 5,6,7. A fixed time after the generation of an EAS coincidence, a pulse was sent to each detector simultaneously to allow for synchronisation of the timing information. At each detector the time stretcher was stopped, and the discriminator inhibited until the digitisation was completed and the digital output buffer loaded. A serial string of 65 1ms pulses from the central electronics clocked the data (in bits) from the scaler to the central electronics, where it was read in by the computer and stored on magnetic tape. Figure 3.4 shows a schematic of the data acquisition system. The total 'dead' time of the system while the data was being logged was about 12 s. This was not a significant dead time for the 400 m array, which recorded an event rate of about 22 per hour.

Following every 13 events the computer initiated a calibration event. During the second season of operation (1978/79), this consisted of simultaneously illuminating a light emitting diode in the field of view of each photomultiplier. The detection of light by each detector generated a coincidence, and the 'event' was recorded in the usual way. Due to the proven high gain stability of the photomultipliers, it was decided that a more useful calibration event would record the pedestals for the charge digitisation system (i.e. the output corresponding to zero input). A calibration event during the third season of operation (1979/80) consisted of the output recorded when the detectors were simultaneously triggered without any illumination of the phototubes other than that from the general night sky background.

Also recorded at the central station were the data from the particle detectors, and information on the weather conditions and event rates.

3.2.5 The Particle Detectors

Four particle detectors were incorporated into the array, co-located with Cerenkov light detectors (see figure 3.1). Each particle detector consisted of a 1 m^2 plastic scintillator viewed end-on by two photomultipliers (see Chantler et al. (1979a)). The detectors were designed to measure two quantities, from which development-sensitive shower parameters could be derived. These were the particle density and the time delay between the particle and light fronts.

Previous measurements of the time delay between the particle and light fronts at large core distances, made at Haverah Park (Shearer (1978)), had shown that the particles lag behind the light (by $\sim$ 40 ns at r = 150 m). This delay arises because of the extra path lengths traversed by the electrons due to Coulomb scattering. Preliminary results from the Dugway array (Chantler et al. (1979b), Orford et al. (1981)) have indicated the sensitivity of this time delay to the cascade development. Further analysis of the particle detector measurements will be presented by Walley (Ph.D. thesis, in preparation).

3.3 CALIBRATION PROCEDURES

Calibrations of the equipment were carried out at frequent intervals throughout the periods of operation of the array. These can be broadly divided into two categories : the calibration of the system gain and the calibration of the timing systems. Further details on some aspects of the calibration procedures have been given by Shearer (1980).

3.3.1 Gain Calibrations

The calibrations of the system gain were designed to measure the following three factors:

(i) the relative gains of the photomultiplier/amplifier systems,

(ii) the response of the photomultiplier/amplifier systems to a fixed number of photons (the absolute gain), and

(iii) the relative internal gains of the digitising systems.

The relative gains of each photomultiplier/amplifier system were measured by flooding the photomultiplier face with light from a green constant current driven light-emitting diode (L.E.D.). The L.E.D. produced a large wide flat-topped pulse of about 5×10^5 photons. The height of this pulse from each detector provided a means of determining the relative gains to an accuracy of about 20%. A refinement in the relative gain assignment to $\lesssim$ 10% was later achieved by a systematic analysis of each detector's response to the Cerenkov light in EAS (Craig, private communication). Additional calibrations of the spectral response of the photomultipliers, carried out at Durham, demonstrated that there was no significant difference between the detectors in the dependence of gain on the wavelength of the light source. Therefore, no systematic errors in the gain calibrations were expected to arise due to the difference in wavelength distributions between the green L.E.D. and the (predominently blue) Cerenkov light signal.

The second technique used for the photomultiplier/amplifier gain calibrations employed a radio-active light pulser. The pulser (NE 130) consisted of Am^{241} distributed in a plastic scintillator (NE 102a); each radio-active decay generating a light flash of a constant number of photons, estimated at 1835 ± 300 (Hartman, private communication (1977)

quoted by Shearer (1980)). The response of a detector to this light flash was, after amplification, a small pulse typically of area 250 mV.ns. This technique offered the advantage of a non-electronic, and therefore stable source, but was not used to measure the relative gains since the accuracy to which the pulse area could be determined was not comparable to the accuracy of the former technique. However, the gain calibration obtained with the light pulser provided a useful intercomparison with the response of the Haverah Park and Volcano Ranch arrays. Calibrations of Cerenkov light detector equipment had also been carried out at each of these sites with an NE 130 light pulser. This allowed the primary energy estimator at Dugway (the photon density at 150 m from the core) to be directly linked to the Haverah Park primary energy estimator (see section 4.3.2).

The digitising electronics was calibrated over its entire dynamic range by injecting a wide flat-topped pulse (of controlled height) into the amplifier; this was then digitised, and the result transmitted to the central computer. The gains of the slicing and integration systems were found to be stable throughout each operating period. The calibration technique provided, however, a useful means of checking each detector's overall performance. The dynamic range of the slices was 50 - 15000 mV.ns, with a measurement error of about 50 mV.ns including the noise from the night sky background light. The dynamic range of the integrator was 250 - 100,000 mV.ns, with a sensitivity of about 500 mV.ns per bit. The pulse area could also be recovered from the slice information (for the majority of pulses) to an accuracy of typically 200 mV.ns.

3.3.2 Timing Calibrations

Calibrations of the timing systems were carried out in order to:

(i) synchronise the measurements of the arrival time of the light pulse at each detector, and

(ii) relate the timing measurements within the pulse at each detector to the time structure of the Cerenkov light pulse before passing through the system.

Figure 3.6 is a schematic of the various time delays which had to be known in order to accurately synchronise the response from each detector. The photomultiplier transit time (D1) varied from one detector to another, since each photomultiplier was operated at a slightly different cathode potential in order to approximately equalise the tube gains. The relative transit times were measured by avalanche pulsing a green L.E.D. in the field of view of the photomultiplier. This produced a large signal with a very fast rising edge. The output from the amplifier was compared on an oscilloscope to a reference signal, allowing a measurement of the transit time to an accuracy of 0.5 ns.

The measurement of the delays D2, D3 and D4, and the calibration of the time stretcher unit itself were carried out using a single procedure. A time interval generator, containing a 20 MHz crystal controlled oscillator, was used to generate time intervals from 0 to 2400 ns. At the start of a time interval a large pulse was sent to trigger the detector (and hence start the time stretcher) at the input to the discriminator module. At the end of the time interval the central coincidence unit was triggered, which then sent a pulse to the detector to stop the time stretcher. The cable used to transmit the start signal from the time interval generator was the same for all detectors, its length being checked between calibrations. By increasing the time interval between triggering the detector and triggering the central coincidence unit the system could be calibrated over its entire dynamic range. The scaled output from each time stretcher unit (in bits) exhibited a simple linear

FIGURE 3.6 A schematic representation of the time delays requiring consideration in order to synchronise the response from each detector.

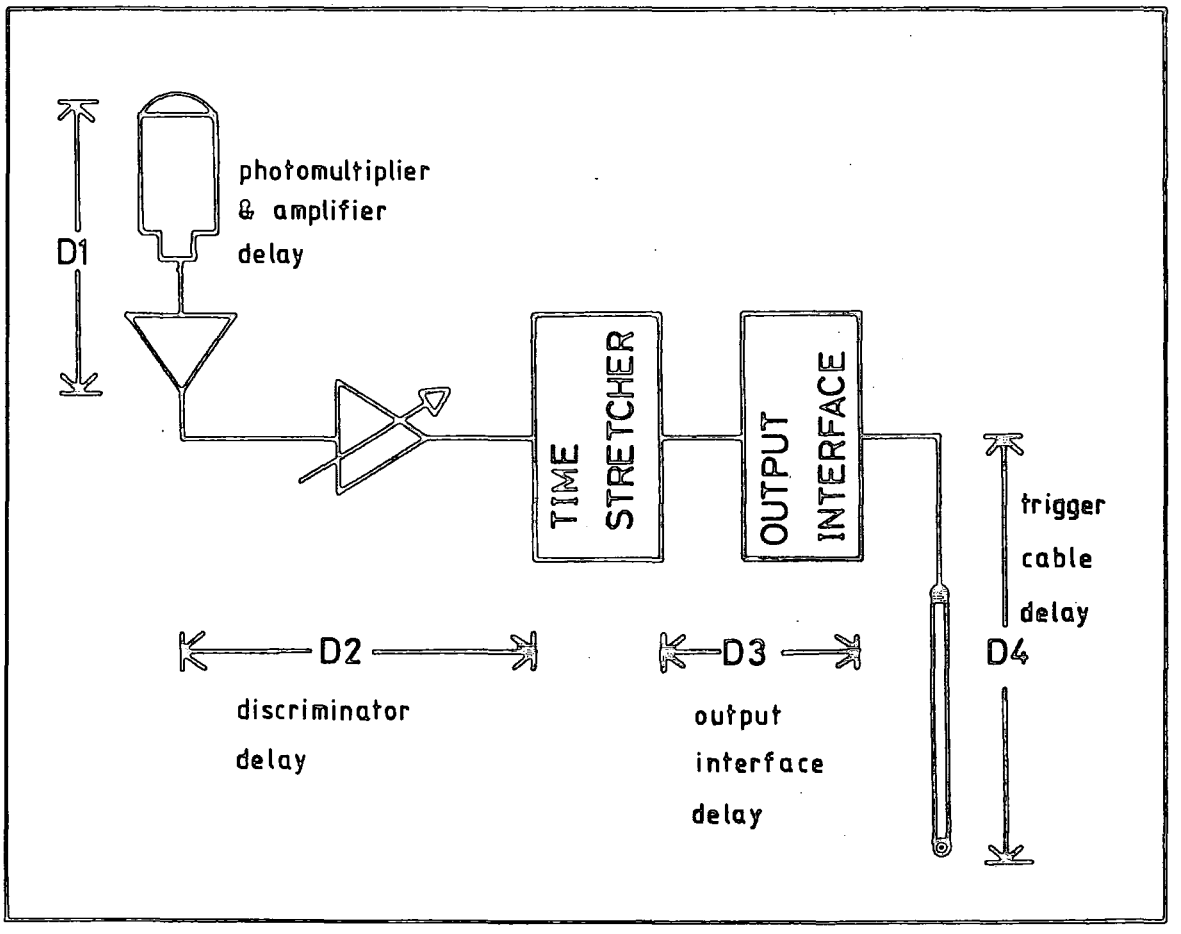

dependence on the time interval (in ns) over the range 0 to 2400 ns; the standard deviation from a linear regression fit was typically 0.5 ns including the bit quantisation error, and the slope was typically 1.46 bits/ns.

The temperature coefficient of the time stretcher was measured by Waddoup and Stubbs (1976) as 0.05% / ^{o}C. Further calibrations of the temperature coefficient were carried out at Dugway, and the change in time stretcher slope per ^{o}C averaged over all the detectors was found to be 0.04%. During the normal winter operating periods the internal detector temperatures were expected to hold to within about 3^{o}C of their thermostated settings, and so the time stretcher calibration slopes could be expected to remain constant to within $\sim$ 0.12%. The dependence of the time stretcher pedestal (the output in bits corresponding to zero time interval input) on temperature was also investigated; the pedestals were found to increase on average by 1 bit per ^{o}C. The temperature dependences of the time stretcher slope and offset combined are expected to be the largest cause of uncertainties in the decalibration of the synchronised timing data, producing errors of typically $\pm$ 3 ns for internal detector temperature variations of $\pm$ 3^{o}C. These uncertainties were found to be consistent with estimates of the random component of the measurement errors obtained from a statistical analysis of the timing responses of the detectors in EAS (see section 4.2.3).

For the synchronisation of the arrival time of the light pulse at each detector it was also necessary to accurately determine the detector positions. The relative coordinates of each photomultiplier face were measured to an accuracy of $\pm$ 5 cm (0.2 ns) using an infra-red tellurometer and theodolite.

In order to interpret the timing information within the pulse (i.e. the slice measurements) it was necessary to know the frequency response

or bandwidth of each photomultiplier/amplifer system. It was possible to detect minor differences in the bandwidth of each detector using the light pulse from the NE 130 radio-active source. The light pulse has been stated by the manufacturers to have a characteristic decay time of 2 ns; it could therefore be used to measure the system's response to a near delta function. The typical detector response was a pulse of FWHM 6.2 ns and rise-time 6.7 ns, including the response of the recording oscilloscope. Each individual system response, measured in this way, has been convoluted with a wide range of simulated pulses for an infinite bandwidth system; this allows for the interpretation of the pulse profiles to be optimised for each detector.

Finally, in order to convert the digitised slice information at each detector into a smooth pulse profile, the position on the time axis at which each slice occurs must be accurately determined. The relative times between the centres of each slice were measured using a high bandwidth oscilloscope to an accuracy of < 0.5 ns (Orford, private communication), and the times of the slices relative to the discrimination time were determined to an accuracy of $\lesssim 1$ ns.

3.4 ENVIRONMENTAL MONITORING

It was important to monitor the sky conditions during each night of operation, so that only those events recorded during stable and clear atmospheric conditions would be used in the analysis. Frequent visual checks of sky clarity were made, but objective criteria were needed, especially since with the automated system personnel were not always present during the whole of each night's run.

To this aim a number of quantities were monitored throughout each night. These included:

(i) the sky clarity (from the star trails recorded by a 35 mm time-lapse camera),

(ii) the sky brightness (recorded by a 2" diameter photomultiplier tube), and

(iii) the rate of air shower coincidences and detector responses.

If any of these records indicated unstable or cloudy conditions, the data would not be included in the analysis. The atmospheric temperature, pressure and humidity were also recorded. Figure 3.7 shows some of the detector and atmospheric monitoring information recorded on the night of 23/24 February, 1979. This night was chosen to illustrate the response of the equipment to conditions of variable sky clarity. A correlation can be seen between the maximum detectable stellar magnitude and the array trigger rate. In addition, the current from the 2" diameter photomultiplier tube clearly indicates an unstable level of night sky background light.

3.5 PERIODS OF OPERATION AND DATASETS RECORDED

The array was run during the autumn and winter months of 1977/78, 1978/79 and 1979/80. For the majority of this time the array layout was as shown in figure 3.1, with the outer ring detectors at 400 m from the array centre. Towards the end of the 1979/80 running period, the array dimension was halved twice, forming 200 m and 100 m arrays, while maintaining the same geometrical configuration. Table 3.1 provides a chronology of the operating periods with details on the number of EAS recorded and the principal primary energy range for each array size.

Part of the 1977/78 period was spent commissioning the array and ensuring that each detector was operating according to its specification. The data recorded during the latter part of this period were used to establish that the showers, when analysed, indicated a cascade development consistent with that observed at Haverah Park.

FIGURE 3.7 Atmospheric monitoring records for a night of variable sky clarity.

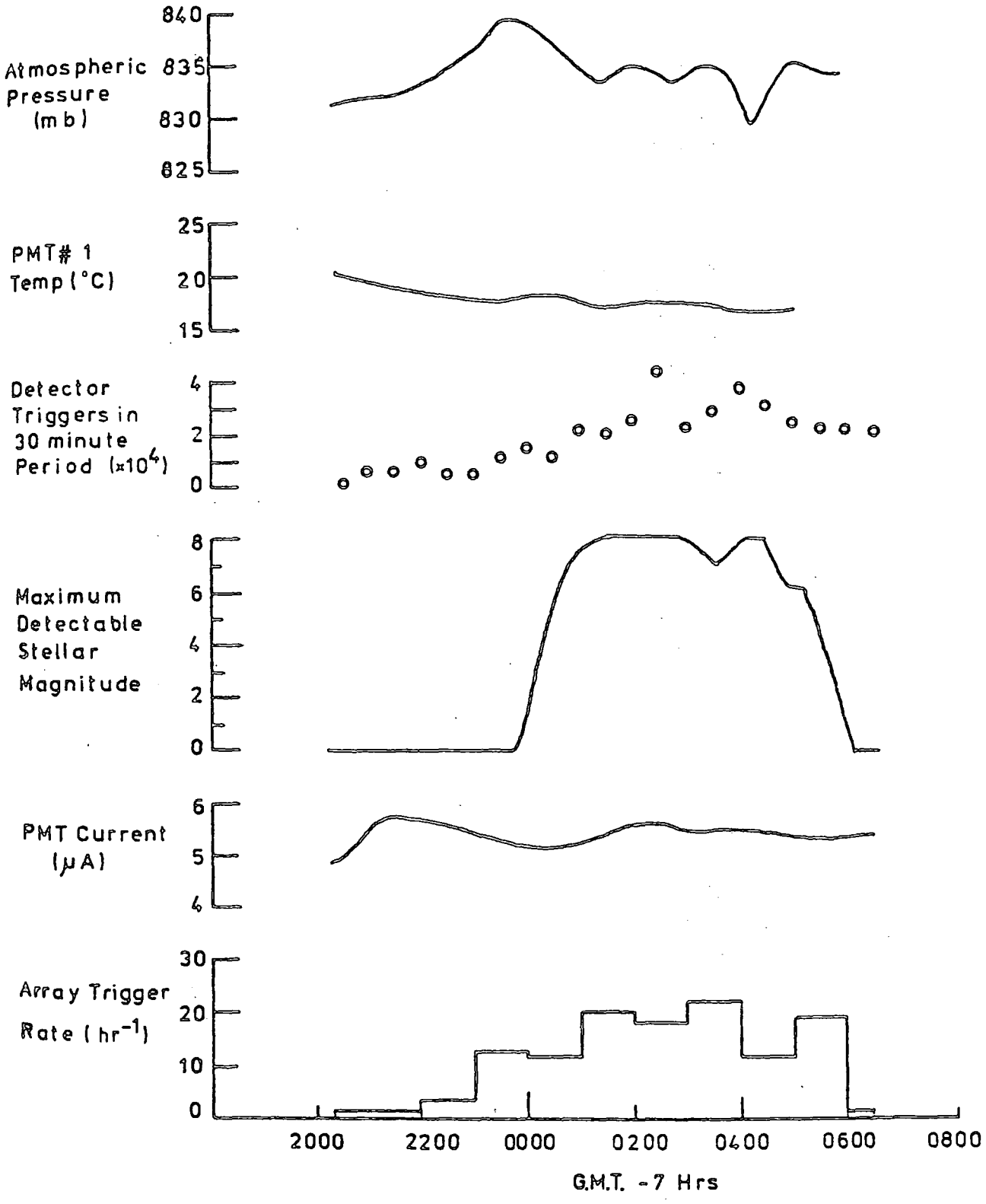

TABLE 3.1

Chronology of running periods for the Dugway atmospheric Cerenkov light experiment.

	ARRAY RADIUS	NO. OF HOURS CLEAR SKY OPERATIONS	NO. OF EAS RECORDED	PRINCIPAL PRIMARY ENERGY RANGE
Sept. 1977 - Dec. 1977	400 m	100	1500	$5 \times 10^{16} - 5 \times 10^{17}$ eV
Oct. 1978 - Mar. 1979	400 m	140	2100	$5 \times 10^{16} - 5 \times 10^{17}$ eV
Sept. 1979 - Dec. 1979	400 m	210	3300	$5 \times 10^{16} - 5 \times 10^{17}$ eV
Jan. 1980 - Feb. 1980	200 m	50	3500	$5 \times 10^{15} - 5 \times 10^{16}$ eV
Mar. 1980	100 m	20	2600	$10^{15} - 10^{16}$ eV

A preliminary analysis of the data recorded during the 1978/79 period has been reported by Andam et al. (1979) and by Shearer (1980). The combined data sample recorded with the 400 m array from both the 1978/79 and the 1979/80 periods contains a total of $\sim$ 5400 EAS triggers satisfying the 'clear sky' criteria. The analysis of the synchronised timing and pulse shape information from this data sample is the principal subject of this thesis. Of course, the majority of EAS triggers contain more than three detector responses; figure 3.8 illustrates the number of 'N-fold' detector responses in this data sample. For most analysis procedures, at least five detector responses per event will be required, allowing for a degree of redundancy in the data fitting routines (see chapter 4). Figure 3.9 shows the frequency distribution of events from each array size as a function of primary energy estimator for showers selected according to the following criteria:

(i) 'clear sky' criteria satisfied,

(ii) $\geqslant$ 5-fold detector response per event,

(iii) shower core impact located within the array, and

(iv) zenith angle (θ) $< 60^{o}$.

Before deployment of the medium (200 m) and small (100 m) arrays, it was considered necessary to change the relative times at which the digital slices within a pulse occurred. The showers detected by these arrays are lower energy and develop higher in the atmosphere, producing narrower and smaller Cerenkov pulses at the observation level. Figure 3.10 illustrates the slicing arrangements adopted for all eight detectors throughout the operation of the medium and small arrays. The slicing was initiated before the 20 mV level (in order to sample the rising edge of the pulse) and spanned a shorter time interval. Owing to the steepness of the primary energy spectrum, large data samples

FIGURE 3.8 The frequency distribution of N-fold events recorded with the 400 m array during 1978/79 and 1979/80.

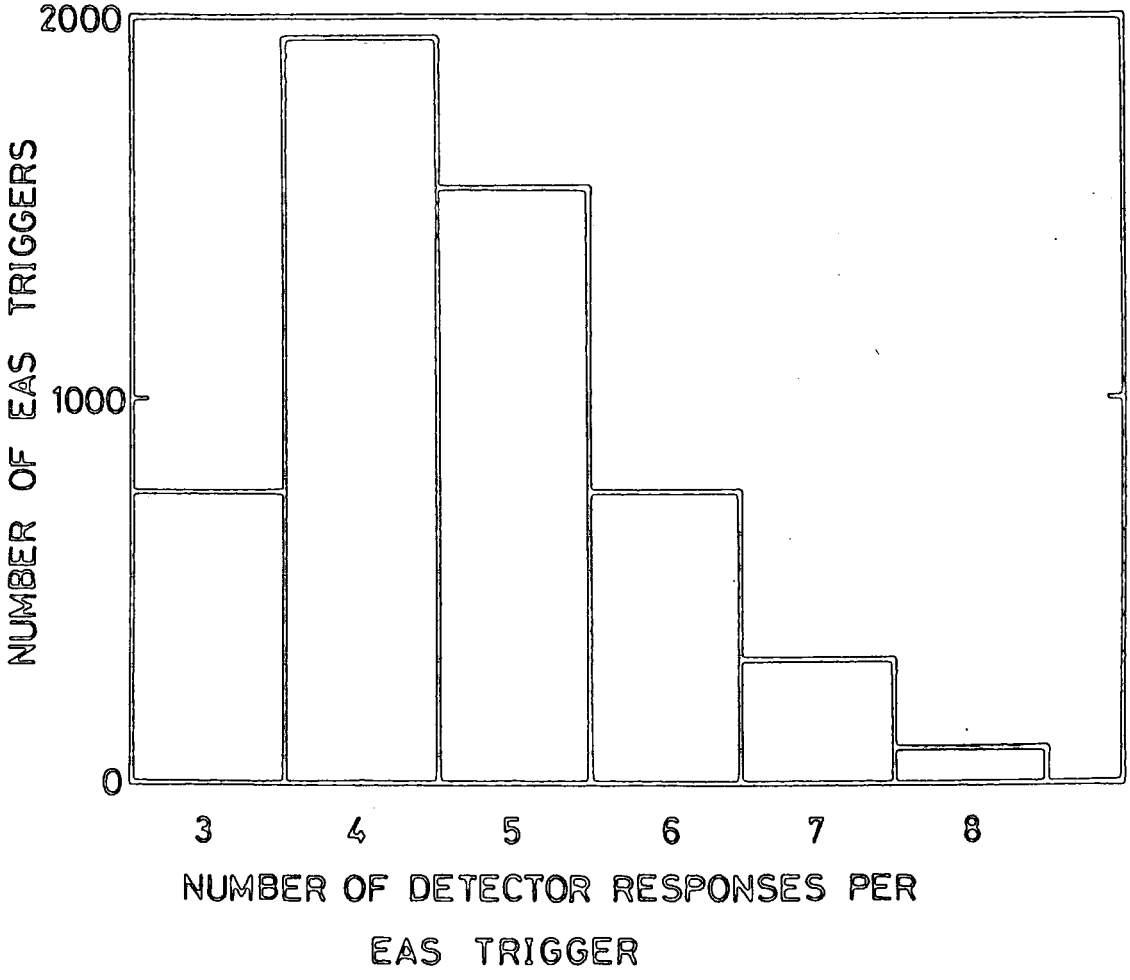

FIGURE 3.9 The distribution in primary energy estimator for showers recorded by the 400 m, 200 m and 100 m arrays. Also shown is a primary energy scale which is applicable to all three array sizes.

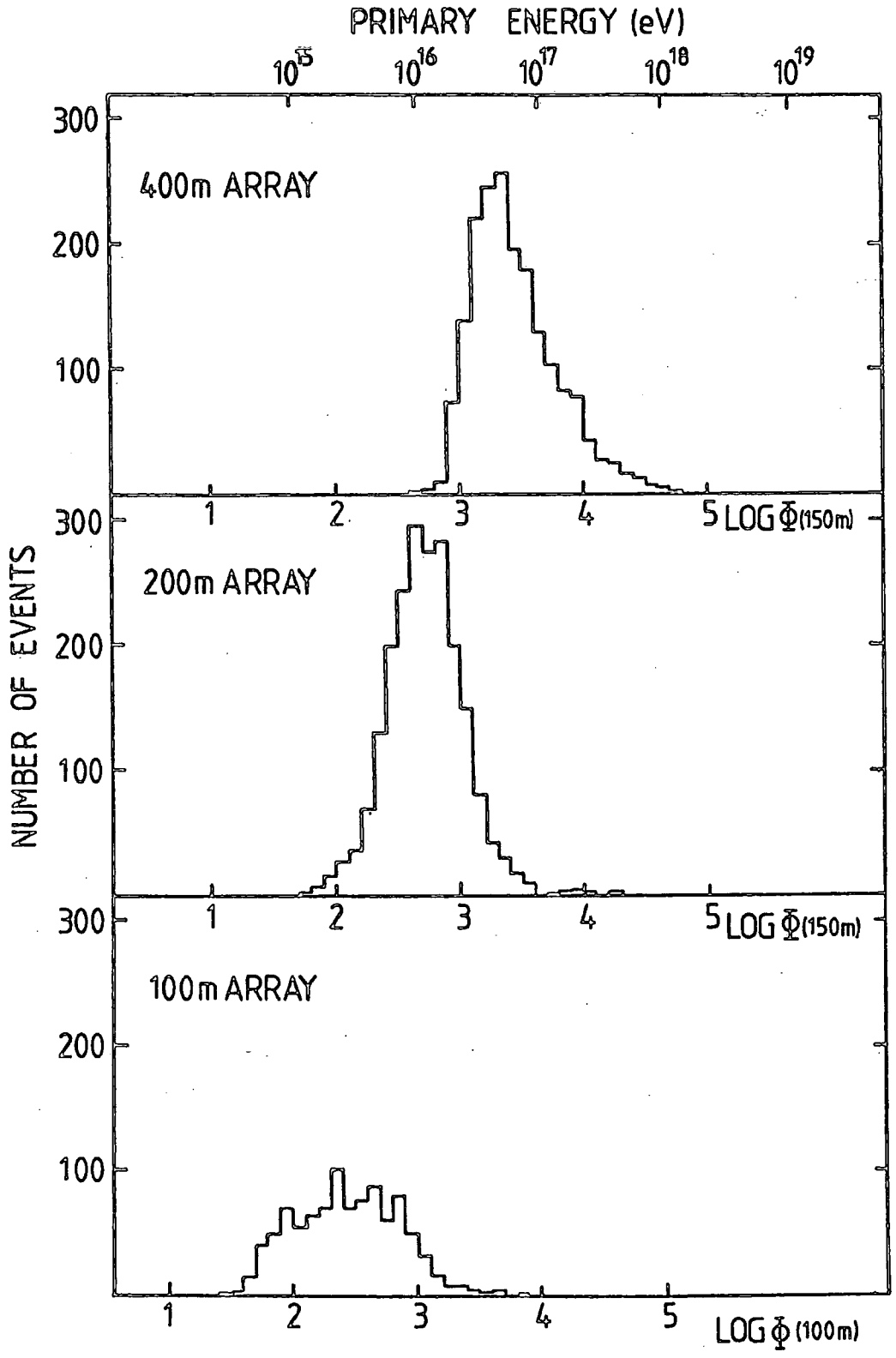

FIGURE 3.10 The nominal pulse shape sampling times adopted for the 200 m and 100 m arrays.

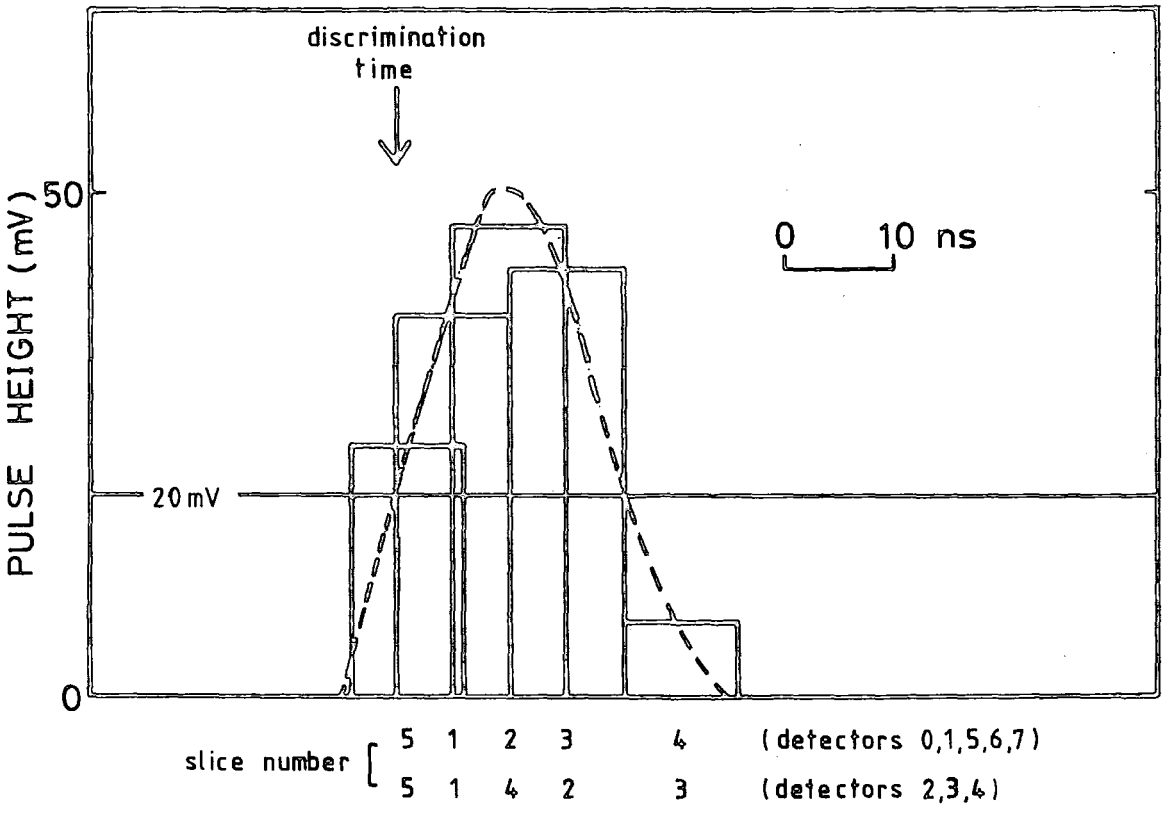

were recorded with these arrays during relatively short periods of operation.

3.6 DATA HANDLING, DECALIBRATION AND PRELIMINARY ANALYSIS

The large volume of digital data recorded demanded that the processing and analysis were carried out in Durham on the main-frame computer. The data were therefore transferred from the magnetic tape cartridges of the Tektronix 4051 mini-computer to main-frame disc file storage, and divided into blocks of manageable size containing no more than one night's data. The data blocks which failed the 'clear sky' criteria were then identified and excluded from the data analysis. Each block was studied in detail, before analysis of the digital records, to identify any anomalies in the response of any detectors, and to examine the calibration event records.

Each EAS event record was then 'decalibrated' and subjected to a preliminary analysis to determine the shower arrival direction, core location and primary energy. The information on each event was visually checked to ensure that the computer analysis was satisfactory, and to establish whether any scaler overflows had occurred. The scalers had a range from 0 to 255 bits, which if used to digitise the complete dynamic range of the analogue system would have provided a sensitivity of 60 mV.ns per bit for the digital slices. The computer program was designed to flag the need for scaler overflows by comparing the area of the pulse measured by the integrator (the integrator scaler did not overflow) to that derived from the slices; the deficit in pulse area derived from the slices indicated the number of scaler overflows required. One or two scaler overflows per pulse could be recovered unambiguously by examining the distribution of slice heights in the pulse. This allowed for the sensitivity of the digital slices to be set to 20 mV.ns per bit. The slice overflow facility was

then only required in a minority of recorded pulses, many of these being narrow 'bandwidth limited' pulses close to the shower core.

The shower arrival direction was determined from the synchronised measurements of the arrival time of the light front (see section 4.2.2). The core location and primary energy estimation were calculated from the distribution of pulse areas (see section 4.3). If any aspect of this analysis was unsatisfactory, due to for example a spurious detector trigger, the fault was corrected and the analysis repeated. After each event had passed through the decalibration and preliminary analysis routines successfully, the information was stored on a separate disc file. This information included:

(i) the date and time of the event,

(ii) the number of detector responses,

(iii) the decalibrated records of the pulse areas, slice heights and the synchronised arrival time of each pulse at the 20 mV level,

(iv) the arrival direction and the radius of curvature of the light front, and

(v) the core location, primary energy estimation and the lateral structure function exponent (η).

This formed the database for selection and further analyses of the data. The storage of the data on disc was arranged so that further information could be added as it became available for selections of events. For example, the results from the pulse shape reconstruction routine (see section 4.4.2), and those obtained from the technique of imaging the cascade development in the atmosphere (see section 4.5.1) were later incorporated into the data store.

CHAPTER 4

DATA REDUCTION PROCEDURES AND ERROR ANALYSIS

4.1 INTRODUCTION

In this chapter a detailed description is given of the reduction procedures which have been developed to determine the arrival directions and energies of cosmic-ray primaries, and to extract parameters which are sensitive to the longitudinal cascade development in individual EAS.

As explained in chapter 3, the measurements available for each EAS provide information on three different aspects of the Cerenkov light signal : the relative arrival times of the light front, the photon densities and the temporal structure of the light pulse at each detector. The procedures developed in order to best utilise this information are described for each category in turn. The application of these reduction techniques is illustrated by reference to a large well-measured shower of primary energy $\sim 4.10^{17}$eV incident at a zenith angle of 32^{o}.

Particular attention has been given to the treatment of measurement error in the synchronised-timing data, and also to quantifying the uncertainties in the derived development-sensitive shower parameters obtained from the timing and pulse shape analyses. Quantitative estimates of all sources of error in development-sensitive parameters are required in order to make an estimation of the intrinsic fluctuations in the cascade development of EAS.

The combination of the synchronised-timing data and the pulse shape information enables the construction of an image of the longitudinal cascade in Cerenkov light in individual EAS. This technique, first applied to the analogue data from the Haverah Park array, is now adapted and optimised for the improved bandwidth digital information from the Dugway array. A method is developed for estimating the uncertainties

on the light front origins obtained by this technique.

4.2 SYNCHRONISED TIMING ANALYSIS

4.2.1 The Curvature of the Light Front

Earlier work at Haverah Park (Orford and Turver (1976)) has demonstrated that the light fronts defined by the times to fixed percentages of the Cerenkov pulse heights are closely spherical. The basis of this method of analysis has been described in chapter 2, and its application to the current data is discussed in detail in section 4.5. Much larger numbers of slightly different measurements relating to the curvature of the light front are available from the Dugway experiment. Measurements have shown that a sphere can also be fitted to the relative times at which the discrimination level was exceeded at four or more detectors. This is a measurement obtainable from the data more directly, since it does not require the reconstruction of the pulse shape.

The computer software package 'MINUIT' (James and Roos (1975)) is used to numerically determine the optimum least-squares fit to a spherical front. A combination of three non-linear optimisation procedures are employed. Firstly, a random 'seek' procedure locates the approximate centre of the sphere. This is then refined using a simplex method (Nelder and Mead (1967)), and finally the function minimum is checked using a gradient procedure. The simplex and gradient procedures are normally repeated two or three times to ensure that a local function minimum has not been found. In general the global function minimum, and hence the origin of the spherical front, is located rapidly and is well defined.

The deviations from sphericity obtained in these fits to the data are extremely small. The r.m.s. of the residuals to the fits is defined by:

$$\text{r.m.s.} = \sqrt{\left(\frac{1}{N}\sum_{i=1}^{N}(t_i - T_i)^2\right)} \qquad 4.1$$

where t_i are the observed arrival times of the light front, T_i the times predicted by the fit, and N the number of detector responses. The average r.m.s. for the fifty-two eight-fold response events from the running period of 1979-80 was found to be 6.1 ns. The corresponding radii of these spheres were typically $\sim$ 5km. Part of this r.m.s. deviation was found to be caused by small systematic effects, which are discussed in section 4.2.3; indeed it was the consistent close proximity to spherical fronts that enabled small systematic errors occurring in the timing data of specific detectors to be identified. Once any systematics have been identified, normal statistical methods assuming Gaussian error distributions can be used to quantify the residual random components of error. The synchronised timing information can then be reliably used in conjunction with the pulse shape data in order to calculate the light fronts fitted to fixed percentages of the maximum light intensity and the corresponding centres of emission in the atmosphere.

The interpretation of the radius of the light front obtained from the discrimination times is not as direct as for the radius fitted to a fixed percentage level of the light pulses. The spherical fit does not, in the former case, correspond to a single light front propagated from effectively a point source, but comprises samples from a continuous sequence of light fronts originating from the 'leading edge' of the longitudinal Cerenkov development in the atmosphere. Although this technique does not directly image the electron cascade development, it is not ruled out that these measurements may provide a development-sensitive shower parameter in their own right.

The result that the light fronts, defined by the fixed discrimination levels of our equipment are closely spherical is supported by the results of the computer simulations of the Durham group. Figure 4.1 illustrates the simulated time delays behind the tangent plane (including the Dugway system response) for an EAS incident at 35^{o} to the zenith with a depth of maximum electron development at 695 $g.cm^{-2}$. The tangent plane delays (TPD) of the fixed discrimination level, and for comparison the ten and one hundred percentage levels of the light pulses are shown against the square of the core distance in the shower plane (r^2). For a spherical front the functional relationship should be of the form:

$$TPD = A + Br^2 \quad . \qquad 4.2$$

Least-squares regressions of this form are shown fitted to the core distance range 100 - 400 m (a range appropriate to much of the observational data). The standard errors for the fits to the ten percent, one hundred percent, and fixed discrimination levels are 0.8, 0.6 and 0.5 ns respectively. Deviations from sphericity are,therefore, not significant within this principal core distance range. Good fits are also obtained for simulated showers incident at zero and forty-five degrees to the zenith, indicating very near spherical light fronts both at fixed percentages of the light signal and for the fixed discrimination level appropriate to the Dugway detectors.

4.2.2 Arrival Directions

The arrival directions of the recorded EAS are determined from the synchronised-timing data, and are based on the spherical fits to the discrimination times described in section 4.2.1. Whether or not the radius of this light front will provide a useful measure of cascade development, we would expect, by symmetry, the origin of the sphere to lie on the same shower axis as defined by the origins of the fronts fitted to the fixed percentage levels of the Cerenkov pulse heights.

FIGURE 4.1 The simulated delay behind the tangent plane of various intensity levels in the Cerenkov light pulse. The calculations are appropriate to an observation depth of 862 $g.cm^{-2}$ and incorporate the Dugway system response.

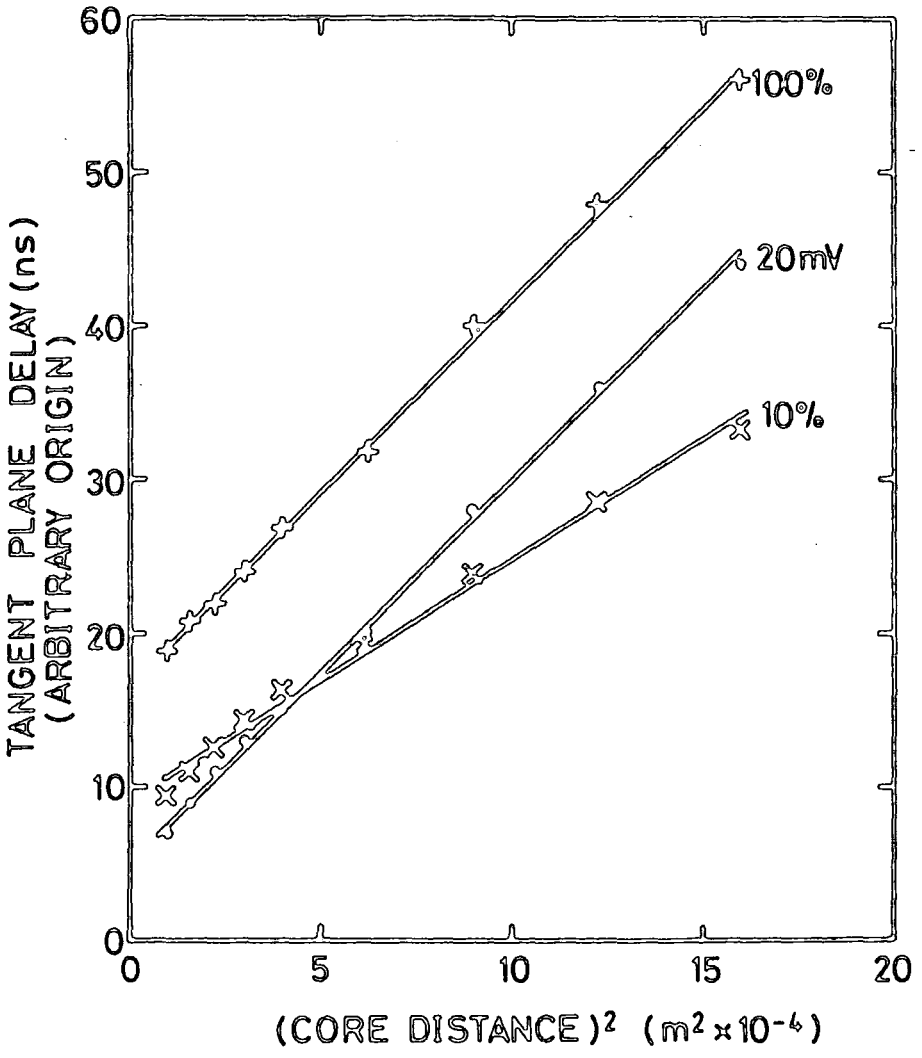

This is illustrated for a typical large EAS event in figure 4.14. The vector joining the origin of the light front to the centre of the array (or, at a later stage in the analysis, the shower core in the ground plane) accurately defines the arrival direction.

The estimation of the uncertainty in the determination of the centres of the spherical fronts is discussed in sections 4.5.2 and 4.5.3. Typical uncertainties in the arrival directions, computed using knowledge of the timing uncertainties, range from 0.4^{o} to 0.2^{o} for five-fold to eight-fold detector responses respectively. An additional component of error of $\sim 0.1^{o}$ must also be taken into consideration, which results from the typical uncertainty in locating the shower core impact on the ground plane (from the separate analysis of the recorded Cerenkov light densities). For the smaller sample of the highest energy events, where a more complete analysis provides a set of colinear origins in the atmosphere, the overall accuracy of the arrival direction determinations is $\lesssim 0.2^{o}$, and is independent of the analysis of the Cerenkov light densities. This comparatively high degree of precision available in determining the arrival directions is one of the novel features of the Cerenkov light technique in recording EAS, and represents an order of magnitude improvement over the precision of particle detector arrays.

4.2.3 Estimation of the Experimental Errors in the Fast-Timing Measurements

On a statistical basis, it would be expected that the effect of the night-sky background light would be to impose random noise on the recorded timing measurements of each detector. From the considerations of section 4.2.1, the light fronts defined by the discrimination times can be assumed to be spherical, provided that any timing responses occurring very close to the shower core are not used. Given that the core locations of the set of EAS under investigation were well distributed on the

ground plane, any systematic non-sphericities in the light fronts would initially appear as an additional random component of noise for each detector. However, further analysis showed no statistical correlation between core distance and the deviations from spherical fits, indicating no evidence for systematic non-sphericities within the resolution of the recording system.

In order to investigate whether the r.m.s. value of the spherical fits contained a systematic component of instrumental error, a special procedure was developed. The timing data of each EAS was fitted with spherical fronts, omitting each detector's response in turn from the fits. The time predicted from a fit excluding a specific detector was differenced from the observed time recorded by that detector, the result being known as the 'exclusive residual'. This procedure was applied to the complete sample of eight-fold events, and the mean values of the exclusive residuals (for each detector) and the corresponding r.m.s. deviations of the fits were calculated. In the absence of systematic effects, it would be expected that the mean reduction in the r.m.s. values of the fits obtained by excluding any detector's response would be approximately the same, and that the corresponding mean exclusive residual would be zero. However, it was found that omitting the response of one particular detector was causing a much more significant reduction in the r.m.s. values, as a result of its decalibrated timing responses being a small and approximately constant amount in error in all showers. Although the reason for this offset remains uncertain, it was decided to use this information to improve upon the decalibration of the timing data. The decalibrated timing responses for this detector were corrected by the amount predicted by its mean exclusive residual, and all the fits were repeated. This process was iterated until the effect on the average r.m.s. of preferentially omitting any one

detector was not significant. In figure 4.2 the mean r.m.s. of the eight-fold fits at each stage of the iteration is shown; it can be seen that the process is rapidly convergent. The mean r.m.s. was reduced to, for example, 2.8 ns for the eight-fold events in the 1979-80 dataset. As no further systematic errors were detectable. the r.m.s. of 2.8 ns can be considered to be composed of random or pseudo-random effects. The removal of the systematic errors by this procedure was found to have no significant effect either on the mean radius of the light fronts, or on the observed variation of radius with zenith angle.

The mean value for the r.m.s. deviations obtained from the spherical fits is not a direct statement about the error variance of the synchronised timing measurements. Consider the method of fitting spherical fronts to the timing data by least-squares. This requires the minimisation of Q^2, where

$$Q^2 = \sum_{i=1}^{N} (t_i - T_i)^2 \quad . \qquad 4.3$$

If the measurement variances (σ_i^2) were used to standardise the residuals, the sum of the squares would be sampled from a chi-square distribution,

$$\text{i.e.} \quad \chi^2 = \sum_{i=1}^{N} \frac{(t_i - T_i)^2}{\sigma_i^2} \quad . \qquad 4.4$$

The expectation value ($<\chi^2>$) for this chi-square distribution is equal to the number of degrees of freedom. If the measurement variances are assumed to be the same on average for each detector, then an estimate for the variance is provided by:

$$\overline{\sigma^2} = \frac{\overline{Q^2}}{<\chi^2>} = \frac{\overline{N.rms^2}}{<\chi^2>} \quad . \qquad 4.5$$

The number of degrees of freedom is equal to N minus the number of

FIGURE 4.2 The improvement in the mean r.m.s. deviation from spherical fits obtained by iteratively removing small systematic errors in the synchronised-timing data.

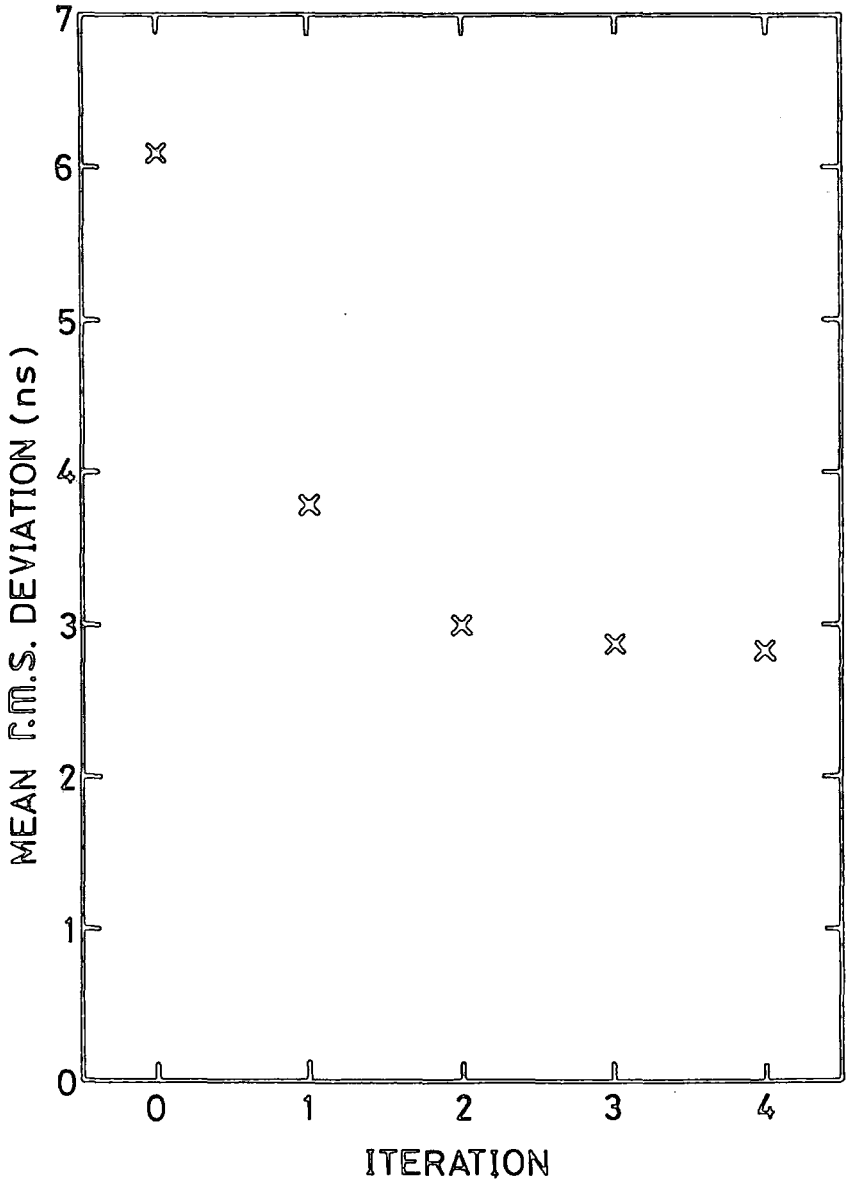

parameters in the fit. For a spherical fit there are four parameters in total. Three are the co-ordinates varied by the optimisation routine to estimate the origin: x,y,z. The fourth arises from the fact that the time of arrival of the light front relative to the light origin is not known; only the relative arrival times at each detector are recorded. Therefore, the mean predicted time $\overline{T}_i$ is constrained to equal the mean observed time $\overline{t}_i$. For an eight-fold fit there are four degrees of freedom, and $\langle\chi^2\rangle = 4$. The measurement error, σ, estimated by this method is 4.5 ± 0.4 ns for the 1979-80 data sample, and 6.6 ± 0.7 ns for the 1978/79 data sample.

The above procedure relies on the assumption that the residuals $(t_i - T_i)$ are normally distributed about zero mean, so that $Q^2/\overline{\sigma^2}$ is sampled from the χ^2 distribution with four degrees of freedom. Figure 4.3 compares the shape of the distribution $Q^2/\overline{\sigma^2}$ with the expected χ^2 distribution. A chi-square goodness of fit test gives a probability of 80% that greater random excursions between the two distributions could occur. This provides a measure of confidence that no significant systematic errors in the timing fits (caused by non-central or non-normal measurement errors) are present.

The random components of error, which have been incorporated into the estimates of variance on the timing measurements, can be attributed to a number of sources :

(i) sky background noise ($\lesssim$ 1 ns),

(ii) small non-sphericities in the structure of the light front (< 1 ns, according to computer simulation predictions),

(iii) small differences in system response between the detectors ($\lesssim$ 1 ns),

(iv) small differences between detectors in the nominal discrimination level setting (< 1 ns),

FIGURE 4.3 Comparison between the distribution of $Q^2/\overline{\sigma^2}$ for the 1979/80 set of 8-fold events and the expected chi-square distribution with four degrees of freedom.

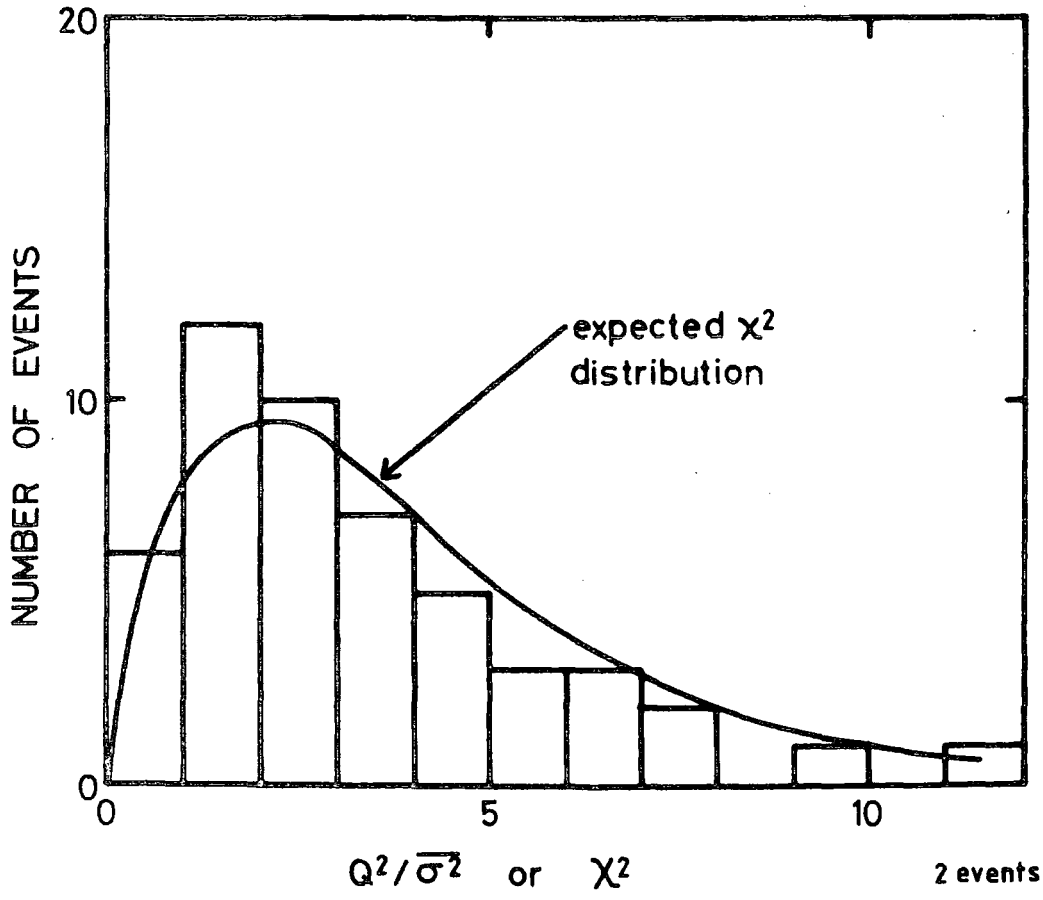

(v) residual random uncertainties in the timing paths at the time of calibration (see section 3.3.2) ($\lesssim$ 1 ns), and

(vi) calibration drift on a short time-scale (so as to be pseudo-random) due to temperature variations of a few ^{o}c within the detectors.

Components (i) to (v) above amount to $\lesssim$ 2 ns when quadratically added, but errors of a few ns might be expected from component (vi) (as described in section 3.3.2), increasing the total expected uncertainty to a value consistent with that derived 'a posteriori' from the residuals in the spherical fits.

In sections 4.5.2 and 4.5.3 consideration will be given to how the timing measurement errors in nanoseconds propagate through the analysis to produce an error in metres or $g.cm^{-2}$ on the apparent origin of the light front in the atmosphere.

4.3 CERENKOV LIGHT PULSE AREA ANALYSIS

In chapter 3, a description was given of the process of recording the Cerenkov light pulse area. The pulse area is proportional to the number of incident Cerenkov light photons. Up to eight such measurements are recorded in each event, providing information on the lateral distribution of the light at ground level. In this section a description is given of the reduction technique used to routinely locate the centre of symmetry of the Cerenkov light pool in the shower plane. The parameterisation of the lateral distribution obtained from this technique provides a development-sensitive measure of the longitudinal cascade and an estimate of the primary energy.

4.3.1 The Lateral Distribution

Measurements of the lateral distribution of Cerenkov light at Dugway (see Shearer (1980)), over a typical core distance range of 50 to 350 m, are found to be consistent with a structure function of the form:

$$\Phi(r) \propto (r + 50)^{-\eta} \quad . \qquad 2.6$$

The departure from a simple power law form is used to take into account the form of the light distribution at small core distances. The exponent (η), observed at Dugway, has been shown to be sensitive to variations in the longitudinal cascade due to changes in zenith angle and primary energy. This form of structure function fits well to the computed lateral distributions from the Durham group's computer simulations. However, it should be noted that the computed exponent (η) is not completely independent of the core distance range sampled.

The data reduction procedure involves a four - parameter fit of the function $\Phi(r)$ to at least four measured densities (ϕ_i), where

$$\Phi_i(r) = A(r_i + 50)^{-\eta} \quad . \qquad 4.6$$

The recorded densities are first normalised to allow for the projection of the photomultiplier face into the shower plane. In equation 4.6, r_i are the distances from the estimated core to the detector positions in the shower plane. The shower plane is accurately known once the arrival direction has been determined from the synchronised-timing analysis. The software package MINUIT is used to simultaneously optimise the core position (x,y), A and η by minimising the sum of the squared weighted residuals (K^2), where

$$K^2 = \sum_{i=1}^{N} \left(\frac{\phi_i - \Phi_i}{\Phi_i} \right)^2 \quad . \qquad 4.7$$

This form of weighted residual was used for the preliminary sorting and analysis of the data. It was chosen to enable a reasonably unbiased fit to the data prior to a detailed analysis of the measurement uncertainties ($\sigma(\phi_i)$). An analysis of the measurement errors (see Craig, Ph.D. thesis in preparation) allows a refinement of the optimisation process by using a chi-square fit of the form:

$$K'^2 = \sum_{i=1}^{N} \left(\frac{\phi_i - \Phi_i}{\sigma(\phi_i)} \right)^2 = \chi^2(N-4) \quad . \qquad 4.8$$

The magnitude of the measurement errors can be refined iteratively from the fits to the data by requiring that the mean value obtained for K'^2 is equal to its expectation value ($<\chi^2(N-4)>$). The samples of events selected for detailed analysis will be subject to this refined core location procedure.

With this data fitting technique the core location and the structure function exponent are optimised simultaneously. The shower core could in fact be approximately located by assuming only the monotonicity of the light intensities with core distance and radial symmetry. But in order to maximise the accuracy of the core location, the form of the structure function should also be taken into account. Figure 4.4 illustrates the structure function fitted to the observed light intensities in the example event.

The expected sensitivity of the structure function exponent (η) to the depth of cascade maximum was described in chapter 2. The interpretation of this quantity in terms of the depth of cascade maximum is, however, slightly dependent on the range of core distances sampled, which varies from shower to shower. An alternative way to parameterise the steepness of the lateral distribution, avoiding this problem, is to take the ratio of the light intensity at two core distances chosen to be well measured for the primary energy of the data sample and the array size. Results of the average depth of cascade maximum derived using this technique have been reported by Chantler et al. (1981) and will be further discussed in chapter 7.

A quantitative evaluation of the uncertainties on the structure function parameterisation and core location requires a detailed study of the effects of measurement errors in the optimisation routine.

FIGURE 4.4 The variation of the recorded light densities with core distance in an EAS event, showing the fitted lateral structure function.

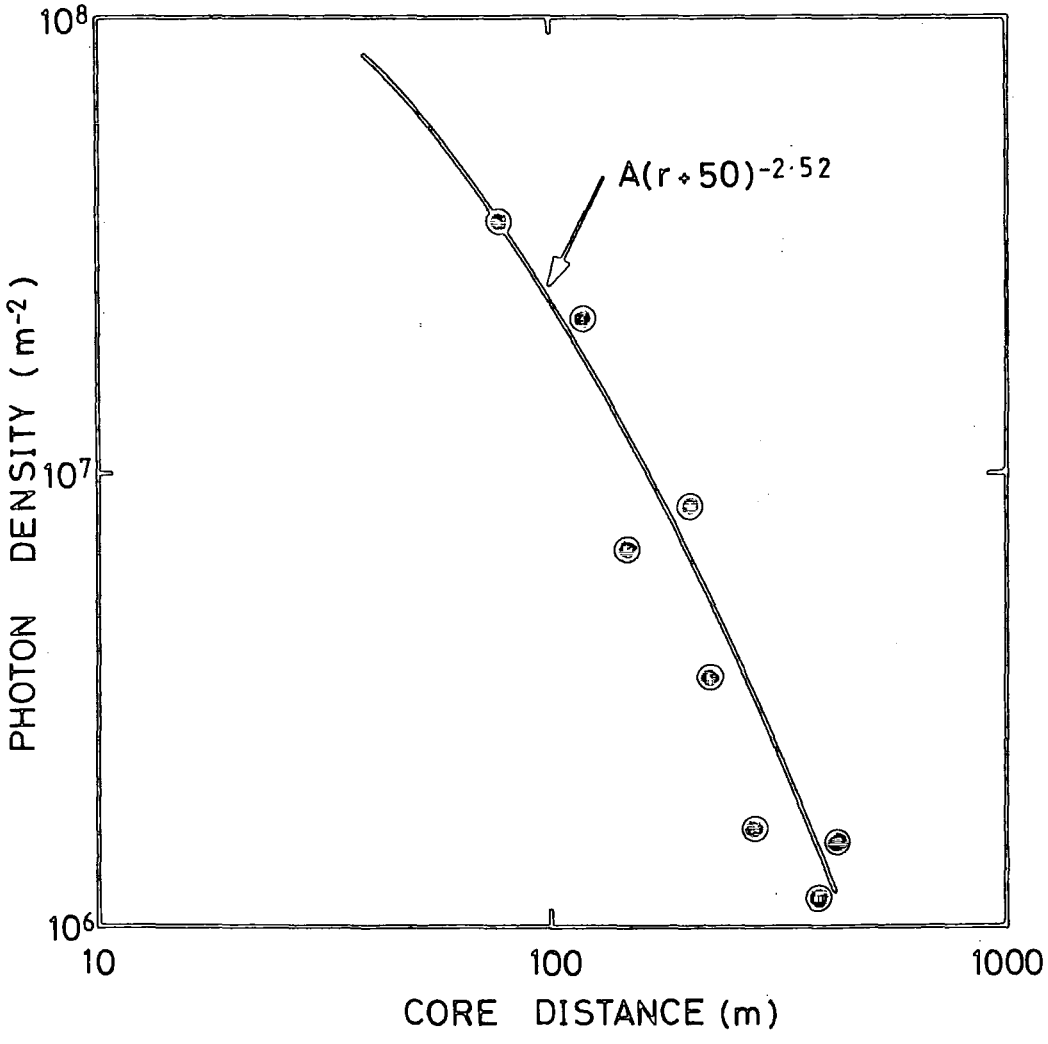

Allowance for the measurement uncertainties will enable the calculation of extent of the genuine fluctuations in the Cerenkov signal caused by fluctuations in the cascade development. A study of this topic is in progress and will be reported by Craig (Ph.D. thesis, in preparation).

4.3.2 Primary Energy Estimation

An important stage in the analysis and interpretation of air-shower data is the assignment of primary energy. Firstly, a parameter must be identified which allows the showers to be ranked in primary energy independently of changes in the cascade development. Secondly, the primary energy estimations must be calibrated in absolute terms, or at least interlinked with the primary energy estimations at other arrays to allow for comparison of cascade development measurements.

The Cerenkov radiation in EAS is a highly penetrating component, and therefore ground level observations of the total light flux could be expected to relate strongly to the total electron number and so to the energy of the primary particle. However, an estimate of the total light flux would require integration over all core distances and extrapolation from the recorded densities. A more directly measurable quantity must be chosen, which should ideally relate uniquely to primary energy independently from variations in the depth of cascade development (produced either by systematic changes with primary energy or by intrinsic fluctuations in the cascade processes).

Sea level observations at Haverah Park showed that the quantity $\Phi(200m)$, the photon density at 200 m from the core, may be a good primary energy estimator (Wellby (1977)). This quantity was found to correlate well with $\rho(500)_{ve}$, the Haverah Park primary energy estimator based on particle measurements (Hillas et al. (1971)), as shown in figure 4.5. Additional support for the use of $\Phi(200m)$ came from results of early computer simulations (Smith and Turver (1973)). Figure 4.6 shows the average lateral distributions (at sea level) predicted for

FIGURE 4.5 The relation between the Cerenkov light density at a core distance of 200 m and the Haverah Park particle-based primary energy estimator. (From Wellby (1977)).

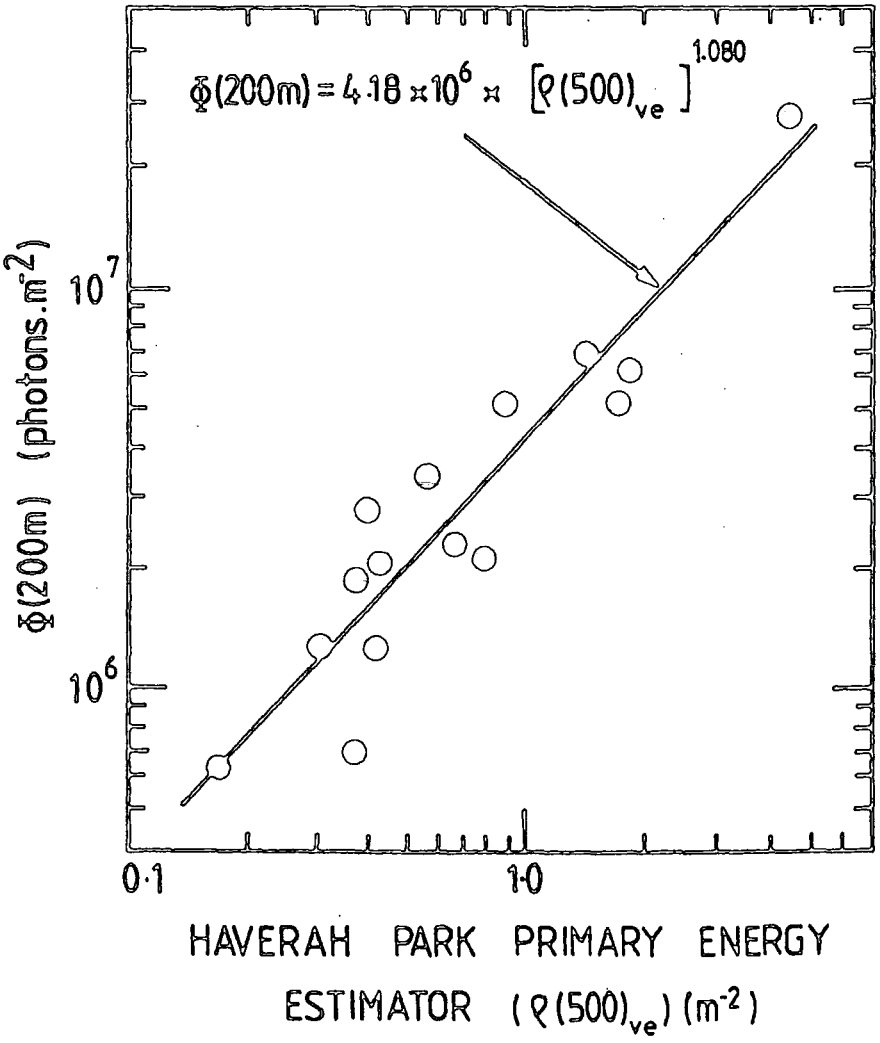

FIGURE 4.6 Calculated lateral distributions at sea level for average showers over a range of primary energy, and those for fluctuating showers at a fixed primary energy.

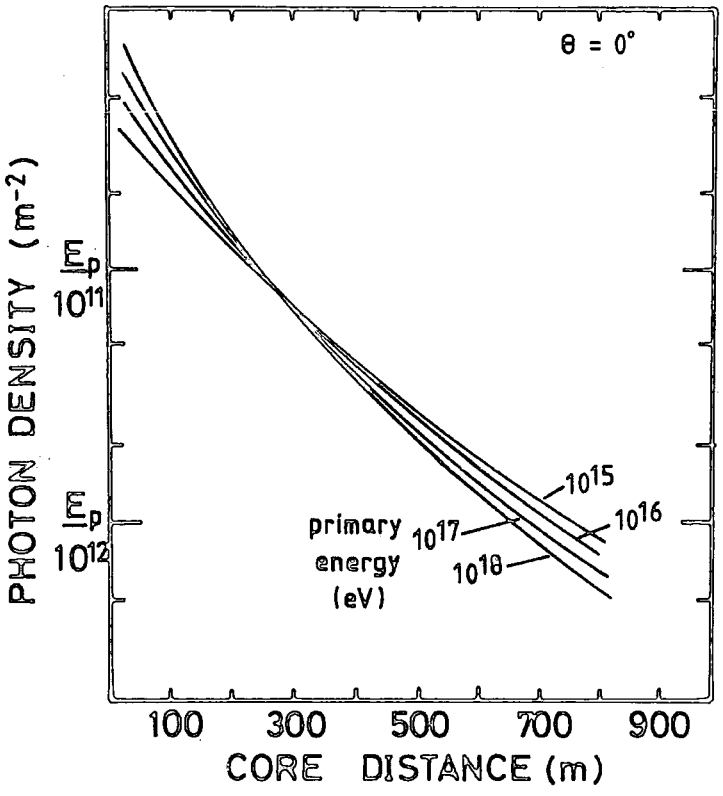

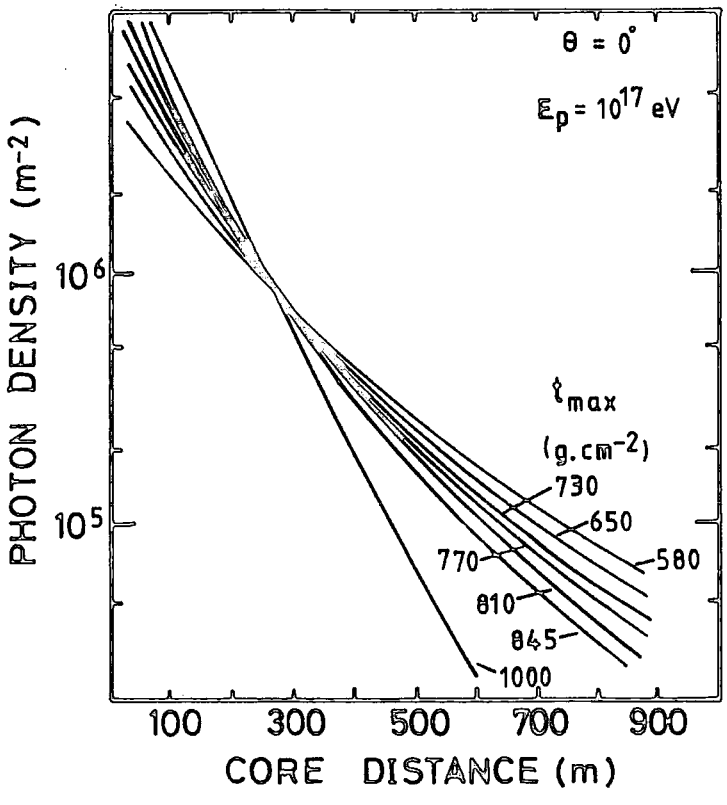

vertically incident proton initiated showers over a range of primary energy, and those for fluctuating showers at a fixed primary energy of 10^{17} eV. The photon density in the region 200 - 300 m from the core can be seen to be directly proportional to primary energy and independent of the fluctuations in cascade development. However, these calculations employed the CKP model for the pion momentum distribution (Cocconi et al. (1961)), which has subsequently been found to be in disagreement with results from accelerator experiments at lower energies (Morrison (1973)). In more recent simulations the CKP model has been replaced by scaling-based models, although some aspects of air showers are less well represented by such models. There is a requirement, therefore, to identify an energy estimator on the basis of the current scaling models, and which is appropriate to the observations at the Dugway altitude.

Figure 4.7 shows the lateral distribution calculated for three zenith angles for average iron-primary induced cascades based on the scaling model. These lateral distributions (which have been multiplied by r^2 for clarity) span four decades of primary energy, but each has been divided by its primary energy so as to produce a range of normalised lateral distributions parameterised by their depths of cascade maximum. It can be seen that there is no unique core distance at which the photon density is totally independent of the depth of cascade maximum. But there is a 'cross over point' which occurs at larger core distances either as the depth of maximum decreases or as the zenith angle increases. A reasonable compromise for showers with their cascade maximum in the range 600 - 800 $g.cm^{-2}$ is $\phi(150m)$, the photon density at 150 m from the core. For vertical showers $\phi(150m)$ exhibits $\lesssim$ 10% change over 100 $g.cm^{-2}$ change in depth of cascade maximum; the variation increasing to about 20% for showers incident at 45^{o}.

FIGURE 4.7 Calculated lateral distributions at an atmospheric depth of 862 g.cm^{-2} for average showers having a range of depths of cascade maximum. The calculations employed the scaling model with constant interaction cross-section.

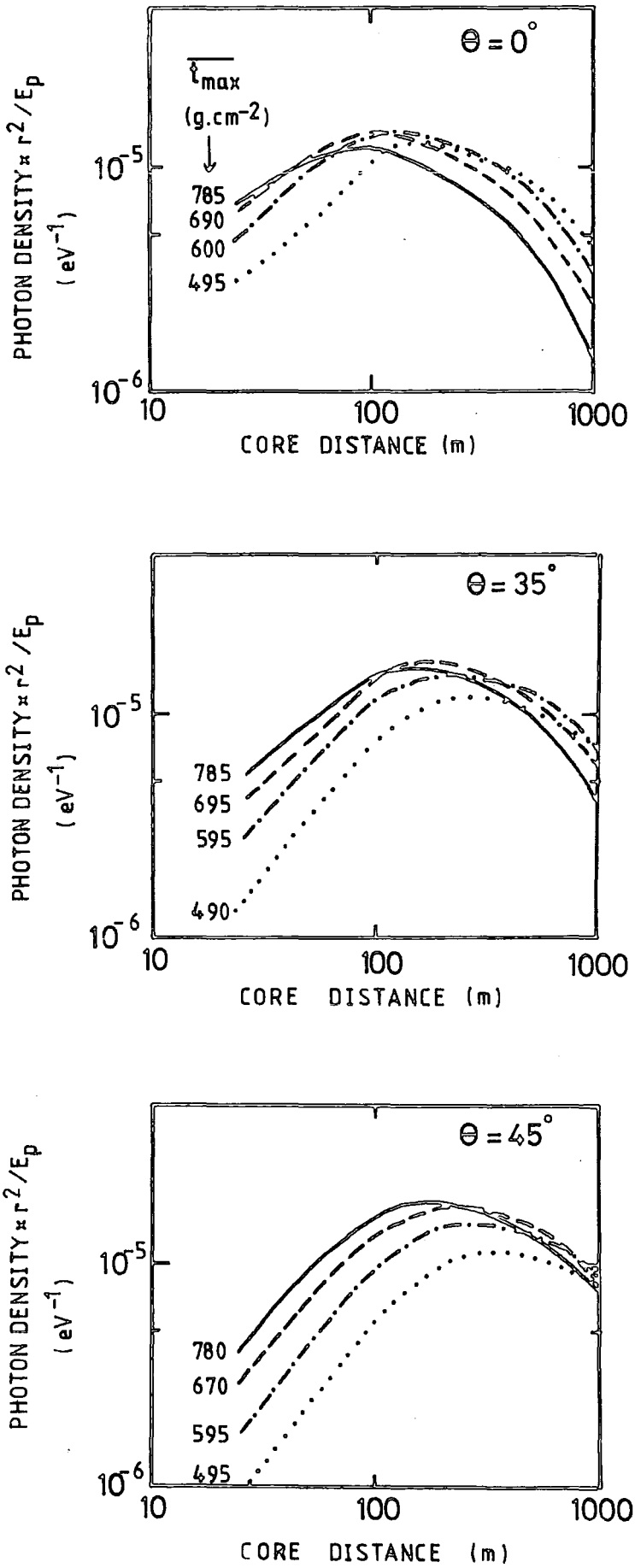

This quantity is readily measurable in showers recorded by the 400 m and 200 m arrays, and has been adopted as the primary energy estimator appropriate to these array sizes. For the lower energy showers recorded by the 100 m array, the preferred core distance for a primary energy estimator would be $\gtrsim$ 500 m. However, the largest core distance at which the photon density is routinely sampled is 100 m, and so in this case Φ(100 m) has, of necessity, been adopted as the primary energy estimator.

An attempt to interpret the energy estimator in terms of an absolute energy assignment is prone to systematic error. Such an interpretation would rely critically on the difficult conversion from mV.ns to photon number, requiring an exact knowledge of the number of photons emitted by the calibration light pulser. It would also require reliance on the absolute photon densities predicted by the model calculations, which are not easily testable. The primary energy assignments can, however, be linked to the energy assignments used at the Haverah Park and Volcano Ranch Arrays. The conversions from the particle-based energy estimators employed at these arrays to primary energy are generally regarded as consistent. Measurements of the Cerenkov light intensity, Φ(200 m), are available from each of these arrays in terms of a standard light unit (s.l.u.), where 1 s.l.u. is the number of photons generated by one flash of the NE 130 light pulser. In showers of assigned energy 10^{17} eV, the measured photon densities were:

Φ(200 m) = 6.95 s.l.u. (Haverah Park, 1016 g.cm^{-2}) and

Φ(200 m) = 9.38 s.l.u. (Volcano Ranch, 834 g.cm^{-2}).

By linear interpolation we would expect Φ(200 m) = 9.02 s.l.u. in a 10^{17} eV shower observed at Dugway (at an atmospheric depth of 862 g.cm^{-2}). This can then be combined with the calibration result that 1 s.l.u. = 243±53mV.ns to predict the Cerenkov light pulse area in a 10^{17} eV shower

observed at Dugway:

$\Phi(200\ m) = 2192\ mV.ns.$

Using the lateral distribution exponent from a simulated average vertical shower, with its depth of cascade maximum at 700 $g.cm^{-2}$, the pulse area at 150 m from the core can be obtained:

$\Phi(150\ m) = 4253\ mV.ns$ (for a primary energy of 10^{17} eV).

This provides the conversion from primary energy estimator (in mV.ns) to primary energy (in eV) to be used for the showers recorded by the 400 m and 200 m arrays. For the 100 m array, the conversion to primary energy must use the corresponding pulse area at 100 m from the core:

$\Phi(100\ m) = 9994\ mV.ns$ (for a primary energy of 10^{17} eV).

These primary energy assignments, being empirically related to the well established and consistent assignments employed at Haverah Park and Volcano Ranch, allow for the interpretation of cascade development measurements over a wide energy range, while minimising the possibility of systematic errors when combining results from the different arrays. The absolute value of the primary energy assignments does,of course, rely on the model calculations (Hillas Model E) used to interpret the particle density measurements.

4.4 CERENKOV LIGHT PULSE SHAPE ANALYSIS

4.4.1 Introduction

The process of recording the Cerenkov light pulse profiles at each detector by means of digitised samples has been described in chapter 3. In this section the technique for reducing the data from the decalibrated Cerenkov pulse shape records is described.

The distribution on the 'time-base' of the digitised samples or 'slices' was specified at the design stage of the experiment on the basis of two main considerations. Firstly, the system bandwidth dictated a minimum pulse width (in response to a delta function input), which in

turn imposed a lower limit on the useful time separation of the slices. And secondly, information on the expected range of pulse shapes was available from computer simulations and earlier experimental work at Haverah Park. The slices were accordingly distributed such that the optimum resolution was obtained by the first three slices in the region where the pulse profile was expected to change the fastest, while the later slices were situated further apart in order to sample the more slowly changing back-edge of the pulse.

The requirement, when reducing the data, is to reconstruct a continuous profile from the digitised slices. This will enable the extraction of the conventional measures of pulse shape, i.e. the FWHM and the rise-time, together with the times to percentage levels of the peak height to be used for imaging the Cerenkov cascade in the atmosphere. As the analysis proceeds to include the many smaller showers with predominantly faster pulses, it is possible that more direct pulse shape measures obtainable from the digital records may be appropriate. However, reconstruction of a continuous pulse profile is important, since it enables the utilisation of the pulse shape parameters which have already been established to be sensitive to the cascade development, as well as allowing comparison with results from other work.

4.4.2 Reconstruction of Pulse Shapes Using a Spline Function

The problem in reconstructing the pulse shape is that of finding a smooth function of time (t), which will fit the observations, i.e. five or six samples of the pulse area and the time at which the fixed discrimination level was exceeded, and behave 'sensibly' between and beyond the observations. It has been found (Orford, private communication) that polynomial fits tend to exhibit oscillations between the data points, and indeed this is always a possibility in any fitting method with too few restrictions on the function's form. The problem arises due to the analyticity of polynomials, i.e. the polynomial's

properties anywhere are defined once the polynomial value and all its finite derivatives are fixed at any point.

The obvious solution, to make purely local fits, introduces piecewise polynomials. These are polynomial segments defined only over a limited range of the independent variable (t). If the piecewise polynomial is constrained so that the time axis is divided into a number of spans delimited by breakpoints or 'knots', with the function value and all its derivatives continuous at the knots, then this constitutes a spline. A description of the theory of spline functions is beyond the scope of this thesis, but useful reviews can be found in Cox (1972) and de Boor (1978). The function most appropriate to this particular data fitting problem was chosen to be the quartic B-spline. This is a function which covers five adjacent spans of the t axis, is zero outside this range, and the exact shape of which depends only on the positions of the six knots. For evenly spaced knots, the shape is symmetrical and vaguely Gaussian. However, considerable flexibility in the shape is possible by varying the six knot positions on the time axis, enabling the function to be fitted to a wide range of unimodal pulses. Initially, consideration was given to using the cubic B-spline, a spline function defined by only five knot positions. However, tests of both functions, using a technique to be described in section 4.4.3, produced significantly better fits with the quartic B-spline.

The algorithm developed for the fitting process involves the evaluation of quartic B-splines using a recurrence relation given by Cox (1972). The positions of the knots are varied until the least-squares fit to the observations is obtained. The goodness of fit is determined by sampling the predicted B-spline in a way analagous to the sampling of the Cerenkov light pulse by the detector, i.e. the function is sampled at the discrimination time and integrated or 'sliced' at

the time specific to that detector from which the observations had originated. Figure 4.8 illustrates quartic B-splines fitted to the decalibrated pulse shape data for the example EAS event. Figures 4.9 and 4.10 show the variation of the FWHM and rise-time of these pulses with core distance in the shower plane.

The core distances at which the pulse shapes are recorded in an EAS depend of course, on where the shower core landed within the array, and this will be influenced to a certain extent by the range of primary energies and zenith angles within a data sample and array selection effects. It is useful, therefore, to derive one or more interpolated pulse shape parameters for each shower at a fixed core distance, for example the FWHM at 300 m,which can be used for comparison between individual showers. An interpolation can be obtained using a weighted regression fit of the FWHM to the form $a + br^2$ (although the exact functional form is not of first order importance for an interpolation). The core distance chosen for the interpolation must be a compromise between a large enough value of r to provide a good sensitivity to the cascade development, and a value small enough so as not to exclude a significant proportion of showers from the dataset due to instrumental threshold effects.

The spline fitting technique has been tested on a range of pulses, and some of its limitations together with estimations of the experimental accuracy obtainable in reconstructing pulse shapes are discussed in the following section.

4.4.3 Estimation of the Errors in Pulse Reconstruction

It is important to estimate how accurately certain pulse shape parameters such as the FWHM, or the time to a fixed percentage of the pulse height, can be determined from the digital records. Firstly, it must be ascertained whether any biases are introduced by the fitting

FIGURE 4.8 The pulse profiles for the example EAS event, reconstructed using quartic B-splines.

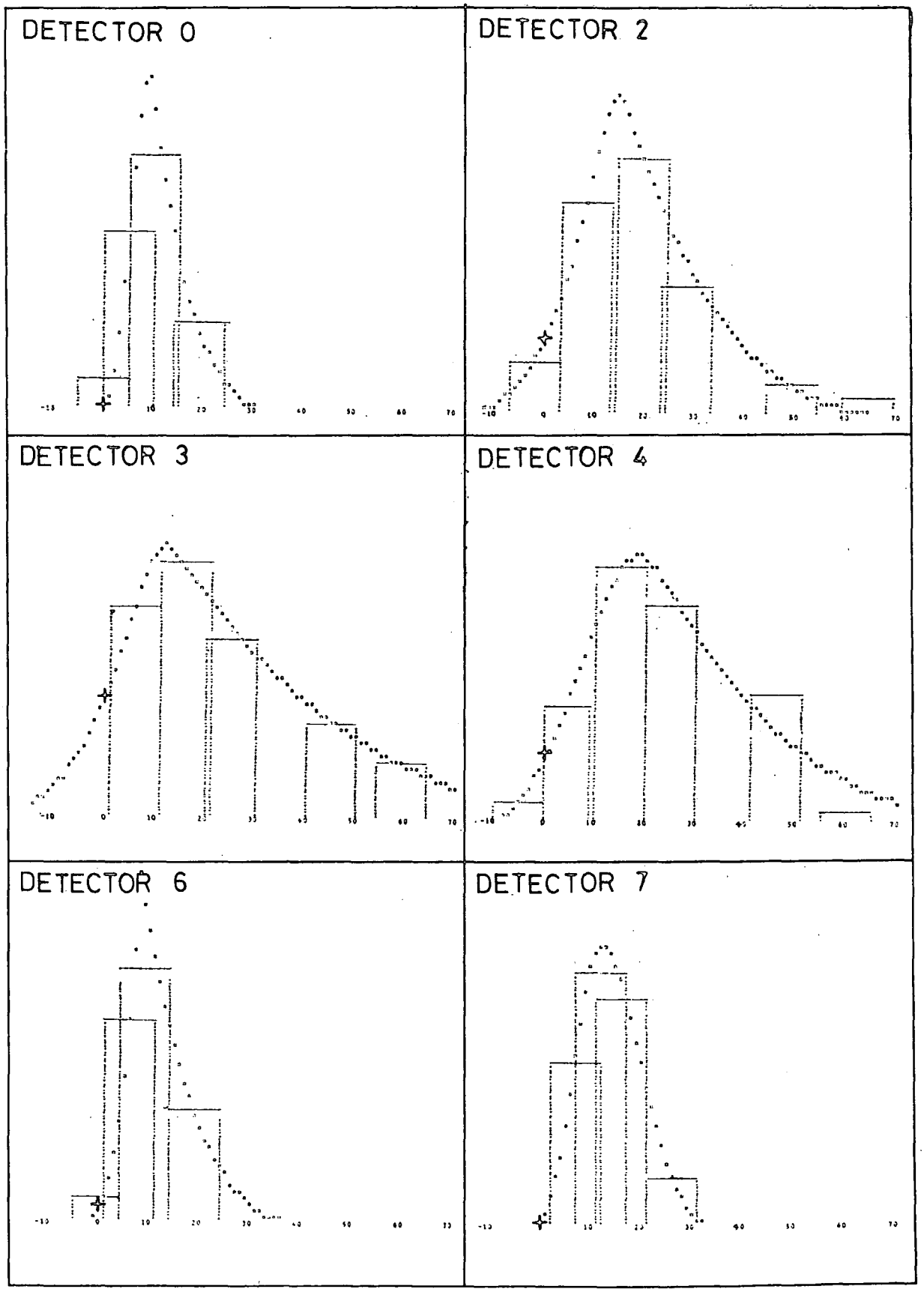

(+ discrimination level)

FIGURE 4.9 The variation of FWHM with core distance for the pulses shown in figure 4.8.

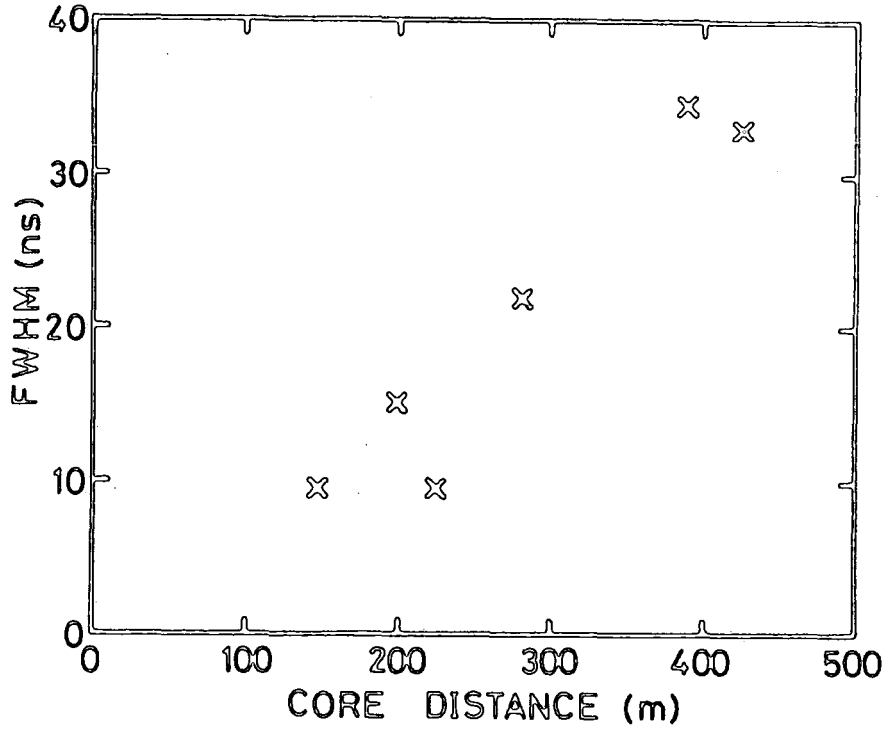

FIGURE 4.10 The variation of rise-time with core distance for the pulses shown in figure 4.8.

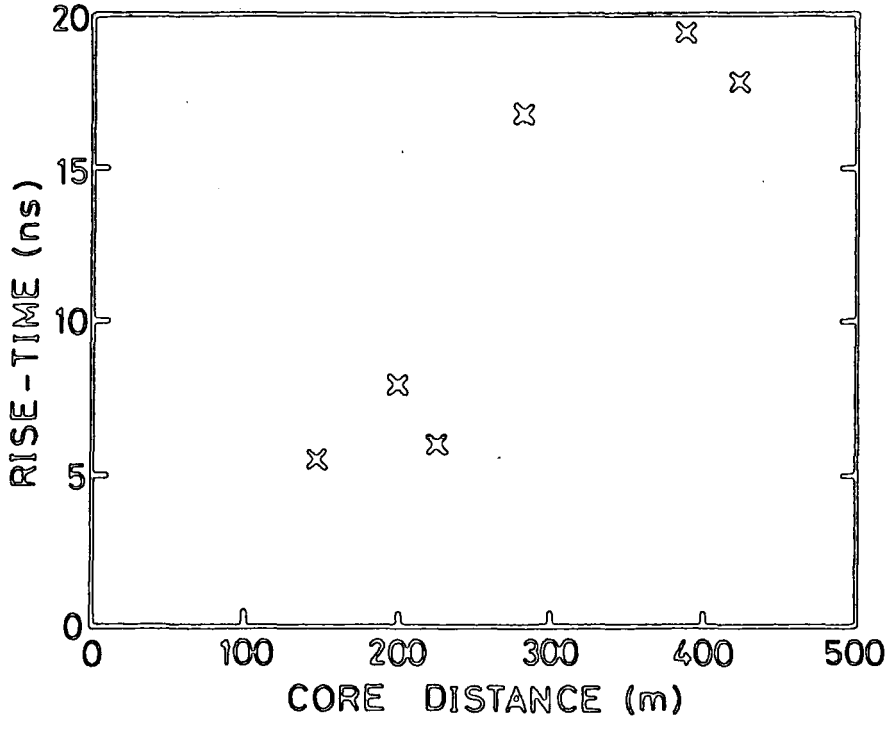

procedure; and secondly, the random components of error must be quantified to enable realistic estimates to be made of the uncertainties on the derived shower parameters.

In order to test the spline fitting procedure, a range of pulses of FWHM from about 7 to 60 ns were selected from the Durham group's computer simulation results. Each of these was scaled to a range of heights, from 25 to 1000 mV, to provide a matrix of test pulses parameterised by FWHM and height. The sampling of these pulses was then simulated, using a computer program, in an analagous way to that in which a Cerenkov light detector samples a light pulse, i.e. at the discrimination time and by making five 'slices'. The bit quantisation of the slice heights that would be imposed by the digitising electronics was also taken into account. Loss of information due to these sampling conditions will, in itself, contribute to the errors in the reconstructed pulse shapes. The five slices and the discrimination time were then supplied to the spline fitting routine, and the resulting fitted curves were compared with the original input pulses. Four examples of these spline fitted pulse shapes of different FWHM are shown in figure 4.11. No significant systematic errors in the reconstructed pulse shapes were found in any region of the matrix. Typical errors on the FWHM were 1.5 ns, on the time to peak height 1.0 ns, and on the pulse area 2.6%.

Having established confidence in the fitting procedure, estimates of the experimental errors under more realistic operating conditions could be made. To allow for the effects of sky background light superposing bandwidth limited noise onto the Cerenkov light pulses, a Gaussian random number generator was inserted into the computer program, and simulated noise with a standard deviation of 5 mV was added to the discrimination level and 'digitised' slices of the test pulses. The value of 5 mV was considered reasonable from measurements of the variance

FIGURE 4.11 Pulse profiles from model calculations (·), with FWHM values as indicated, have been sliced as if by a Cerenkov light detector. The slices (----) have been supplied to the spline fitting routine. The fitted B-splines (*) and the predicted slice heights (pppp) are indicated.

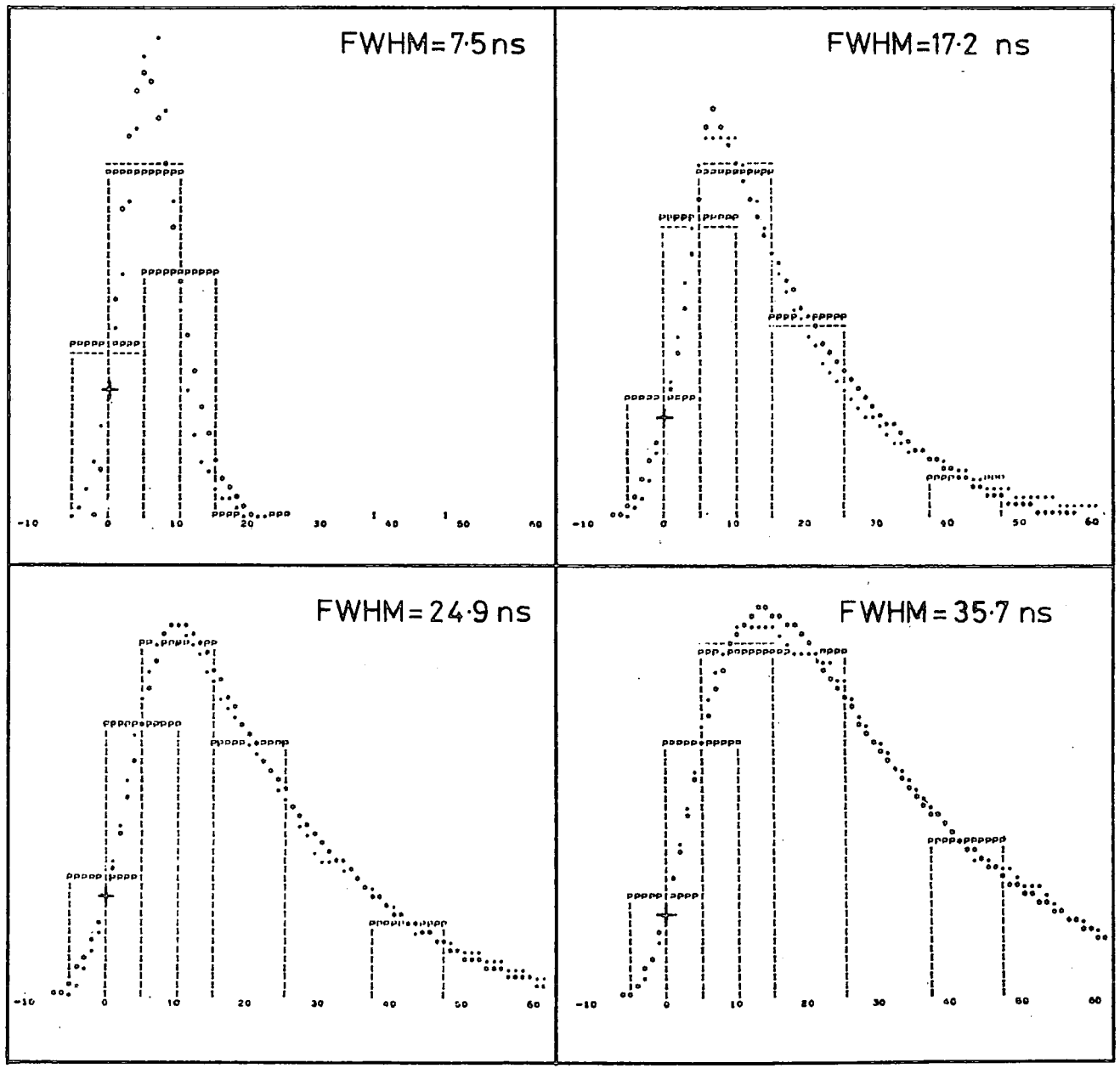

on the slice pedestal calibrations recorded with the photomultiplier tubes energised and viewing the night sky. The fitting routine incorporating the effects of noise was tested on the range of pulse shapes, each fit being repeated ten times in order to establish the average effects of the noise, and to obtain the standard deviations of the required pulse shape parameters. In general, there were no significant systematic differences between the input pulse parameters and the reconstructed pulse parameters. One exception to this was the tendency for the pulse rise-time to be systematically overestimated especially for small pulses with small signal to noise ratio. However, it would be possible to quantitatively remove this second order effect from the data on the basis of this work. As would be expected, the extent to which the noise affected the reconstructed pulse shapes was determined primarily by the height of the pulse and very little by the width. The effects of noise became of little significance for pulses greater than 100 mV in height (5 x threshold). Examples of the random errors on the times to percentage levels of the pulse height are shown in figure 4.12, illustrating that the time to the peak of the pulse is the most accurately measured parameter for small pulses where the effects of noise are greater. The errors on the times to fixed percentage levels are important since they propagate through the analysis to contribute to the error on the fitted radius of the light front.

The standard deviations on the fitted FWHM and rise-time are shown in figure 4.13. For pulses which are not significantly greater than the discrimination level (20 mV), the accuracy of the estimated parameters is obviously limited due to extrapolation outside the span of the digitised samples. The error estimations on the FWHM and rise-time can be used to enable more realistic weighted regressions of these parameters

FIGURE 4.12 The uncertainty in the fitted times to various percentage levels of the pulse height as a function of pulse height. The standard deviations include the simulated effects of sky noise.

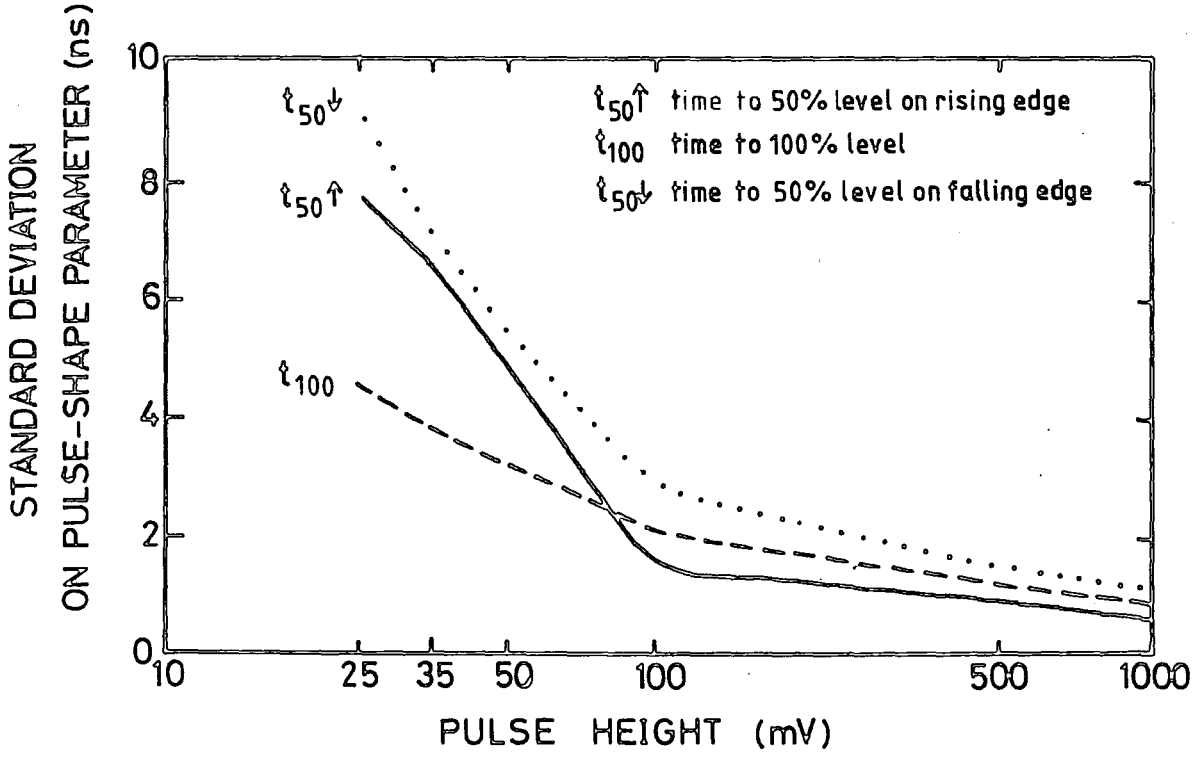

FIGURE 4.13 The uncertainty on the fitted FWHM and rise-time as a function of pulse height. The standard deviations include the simulated effects of sky noise.

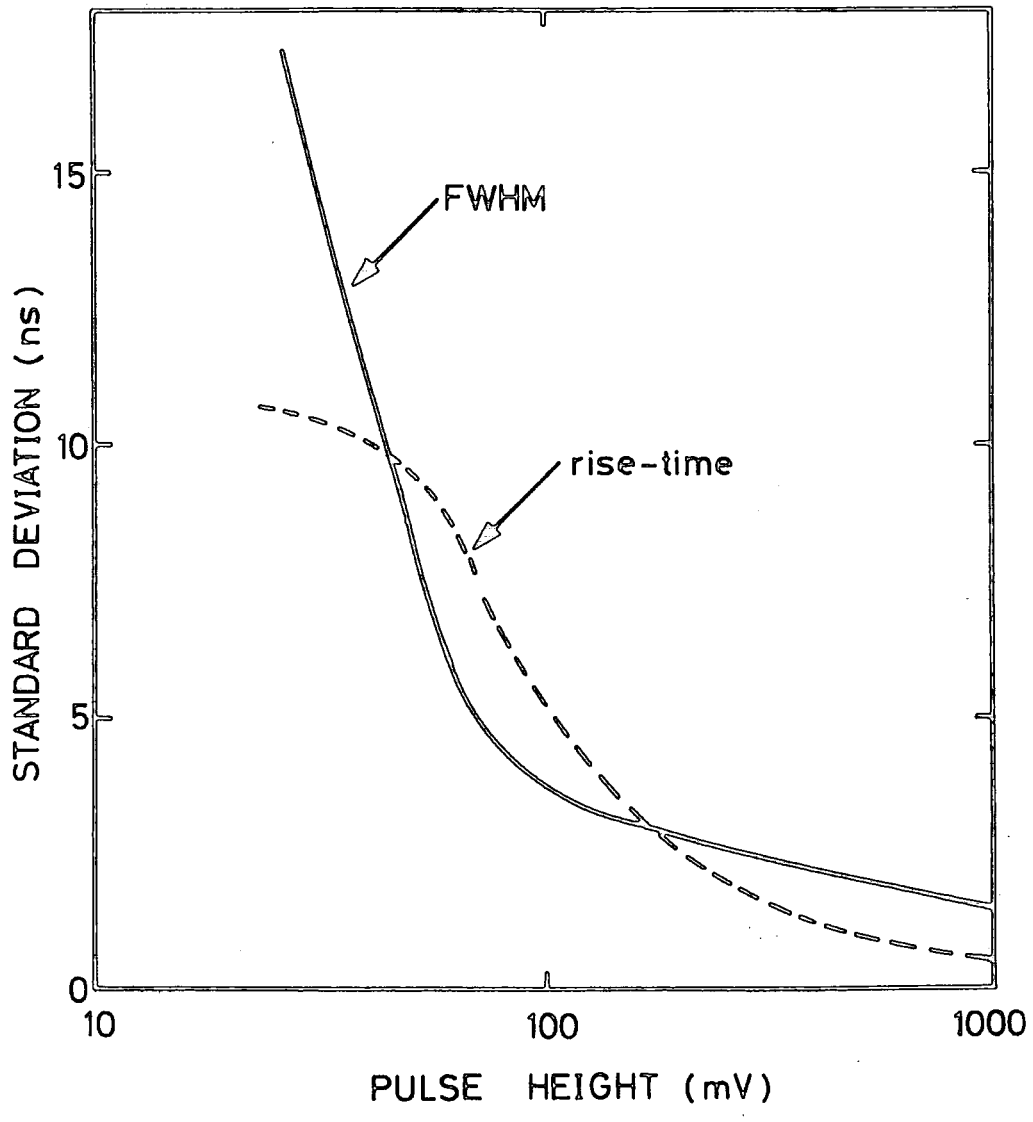

against core distance (helping to fulfil the theoretical requirement of constant or standardised variance for regression fits), and hence to optimise the estimates of the interpolated parameters.

A possible criticism of this spline fitting technique is that with small pulses, where the noise level becomes a significant fraction of the slice heights, the function has too much freedom. In some cases, for example, the function adopts an apparently 'non-physical' shape with too sharp a peak or too slow a rising edge than would appear reasonable, owing to lack of restriction on the function's form. However, these effects can usually be treated as random errors on the derived parameters and have necessarily been incorporated in the quantification of the measurement errors. The use of an analytical function, with more severe constraints on its behaviour based on an 'a priori' knowledge of the shapes of Cerenkov pulses, might produce improved pulse shape reconstruction in certain cases.

A disadvantage of the spline fitting procedure should be mentioned, namely the large amount of C.P.U. computer time required to numerically optimise a six-parameter function. For this reason, not all the pulses recorded at Dugway will be spline-fitted and analysed for the work presented in this thesis, but rather a selection of data will be considered in detail prior to the analysis of a more complete dataset.

4.5 IMAGING THE CASCADE DEVELOPMENT FROM CURVATURE MEASUREMENTS

4.5.1 The Depth of Origin of the Cerenkov Light Signal

As discussed in chapter 2, spherical fronts fitted to the times to fixed percentage levels through the recorded light pulses can be used to construct an image of the growth and decay of the Cerenkov light cascade in the atmosphere. Since the Cerenkov light produced is directly linked to the electromagnetic cascade, this presents a way of mapping or imaging the longitudinal cascade development of extensive air showers.

The analysis technique requires the combination of two sets of measurements: the synchronised time of arrival of the light front, i.e. the discrimination time (t_i), is added to the time within the pulse (p_i) between the discrimination time and the time to a fixed percentage level of the pulse height. If four or more measurements are available in an event, then a spherical front can be fitted. In practice, at least five responses are used to provide a degree of redundancy.

The spherical fronts are numerically determined by minimising the sum of the weighted squared residuals. This is essentially a standardised chi-square fit of the form:

$$S^2 = \sum_{i=1}^{N} \frac{[(t_i + p_i) - T_i]^2}{\varepsilon_i^2} \qquad 4.9$$

in which S^2 should be sampled from a χ^2 distribution with N-4 degrees of freedom. The weighting factors (ε_i^2) are formed by the quadratic addition of the variance (σ^2) derived in section 4.2.3 for the synchronised-timing measurements (t_i), and the variance estimated in section 4.4.3 on the time within the pulse (p_i). The variance on p_i is estimated for each detector response as a function of pulse height using the information illustrated in figure 4.12. The optimisation procedure utilises the computer software package MINUIT.

Figure 4.14 illustrates the light origins corresponding to a set of six percentage levels of the recorded light pulses for the example EAS event. The origins are colinear, and show the trajectory of the EAS through the atmosphere in the two orthogonal planes (x-z, y-z). A straight line fitted through these points has a standard error of $\sim$ 8m. Extrapolation gives the location of the shower core in the ground plane. The core position located by this method is generally found to be in good agreement with that determined by the separate analysis of the Cerenkov light intensities (within 30 m in the example event). This

FIGURE 4.14 The image of the cascade development for the example EAS event, reconstructed from synchronised measurements of the pulse time-structure.

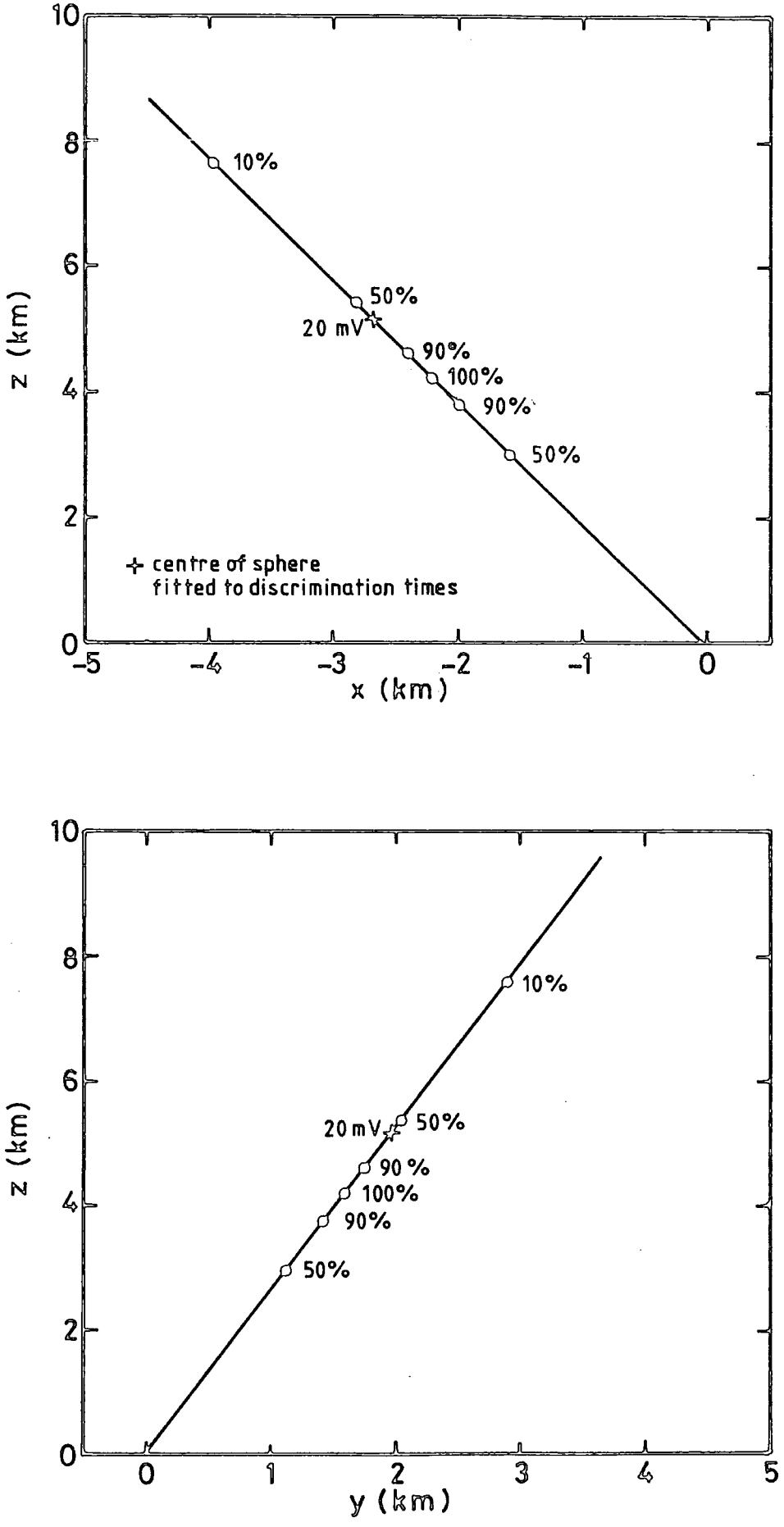

method has the advantage that the core can be located even when it falls outside the array boundaries, whereas the core position cannot, in these circumstances, be uniquely determined from the Cerenkov light densities (since the estimates of the core location and the lateral distribution exponent would not be independent). Also shown in figure 4.14 is the origin of the spherical front fitted to the discrimination times. This is located at only $\sim$ 15 m from the linear fit through the other points, providing confidence in the determination of the arrival directions by using the discrimination times alone. The spatial separation of the light origins along the shower axis is related to the rate of development of the cascade. This is illustrated in figure 4.15 which shows the build up and decay of the Cerenkov light image as a function of $g.cm^{-2}$ track length or depth into the atmosphere.

It is envisaged that this technique will be applied to a sample of well measured, high energy events, in which an optimum number of pulse shape records are available. Measurements of the average characteristics and fluctuations in the Cerenkov light image obtained using this technique will be discussed in chapter 6. An estimate of the extent of the fluctuations in depth of Cerenkov light origin between showers, due to fluctuations in the depth of electron cascade development, will require consideration of the uncertainties on the fitted parameters. A method of estimating the uncertainties in the Cerenkov light origins in individual showers is discussed in the following section.

4.5.2 The Experimental Uncertainty in Locating the Cerenkov Light Origins

The experimental errors on the derived light origins in the atmosphere depend on several factors. Firstly, the number of detector responses used in the fit, and hence the number of degrees of freedom available, influences the accuracy to which the light origin can be determined. Secondly, the geometry and spatial separation of the

FIGURE 4.15 The reconstructed image of the cascade in Cerenkov light as a function of depth into the atmosphere.

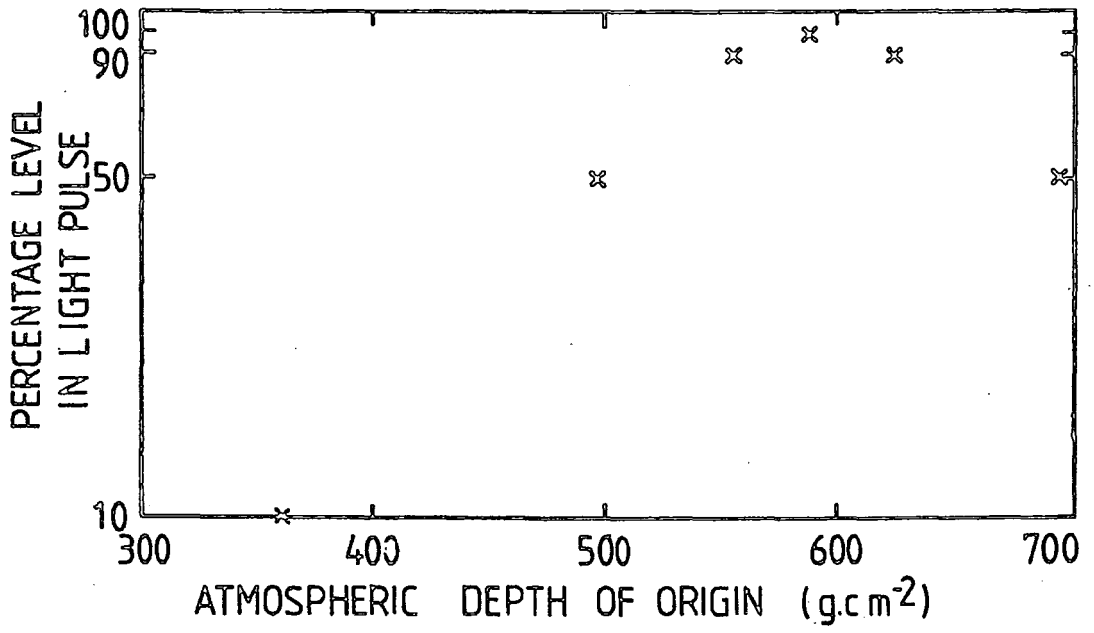

triggered detectors when projected into the shower plane affects the amount of useful information recorded. This is because the tangent plane delays, illustrated in figure 4.1 for a simulated shower, should be sampled over the greatest possible region of the light front to maximise the signal to noise ratio. As the zenith angle increases, for example, the reduction in the size of the array when projected into the shower plane results in a reduction of the effective baseline from which the curvature of the light front can be measured. Also, some geometrical configurations of triggered detectors are less favourable towards determining the radius of a spherical front than others. Thirdly, the signal to noise ratio is inherently greater for showers developing closer to the array, which have a steeper increase of tangent plane delay with core distance. Finally, the size of the measurement errors (in ns) has a direct influence on the size of the error on the estimated light origin. Incorporation of the error variances (ε_i^2) in the function to be minimised (equation 4.9) serves to standardise the function, giving it statistical meaning.

There is no analytic expression for the uncertainty on the perceived light origin due to the above-mentioned factors. However, a displacement from the coordinates of the light origin is mapped by an increment in the function S^2, and error estimations can be made by examining the behaviour of S^2 in the region around its minimum value. The theoretical requirements to make an error estimation are that the distribution of the K estimators ($\underset{\sim}{X}$) of the K parameters ($\underset{\sim}{x}$) is normal many dimensional with $\overline{\underset{\sim}{X}} = \overline{\underset{\sim}{x}}$ and with a non-singular covariance ($\underset{\sim}{V}$). Under these conditions, the covariance form $(\underset{\sim}{x} - \underset{\sim}{X})^T \underset{\sim}{V}^{-1} (\underset{\sim}{x} - \underset{\sim}{X})$ has a chi-square distribution with K degrees of freedom (Eadie et al. (1971)). A hypersurface, of constant probability density is then defined by:

$$(\underset{\sim}{x} - \underset{\sim}{X})^T \underset{\sim}{V}^{-1} (\underset{\sim}{x} - \underset{\sim}{X}) = \text{constant} = \chi^2_\beta (K) \qquad 4.10$$

where β is the probability content within the hypersurface, and $\chi^2_\beta(K)$ is the β-point on the theoretical chi-square distribution with K degrees of freedom.

In practice, therefore, the joint one standard deviation confidence region in x,y,z - space on the fitted light origin can be delimited by the surface:

$$S^2 = S^2_{min} + \chi^2_{0.68}(3) \qquad 4.11$$

where $\chi^2_{0.68}(3) = 3.5$. This is the surface of an ellipsoid, the proportions of the axes depending on the correlations between the estimators. The largest axis of this ellipsoid (and hence the largest component of error) is always found to be aligned along the radius vector (i.e. the shower trajectory).

A more convenient representation of the problem can be made in the polar coordinate system : r, θ, ϕ. Here, the one standard deviation confidence interval on the radius estimator (R) might be represented, irrespective of the errors on the other two estimators, using:

$$S^2 = S^2_{min} + \chi^2_{0.68}(1) \qquad 4.12$$

where $\chi^2_{0.68}(1) = 1.0$. This defines the surfaces of a spherical shell, the inner and outer radii of which delimit the confidence region on R. This reduces to a one dimensional problem, since the arrival direction is comparatively accurately known from the optimisation routine, and so the value of S^2 can be sampled in increments along the shower trajectory until equation 4.12 is satisfied. However, this error estimation is strictly valid only if R is normally distributed. As will be discussed in the following section, deviations from Gaussian behaviour would entail the use of a slightly larger increment on S^2 to obtain the 68% confidence interval on R. Figure 4.16 illustrates,

FIGURE 4.16 The region around the origin of the optimum spherical fit to the synchronised times of the pulse height maxima.

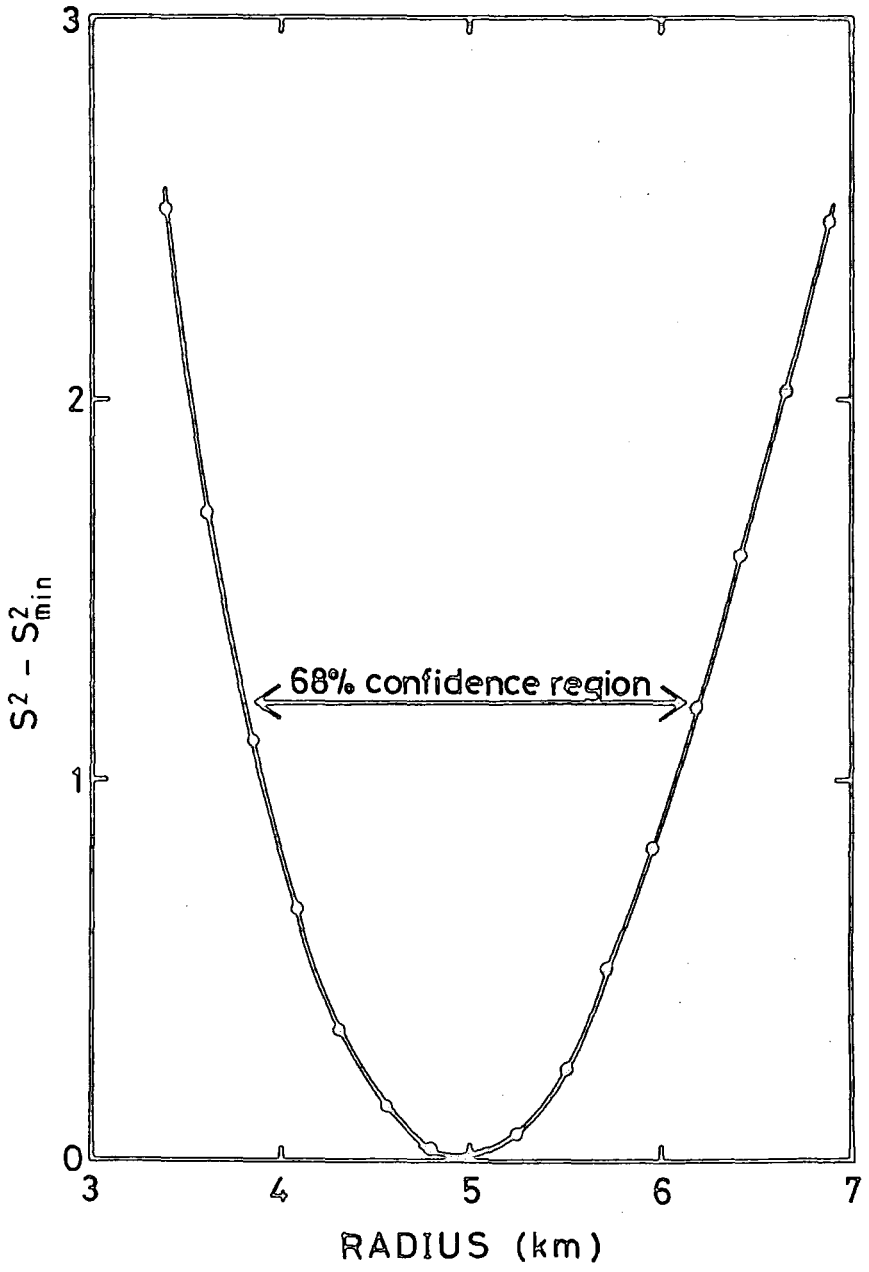

for the example EAS event, the variation of S^2 along the shower trajectory for the fit to the times of maximum recorded light intensity. The function S^2 exhibits in this case, as for the majority of events, a smooth parabolic minimum allowing for unambiguous evaluation of the required confidence interval.

The identification of an error estimator on the atmospheric depth of origin of the light front requires further consideration. A direct transformation of the error on the radius estimate to an error in $g.cm^{-2}$ may not be correct, since depth is a function of both r and θ, and may exhibit a different probability density distribution. Moreover, the transformation of an interval in metres to $g.cm^{-2}$ has a non-linear dependence on the region of the atmosphere involved. Therefore an error estimation in $g.cm^{-2}$ should be made in the region of the atmosphere centred on the expected depth rather than on the fitted origin.

In view of the importance of reliably determining the experimental errors towards the aim of quantifying the fluctuations in the cascade development, it was considered necessary to set up a computational model. These calculations, described in the following section, enable the statistical assumptions to be tested under realistic conditions, provide 'empirically' an error estimator for the depth of origin of the light front, and enable the parameter estimators to be examined for biases.

4.5.3 Monte Carlo Calculations of the Effects of Timing Errors on the Determination of the Cerenkov Light Origins

A computer program was developed to simulate, under controlled conditions, the effects of noise (in the timing measurements) on the perceived light origin, using the following Monte Carlo procedure. A 'light' origin in space is chosen, and the theoretical light transit times to each detector's coordinates are calculated. A Gaussian random number generator adds random noise with a known standard deviation to

these transit times. The same multi-parameter optimisation routine as used for the experimental data is then used to minimise the standardised chi-square function, and to estimate the origin of the simulated light front. These calculations were repeated a large number of times in order that effects of noise could be assessed, and to enable the other factors contributing to the signal to noise ratio, i.e. the arrival direction, the atmospheric depth of the light origin and the pattern of contributing detectors to be taken into consideration.

A number of conclusions could be drawn from the results of this exercise. Firstly, the standardised chi-square function (S^2) was found to be distributed as the expected $\chi^2(N-4)$ distribution (where N is the number of detector responses), with $\overline{S^2}$ equal to the number of degrees of freedom (N-4). This is important since it implies that the time delay estimators (T_i) are normally distributed,which is by no means true in general for estimators obtained through non-linear optimisation. The assumption that the mean value of the standardised chi-square function should in practice equal the number of degrees of freedom was a fundamental assumption in the estimation of the error variance (σ^2) on the synchronised-timing measurements (see section 4.2.3).

The confidence intervals, suggested by statistical theory, could be tested since both the input and the fitted parameters were known. The probability content in x,y,z -space within the surface $S^2_{min} + \Delta S^2$ was evaluated by calculating the percentage of cases for which the input light origin lay within this surface. In figure 4.17 the variation of probability content with ΔS^2 is compared to the expected cumulative $\chi^2(3)$ distribution. It can be seen that the value of ΔS^2 which delimits the joint one standard deviation confidence region on the fitted light origin (X,Y,Z) is in good agreement with expectation, as indeed is the whole probability distribution. The probability

FIGURE 4.17 The probability distributions for various parameterisations of the fitted light front compared with cumulative chi-square distributions.

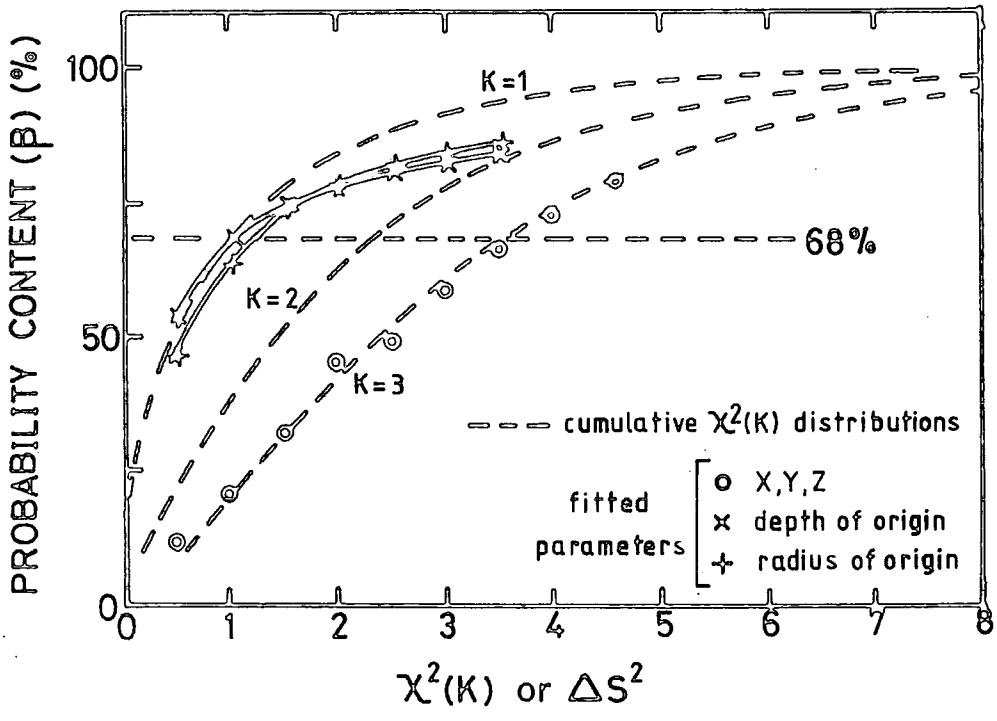

distribution for the radius estimator (R) was obtained from the percentage of cases for which the input radius was contained with the bounds $S^2_{min} + \Delta S^2$ in r-space. This is compared with the expected cumulative $\chi^2(1)$ distribution in figure 4.17, showing that the radius estimator is not sampled from a normal distribution, and that a 68% probability content is contained within the interval $\Delta S^2 \simeq 1.2$. In order to obtain an error estimator for the atmospheric depth of origin of the light front, the interval in r-space was transformed to an interval in $g.cm^{-2}$ in the region centred on the mean input depth. The probability content for various values of ΔS^2 was then defined as the percentage of cases in which the fitted depth lay within this interval. As can be seen in figure 4.17, the 68% confidence interval on the atmospheric depth of origin is satisfactorily described by $\Delta S^2 \simeq 1.0$.

The calculations described above were tailored to the experimental dataset chosen for the analysis of the depth of origin of the Cerenkov image maximum (see chapter 6). The initial conditions for each optimisation, i.e. the arrival direction and the number and configurations of triggered detectors were taken from the experimental data. Each simulated event was repeated several times with a different randomisation of the transit times, but with the standard deviation of the timing errors appropriate to that estimated for the experimental measurements. The input depths of origin were derived, via model calculations, from a plausible prior distribution of depths of electron maximum. Having been derived under these conditions, the error estimators are expected to be reliable when applied to the experimental measurements.

These Monte Carlo calculations also provided the opportunity to test whether the estimators, especially the atmospheric depth of the light origin, will be unbiased over an appropriate range of observational conditions. Since the analysis of the Cerenkov light signal from EAS

will involve measurements of light originating from a range of altitudes and zenith angles, and with widely varying signal to noise ratio, it is reasonable to enquire whether any systematic errors could arise under these conditions from the effects of the random timing errors in the non-linear optimisation processes. Figures 4.18 to 4.20 show the mean fitted depth of origin corresponding to an input depth of 550 $g.cm^{-2}$. The signal to noise ratio has been changed by systematically varying the standard deviation on the transit times, the number of detector responses and the zenith angle respectively. Each point is derived from 100 simulated events distributed uniformly in azimuth angle; the mean, standard error and standard deviation of the distributions of fitted depths are shown in each case. Figure 4.21 shows the effects of varying the input depth of origin while retaining the other initial conditions constant. Each of these figures illustrates how the accuracy of the fits is reduced rapidly by an increase in signal to noise ratio. In particular, at a certain level of signal to noise ratio, the mean fitted depth of origin exhibits a bias. This bias is of the same sign whichever one of the initial conditions was principally responsible for the low signal to noise ratio. Clearly, the interpretation of an experimentally derived distribution of depths of Cerenkov light origin must take this effect into consideration.

FIGURE 4.18 The error on the fitted depth of light origin as a function of the standard deviation on the timing measurements.

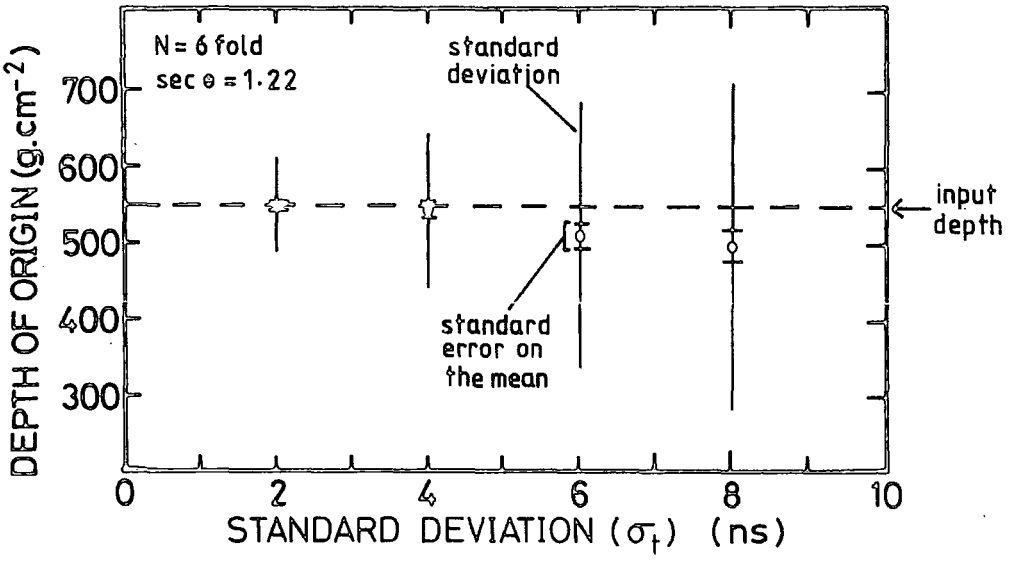

FIGURE 4.19 The error on the fitted depth of light origin as a function of the number of detector responses.

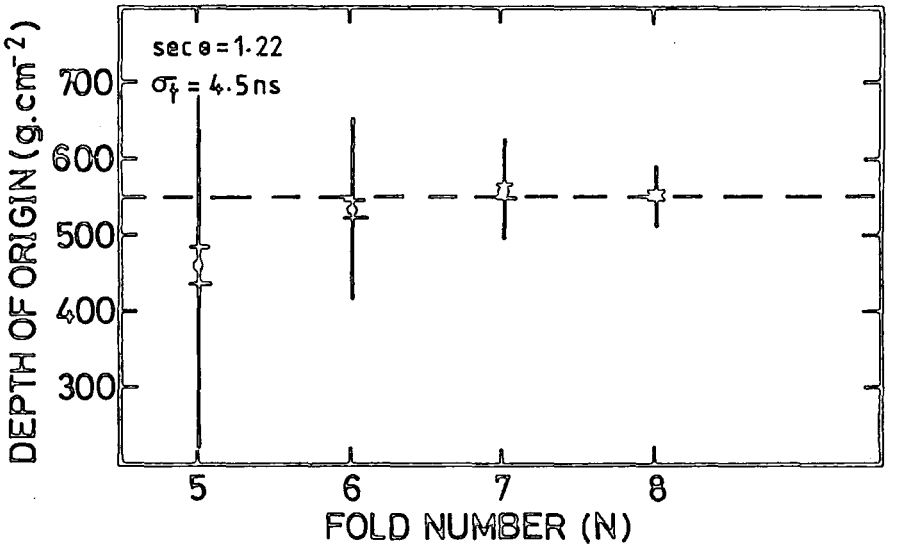

FIGURE 4.20 The error on the fitted depth of light origin as a function of the secant of the zenith angle.

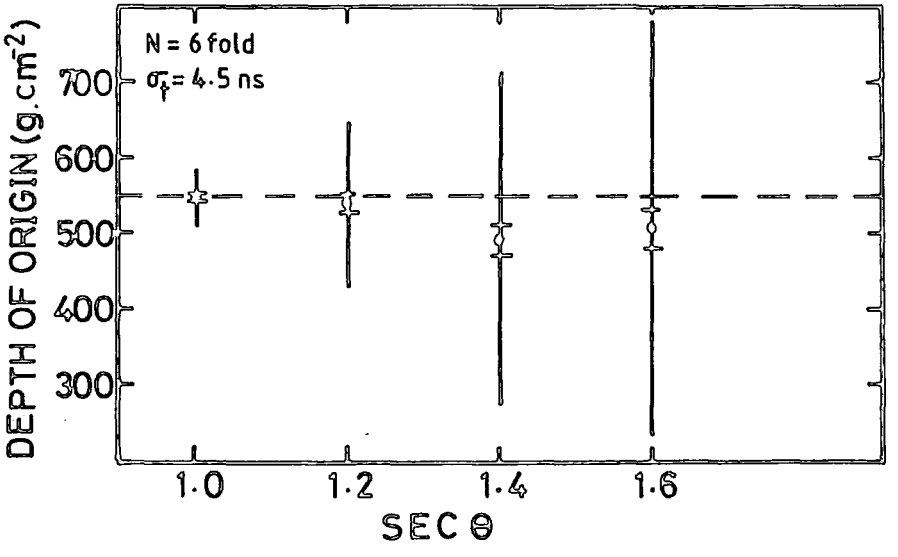

FIGURE 4.21 The error on the fitted depth of light origin as a function of the true depth of light origin.

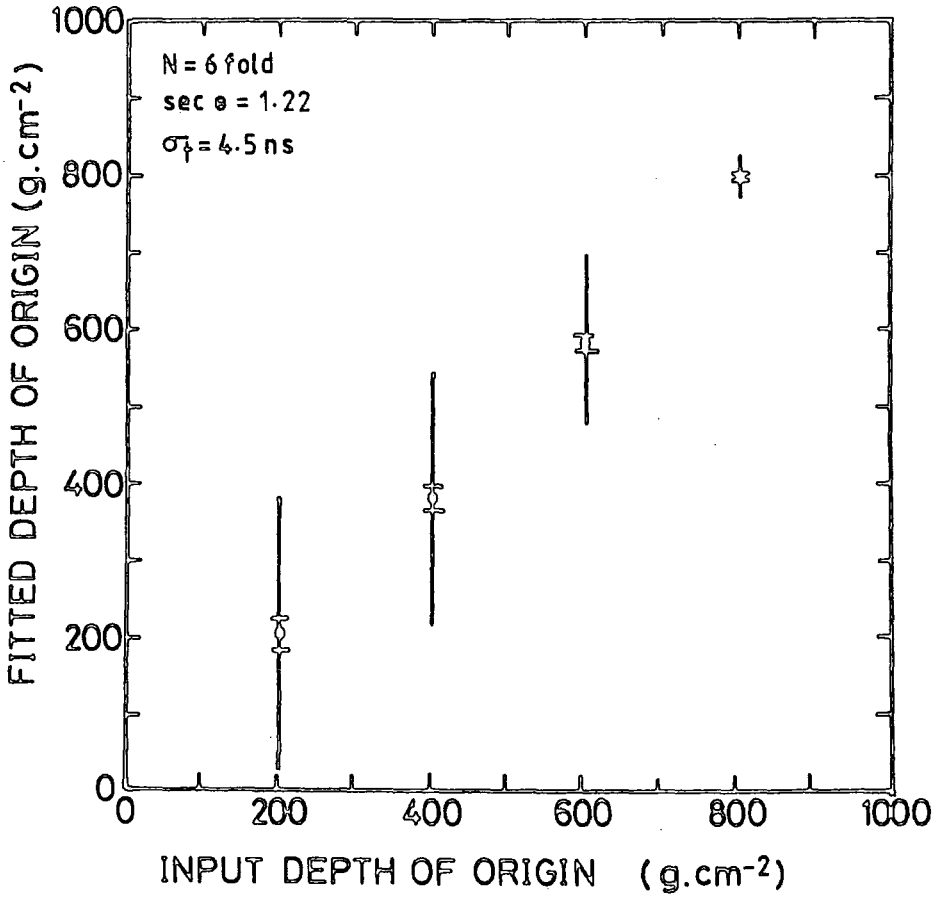

CHAPTER 5

THE CERENKOV LIGHT PULSE SHAPE IN EAS

5.1 INTRODUCTION

In this chapter a detailed analysis is presented of a selection of the Cerenkov light pulse shape data recorded by the Dugway array (in its 400 m configuration) during the running periods of 1978/79 and 1979/80. The aspect of the pulse shape investigated here is the full width at half the maximum height (FWHM). While this is not the only pulse shape parameter containing information on the cascade development, it exhibits, according to model calculations, a greater sensitivity to the depth of cascade maximum than for example the pulse rise-time. In addition, it is evident (see figure 4.13) that the FWHM can be derived from the digital records to a comparable or greater accuracy than the rise-time for the majority of pulses. The B-spline reconstructed rise-time measurements also have the disadvantage that they cannot always be considered unbiased estimators of the true rise-time, and if used require detailed correction factors.

The average depth of cascade maximum is derived from the measured average FWHM values, after due allowance has been made for the systematic variations in the FWHM with core distance and shower zenith angle. The variations in the FWHM at 250 m from the core (FWHM (250 m)) that occur between showers are investigated. When all known systematic variations are removed and allowance made for the measurement errors the residual fluctuations are quantified. This provides an estimate of the width of the underlying distribution in depths of cascade maximum resulting from intrinsic fluctuations in EAS production mechanisms.

5.2 THE DATASET

The data selected for the analysis of the average behaviour of the Cerenkov light pulse FWHM are described below. A more rigorous selection from within this dataset was required for the analysis of the

variations in the FWHM (250 m) between showers. These additional selection criteria are described in section 5.6.1.

5.2.1 Selection of Data Used for Analysis

For the purposes of this thesis, a comparatively small sample of high quality data was required in order to gain a detailed understanding of the data, and to establish the analysis techniques prior to the consideration of a larger sample. To this end high energy events were selected with primary energy estimator $\log_{10}\Phi$ (150 m) ≥ 3.75. From these events only those with five or more detector responses were selected, to allow for a degree of redundancy in the core fitting procedure. Events for which the core was not confined within the array boundaries were discarded. As a further precaution against the selection of events with large uncertainties in the core locations, a cut was imposed on the goodness of fit criterion (χ^2) for the core fitting procedure. For each fold number, those events with a χ^2 value corresponding to less than 5% probability were rejected. Only well measured pulse profiles were required for analysis, and so a cut was also imposed on the goodness of fit criterion (r.m.s.) of the B-spline pulse shape reconstructions. Specifically, pulses were rejected when the r.m.s. deviation between the B-spline and the digitised samples exceeded 15% of the maximum slice height. In general, this cut became important only for small pulses of height $\leq$ 30 mV. Finally, very large pulses in which more than two scaler overflows had occurred (see section 3.6) were discarded to avoid the possibility of including ambiguous pulse profile reconstructions in the dataset.

The events in this data sample, being at the highest primary energies recorded by the array, offer three important advantages. Firstly, the pulses are generally wider than those recorded at the same core distance in showers of lower primary energy, providing more signal

relative to the impulse response of the detecting system. Secondly, the pulse heights are generally greater than those recorded at lower energies, providing a better signal to sky-noise ratio and hence more accurate pulse width reconstructions. Finally, the higher the energy of the data sample, the less it will be prone to shower selection bias.

The requirement of a certain minimum number of detector responses in each event places a constraint on the lateral distribution of Cerenkov light pulse heights required. For example, a broad lateral distribution (produced by a high developing shower) will fulfil the selection criteria more readily than a steep lateral distribution (produced by a deep developing shower). This difference in selection probability, between showers having different depths of cascade maximum, becomes less significant with increasing primary energy. As the pulse heights increase with increasing primary energy, they are more likely to exceed the fixed discrimination threshold of the Cerenkov light detectors. Figure 5.1 illustrates the dependence of the selection probability on the primary energy estimator and the depth of cascade maximum. The selection probabilities represent the percentage of simulated vertical events (based on model calculations) fulfilling the selection criteria out of 1000 events with core locations assigned randomly within the array. It can be seen that restricting the analysis to the comparatively high energy events ($\log_{10}\Phi$ (150 m) $\gtrsim$ 3.75) reduces the selection bias to a very low level. For inclined showers, the selection bias is further reduced due to the inherent broadening of the lateral distribution.

5.2.2 General Characteristics of the Dataset

Following the preliminary sorting and analysis of the data (section 3.6), refinements in the relative detector gain assignments (to accuracies of $\sim$ 10%) and in the core fitting technique (see section 4.3.1) became available. The core fitting analysis was repeated,

FIGURE 5.1 The dependence of shower selection probability on depth of cascade maximum and primary energy estimator. The shaded region is an indication of the extent of the intrinsic fluctuations in t_{max}(1 σ) expected for a protonic composition and an interaction cross-section increasing as log s.

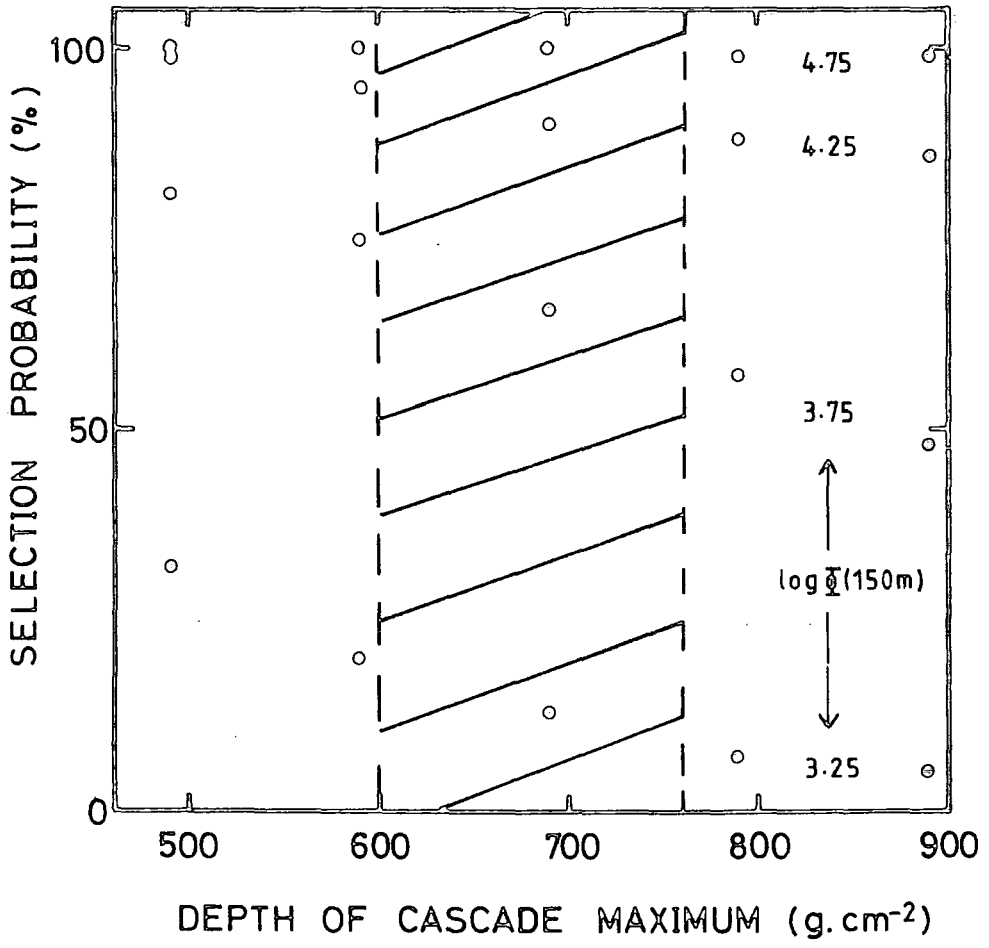

producing core distances accurate to $\sim$ 10 m (Craig, private communication) and improved primary energy estimations. A total of 147 events with zenith angles from 0^{o} to 45^{o} satisfied the selection criteria. Figures 5.2 and 5.3 show the distributions in zenith angle and primary energy estimator for this data sample. The differential primary energy spectrum is normally described by the form:

$$N(E_p)dE_p \propto E_p^{-\lambda}dE_p \qquad 5.1$$

A weighted least squares fit to this data sample gives a value for the exponent (λ) of 1.8 $\pm$ 0.2. This should be compared to measurements of the energy spectrum (Bower et al. (1981)) which yield an exponent of $\sim$ 3. This flattening of the energy distribution is principally the consequence of the bias towards selection of higher energy showers regardless of t_{max}, although a slight bias towards showers with small t_{max} is expected for near vertical showers of the lowest energy, as indicated in figure 5.1.

Figure 5.4 shows the distribution in core distance for the 471 available pulse shape measurements. The maximum core distance at which a measurement is available in an event depends to a certain extent on the primary energy, but also on the lateral distribution of the Cerenkov light and hence on the depth of shower maximum. The consequences of this for the interpretation of the average behaviour of the FWHM with core distance are considered further in section 5.5.

5.3 DECONVOLUTION OF THE MEASURED PULSE FWHM

To allow for the degradation of the Cerenkov light pulse by the detecting systems, it was necessary to know the impulse response of each detector. This was achieved by recording the response to a radioactive light pulser as described in section 3.3.2. Two methods were considered for removing the effects of the system bandwidth from the B-spline pulse reconstructions. The first of these, matrix deconvolution,

FIGURE 5.2 The zenith angle distribution of the showers selected for the analysis of the FWHM.

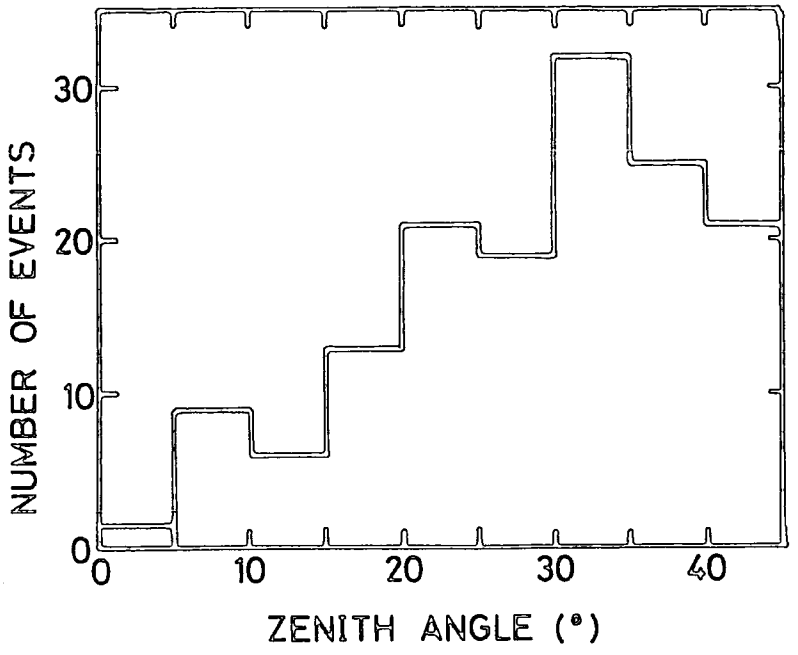

FIGURE 5.3 The distribution in primary energy estimator of the showers selected for the analysis of the FWHM.

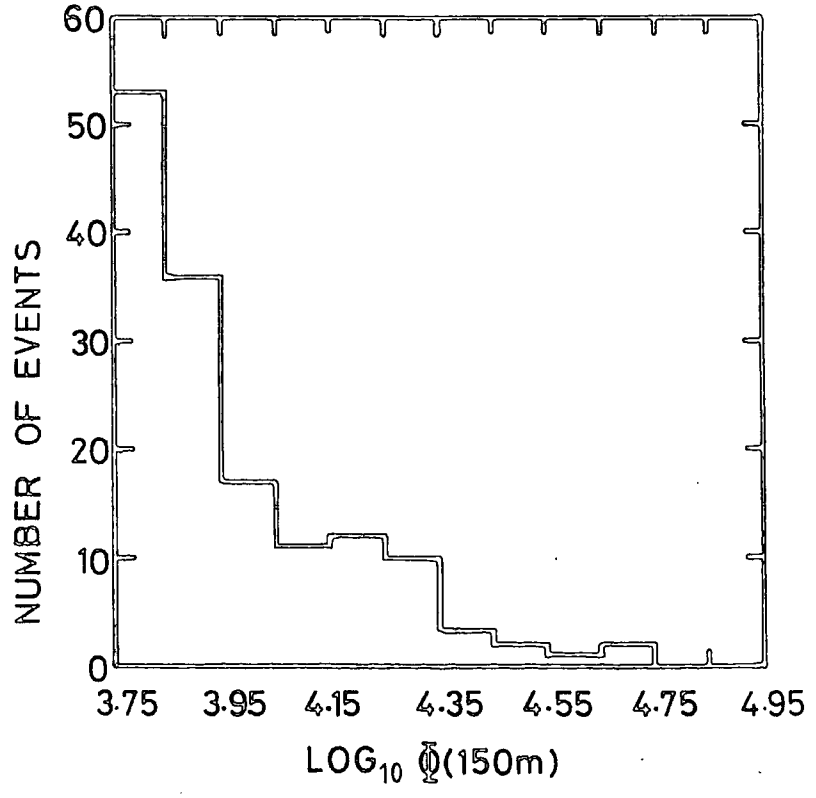

FIGURE 5.4 The distribution in core distance of the pulse profiles selected for the analysis of the FWHM.

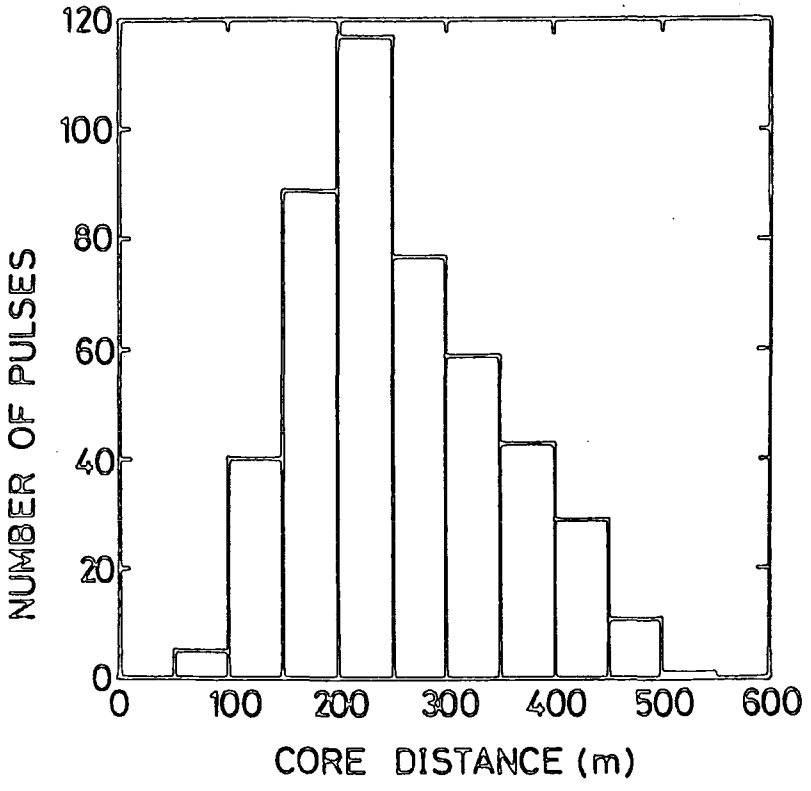

was found to be tenable only for the very high signal/noise ratio pulses considerably wider than the system impulse response. Otherwise, matrix conditioning problems precluded the use of this technique. The second method, which is the technique adopted here, involves the convolution of the system response with a wide range of pulse profiles generated from the model calculations for an infinite bandwidth system. It was found that for pulses of FWHM $\gtrsim$ 5 ns (before convolution) there is an almost unique transformation to the convoluted FWHM irrespective of the conditions of the origin of the pulse (the primary energy, depth of cascade maximum etc). Little information can be expected for pulses narrower than this, since the transformation becomes strongly influenced by the shape of the pulse as a whole. Figure 5.5 is an example of the impulse response for one of the detectors; and figure 5.6 shows the result of convoluting this with pulse profiles from model calculations. Similar convolution curves were generated using the measured system response of each detector, enabling the 'deconvolution' of the measured Cerenkov light pulse FWHM.

The deconvoluted FWHM measurements for each detector were plotted against core distance, and a comparison between each detector's average response was made. This was necessary to ensure that the measurements from different detectors, each with slightly different distorting effects, could be reliably combined. On this basis, the pulse shape measurements of one of the detectors had to be excluded from the analysis, since the average response differed significantly from that recorded by the other detectors.

5.4 POSSIBLE CAUSES FOR THE VARIATIONS IN THE FWHM OF THE LIGHT PULSE

5.4.1 Differences in the FWHM within Showers

Table 5.1 lists each of the factors expected to contribute to the observed differences in the FWHM occurring both within an individual

FIGURE 5.5 The response of a Cerenkov light detector to the near delta-function light pulse from a radio-active light pulser.

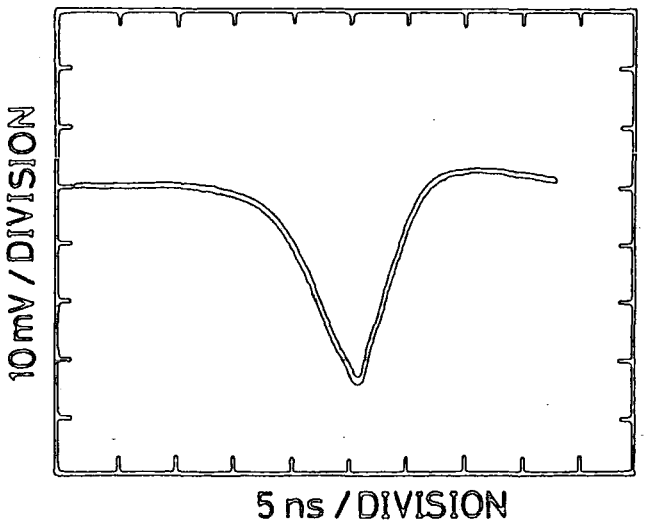

FIGURE 5.6 The impulse response of a Cerenkov light detector has been convoluted with pulse profiles from model calculations computed for an infinite bandwidth system. The result is a 'deconvolution curve' to be used for the interpretation of the recorded FWHM.

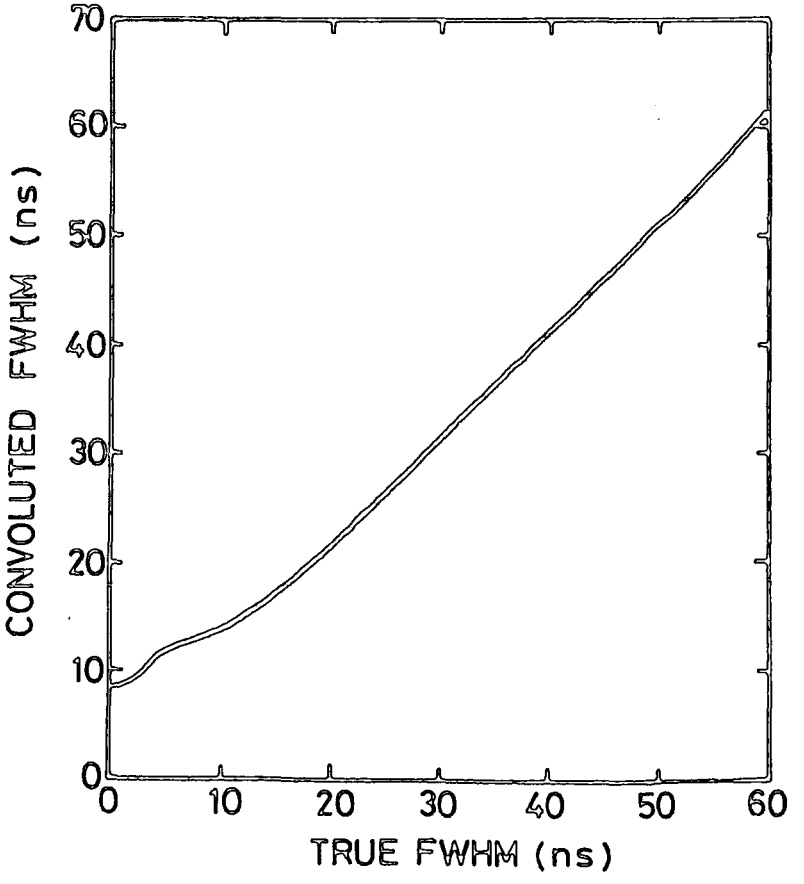

TABLE 5.1

Possible factors contributing to the variations in the measured FWHM.

WITHIN SHOWERS

1. The monotonic increase of FWHM with core distance.
2. Measurement errors in the FWHM.
3. Errors in the core distance estimations.
4. Deviations from radial symmetry due to the influence of the geomagnetic field.

BETWEEN SHOWERS

5. The zenith angle.
6. The primary energy.
7. The atmospheric pressure.
8. Fluctuations in the depth of cascade maximum due to intrinsic fluctuations in the cascade development processes.

shower and between showers. As indicated in section 2.3.4, the observed Cerenkov light pulse shape is influenced principally by path length differences from the centres of Cerenkov light emission in the atmosphere to the detectors. One manifestation of this, and indeed the largest single cause of variation in the FWHM, is the monotonic increase in pulse width with distance from the shower core. An example of the variation within a single shower was provided in figure 4.9. Computer simulation predictions and earlier experimental observations at Haverah Park show the dependence of the FWHM on core distance to be adequately described by the form:

$$\text{FWHM} = a + b\, r^2 \qquad 5.2$$

for pulses greater than about 150 m from the core.

The other factors in table 5.1 contributing to variations in FWHM within showers can be treated largely as random deviations about the functional dependence of equation 5.2. Errors in the FWHM measurements are by far the largest source of deviations. Errors in the core distance assignments due to measurement errors in the Cerenkov light intensities are comparatively small ($\lesssim$ 10 m). However, when the angle of inclination of a shower to the Earth's magnetic field is large, a distortion of the radial symmetry can result due to the polarisation of the electron and positron components of the electromagnetic cascade (e.g. Orford et al. (1975)). While this will be treated as a pseudo-random contribution to the deviations about the functional dependence within a shower, it will be necessary to check that extreme variations in the FWHM between showers are not correlated with this effect. Variations of the FWHM within a shower due to differences in the local zenith angle between different detectors would not be significant. The finite opening angle of the Cerenkov light detectors (half angle $\sim 65^{\circ}$) should not be of importance for the restricted zenith angle range (0° - 45°) of the data sample.

5.4.2 Differences in the FWHM between Showers

The cause of the largest component of the variations in the FWHM between showers is the zenith angle dependence. As the zenith angle increases, the cascade develops progressively further away from the array, lessening the differences in the arrival time between Cerenkov light originating from different stages of the shower development. A significant narrowing of the light pulse therefore occurs with increasing zenith angle.

An increase in the primary energy is accompanied by an increase in t_{max} and therefore produces an increase in the FWHM. Model calculations suggest a dependence of 2 - 4 ns per decade of primary energy at a core distance of 250 m in vertical showers. Since the extreme range of primary energy in the sample is only a decade, both the core distance and zenith angle dependences must be carefully removed before the energy dependence might be resolvable.

The FWHM is also expected to be dependent on the atmospheric pressure. The atmospheric pressure is an indicator of the atmospheric density, and the probability per unit path length of a primary cosmic ray particle interacting with an air nucleus is proportional to the atmospheric density. When the atmospheric pressure increases, the particle interactions tend to occur higher in the atmosphere, decreasing the depth of cascade maximum, and hence decreasing the FWHM.

In order to deduce the mean of depth of cascade maximum corresponding to the mean primary energy of the data sample, the systematic dependences of the FWHM on core distance and zenith angle must be taken into account. To estimate the extent of the fluctuations that occur between showers, due to fluctuations in the depth of cascade development, it will be necessary to take account of any variations caused by factors 1 - 7 in table 5.1.

5.5 THE AVERAGE CASCADE DEVELOPMENT FROM THE AVERAGE BEHAVIOUR OF THE FWHM WITH CORE DISTANCE AND ZENITH ANGLE

In this section, each Cerenkov light pulse is treated as an independent measurement without regard to its belonging to an 'event' comprising of several such measurements. The objective is to estimate, by comparison with model calculations, the mean depth of cascade maximum which would give rise to the observed average behaviour of the Cerenkov light pulse FWHM.

Model calculations of the dependence of the FWHM on the depth of cascade maximum are available for a wide range of core distances and zenith angles (McComb and Turver (1981a)). In principle, each FWHM measurement could be interpreted individually (in terms of t_{max}) by interpolating the model predictions to the exact zenith angle and core distance of the recorded pulse. In practice, however, the presence of measurement errors in the FWHM estimates would necessitate extrapolation outside the range of depths of maximum considered by the model calculations. The FWHM measurements were therefore divided into the core distance (r) and secant zenith angle (sec θ) bins shown in table 5.2, and the mean values calculated for each bin. Figure 5.7 shows the dependence of the mean FWHM with core distance and zenith angle. Using the model calculations shown in figure 5.9, each mean FWHM value was transformed to depth of maximum by interpolating the simulation results to the mean zenith angle and mean core distance of the bin. These $\overline{t_{max}}$ estimates are shown in figure 5.8 and listed in table 5.2. As explained in section 2.3.4, the transformation from FWHM to depth of cascade maximum is not dependent on the primary mass, primary energy or the model of hadronic interactions used in the computer simulations.

The weighted mean of the 20 depth of maximum estimates shown in figure 5.8 is 672 ± 23 $g.cm^{-2}$. However, this value must be treated

TABLE 5.2

Data on the FWHM of the light pulse binned by core distance and secant zenith angle.

SECθ	r	$\overline{SEC\theta}$	$\bar{r}$	$\overline{FWHM}$	$\overline{t_{max}}$	NUMBER OF PULSES
$1.0 \leqslant sec\theta < 1.1$	$150 \leqslant r < 200$	1.06	175	12.8±0.8	840± 30	28
	$200 \leqslant r < 250$	1.05	228	22.0±1.3	765± 40	28
	$250 \leqslant r < 300$	1.05	273	27.5±1.8	670± 45	29
	$300 \leqslant r < 350$	1.06	321	31.9±1.8	590± 35	17
	$350 \leqslant r < 400$	1.04	373	46.5±7.7	640±110	12
$1.1 \leqslant sec\theta < 1.2$	$150 \leqslant r < 200$	1.16	177	9.4±1.0	805± 50	26
	$200 \leqslant r < 250$	1.15	227	15.6±1.0	700± 35	37
	$250 \leqslant r < 300$	1.15	274	21.6±1.7	640± 45	22
	$300 \leqslant r < 350$	1.15	323	27.4±2.2	590± 40	15
	$350 \leqslant r < 400$	1.16	373	38.8±5.2	640± 80	9
$1.2 \leqslant sec\theta < 1.3$	$150 \leqslant r < 200$	1.25	180	7.0±1.1	765± 50	20
	$200 \leqslant r < 250$	1.25	226	11.2±1.2	630± 40	29
	$250 \leqslant r < 300$	1.23	270	23.8±2.2	755± 40	15
	$300 \leqslant r < 350$	1.23	330	27.5±2.7	605± 40	15
	$350 \leqslant r < 400$	1.25	375	32.3±4.3	580± 70	11
$1.3 \leqslant sec\theta < 1.4$	$150 \leqslant r < 200$	1.34	179	6.4±0.9	865± 90	15
	$200 \leqslant r < 250$	1.35	231	9.4±1.2	600± 55	21
	$250 \leqslant r < 300$	1.34	270	13.7±2.1	545± 55	10
	$300 \leqslant r < 350$	1.34	335	22.8±2.4	550± 40	11
	$350 \leqslant r < 400$	1.35	377	28.1±2.9	540± 45	11

Total number of pulses = 381

FIGURE 5.7 Data on the average variation of the FWHM with core distance and zenith angle.

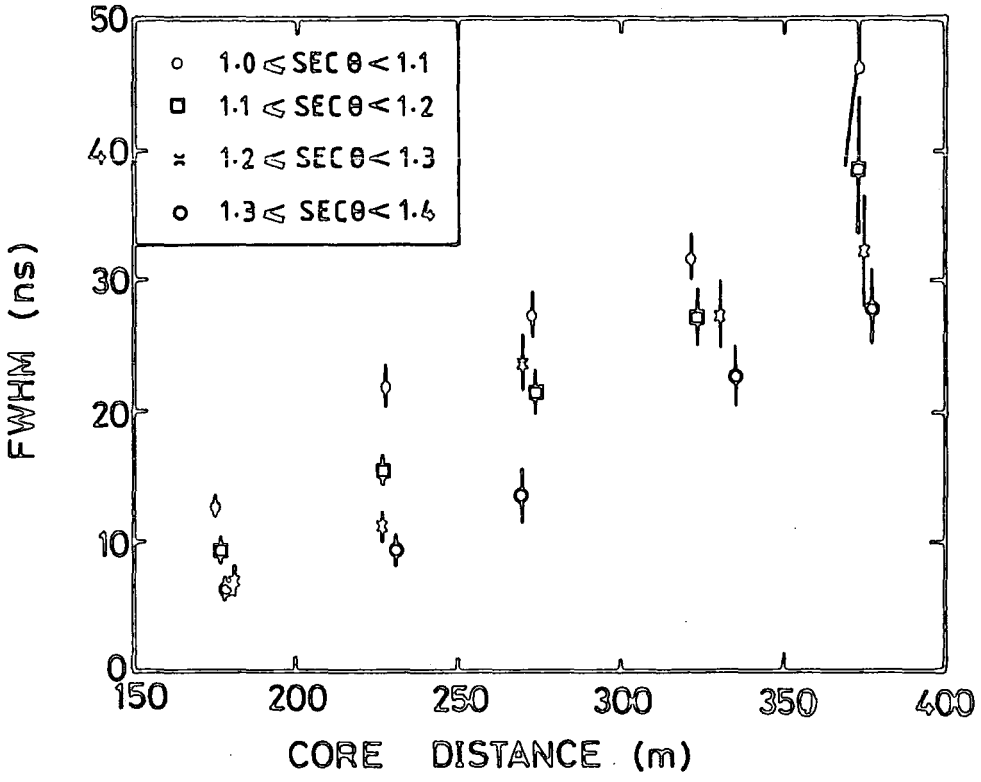

FIGURE 5.8 The interpretation of the FWHM data of figure 5.7 in terms of mean depth of cascade maximum.

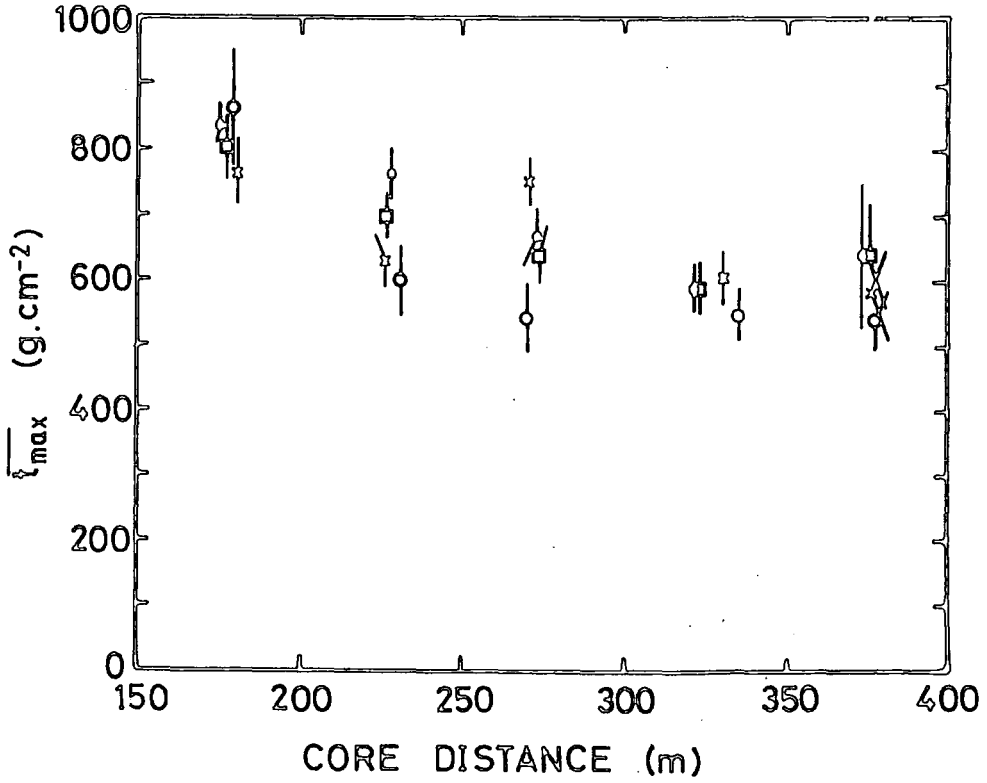

FIGURE 5.9 The simulated dependence of the FWHM on core distance, zenith angle and depth of shower maximum. The calculations are for an infinite bandwidth system located at an atmospheric depth of 862 g.cm^{-2}. The curves shown are for average iron-nucleus induced cascades, computed using the scaling model with constant interaction cross-section.

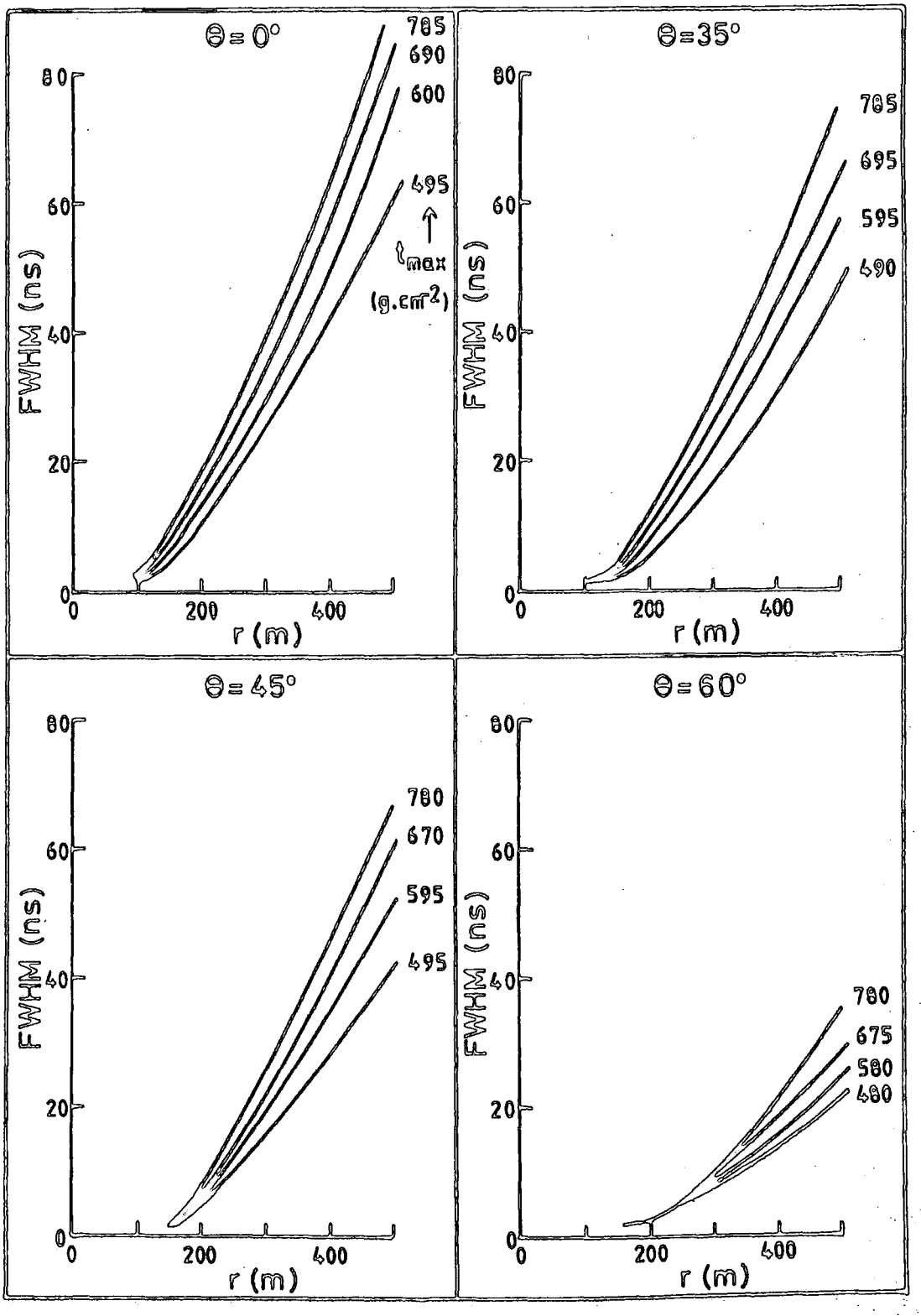

with caution since the figure suggests a systematic decrease in the depth of maximum with increasing core distance. At core distances > 300 m some decrease in depth of maximum with increasing core distance could be expected. Figure 5.10 shows the dependence of the simulated maximum distance at which a detector will respond on the depth of cascade maximum. These calculations are appropriate to showers of primary energy estimator $\log \Phi$ (150 m) = 3.75. At large core distances there is a preference for the detection of pulses from showers with smaller depths of cascade maximum.

At core distances < 200 m, the mean pulse width appears broader than expected from the model calculations, resulting in larger than average depth of maximum estimates (figure 5.8). However, the results at core distances < 200 m are considered less reliable than those at larger core distances for the following reasons. Firstly, for pulses with FWHM $\lesssim$ 10 ns the 'deconvolution' process is generally less reliable and depends critically on the accuracy to which the impulse response is known. The shape of the deconvolution curve can result in a small error in the observed FWHM being transformed into a larger error in the deconvoluted FWHM. Secondly, it can be seen from the model calculations (figure 5.9) that an increase in the FWHM of only 2 ns at 175 m from the core in a vertical shower corresponds to an increase in the depth of maximum of $\sim$ 100 $g.cm^{-2}$. A small systematic error in the mean FWHM would therefore give rise to a comparatively large error in the estimated depth of cascade maximum.

A more detailed illustration of the core distance dependence for the almost bias-free range 150 - 300 m is given for each of the zenith angle bins in figures 5.11 to 5.14. Each individual FWHM measurement has been plotted together with an approximate estimate of its one standard deviation error flag. The errors have been calculated from the simulated accuracy of the B-spline pulse reconstructions (see figure 4.13), and

FIGURE 5.10 The dependence of the maximum triggering core distance on depth of cascade maximum and zenith angle.

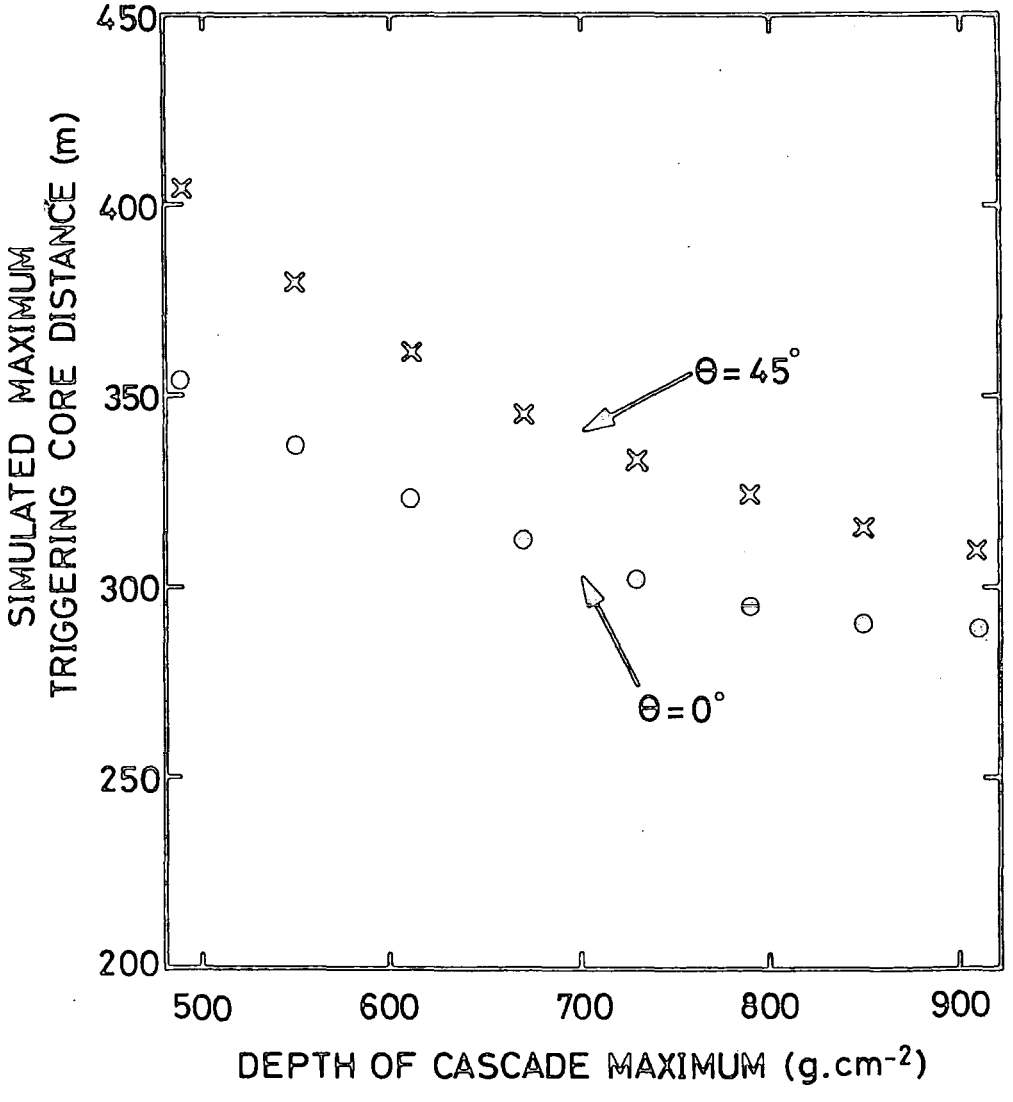

FIGURE 5.11 Measurements of the FWHM in the zenith angle range $1.0 \leqslant \sec\theta < 1.1$.

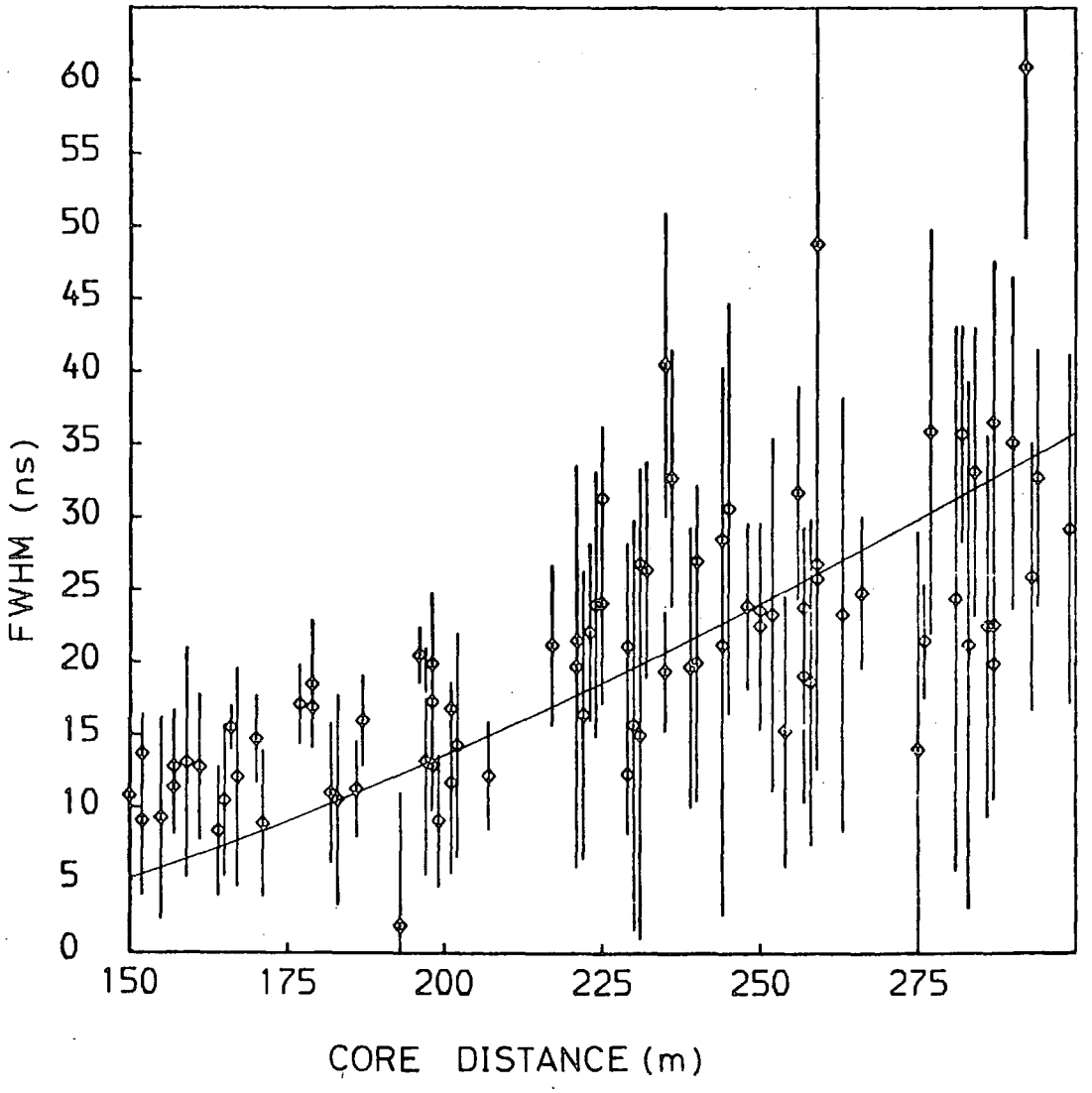

FIGURE 5.12 Measurements of the FWHM in the zenith angle range $1.1 \leqslant \sec\theta < 1.2$.

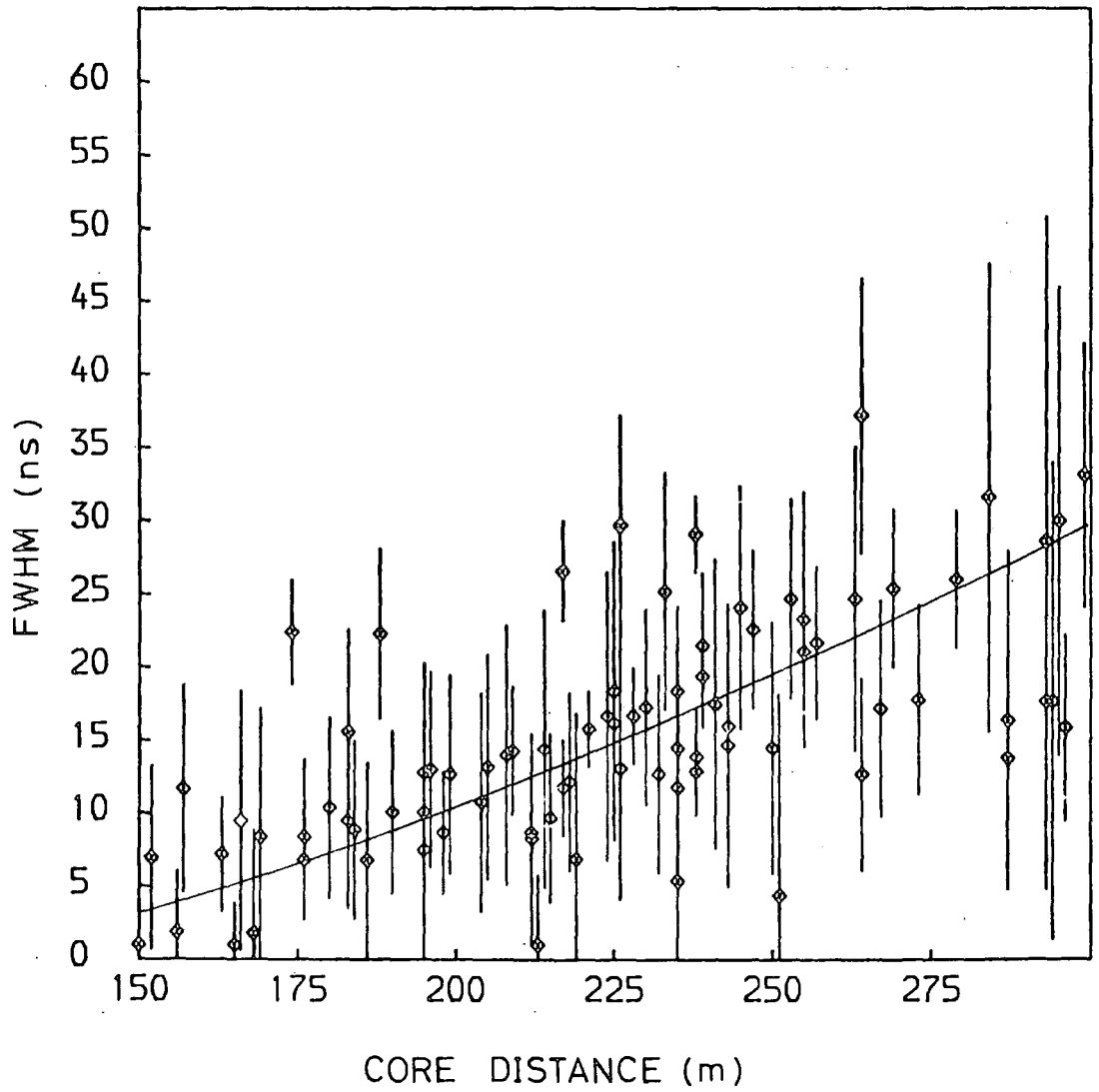

FIGURE 5.13 Measurements of the FWHM in the zenith angle range $1.2 \leqslant \sec\theta < 1.3$.

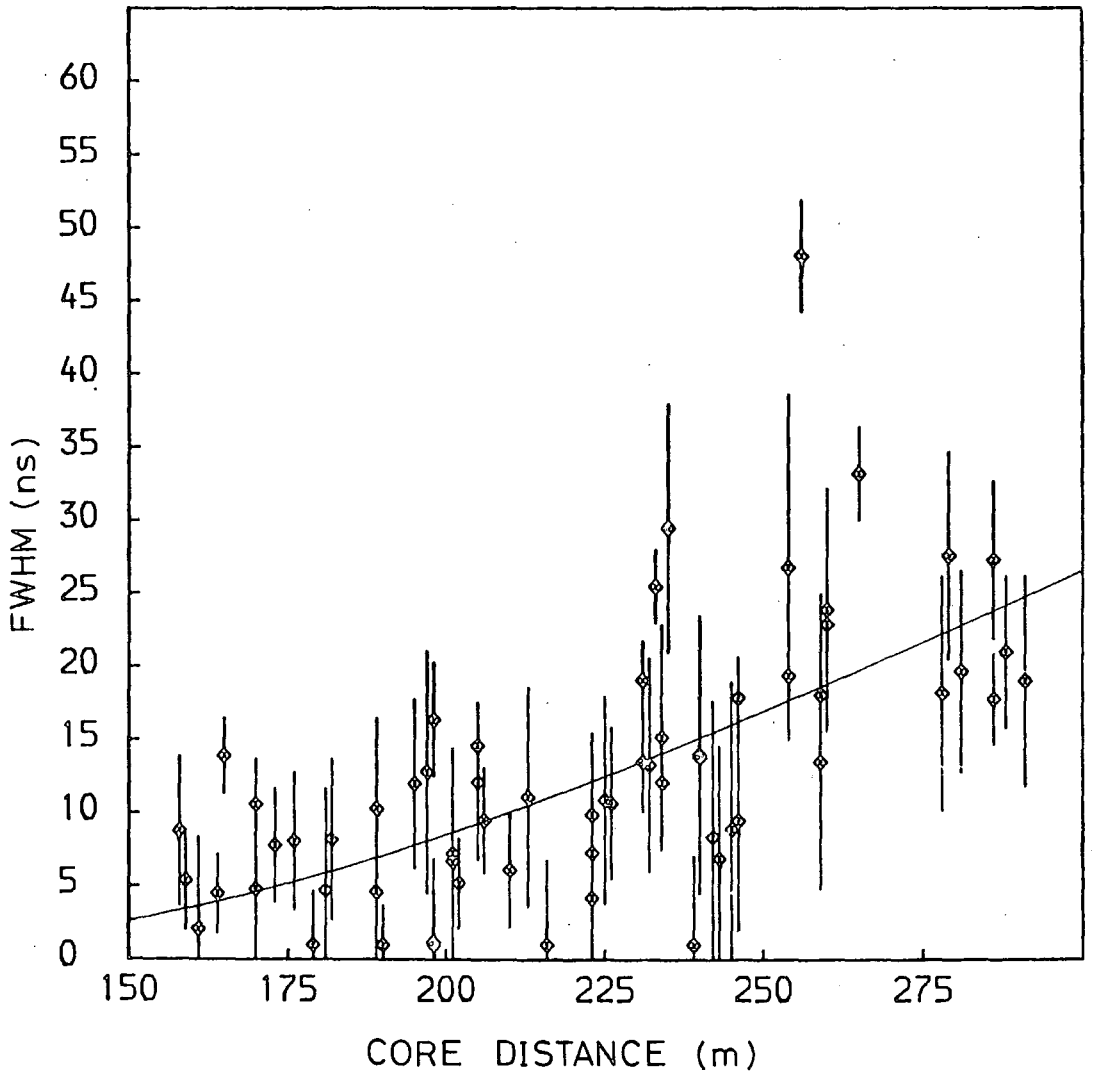

FIGURE 5.14 Measurements of the FWHM in the zenith angle range $1.3 \leqslant \sec\theta < 1.4$.

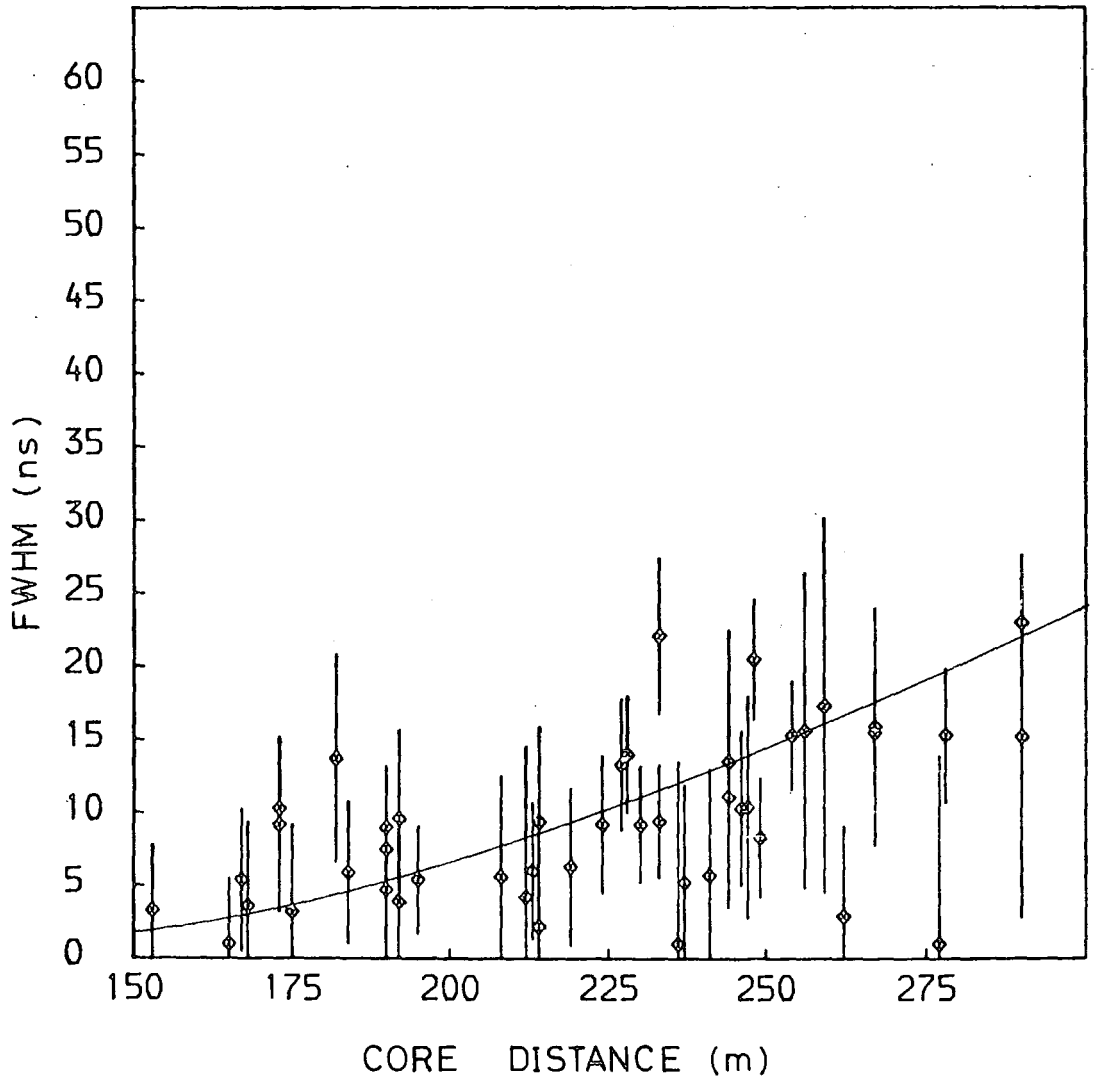

transformed by the slope of the appropriate deconvolution curve. In each figure the data are compared with the prediction from model calculations for a depth of cascade maximum of $\sim$ 720 g.cm^{-2} (the weighted mean of the estimates in this core distance range from figure 5.8). A possible explanation for the systematically large mean FWHM estimates in the range 150 - 200 m and sec > 1.1 is apparent in figures 5.12 to 5.14. The effects of noise on the FWHM are, after deconvolution, more likely to produce larger overestimates than underestimates, simply because negative values of the deconvoluted FWHM are not permissible. However, the discrepancy between the model calculation and the data appears significant in the range 150 - 200 m and sec < 1.1. This is perhaps the most difficult region for the computer simulations to predict with complete accuracy. Near vertical showers lose part of the falling edge of the cascade at the Dugway altitude, and a certain amount of the Cerenkov light pulse produced at low altitudes is not seen due to geometric cut-off effects. The difficulties are enhanced at small core distances, where a larger contribution to the pulse width comes from Cerenkov light originating at low altitudes (see figure 2.10).

On the basis of the foregoing considerations, the most reliable core distance range to use for estimating the mean depth of cascade maximum from the binned results of figure 5.8 is probably 200 - 300 m. The weighted mean of the 8 depth of maximum estimates in this range (using the relative magnitudes of the error assignments) is 678 $\pm$ 25 g.cm^{-2}. The size of the confidence interval reflects a possible slight systematic difference between the zenith angle dependence of the data and that predicted by model calculations. The mean primary energy estimator (log Φ (150 m)) is 3.96, which corresponds to a primary energy of 2.1 x 10^{17} eV.

5.6 FLUCTUATIONS IN THE CASCADE DEVELOPMENT BETWEEN SHOWERS

5.6.1 The Choice of Development-Sensitive Shower Parameter and its Selection Criteria

To compare the Cerenkov light pulse FWHM between showers it is necessary to first remove the systematic core distance dependence within each shower. For an event in which several pulse shape measurements are available, a weighted least-squares fit to the functional form of equation 5.2 can provide an estimate of the FWHM at a fixed core distance(d). The relative weights of the FWHM measurements within a shower can be derived from the estimated accuracy of the B-spline fits transformed by the slope of the deconvolution curve. An estimate of the one standard deviation confidence interval (σ_d) on the fitted value at the core distance d can be obtained from the least-squares analysis, and serves to quantify the random variations within a shower.

Two additional selection criteria were required. First, each event was required to have at least one measurement at a core distance > d to avoid extrapolation. It was shown in figure 5.10 that the maximum distance at which a detector can trigger in an EAS is dependent on the depth of cascade maximum. Since a bias towards the selection of pulses from high developing showers is incurred at core distances $\gtrsim$ 300 m, the core distance (d) chosen for comparison between showers was 250 m. Secondly, a minimum of three FWHM measurements at core distances > 150 m was required (pulses inside 150 m were not used). This is the minimum number needed in order to evaluate the constants 'a' and 'b' (equation 5.2) and σ_d. The subset of events satisfying these criteria were selected from the dataset, providing 75 showers for the analysis of the FWHM (250 m).

The selection probabilities for this more stringently selected dataset were calculated (using the computer simulation results), and a subset for a zenith angle of 35^{o} are shown as a function of depth of cascade maximum and primary energy estimator in figure 5.15. Allowance was made in the calculations for the FWHM responses of only seven out of the eight detectors being used. A certain amount of bias in favour of high developing showers is evident, and consideration will be given to this in the analysis of the development fluctuations.

5.6.2 The Variation between Showers of the FWHM at 250 m

The values of the FWHM (250 m) obtained from the regression fits in individual showers are shown in figure 5.16. The dependence on secant (zenith angle) is compared with that from model calculations. There is an indication that the decrease in FWHM (250 m) with increasing zenith angle is slightly greater than expected from the model calculations, although this trend may not be very significant. Also indicated in the figure is whether each event has a primary energy estimator greater or less than 4.25 (the centre of the energy range). The extreme variation in the FWHM (250 m) expected due to the decade primary energy range is less than 4 ns for vertically incident showers. In addition, the majority of events have primary energies closer to the lower limit of the range, with the result that the expected r.m.s. deviation due to the r.m.s. spread in primary energy is less than 0.7 ns. The presence of this small underlying primary energy dependence is difficult to establish in view of the magnitude of the other sources of variation between showers. The magnitude of one of these sources of variation, the random uncertainty in the FWHM (250 m) due to the measurement errors, is indicated for each data point. However, the extent of the variations between data points appears larger than could be reasonably accounted for by the measurement errors, suggesting the

FIGURE 5.15 The selection probability of showers selected for the analysis of the FWHM (250 m) as a function of depth of cascade maximum and primary energy estimator.

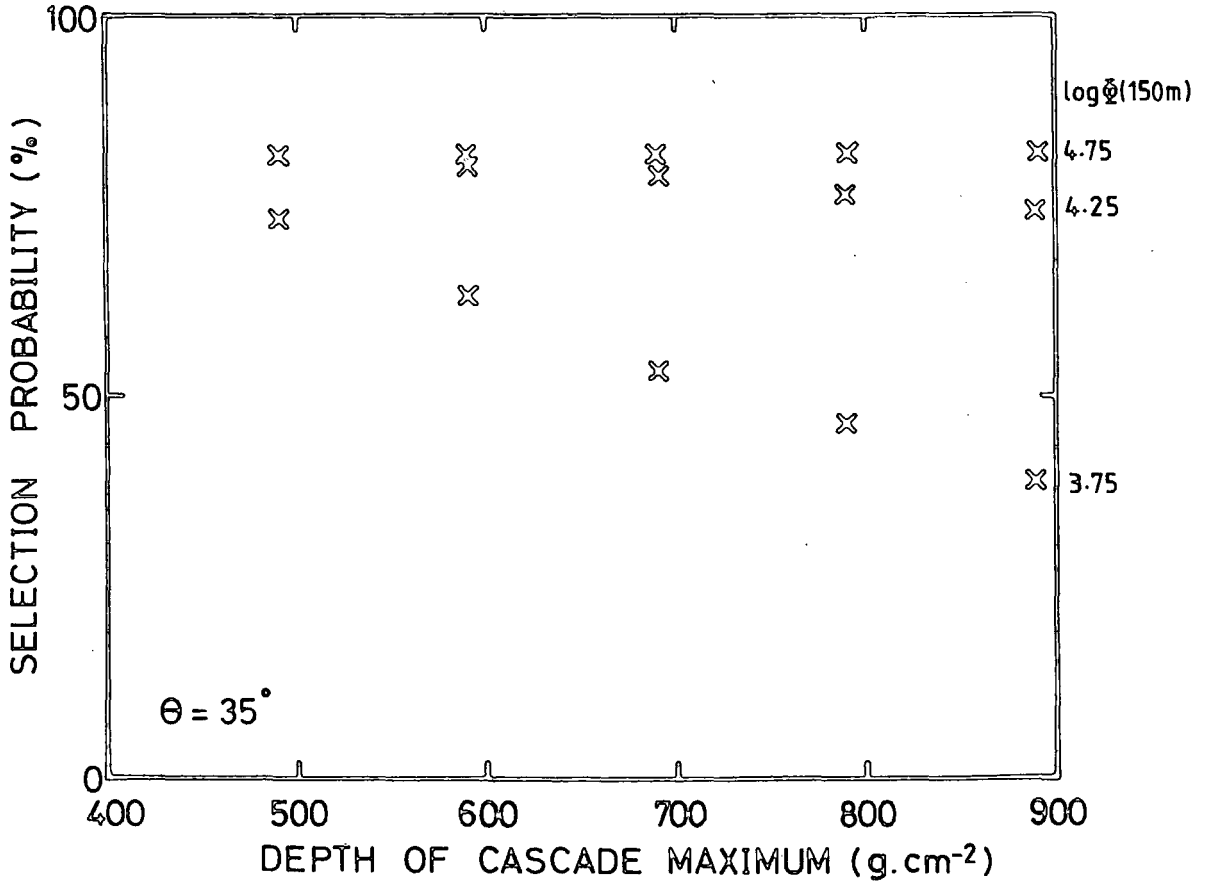

FIGURE 5.16 Measurements of the FWHM (250 m) in individual showers. The curves shown are from the results of model calculations for average showers (parameterised by the form of equation 5.4).

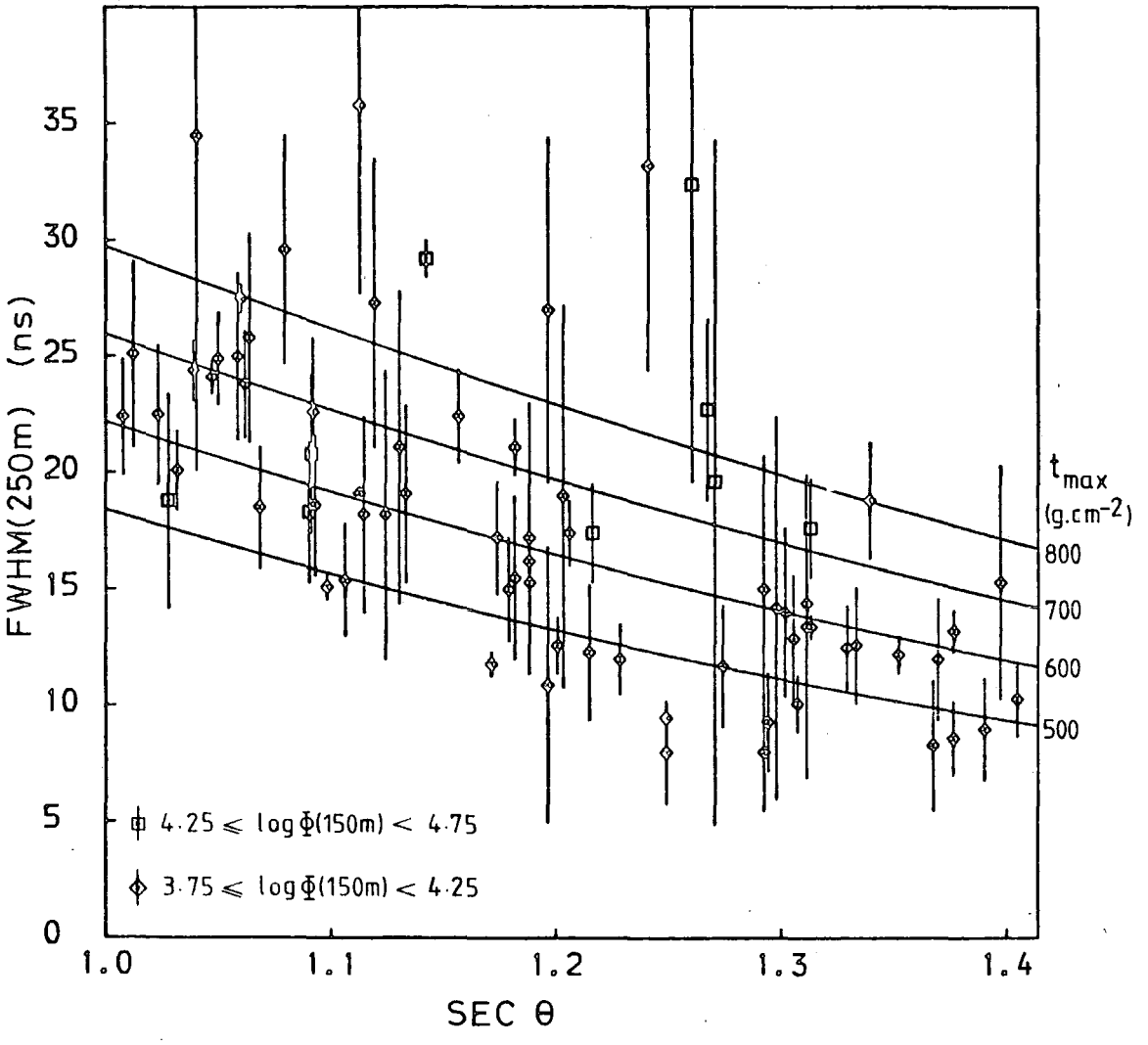

possibility of significant shower development fluctuations.

5.6.3 A Technique for the Estimation of the Fluctuation in the FWHM by Multiple Regression Analysis

The purpose of the technique described in this section is to deduce, from an 'a posteriori' analysis of the data, the fluctuations in the FWHM (250 m) caused by fluctuations in the depth of cascade maximum. Rather than interpreting each data point of figure 5.16 in terms of depth of cascade maximum, any systematic dependence present in the data (principally zenith angle and primary energy) is removed by fitting a suitable functional form. Model calculations for average showers in the range of zenith angles 0^{o} to 60^{o} show the behaviour of the FWHM (250 m) to be well represented by the form:

$$\text{FWHM (250 m)} = A + B.\sec\theta + C.\sec^2\theta + D.\log E_p . (\sec^2\theta - 4) \quad 5.3$$

or $$\text{FWHM (250 m)} = F + G.\sec\theta + H.\sec^2\theta + J.t_{max}.(\sec^2\theta - 4). \quad 5.4$$

It should be noted that the sensitivity of the FWHM (250 m) to the depth of cascade maximum (or primary energy) decreases with zenith angle, and is completely insensitive at a zenith angle of 60^{o}. Fitting the data to the functional form of equation 5.3 allows for a fair degree of flexibility in the zenith angle dependence should it differ from that predicted by the model calculations.

An optimal fit to the data requires a weighted multiple regression. The solution corresponds to the minimum value of the sum of the standardised squared residuals:

$$\sum_{i=1}^{n} \frac{(f_i - F_i)^2}{\sigma_{t_i}^2} \quad 5.5$$

where f_i are the data points (FWHM (250 m)), F_i are the values predicted by the fit, and $\sigma_{t_i}^2$ are the total variances. Each value of $\sigma_{t_i}^2$ is

comprised of the measurement variance ($\sigma^2_{d_i}$) and the fluctuation variance ($\sigma^2_{F_i}$). Assuming normal distributions these can be quadratically combined:

$$\sigma^2_{t_i} = \sigma^2_{d_i} + \sigma^2_{F_i} \qquad 5.6$$

Since the fluctuation variances ($\sigma^2_{F_i}$) are unknown, an ordinary least squares regression (unweighted) must first be carried out to obtain an initial set of regression coefficients. Following this, a first estimate of the fluctuations can be obtained by relaxation of $\sigma^2_{F_i}$ until the following equality is obtained:

$$\sum_{i=1}^{n} \frac{(f_i - F_i)^2}{\sigma^2_{d_i} + \sigma^2_{F_i}} = \langle\chi^2\rangle = n - 4 \quad . \qquad 5.7$$

This step in the procedure is based on the assumption that the standardised residuals are normally distributed; therefore the sum of the squared standardised residuals should be sampled from a chi-square distribution with an expectation value ($\langle\chi^2\rangle$) equal to the number of degrees of freedom. The confidence interval on the fluctuation estimate can be obtained by further relaxation to the points on the χ^2 distribution delimiting 68% probability content.

The fluctuation in the FWHM (250 m) will itself be a weak function of the zenith angle. It is assumed here that the dependence is the same as for the sensitivity of the FWHM (250 m) to changes in the average depth of cascade maximum (see equation 5.4),

i.e. $$\sigma_{F_i}(\sec\theta_i) = \text{constant} \cdot \sigma(t_{max}) \cdot (\sec^2\theta_i - 4) \qquad 5.8$$

where $\sigma(t_{max})$ is the standard deviation of the underlying distribution of depths of cascade maximum. Alternatively, this can be expressed as:

$$\sigma_{F_i}(\sec\theta_i) = -\frac{1}{3}\sigma_F(1) \cdot (\sec^2\theta_i - 4) \qquad 5.9$$

where $\sigma_F(1)$ is the standard deviation of the fluctuations in the FWHM (250 m) for vertical showers.

Having obtained an initial estimate of the fluctuations in the FWHM (250 m), a weighted multiple regression (using the total variance estimates in the weighting factors) can be carried out to re-estimate the systematic variations and the fluctuations. The process can be further iterated to obtain convergence to an optimal set of estimates.

5.6.4 Allowance for Selection Effects

The selection probabilities for individual events can be calculated from the data, thus avoiding reliance on model calculations. Since the lateral distribution of pulse heights for each event is known, this can be extrapolated to obtain the maximum core distance at which a detector could trigger. By generating 1000 such lateral distributions, at constant zenith angle, with core locations assigned randomly within the array and with a uniform distribution in azimuth angle, the percentage of times (P_i) that the event would have satisfied the selection criteria can be calculated. Each event can then be weighted in the multiple regression analysis according to its selection probability. Specifically, the sum of the square standardised residuals becomes:

$$\sum_{i=1}^{n} \frac{(f_i - F_i)^2}{(\sigma_{d_i}^2 + \sigma_{F_i}^2) P_i'} \qquad 5.10$$

where P_i' are the selection probabilities normalised according to:

$$\frac{1}{P_i'} = \frac{n \frac{1}{P_i}}{\sum_{i=1}^{n} \frac{1}{P_i}} \quad , \qquad 5.11$$

i.e. $$\sum_{i=1}^{n} \frac{1}{P_i'} = n \quad . \qquad 5.12$$

5.6.5 Results

Application of the analysis technique described in sections 5.6.3 and 5.6.4 yields the following parameterisation of the average behaviour of the FWHM (250 m):

$$\text{FWHM (250 m)} = (133.3 \pm 56.1) - (136.4 \pm 92.4)\sec\theta + (37.9 \pm 39.1)\sec^2\theta + (0.74 \pm 1.08)\log_{10}\Phi(150\text{ m}) \times (\sec^2\theta - 4) \qquad 5.13$$

with a multiple regression coefficient of 0.98.

The estimate of the fluctuations in vertical showers ($\sigma_F(1)$) obtained from this fit is 3.0 ± 0.4 ns. The low significance of the fourth regression coefficient in equation 5.13 implies that the primary energy dependence is unresolved. However, as was indicated in section 5.6.2, the inherent r.m.s. variation due to primary energy is probably less than 0.7 ns. Quadratic subtraction of this quantity from $\sigma_F(1)$ implies that the fluctuation estimate is likely to be affected by less than 0.1 ns, which is well within the statistical uncertainty of 0.4 ns.

Figure 5.17 shows the distribution of standardised residuals $(f_i - F_i)/\sigma_{t_i}$ folded with the selection probabilities (P_i'). This distribution is consistent with a standard normal distribution : an assumption that provided the basis for the calculation of $\sigma_F(1)$. Possible contributions to the residuals from other sources are examined in section 5.6.7.

The contribution to these results made by the selection probabilities (P_i) is minimal. However, one disadvantage of this procedure is that it assumes all regions of the underlying distribution have been adequately sampled. But if the selection effects and the limited statistics conspire to exclude part of the underlying distribution from the data sample, weighting the data points 'a posteriori' may not be sufficient to estimate the standard deviation of the underlying distribution. In the following section this problem is investigated by testing the multiple

FIGURE 5.17 The distribution of standardised residuals about the multiple regression fit to the FWHM (250 m) data. The standard normal distribution is shown for comparison.

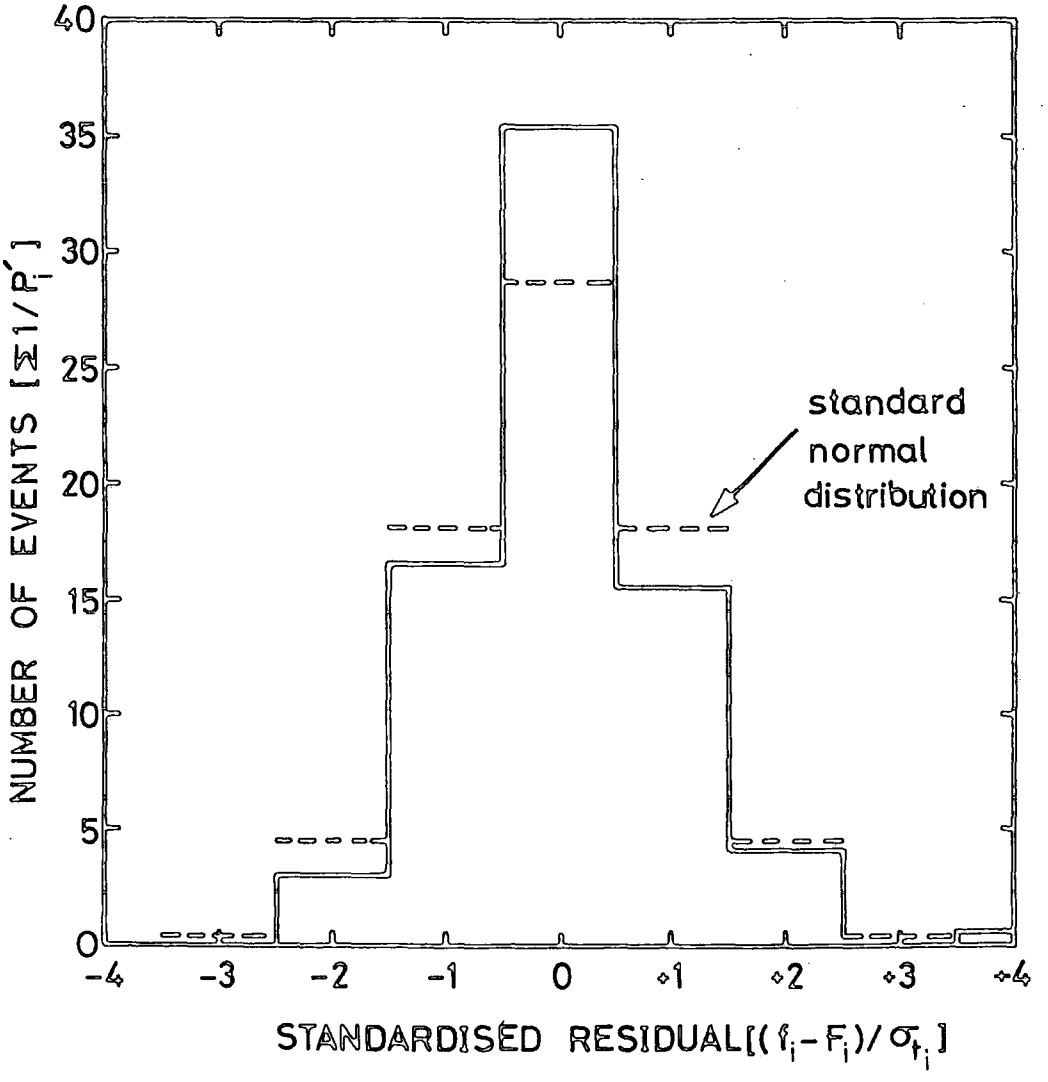

regression analysis under controlled conditions using simulated data. This procedure serves to test whether the estimator $\sigma_F(1)$ and its confidence interval can be expected to be unbiased. This is also important in view of the comparatively low significance of some of the regression coefficients in equation 5.13.

5.6.6 Monte Carlo Simulations of the Multiple Regression Analysis

The first stage in the simulation of the multiple regression analysis is the generation of a prior distribution in depths of electron maximum (t_{max}). This distribution is parameterised by its mean ($\overline{t_{max}}$), its standard deviation ($\sigma(t_{max})$) and the elongation rate (the rate of change of t_{max} with primary energy). Appropriate primary energy and zenith angle distributions are assumed. The selection probabilities are calculated for each simulated event, so that the selection effects expected in the real data sample can be incorporated into the simulated data sample. Each t_{max} value is converted to FWHM (250 m) using the prediction from model calculations (parameterised by equation 5.4).

Before carrying out the multiple regression analysis each simulated FWHM (250 m) is made to be in error using a Gaussian random number generator. The standard deviations used for the Gaussian errors are taken from the real data sample. The size of each error flag used in the weighted regression was itself subject to a random error. The selection probabilities calculated for each event were also subject to an appropriate error before being used in the regression analysis. The whole procedure was repeated with a number of different prior distributions, each of which comprised of the same number of events as the real dataset. Figure 5.18 shows the $\sigma_F(1)$ estimates as a function of $\sigma(t_{max})$. These results are in good agreement with the expectation from model calculations alone (dashed line), implying that the $\sigma_F(1)$ estimate obtained for the real data can be expected to be unbiased. The error

FIGURE 5.18 Results obtained from the application of the multiple regression analysis technique to simulated datasets, each having a different value of σ (t_{max}).

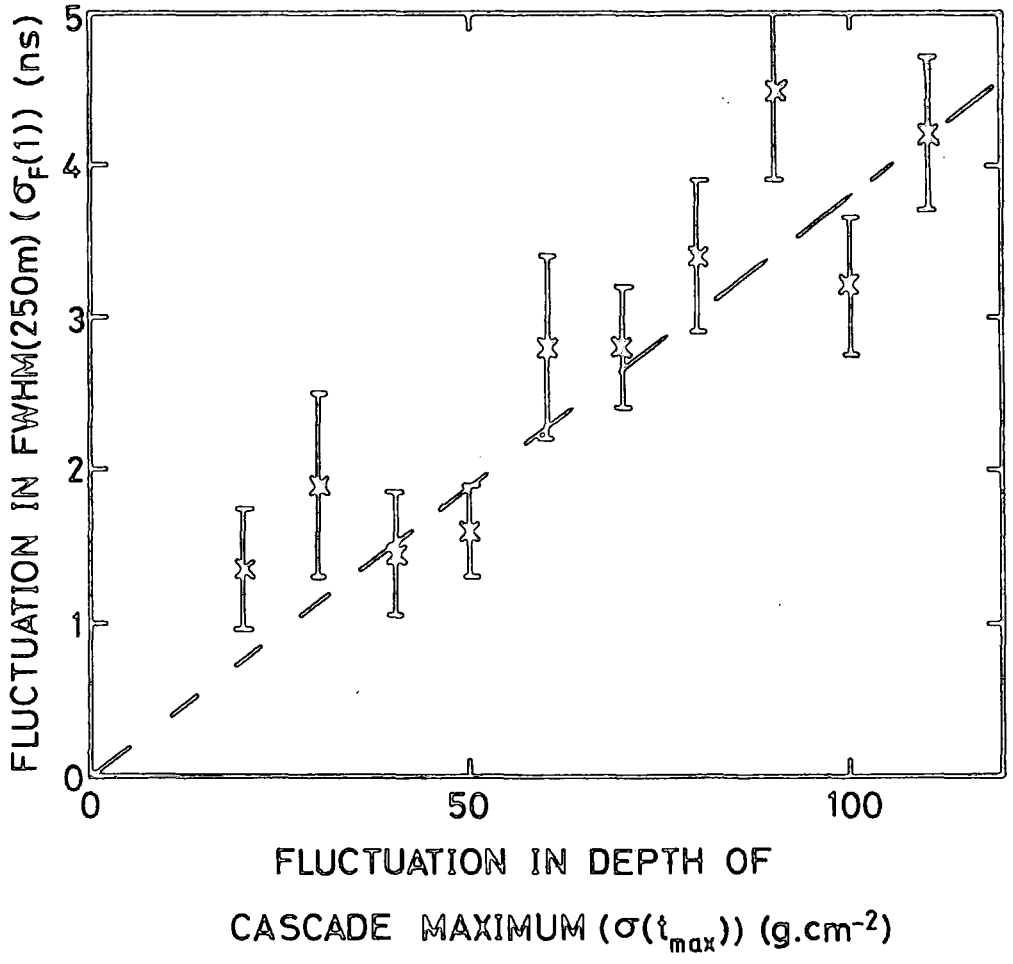

estimator for $\sigma_F(1)$ (see section 5.6.3) was found to be a reasonable representation for the one standard deviation confidence interval. On this basis, the estimate of $\sigma_F(1)$ obtained from the real data transforms to an estimate of the intrinsic fluctuations in the depth of cascade maximum of 79 ± 11 $g.cm^{-2}$. The low significance obtained for the primary energy coefficient in equation 5.13 was reproduced for the simulated data in all cases where significant fluctuations were present.

5.6.7 Investigation of Other Possible Contributory Factors to the Fluctuations between Showers

In table 5.1 each of the factors expected to contribute to the variations in the observed FWHM within a shower was listed. The components of error due to factors 2 - 4 were treated as random and quantified as a confidence interval on the fitted value at 250 m. As a check that no systematic component of error due to factor 3 has contributed to the fluctuation estimate, the standardised residuals from the multiple regression fit are shown in figure 5.19 plotted against the goodness of fit (reduced χ^2) values from the core location analysis. There is no significant increase in the magnitude of the residuals for the less well fitted showers.

The influence of the Earth's magnetic field can distort the radial symmetry of showers, as indicated in section 5.4.1. This effect can be expected to be proportional to the sine of the angle between the magnetic field lines and the shower trajectory (sin α). In figure 5.20 the standardised residuals are plotted against sin α, indicating no significant increase in the magnitude of the residuals with increasing sin α. This implies that the treatment of this effect as a pseudo-random error within each shower was sufficient.

The remaining factor to be examined in table 5.1 is the possible dependence of the FWHM on the atmospheric pressure. Figure 5.21 shows no

FIGURE 5.19 Scatter plot of the standardised residuals against the reduced χ^2 values from the core fitting procedure.

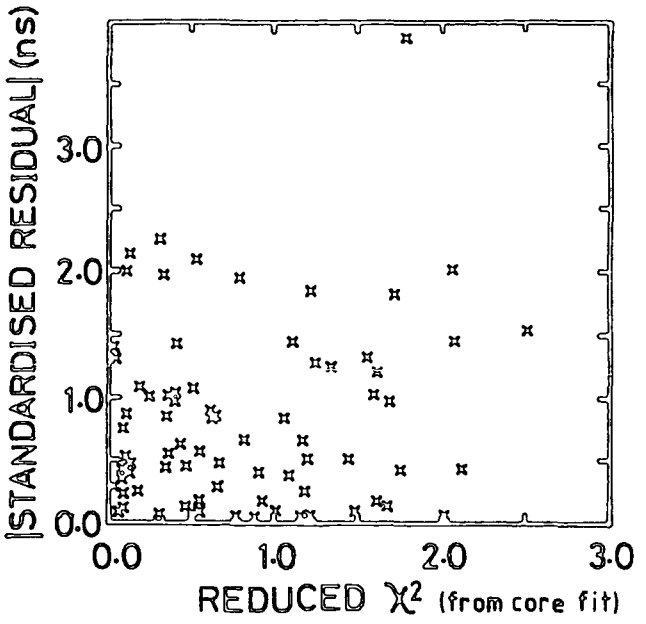

FIGURE 5.20 Scatter plot of the standardised residuals against sinα.

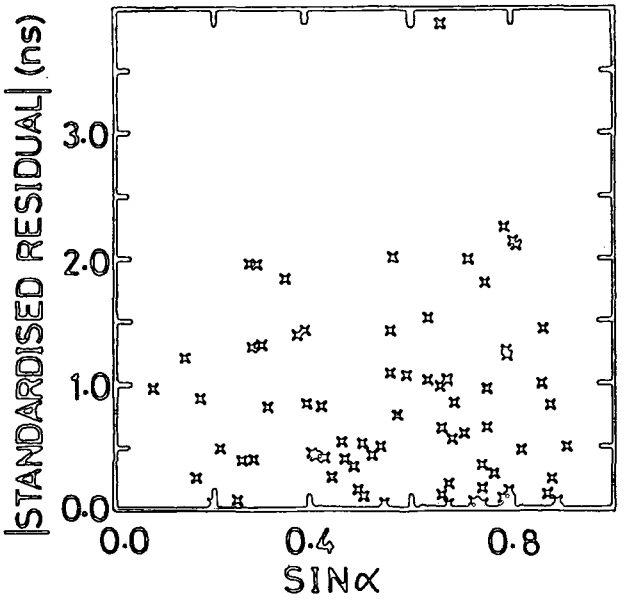

FIGURE 5.21 Scatter plot of the standardised residuals against atmospheric pressure.

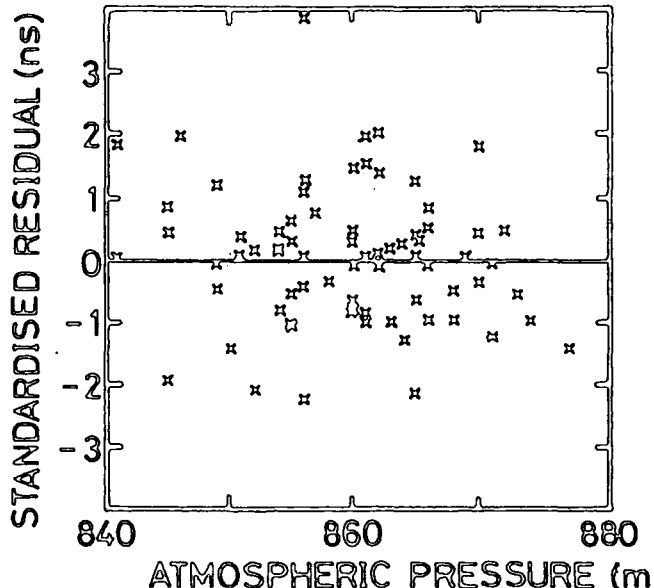

significant correlation between the standardised residuals and the atmospheric pressure. This is not unexpected, since the r.m.s. pressure variations represent only ± 10 $g.cm^{-2}$ variation in atmospheric thickness. When quadratically combined with the intrinsic fluctuations in shower development this would not in any case constitute a significant error in the fluctuation estimate.

5.7 CONCLUSIONS

The core distance dependence of the FWHM in the range 150 - 300 m is found to be in good agreement with the predictions from model calculations, with the exception of the near-core vertical showers. There is an indication that the average zenith angle dependence at a core distance of about 250 m may be slightly stronger than for the model calculations; however, the reason for this is not understood at present. The average depth of cascade maximum for showers of energy 2.1×10^{17} eV interpreted from data in the core distance range 200 - 300 m and zenith angle range 0^{o} - 45^{o}, is 678 ± 25 $g.cm^{-2}$. The intrinsic fluctuation in the FWHM (250 m) for vertical showers, due to the stochastic nature of the cascade processes, is found to be 3.0 ± 0.4 ns. This corresponds to a standard deviation in the underlying distribution of depths of cascade maximum of 79 ± 11 $g.cm^{-2}$.

CHAPTER 6

THE ATMOSPHERIC DEPTH OF ORIGIN OF CERENKOV LIGHT IN EAS

6.1 INTRODUCTION

Measurements of the synchronised time of arrival of the Cerenkov light pulse at widely spaced detectors provide information on the curvature of the light front. With the assumption that the light front is spherical (see section 2.3.6), the measurements can be used directly to estimate the centre of light emission in the atmosphere. In this chapter the synchronised-timing data is used in conjunction with the pulse profile measurements in an analysis of the arrival time of the light at the maximum recorded intensity. From this analysis, the depth in the atmosphere of the maximum perceived image of the cascade in Cerenkov light (D_{100}) is obtained in individual showers. The advantage in using the quantity D_{100} is that since it corresponds to the peak of each recorded light pulse it has the least experimental error due to the combined effects of sky noise and the pulse shape fitting procedure.

The observed distribution in D_{100} is interpreted, with the aid of the model calculations and consideration of the measurement errors, in terms of the mean depth of electron cascade maximum. The sensitivity of the measurements to the fluctuations in the cascade development is examined.

6.2 THE DATASET

As for the analysis of the FWHM, events were selected with zenith angles in the range 0^{o} to 45^{o} and with at least five detector responses. Since a spherical fit to the timing data requires a minimum of four measurements at large core distances, additional more stringent selection criteria were necessary. Each event was required to have at least five pulse shape measurements at core distances greater than 100 m (pulses inside 100 m were discarded), including at least one measurement outside

300 m. Poorly reconstructed pulse profiles were rejected according to the criterion described in section 5.2.1. To obtain a sufficiently populated data sample using these selection criteria a minimum primary energy estimator (log Φ (150 m)) of 3.45 was required. A sample containing 52 events was selected, with a mean primary energy of 1.7×10^{17} eV. The zenith angle and primary energy distributions are shown in figures 6.1 and 6.2 respectively.

6.3 THE DEPTH OF CERENKOV LIGHT MAXIMUM (D_{100})

6.3.1 Measurements in Individual Showers

The synchronised time of arrival of the light pulse at each detector (t_i) was added to the time interval within each pulse (p_i) between the discrimination time and the time to the peak of the pulse. The optimal spherical fit to these timing measurements was obtained using the weighted non-linear optimisation routine as described in section 4.5.1. The finite system response time was not removed from p_i since the small differences in detector response times were not considered significant for this measurement. The depth into the atmosphere of the centre of the spherical front (D_{100}) was calculated, and the 68% confidence interval was estimated using the procedure described in section 4.5.

Figure 6.3 shows the values of D_{100} plotted against the secant of the zenith angle. The model predictions incorporating the Dugway system response are shown for comparison. The data are not inconsistent with the model predictions, and there may be some indication of the zenith angle variation discussed in section 2.3.6. The data points in the figure are subdivided and indicate whether an event has a primary energy estimator (log Φ (150 m)) greater or less than 3.95. However, the underlying primary energy dependence is difficult to establish in view of the extent of the measurement errors and the fluctuations in cascade development. It should be noted that although the size of the error

FIGURE 6.1 The zenith angle distribution of the data sample selected for the analysis of D_{100}.

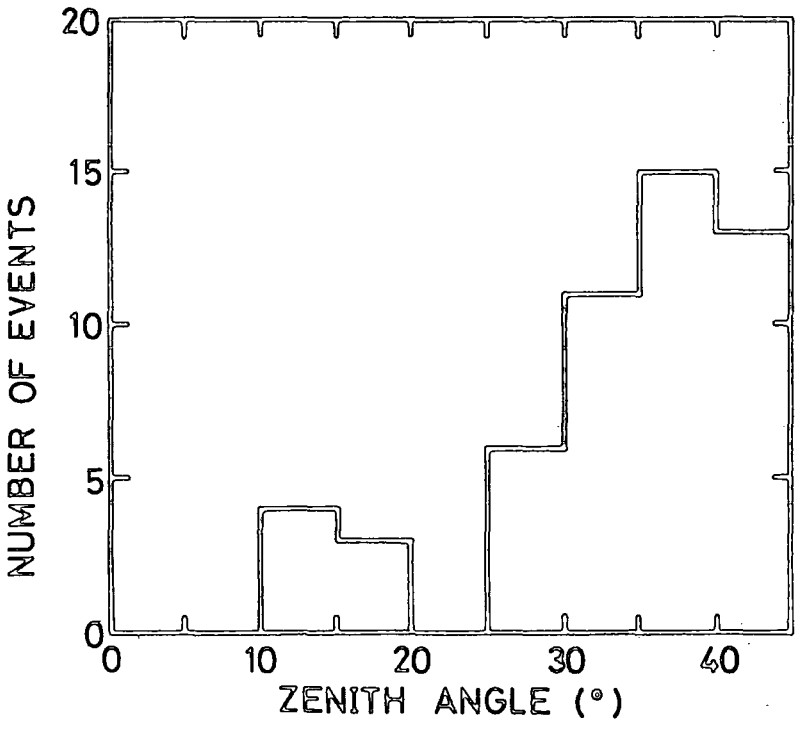

FIGURE 6.2 The distribution in primary energy estimator of the data sample selected for the analysis of D_{100}.

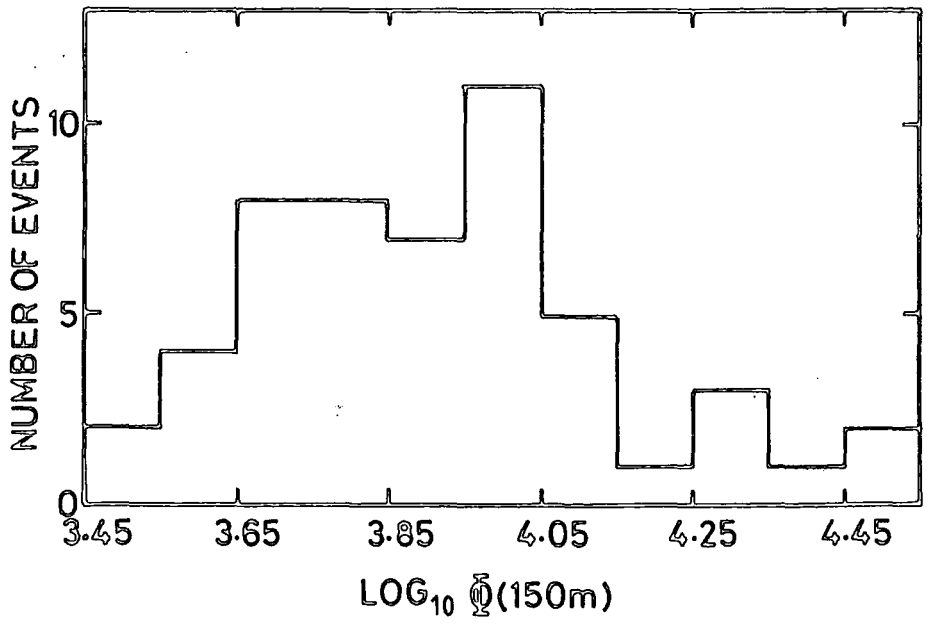

FIGURE 6.3 Measurements of the depth of Cerenkov light maximum (D_{100}) in individual showers. The curves represent the results of model calculations incorporating the Dugway system response.

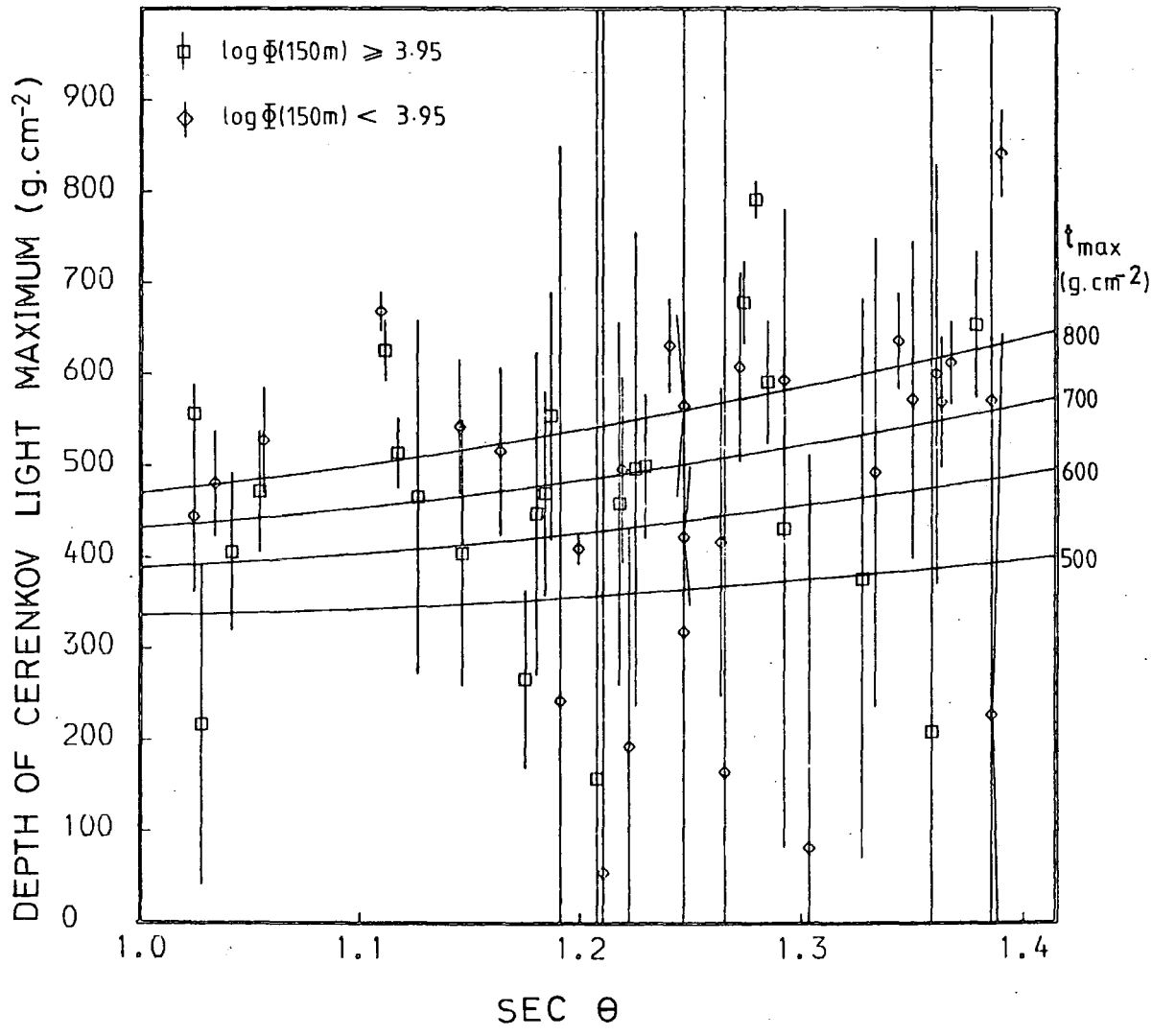

flags is undefined for a few of the events, the global function minimum (the minimum value of S^2 in equation 4.9) is still well defined. In other words, although the 68% confidence interval is extremely large in some cases, the confidence region at about the 50% level is considerably smaller. These events have therefore not been discarded since their information content is probably of some value.

Also calculated for each event were the depths of origin corresponding to a sequence of percentage levels in the light signal, i.e. the 10%, 50% and 90% levels on the rising edge, and the 90% and 50% levels on the falling edge. In general, this sequence of light origins ranked monotonically with increasing atmospheric depth, as in the example shown in figure 4.15. However, owing to the increased size of the measurement errors in these quantities, attention is focussed here on the interpretation of the measurements of D_{100}.

6.3.2 Principal Factors Affecting the Observed Distribution in D_{100}

The depth of Cerenkov light maximum is strongly coupled to the depth of electron cascade maximum (t_{max}). Changes in t_{max} due to fluctuations in the cascade development and to primary energy variations are reflected by corresponding changes in the depth of Cerenkov light maximum.

The perceived depth of Cerenkov light maximum (D_{100}) is expected to depend also on the zenith angle (as explained in section 2.3.6). It is evident from figure 6.3 that an interpretation of the observations must also include a careful consideration of the measurement errors. It has been shown (see figures 4.18 to 4.20) that the mean observed depth is not expected to be an unbiased estimator. Nor is the weighted mean of the observations unbiased, since the size of the error flags is expected to correlate with the underlying depth of origin of the light

front (see figure 4.21). In addition to these factors, there will be a slight bias in the observed distribution of D_{100} owing to the preferential selection of showers with small t_{max}.

6.4 INTERPRETATION OF THE MEASUREMENTS OF THE DEPTH OF CERENKOV LIGHT MAXIMUM

The objective is to infer, from the observed distribution of D_{100}, the mean ($\overline{t_{max}}$) and if possible the fluctuation ($\sigma(t_{max})$) in the underlying distribution of depths of electron cascade maximum. This will enable comparison with measurements of the cascade development made using other techniques. In order to take account of the measurement biases and the other factors described in section 6.3.2, a number of hypothetical t_{max} distributions were adopted, and the expected D_{100} distributions simulated. Comparison between observed and simulated D_{100} distributions enables the validity of the initial assumptions in the t_{max} distributions to be tested. A detailed description of the procedure follows.

6.4.1 Monte Carlo Simulation of D_{100} Distributions

For each prior distribution in t_{max}, a mean depth $(\overline{t_{max}})_K$ was selected. The distribution in t_{max} due to the finite primary energy range was incorporated by sampling from an appropriate energy spectrum and assuming an elongation rate of 90 $g.cm^{-2}$/decade. (The value of the elongation rate was ascertained at a later stage not to be of first order importance for the results of the analysis procedure). The zenith and azimuth angle distributions were taken from the real data sample. Each value of t_{max} was then converted to depth of Cerenkov light maximum using a parameterisation of the results from model calculations. As explained in section 2.3.6 this transformation is not dependent on the primary mass or the model of hadronic interactions used in generating the simulated cascades.

The light transit times from the simulated centres of Cerenkov light emission to the detector coordinates were calculated. These transit times were randomised by sampling from a Gaussian distribution with a standard deviation equal to that estimated for the experimental measurement errors. The pattern of contributing detectors for each simulated event was taken from the real data sample. The simulated events were analysed, using the same non-linear optimisation routine as for the real events, providing a simulated D_{100} distribution containing $\sim$ 500 events. Similarly, distributions were obtained for 26 values of $(\overline{t_{max}})_K$ at 20 g.cm^{-2} intervals from 400 to 900 g.cm^{-2}.

6.4.2 Comparison between Observed and Simulated D_{100} Distributions

The experimental D_{100} distribution was binned into 7 intervals of approximately equal frequency. Each of the 26 simulated D_{100} distributions was divided into the same bins, and the result was incorporated into a (7 x 26) 2-dimensional matrix, D(7 x 26). To allow for the fluctuations in t_{max}, this matrix was sampled using a discrete approximation to a Gaussian distribution, $G_{L,M}$, with mean $(\overline{t_{max}})_L$ and standard deviation $\sigma(t_{max})_M$:

$$D(7 \times 26) \; * \; G_{L,M}(26 \times 1) \; = \; D_{L,M}(7 \times 1) \qquad 6.1$$

In this way the effects of fluctuations in t_{max} on the D_{100} distributions were incorporated into the 7-element matrices $D_{L,M}$. This obviated the need for a large number of additional simulations for a range of values of $\sigma(t_{max})$ for each value of $(\overline{t_{max}})_K$.

Before comparison between the simulated distributions ($D_{L,M}$) and the observed distribution, it was necessary to take account of the selection effects. The selection probability for each real event was calculated using the lateral distribution of pulse heights, as described in section 5.6.4. This provided a second-order correction to the observed D_{100}

distribution. An alternative method would have been to use the selection probabilities derived from the model calculations in order to incorporate the selection bias into the simulated distributions. At the time this analysis was carried out, the software for calculating the selection probabilities using the latter technique was not available. However, it has since been established that the two methods produce consistent results.

Simulated distributions ($D_{L,M}$) for a wide range of values of $(\overline{t_{max}})_L$ and $\sigma(t_{max})_M$ were compared with the observed distribution using the χ^2 test. The region around the minimum χ^2 value is shown in figure 6.4. It can be seen that there is almost no sensitivity to $\sigma(t_{max})$ using this technique. The optimal fit is obtained for $\overline{t_{max}} = 730 \pm 35$ g.cm^{-2}. Figure 6.5 shows the observed distribution in D_{100} (corrected for selection effects) and the expectation for $\overline{t_{max}} = 730$ g.cm^{-2}.

Since the measurement errors are a major influence on the shape of the perceived D_{100} distribution, it is important to verify that the magnitude of the errors used in the analysis is correct. As explained in section 4.5.1 the errors are estimated by quadratically combining the error on the synchronised time of arrival of the light pulse with the error on the pulse profile reconstruction. The errors are used in the weights for the data-fitting routine and therefore influence the magnitude of the sum of the squared standardised residuals (S^2 in equation 4.9). Figure 6.6 shows the distributions in S^2 for the observed and simulated data sets. The two distributions are consistent, implying that the estimations of the experimental measurement errors are satisfactory.

6.4.3 Fluctuations in the Cascade Development

In order to investigate further the possibility of determining the fluctuations in the cascade development, small systematic variations in D_{100} due to the zenith angle and primary energy ranges were removed

FIGURE 6.4 The goodness of fit between the observed D_{100} distribution and the distributions simulated for a range of values of $\overline{t_{max}}$ and $\sigma(t_{max})$.

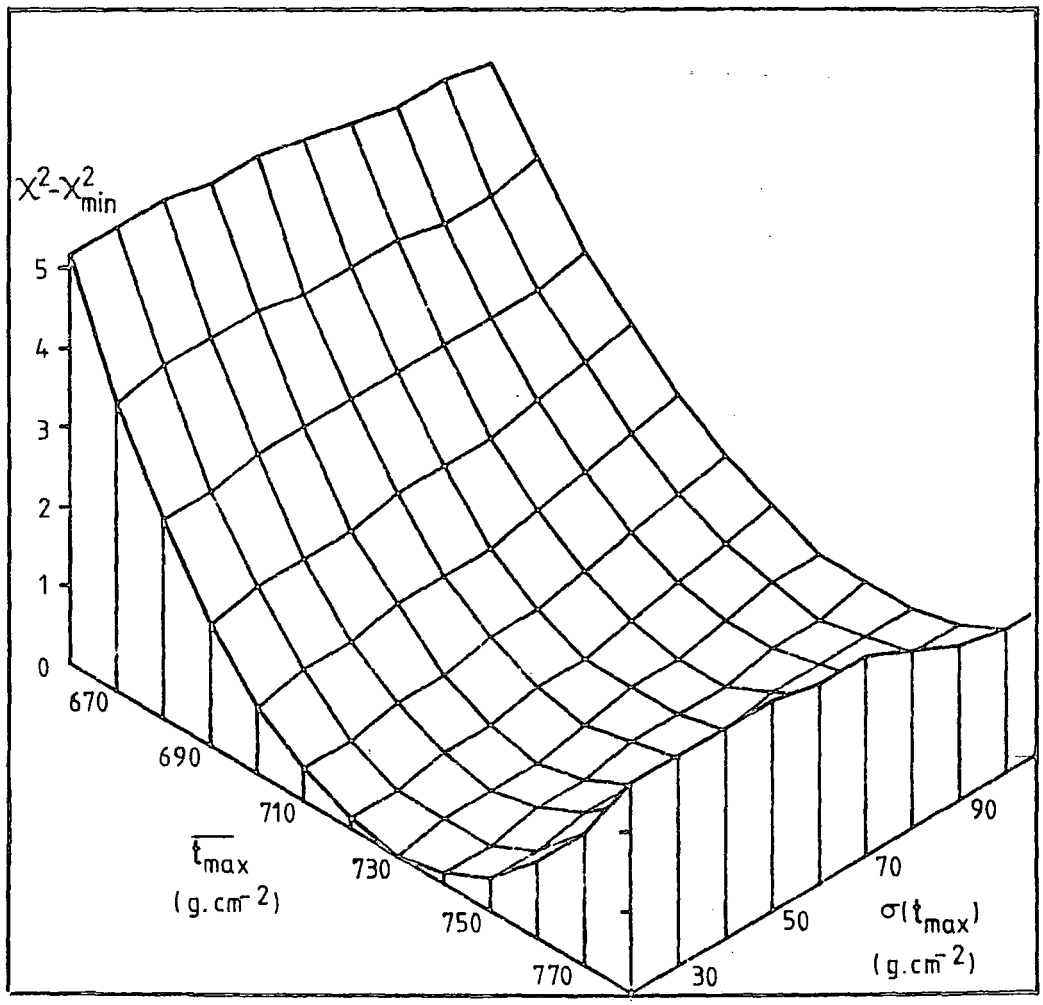

FIGURE 6.5 The observed distribution in D_{100} compared with the expected distribution for t_{max} = 730 g.cm^{-2} and $\sigma(t_{max})$ = 100 g.cm^{-2}.

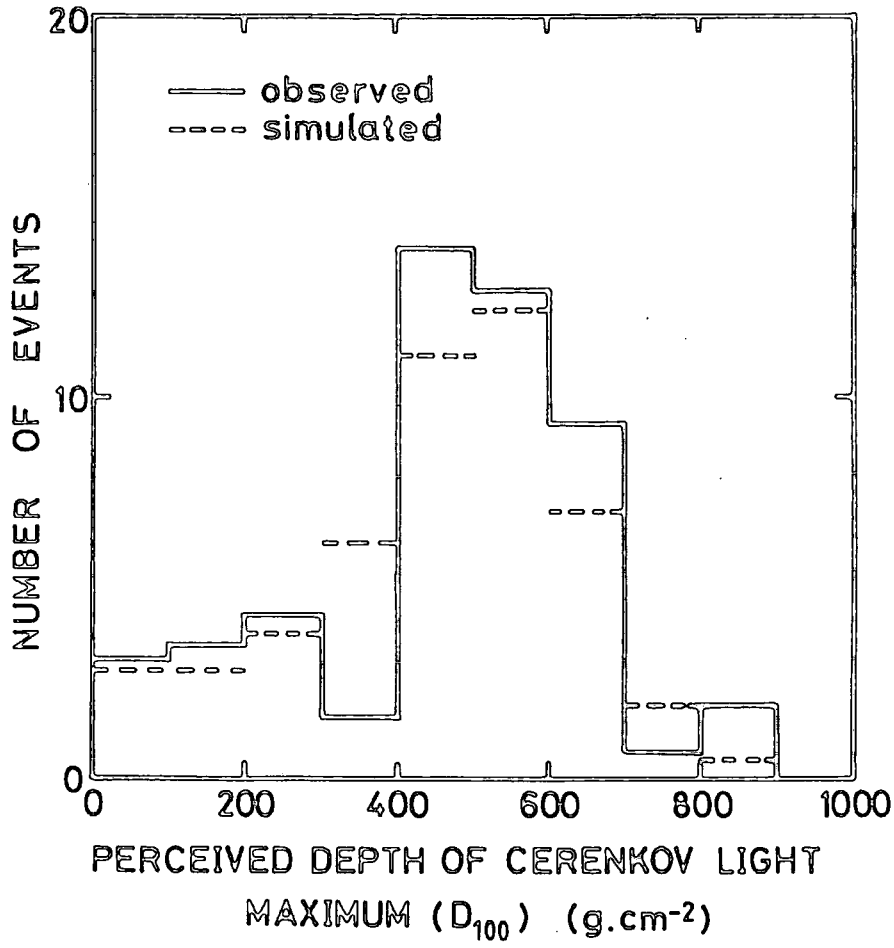

FIGURE 6.6 The distribution in S^2 for the observed and simulated datasets.

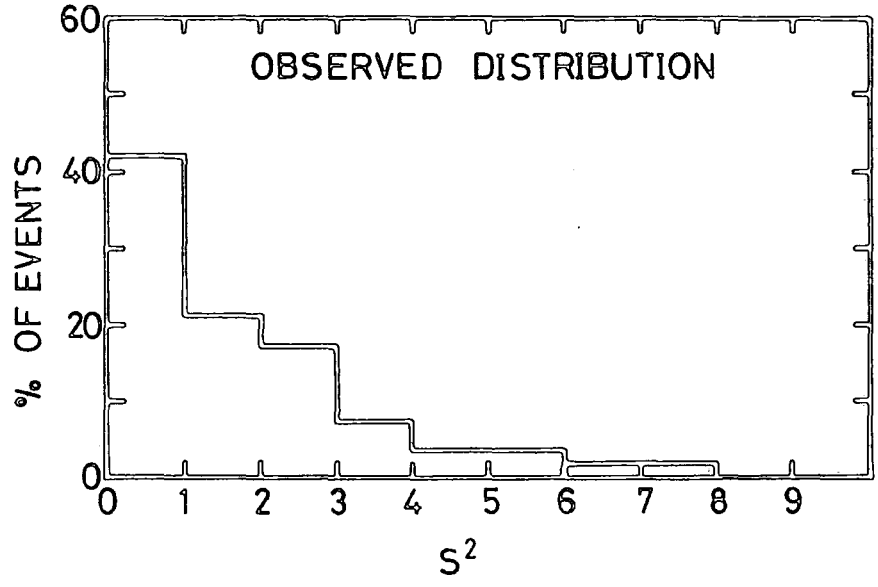

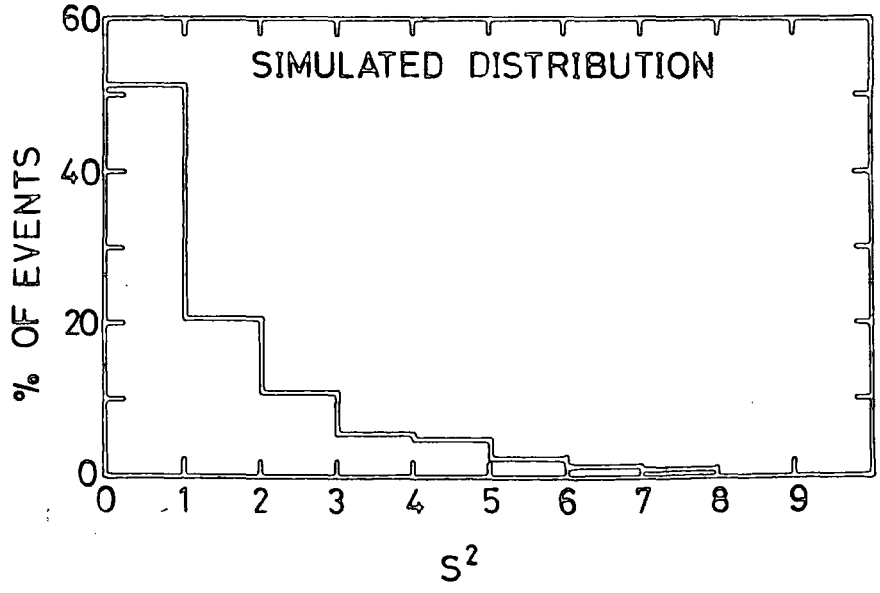

using a least squares regression of the form:

$$D_{100} = A + B \sec\theta + C \log \Phi\ (150\ m). \qquad 6.2$$

The fit was weighted using the selection probabilities calculated for each event. The availability of confidence intervals on each value of D_{100} enabled the intrinsic fluctuations in D_{100} to be calculated from the residuals of the fit (using the method described in section 5.6.3). To interpret the results of this procedure, the same analysis was carried out on simulated datasets with a fixed $\overline{t_{max}}$ of 730 g.cm^{-2} but with a range of values of $\sigma(t_{max})$. This technique provided an estimate for $\sigma(t_{max})$ of 120 g.cm^{-2}, with a one standard deviation confidence region of $0<\sigma(t_{max})<190$ g.cm^{-2}.

6.5 CONCLUSIONS

The depths of Cerenkov light maximum have been derived from measurements of the curvature of the light front in 52 showers of mean primary energy 1.7×10^{17} eV. The measurements have been interpreted, with the aid of model calculations and consideration of the measurement errors, in terms of the underlying distribution of depths of electron cascade maximum. The estimated mean depth of electron cascade maximum ($\overline{t_{max}}$) is 730 ± 35 g.cm^{-2}. The transformation from the measurement errors (in ns) to the uncertainty in D_{100} (in g.cm^{-2}) has been made for each shower. However, these uncertainties proved too large to enable an accurate determination of the fluctuations in the cascade development with this data sample.

CHAPTER 7

COMPARISON WITH COMPUTER SIMULATION PREDICTIONS AND WITH OTHER WORK

7.1 INTRODUCTION

In this chapter the results on the depth of cascade maximum derived in chapters 5 and 6 are discussed in the context of the many other results recently obtained from the Dugway experiment. The results are compared with the Durham group's computer simulation predictions for a range of models of the high-energy nuclear interactions incorporating scaling in the fragmentation region. Within the framework of these models, and assuming that no drastic changes in the nuclear physics are taking place, the data are interpreted in terms of the broad characteristics of the primary mass composition.

Direct comparison of the measured Cerenkov light parameters with those recorded at other arrays is not attempted because of the difference in experimental systems and the difference in altitude between Dugway and the other array locations. Instead, comparison is made between the inferred depth of maximum estimates from Dugway, Haverah Park and other arrays derived from both Cerenkov light and particle measurements. The implications of these combined results for the primary mass composition and for the nuclear interaction models are considered.

7.2 THE MEAN DEPTH OF CASCADE MAXIMUM ($\overline{t_{max}}$)

7.2.1 Measurements from the Dugway Experiment

In addition to the $\overline{t_{max}}$ estimates derived from the pulse shape and front curvature measurements (described in chapters 5 and 6), a number of other values have been derived from both the lateral distribution and pulse shape data. These analyses have proceeded in parallel with the present work, and only a brief outline is provided here since a detailed description will be given elsewhere (e.g. Craig, Ph.D. thesis in

preparation). Table 7.1 is a compilation of the $\overline{t_{max}}$ results currently available from the Dugway data.

The flexible geometry of the Dugway array enabled data to be recorded over a wide range of primary energy. Estimates of $\overline{t_{max}}$ have been derived from the lateral distribution data recorded with the 400 m, 200 m and 100 m array configurations. This was achieved using the development - sensitive parameter $\Phi(r_1)/\Phi(r_2)$, the ratio of the Cerenkov light densities at the core distances r_1 and r_2. The appropriate ratios, chosen to be well measured for each array size, were Φ(100 m)/Φ(250 m), Φ(75 m)/Φ(150 m) and Φ(50 m)/Φ(100 m) respectively. Individual Cerenkov light density measurements were normalised by dividing by the primary energy estimator, and then binned by core distance, primary energy estimator and zenith angle. The average steepness of the lateral distribution, parameterised by $\Phi(r_1)/\Phi(r_2)$, was calculated for each primary energy and zenith angle. An example of the zenith angle dependence of $\Phi(r_1)/\Phi(r_2)$ obtained with a 200 m array data sample is shown in figure 7.1. Each data point in the figure was transformed to an estimate of $\overline{t_{max}}$ by comparison with the model calculations, and the weighted mean of these estimates is shown in table 7.1.

A preliminary analysis has been made of the Cerenkov light pulse FWHM data from the showers recorded by 200 m array. The FWHM in the narrow core distance range 190 - 200 m has been binned by zenith angle and primary energy estimator. An example of the dependence of the mean FWHM (190 - 200 m) on zenith angle is shown in figure 7.2. The necessity of dealing carefully with data in an interval of core distance as small as 190 - 200 m is clear. Comparison with the model calculations enables the transformation of each data point to an estimate of $\overline{t_{max}}$. The weighted mean of these estimates is also shown in table 7.1. A similar analysis is not possible for showers recorded by the 100 m array, since

TABLE 7.1

Measurements of the mean depth of cascade maximum from the Dugway experiment.

ARRAY SIZE	TECHNIQUE		PRIMARY ENERGY (eV)	$\overline{t_{max}}$ (g.cm^{-2})
400 m	light-front curvature		1.7×10^{17}	730 ± 35
	FWHM		2.1×10^{17}	678 ± 25
	lateral distribution	(	3.2×10^{17}	694 ± 26
		(	1.6×10^{17}	633 ± 16
		(	9.5×10^{16}	624 ± 11
200 m	FWHM	(	6.5×10^{16}	646 ± 44
		(	3.1×10^{16}	581 ± 26
	lateral distribution	(	3.4×10^{16}	555 ± 40
		(	2.4×10^{16}	548 ± 15
		(	1.5×10^{16}	520 ± 12
		(	9×10^{15}	490 ± 20
100 m	lateral distribution	(	3.1×10^{16}	555 ± 60
		(	1.2×10^{16}	482 ± 16
		(	6.3×10^{15}	472 ± 18
		(	3.0×10^{15}	<520± 20

FIGURE 7.1 Measurements of $\overline{\Phi(75\ m)/\Phi(150\ m)}$ obtained from a sample of events, recorded with the 200 m array, with a mean primary energy of 3.4×10^{16} eV.

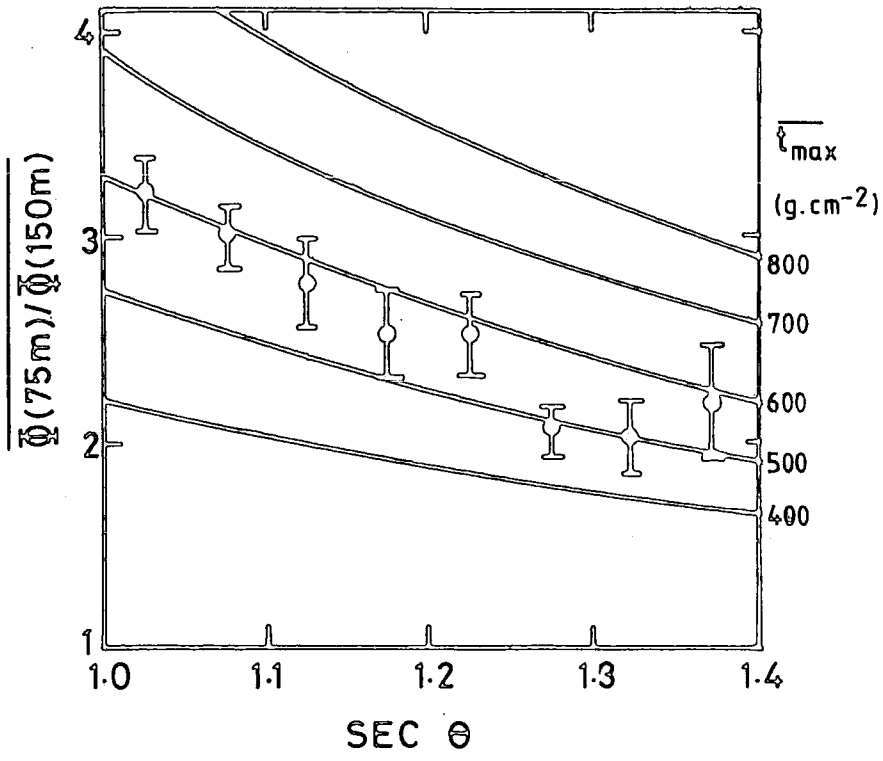

FIGURE 7.2 Measurements of the $\overline{FWHM}$ in the core distance range 190 - 200 m. The mean core distance is indicated for each data point. The data sample was recorded with the 200 m array and has a mean primary energy of 3.1×10^{16} eV.

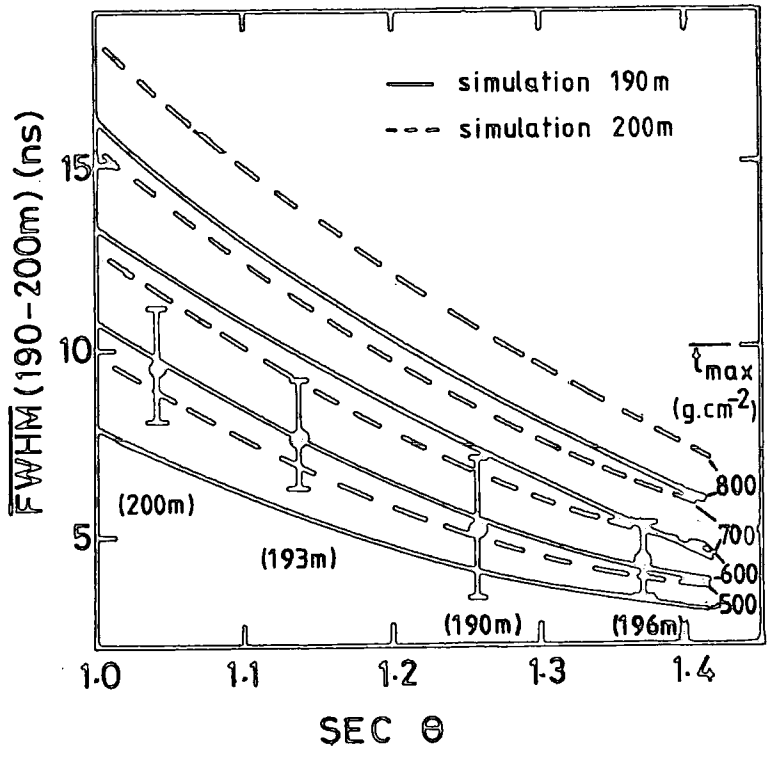

the pulse shape shows no sensitivity to t_{max} at core distances $\lesssim$ 150 m (Orford and Turver (1980), McComb and Turver (1981a), Hillas (1982)).

7.2.2 Comparison with Computer Simulation Predictions

In figure 7.3, the $\overline{t_{max}}$ results of table 7.1 are plotted against primary energy and compared with predictions from the Monte Carlo model calculations. It should be emphasised that the $\overline{t_{max}}$ data points have been derived from the Cerenkov light measurements using transformations which are independent of the primary mass, primary energy and the model of hadronic interactions used in the calculations. Further, since the same set of computer simulations was used for the interpretation of all the measurements, systematic errors in the derivation of $\overline{t_{max}}$ have been minimised. Overlap between $\overline{t_{max}}$ estimates derived from measurements made with arrays of different sizes and with different development-sensitive parameters provides confidence in the combination of the results over a wide primary-energy range.

The data are compared with the computer simulation predictions for average showers initiated by proton and iron nucleus primaries. The models incorporate scaling in the fragmentation region, a range of multiplicities in the central region (increasing with energy as log E, $E^{1/4}$ and $E^{1/3}$), and a range of interaction cross sections (constant, and increasing as log s and $\log^2 s$).

The $\overline{t_{max}}$ estimates from the front curvature and pulse shape measurements at $\sim 2 \times 10^{17}$ eV (derived in chapters 5 and 6) are in reasonable agreement with the values derived from the lateral distribution of Cerenkov light observed at Dugway in showers of similar energy. These results on their own could be interpreted as arising from heavy primaries together with a model incorporating scaling in the central region. Alternatively, a mixed/light mass composition could be inferred

FIGURE 7.3a Comparison with model calculations incorporating scaling in the central region.

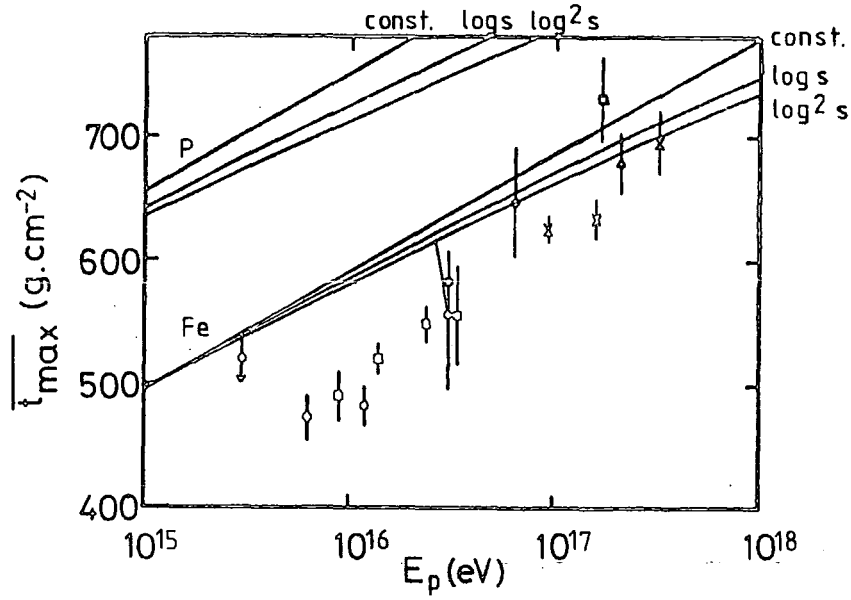

FIGURE 7.3b Comparison with model calculations incorporating an $E^{1/4}$ central-region multiplicity.

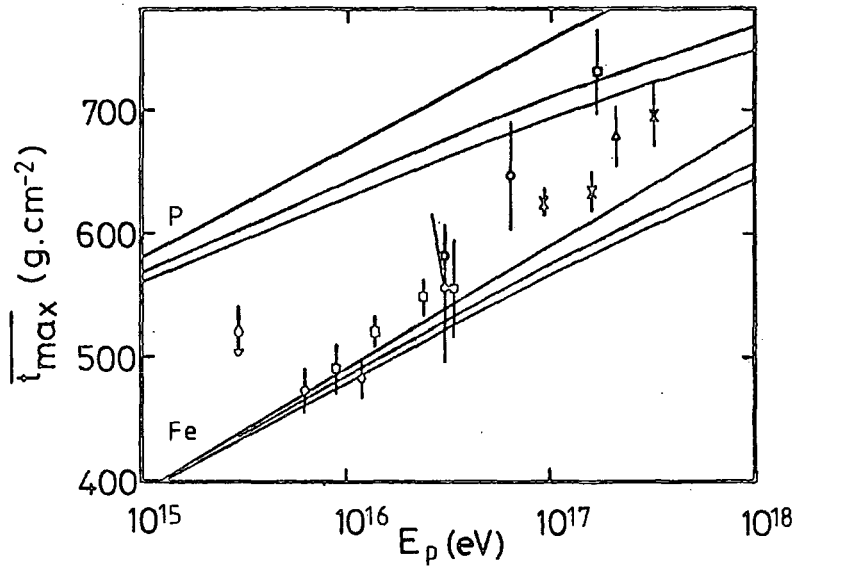

FIGURE 7.3c Comparison with model calculations incorporating an $E^{1/3}$ central-region multiplicity.

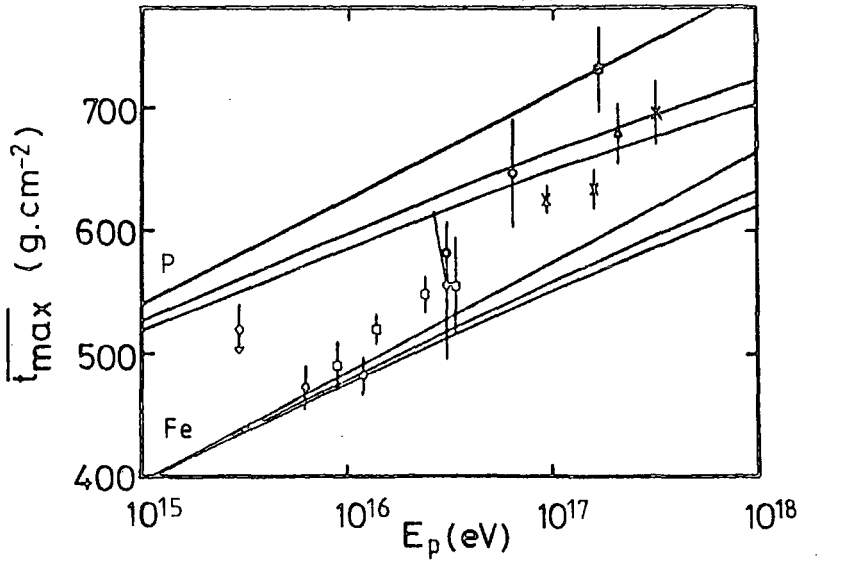

from models incorporating $E^{1/4}$ or $E^{1/3}$ multiplicities in the central region. However, if the results of figure 7.3 are interpreted as a whole, considerably more information on the primary mass composition emerges.

When comparing the data with the model predictions, both the absolute values of $\overline{t_{max}}$ and the rate of change of $\overline{t_{max}}$ with primary energy (the elongation rate) should be considered. Firstly, it is reasonable to assume that the data points should be bounded by the predictions for proton and iron nucleus primaries. Clearly, the predictions from the models with scaling in the central region (figure 7.3a) are not compatible with this assumption. Secondly, consider the elongation rate in the range 6.3×10^{15} - 3.2×10^{17} eV. This range excludes the lowest energy data point, which is thought to be biased in a way for which reliable allowance cannot be made and therefore considered to be an upper limit. A weighted linear regression gives an elongation rate of 135 ± 9 g.cm^{-2} per decade. This value is significantly greater than any of the model predictions for a constant primary mass composition, which range from 60 to 100 g.cm^{-2} per decade. It is further noted that models which incorporate a violation of scaling in the fragmentation region (e.g. the CKP and high multiplicity models) predict even smaller elongation rates than scaling-based models.

A plausible interpretation of the data, based on any of the models of figures 7.3b and 7.3c, is that the mean primary mass number is $\sim$ 56 at 10^{16} eV, and decreases with primary energy until at least 2×10^{17} eV. However, as the primary energy increases from 10^{16} eV, estimation of the mean mass number becomes increasingly dependent on the choice of interaction cross section and the central-region multiplicity. The models incorporating a constant cross section could be considered to be the least plausible, since (as was indicated in

chapter 1) both cosmic ray and accelerator measurements suggest that the pp cross section increases over the range 10^{11} to 5 x 10^{13} eV. With the additional assumption that the cross section rises as log s or $\log^2 s$ (both are reasonable extrapolations from accelerator data), the mass composition at 2 x 10^{17} eV could be inferred to be protonic for an $E^{1/3}$ multiplicity, or light/mixed for an $E^{1/4}$ multiplicity.

7.2.3 Comparison with Other Work

The primary energy intercalibration of the Dugway and Haverah Park arrays (see section 4.3.2) allows reliable comparison of the $\overline{t_{max}}$ results from these two arrays without introducing the systematic uncertainties in the primary energy domain often encountered when comparing data from different experiments. In figure 7.4 results from three experiments at Haverah Park have been added to those from the Dugway experiment. The results from the Cerenkov-light experiment at Haverah Park (Hammond et al. (1978)) are the combination of results on the lateral distribution, pulse shape and light front curvature in a small number of showers. The muon-core angle measurements (Gibson et al. (1981a)) and the muon/electron number ratio measurements (Blake et al. (1979)) also provide model-independent $\overline{t_{max}}$ estimates provided that scaling remains valid in the fragmentation region (McComb and Turver (1982b)). The same set of computer simulations was used in the derivation of $\overline{t_{max}}$ from all four experiments. Reasonable agreement between the measurements is obtained in the region of overlap at $\sim$ 2 x 10^{17} eV. The measurements are compatible with models incorporating an $E^{1/4}$ or $E^{1/3}$ central-region multiplicity, with the exception of the muon/electron number results which favour an $E^{1/4}$ multiplicity. There is a clear suggestion that the large elongation rate observed in the Dugway results does not continue to energies $\gtrsim 10^{18}$ eV.

FIGURE 7.4a Comparison with model calculations incorporating an $E^{1/4}$ central-region multiplicity.

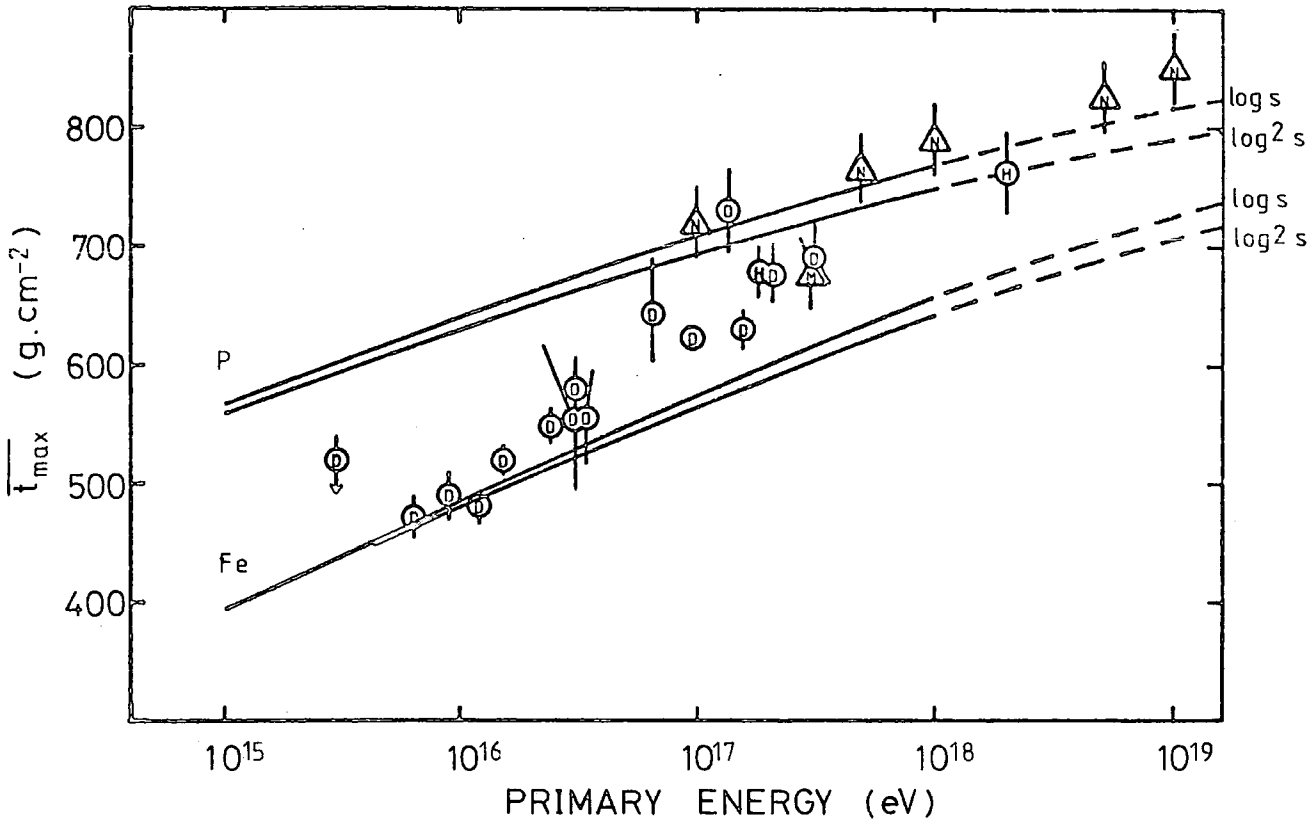

FIGURE 7.4b Comparison with model calculations incorporating an $E^{1/3}$ central-region multiplicity.

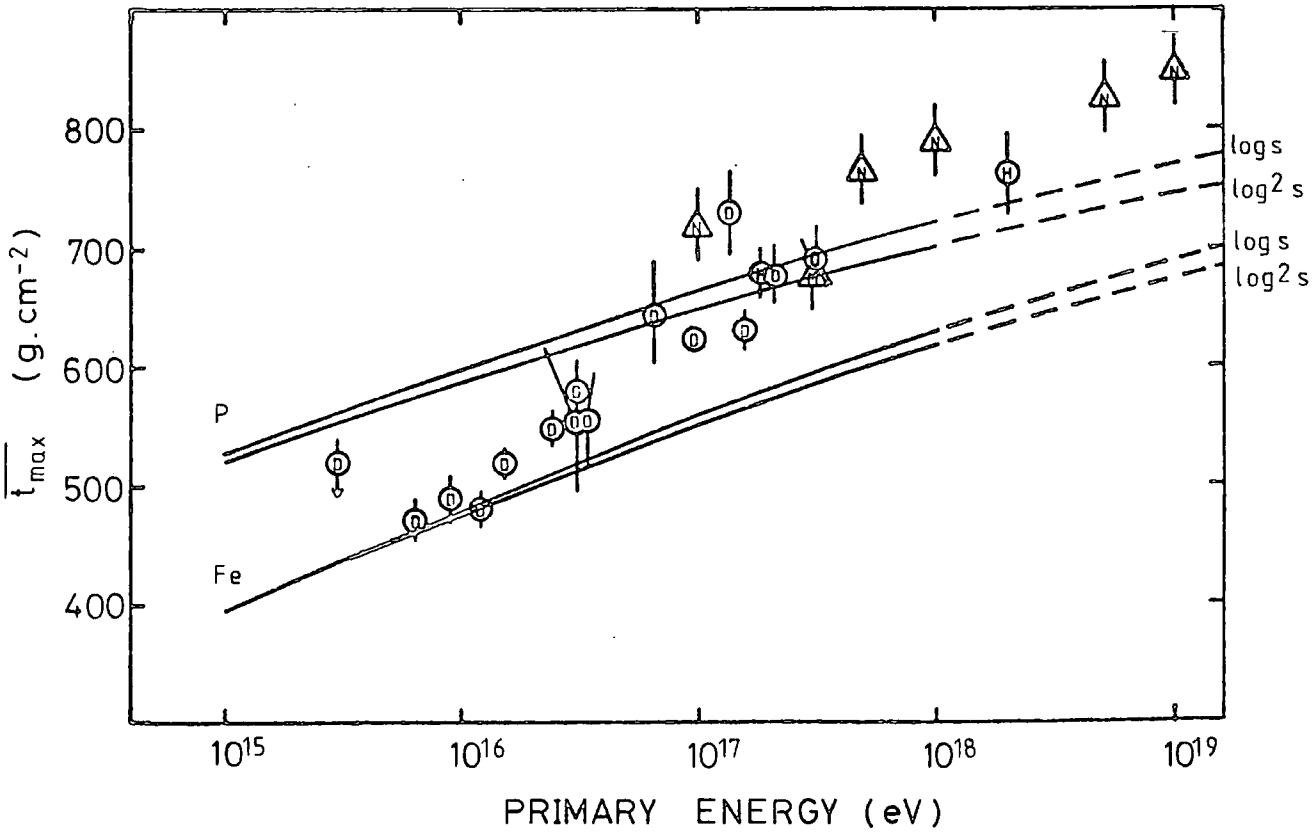

Firm evidence for a reduction in the elongation rate for energies $\gtrsim 10^{18}$ eV is also found in two other sets of data from Haverah Park: the deep water detector lateral distribution and rise-time measurements, from which only the elongation rate and not absolute $\overline{t_{max}}$ estimates are so far available. Figure 7.5 shows the five elongation rate measurements currently available from the Dugway and Haverah Park experiments. Also shown in the figure are the predictions from model calculations for a constant mass composition. The elongation rate at $\sim 10^{18}$ eV is consistent with the expectation for a constant (or nearly constant) mean mass number. Since there are only small differences between the predictions of the different models compared with the spread in the measurements, it is not possible to place any further constraints on the choice of model/mass composition on the basis of these results.

In figure 7.6 the $\overline{t_{max}}$ results from Dugway and Haverah Park are compared with those from other experiments. It should be emphasised that in comparing results in this way there is the possibility of introducing systematic errors in the relative primary energy assignments. Equally seriously, residual systematic differences in $\overline{t_{max}}$ may also be present due to selection biases in the data and to the different methods employed in interpreting the measurements. Despite these expected effects there is a measure of agreement between the results from many experiments. The Cerenkov-light measurements of Tornabene (1979) and the particle measurements of Antonov et al. (1981) suggest the presence of a significant 'heavy' component in the primary mass composition at $\sim 10^{15}$ eV. The Cerenkov light measurements from the Buckland Park array suggest a large elongation rate between 10^{16} and 10^{17} eV, although inconsistencies in this work have been pointed out (Orford and Turver (1980)). The Cerenkov light measurements from the Yakutsk array at

FIGURE 7.5a Comparison with model calculations incorporating an $E^{1/4}$ central -region multiplicity

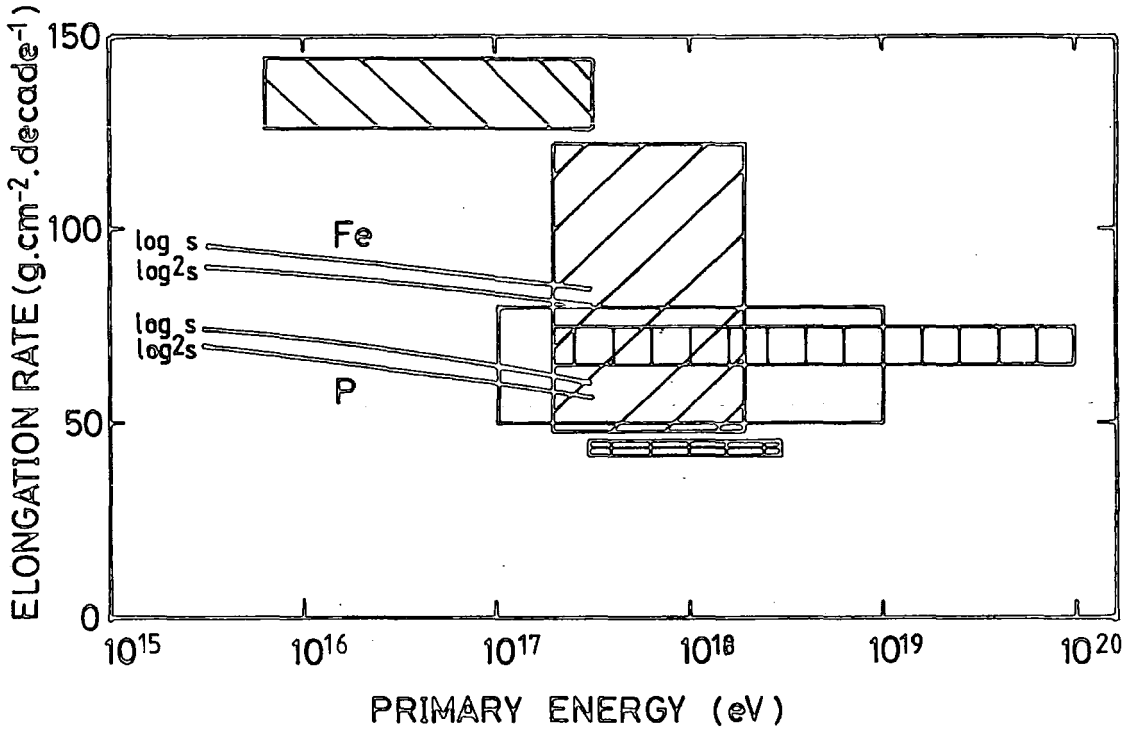

FIGURE 7.5b Comparison with model calculations incorporating an $E^{1/3}$ central-region multiplicity.

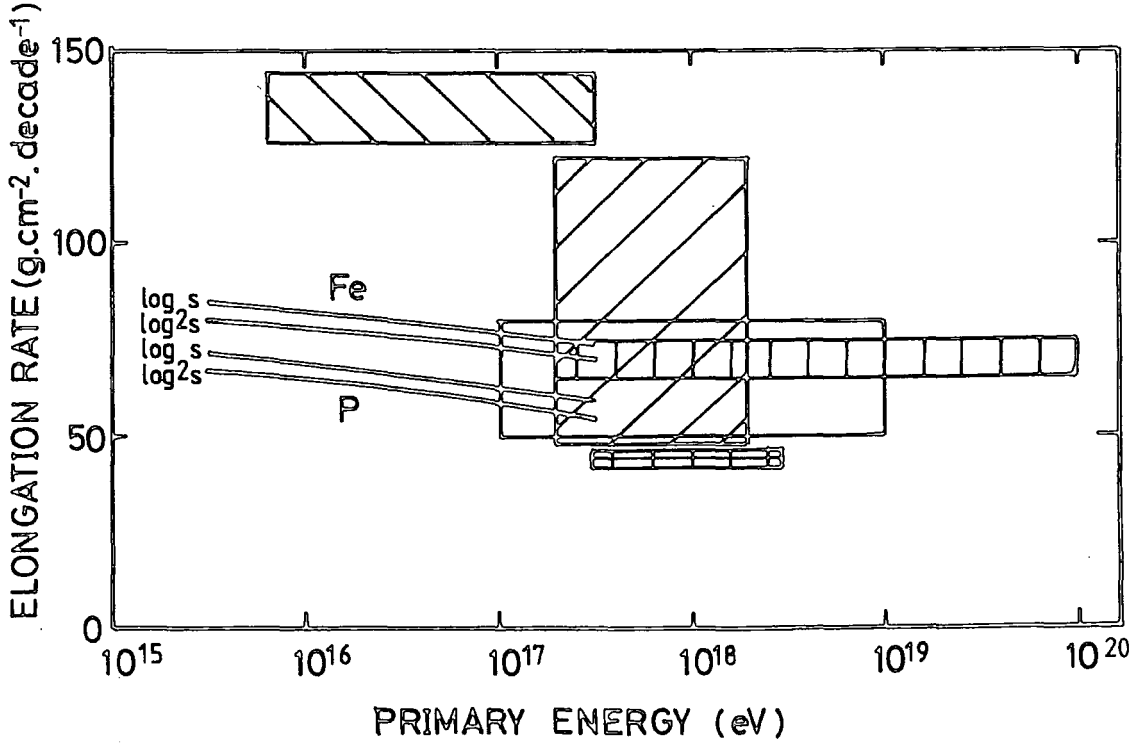

FIGURE 7.6a Comparison with model calculations incorporating an $E^{1/4}$ central-region multiplicity.

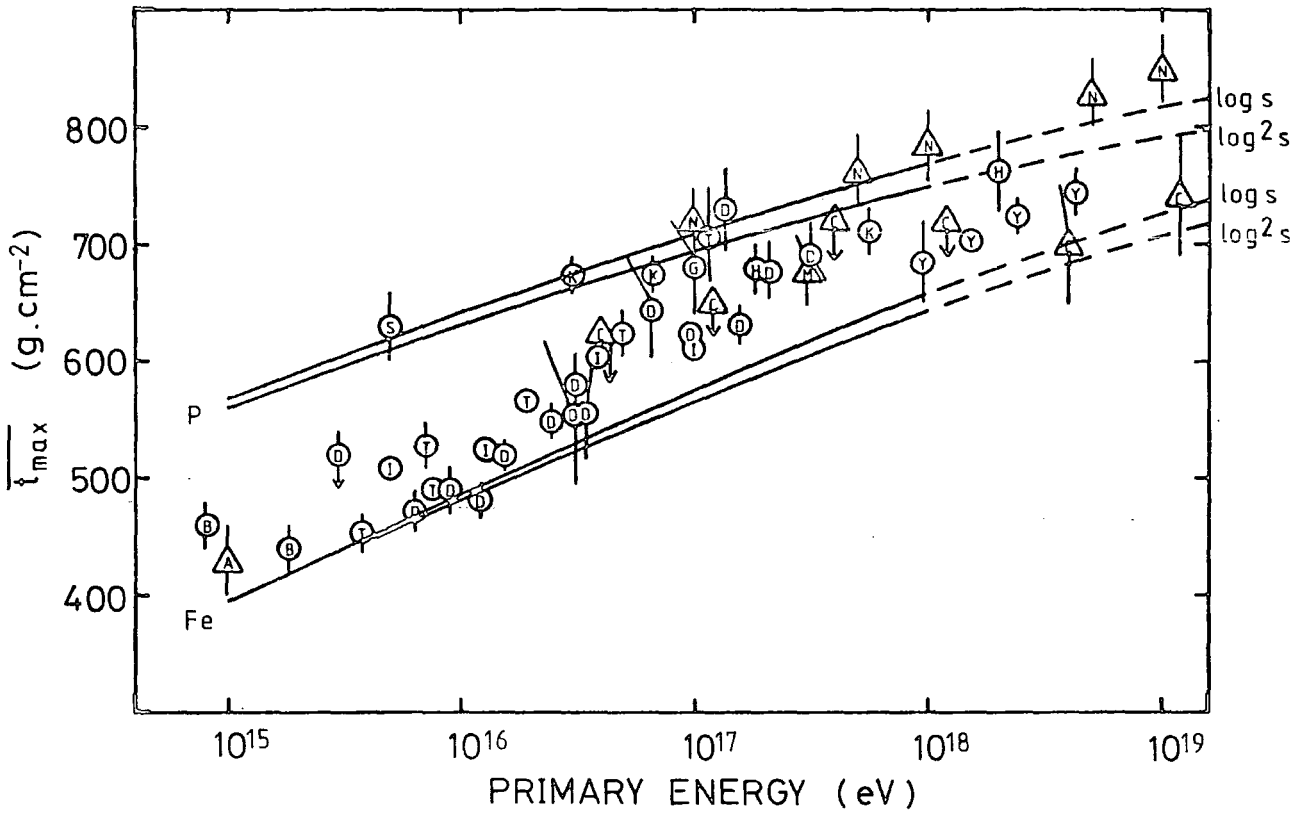

FIGURE 7.6b Comparison with model calculations incorporating an $E^{1/3}$ central-region multiplicity.

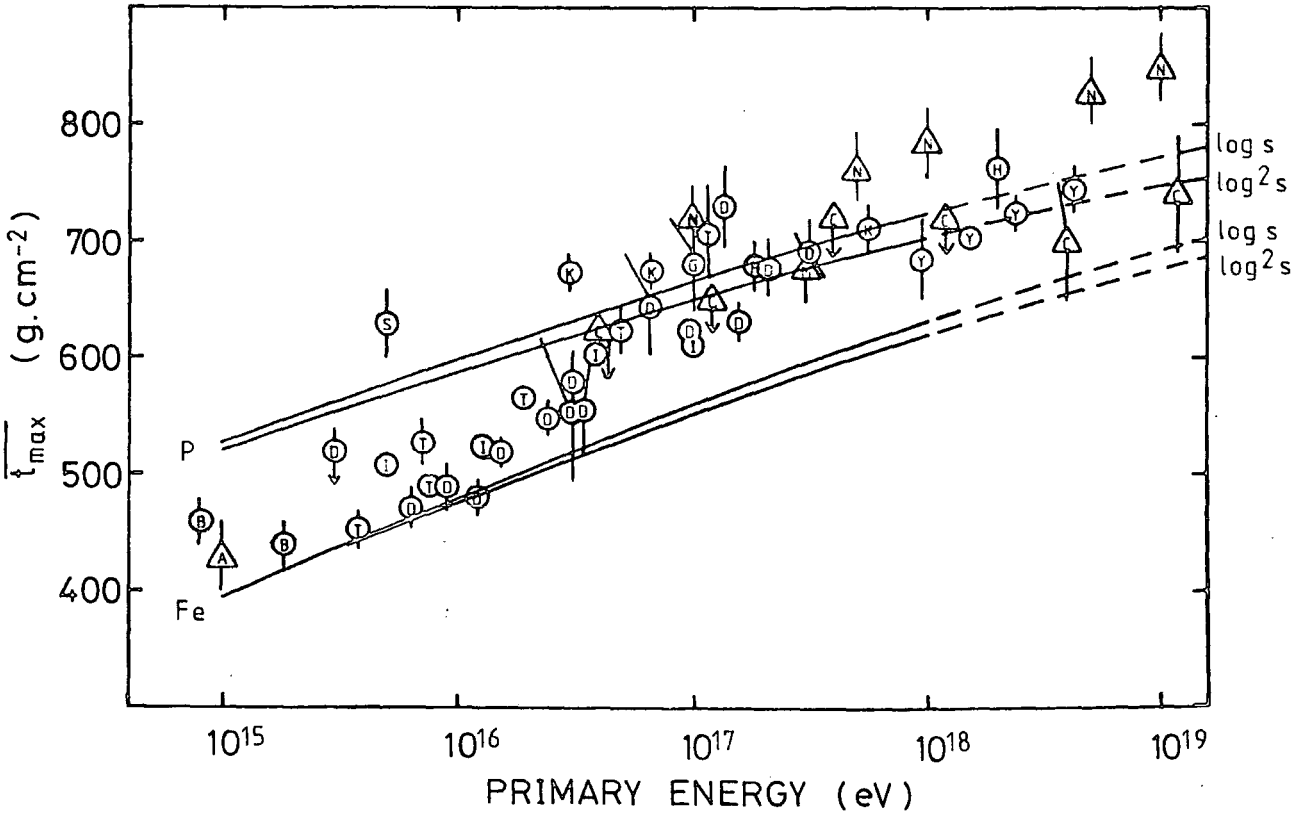

energies $\gtrsim 10^{17}$eV provide $\overline{t_{max}}$ results in broad agreement with those from Dugway and Haverah Park, although the muon/electron number results from Haverah Park appear to give slightly large $\overline{t_{max}}$ values. The electron cascade development curves from the Chacaltaya array (Aguirre et al. (1979)) provide $\overline{t_{max}}$ estimates at the highest energies, and upper limits at lower energies. (It should be stated that the assignment of $\overline{t_{max}}$ values to these development curves is, to some extent, a matter of taste).

On balance, the overall results from this wide range of measurements support the conclusions drawn from the Dugway data alone in section 7.2.2. In particular, there is support for a large elongation rate at energies $\sim 10^{16}$ - 2 x 10^{17} eV. In the framework of the current hadron interaction models this strengthens the case for a decrease in mean mass number over this energy range.

7.3 THE FLUCTUATION IN THE DEPTH OF CASCADE MAXIMUM ($\sigma(t_{max})$)

In this section, the fluctuation result derived in chapter 5, from measurements of the FWHM (250 m), is compared with computer simulation predictions and other work. At present this is the only fluctuation measurement available from the Dugway data, although analysis of the lateral distribution data is expected to lead to further results in the near future.

7.3.1 Comparison with Computer Simulation Predictions

Computer simulation results are available for fluctuating showers initiated by proton and iron nucleus primaries. The calculations for fluctuating showers initiated by iron primaries (Dixon and Turver (1974) and Dixon et al. (1974)) incorporate the gradual break-up of the iron nucleus in the atmosphere based on nuclear emulsion data. The simulation technique still forms the basis of more recent calculations (Gaisser and Stanev (1982)). The fragmentation of the iron nucleus

is, in fact, the dominant factor in determining the magnitude of the fluctuations in the longitudinal cascade development, rather than the model of the high-energy interactions. The relative standard deviation in the depth of cascade maximum ($\sigma(t_{max})/\overline{t_{max}}$) is only weakly dependent on the primary energy, and has a value of $\sim$ 4% at 10^{17} eV. The simulations of fluctuating showers initiated by proton primaries (Protheroe and Turver (1979)) have recently been extended by the Durham group for a range of scaling-based models (McComb, unpublished). $\sigma(t_{max})$ is found to be dependent on the interaction cross section but not on the central-region multiplicity.

In figure 7.7 the experimental measurements of $\sigma(t_{max})$ and $\overline{t_{max}}$ (both from the FWHM (250 m) analysis) are simultaneously compared with model predictions for showers of the same energy (2.1×10^{17} eV). The model calculations are for showers initiated by proton and iron nucleus primaries. On the basis of a simple two-component approximation to the mass composition, predictions are also made for $\overline{t_{max}}$ and $\sigma(t_{max})$ corresponding to a mixture of various percentages of iron nuclei and protons. The figure demonstrates clearly the advantage of 'simultaneous' measurement of both $\overline{t_{max}}$ and $\sigma(t_{max})$ if the effects of the mass composition and nuclear physics are to be resolved. The measurements are not consistent with the models incorporating scaling in the central region (as was deduced from the $\overline{t_{max}}$ estimates alone at lower energies). A model incorporating an $E^{1/4}$ multiplicity (model iv) with a mixed composition (30% Fe : 70% P), or a model incorporating an $E^{1/3}$ multiplicity (model ii) with a protonic composition, is favoured. However, since each curve represents an idealised case, and the accuracy of the end points is typically $\pm$ 10 g.cm^{-2} in each dimension, it is not possible to exclude models i or v on the basis of these results. The hypothesis of a predominently iron composition at this energy can, however, be

FIGURE 7.7

The mean and standard deviation of the depth of cascade maximum. ● - experimental result from the pulse shape data. × -values predicted by Monte Carlo simulations for iron nucleus and proton primaries. The curves represent the predictions for different percentages of iron nuclei and protons on the basis of a two-component approximation to the primary composition. The central-region multiplicities and the interaction cross-sections for each curve are shown below.

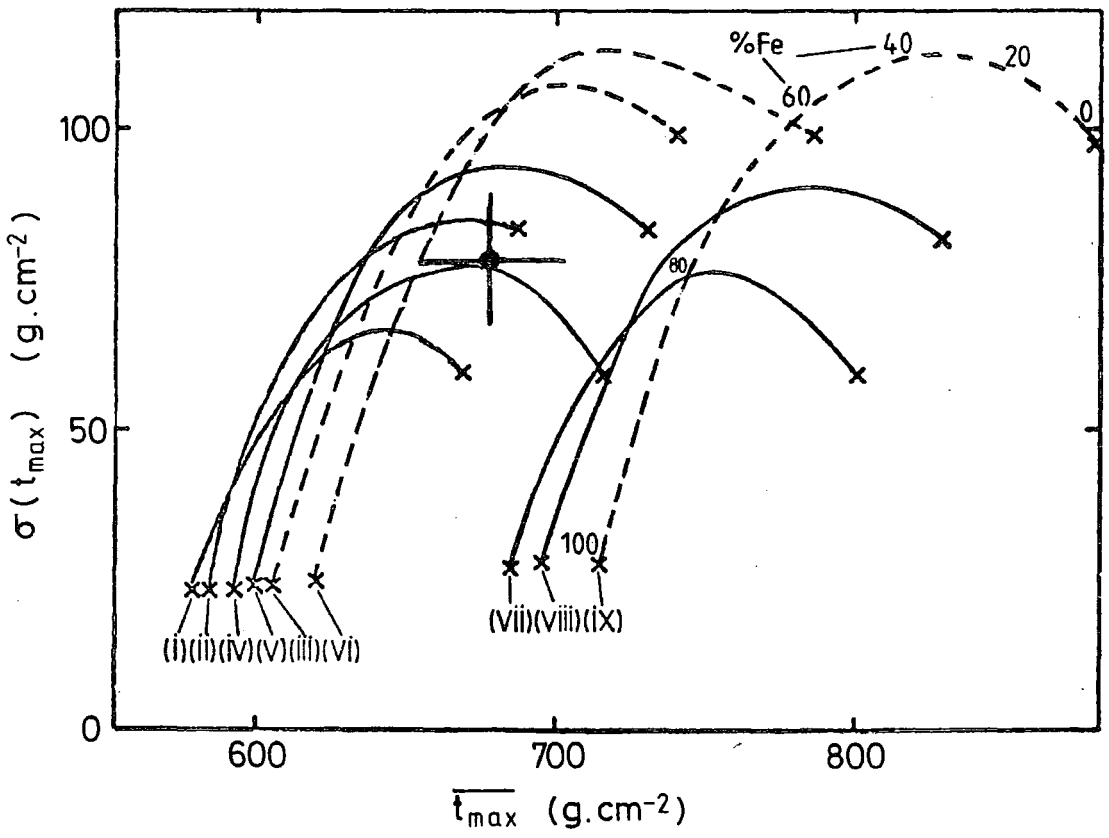

(i) $E^{1/3}$, $\log^2 s$ (iv) $E^{1/4}$, $\log^2 s$ (vii) $\log E$, $\log^2 s$

(ii) $E^{1/3}$, $\log s$ (v) $E^{1/4}$, $\log s$ (viii) $\log E$, $\log s$

(iii) $E^{1/3}$, constant (vi) $E^{1/4}$, constant (ix) $\log E$, constant

rejected with a high degree of confidence regardless of the choice of interaction model.

7.3.2 Comparison with Other Work

The present work represents the only simultaneous measurements of $\overline{t_{max}}$ and $\sigma(t_{max})$ currently available, with the exception of the Cerenkov light measurements of Kalmykov et al. (1979); however, no information was published in the latter work on the mean or distribution of primary energy appropriate to the data sample, which encompassed two decades of primary energy. A comparison with other work must, therefore, be restricted to the published results of $\sigma(t_{max})$ alone. A survey of $\sigma(t_{max})$ measurements is shown in figure 7.8 with an indication of either the mean primary energy or the range of primary energy of each data sample. Also shown in the figure are the computer simulation predictions for 10^{17} eV showers initiated by proton and iron nucleus primaries. There is reasonable agreement between the measurements, all of which clearly exclude the possibility of a predominently heavy composition at energies $\gtrsim 2 \times 10^{17}$ eV. At these energies there appears to be no significant energy dependence of $\sigma(t_{max})$: a result which is indicative of a constant or nearly constant mass composition.

7.4 CONCLUSIONS

The measurements of $\overline{t_{max}}$ from the present work, for showers of primary energy $\sim 2 \times 10^{17}$ eV, are found to be consistent with other measurements from Dugway in showers of similar energy and with measurements from other experiments. Interpreted on their own, these measurements are consistent with a wide range of models incorporating scaling in the fragmentation region and with a wide range of primary mass compositions. However, the simultaneous interpretation of the $\overline{t_{max}}$ and $\sigma(t_{max})$ measurements from the pulse shape data suggests further constraints on the nuclear physics model and mass composition. Models

FIGURE 7.8 A survey of measurements of the fluctuation in the depth of cascade maximum. The model predictions for pure proton and pure iron primary compositions are shown for comparison.

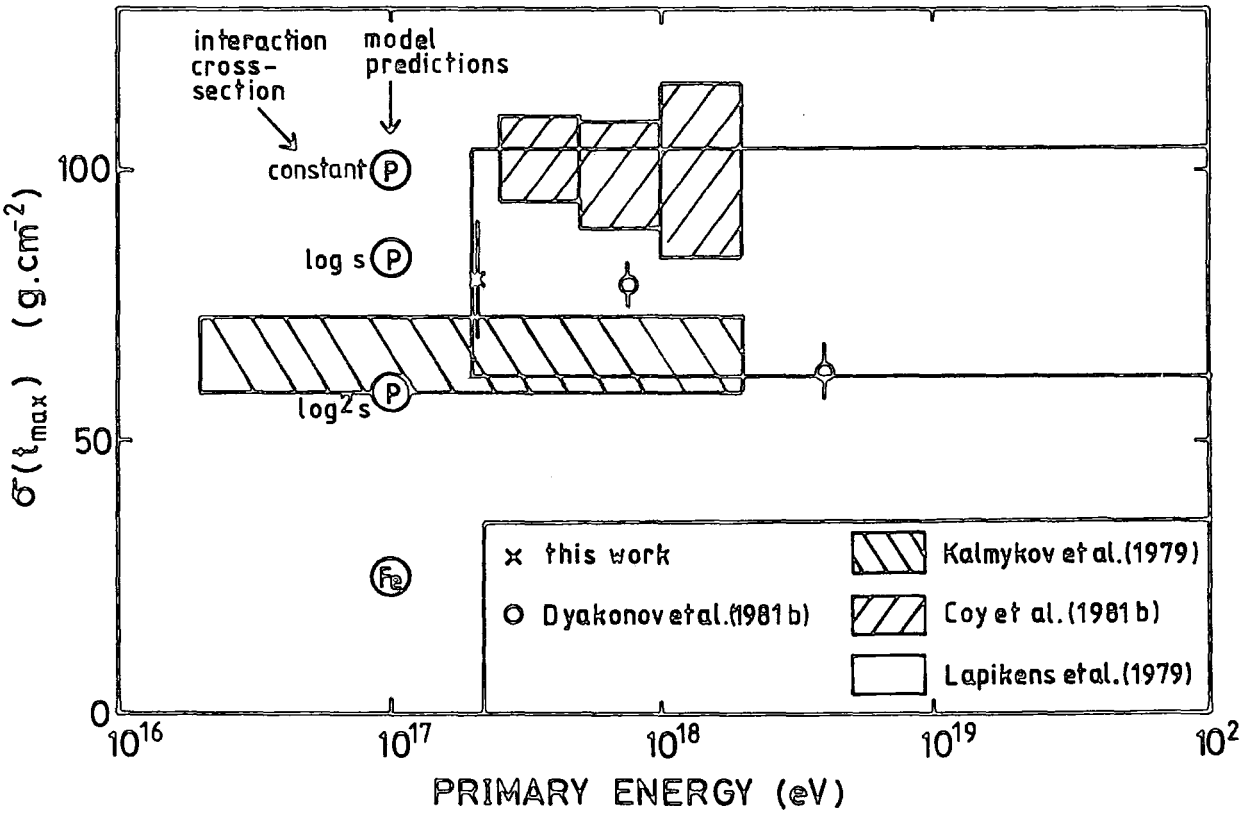

incorporating $E^{1/4}$ or $E^{1/3}$ central region multiplicities are favoured, with a mixed or protonic mass composition at an energy $\gtrsim 2 \times 10^{17}$ eV.

Measurements of $\overline{t_{max}}$ over a wide energy range are available from the Dugway data, and suggest a much larger elongation rate than would be expected for a constant mass composition and interaction models incorporating scaling in the fragmentation region. The results are not consistent with models incorporating scaling in the central region, but can be interpreted in the framework of models incorporating enhanced central-region multiplicities ($E^{1/4}$ or $E^{1/3}$). On the basis of these models, the mean primary mass number appears to be ~ 56 at 10^{16} eV, and decreases with increasing primary energy until at least 2×10^{17} eV. A compilation of $\overline{t_{max}}$ results from a wide range of other experiments supports this trend observed in the Dugway data. Measurements of the elongation rate from experiments at Haverah Park are consistent with the expectation for a constant or nearly constant mass composition at energies $\gtrsim 2 \times 10^{17}$ eV. Measurements of $\sigma(t_{max})$ from Haverah Park and other experiments are consistent with the present work and with the model predictions for a protonic or mixed composition. These results also suggest no appreciable primary energy dependence in the mass composition at energies $> 2 \times 10^{17}$ eV.

CHAPTER 8

CONCLUSIONS AND FUTURE WORK

8.1 CONCLUSIONS

Measurements of the pulse shape and curvature of the Cerenkov light front have been made in showers of energy $\sim 2 \times 10^{17}$ eV. Direct comparison with simulation results has enabled the interpretation of these measurements in terms of $\overline{t_{max}}$. This interpretation is independent of the details of the interaction model. The results are found to be consistent with model calculations based on scaling in the fragmentation region.

Calculations of the measurement uncertainties permitted an accurate estimation of $\sigma(t_{max})$ from the pulse shape data. The simultaneous interpretation of $\sigma(t_{max})$ and $\overline{t_{max}}$ from this data sample implies certain constraints on the choice of model/primary mass composition: a mixed or protonic composition is favoured, with a model incorporating an enhanced central-region multiplicity ($E^{1/4}$ or $E^{1/3}$). The measurement errors in the front-curvature measurements (based on the synchronised-timing data) proved too large to enable an accurate estimate of the fluctuations from the observed spread in the depth of origin of the Cerenkov light maximum.

The flexible geometry of the Dugway array enabled data to be recorded in the absence of serious selection biases over a wide range of primary energy. The $\overline{t_{max}}$ results derived from these data could be expected to be largely free from the problems often associated with combining results from widely differing experiments, each employing its own interpretative methodology. Models incorporating an enhanced central-region multiplicity (as opposed to that following from scaling) are required to encompass the observations. However, a significantly

larger elongation rate is found than the expectation for a constant mean mass number. This suggests a change in the mass composition from one containing predominently heavy nuclei at 10^{16} eV to a protonic or mixed composition at 2×10^{17} eV.

The present inferences on the mass composition, from observations of the longitudinal electron cascade development, should be viewed in the wider context of recent interpretations of other experimental results. Evidence for an increasing proportion of heavy nuclei in the primary composition at $\sim 10^{15}$ eV has been found from the arrival-time distribution of hadrons in the shower core (Cowsik et al. (1981)). Further evidence for an enhancement of heavy nuclei comes from a study of core densities in showers of energy $\sim 3 \times 10^{15}$ eV (Hillas (1981b)). This work suggests that the primaries have a much shorter mean free path than would be expected for protons. In contrast, measurements of the muon/electron number (Nikolsky et al. (1981)) have been interpreted as evidence for a constant 'normal' composition in the energy range $10^{15} - 10^{16}$ eV. At energies $\gtrsim 10^{17}$ eV, very few interpretations of the data in terms of the primary composition have been published, although there is some concensus that large development fluctuations are present, indicating that the primaries are not exclusively heavy nuclei.

It should be re-emphasised that much of the interpretation of EAS data in terms of the primary composition depends on the validity of the interaction models, which are themselves based on extrapolations from accelerator data. The interpretation of the behaviour of $\overline{t_{max}}$ with primary energy presented here relies on the continuing validity of scaling in the fragmentation region. (However, the derived $\overline{t_{max}}$ values themselves are expected to remain valid over a wide range of interaction models). Gaisser et al. (1978) reviewed a wide body of

EAS data from 10^{15} to 10^{18} eV, and concluded that there was no compelling case for a violation of scaling in the fragmentation region. Alternatively, some measurements have been interpreted as being better described by high multiplicity models (e.g. those discussed by Kakimoto et al. (1981)), and others by the CKP model (e.g. Nikolsky et al. (1981)). It is fair to say that no single model of particle physics has yet been shown to be entirely consistent with all air-shower data.

A possibility that cannot be discounted is that the observed dependence of $\overline{t_{max}}$ on primary energy is due to changes in the nature of the high-energy interactions, rather than changes in the primary composition. For example, there is evidence that occasionally air showers of primary energy $\sim 10^{15}$ eV produce 'Centauro' interactions (Lattes et al. (1975)), in which a high multiplicity of hadrons is produced but no neutral pions. If the cross-section of Centauro-type interactions were a significant fraction of the total cross section at higher energies then this would produce an early-developing average cascade, which might appear similar to that expected for a primary beam of iron nuclei.

It is clear, however, that exotic particle interactions are not required to accommodate the present results. The behaviour of the primary mass composition suggested by the interpretation of these results in the framework of scaling-based models has, if correct, important astrophysical implications. An explanation for the dependence of mean mass number on primary energy might follow from models of galactic diffusion previously developed to account for the steepening of the energy spectrum at $\sim 3 \times 10^{15}$ eV (e.g. Bell et al. (1974)) and also to explain the arrival-time distribution of hadrons in the shower core (Cowsik et al. (1981)). Protons might be expected to escape from the confinement of galactic magnetic fields between 10^{14} and 10^{15} eV. Lower rigidity particles would be trapped until higher energies, iron nuclei

not escaping until a factor of 26 higher in energy than protons. This mechanism could, therefore, result in a dispersion of the spectral intensities of the various cosmic-ray nuclei, and in a predominance of heavy nuclei near 10^{16} eV. In this scenario, an extragalactic component might be invoked to explain the lighter composition observed at higher energies.

Alternatively, the observed behaviour of the primary composition might be at least partially attributable to the production of cosmic rays by pulsars. Karakula et al. (1974) proposed that galactic pulsars might largely account for the energy spectrum in the region of the 'knee' at $\sim 3 \times 10^{15}$ eV. An abrupt fall-off in the proton spectrum from pulsars is predicted at $\sim 10^{16}$ eV, whereas heavier nuclei could be accelerated to higher energies. Again, a component from another source would be required to account for the lighter composition at energies $\gtrsim 2 \times 10^{17}$ eV.

The present work has clearly demonstrated the value of the Cerenkov light technique in providing information on the longitudinal cascade development of large EAS and hence the mass composition of the primary beam. The Dugway experiment has been successful in obtaining measurements of Cerenkov radiation with a higher resolution than previously available. In addition, the versatility of the equipment enabled measurements to be made over a very wide range of primary energy. The availability of detailed computer simulations of EAS, tailored to the observations, has permitted the interpretation of the data, with the minimum of ambiguity, in terms of the longitudinal cascade development. The results have provided an exciting insight into the nature of the high-energy cosmic-ray primaries.

8.2 FUTURE WORK

The analysis of the Dugway data is continuing. The pulse shape data at energies lower than the sample analysed in this thesis have not yet been fully exploited, and offer the potential of further $\overline{t_{max}}$ estimates in the range $5 \times 10^{16} - 10^{17}$ eV, but not in the lower energy band $5 \times 10^{15} - 5 \times 10^{16}$ eV which is now of more pressing importance.

Analysis of the lateral distribution data has already provided $\overline{t_{max}}$ estimates over the range $6 \times 10^{15} - 3 \times 10^{17}$ eV, and an analysis of the fluctuations over and above those caused by measurement uncertainties is now nearing completion. A clear prediction is amenable to test from the present interpretation of the $\overline{t_{max}}$ measurements: a small fluctuation value ($\sigma(t_{max}) \sim 25$ g.cm^{-2}) is expected at an energy of $\sim 10^{16}$ eV. If this is established, the case for a predominently heavy primary composition at this energy would be much strengthened. Conversely, if $\sigma(t_{max})$ at this energy is found to be large, the validity of the above conclusions, and of the nuclear physics models which have been scaled up from accelerator energies, will be placed in serious doubt.

The new $p\bar{p}$ collider experiments at CERN and FNAL are expected to provide measurements of the characteristics of strong interactions at energies up to $\sim 10^{15}$ eV per nucleon. This in turn will provide a firmer basis for future interpretations of EAS data in the energy range $10^{15} - 10^{18}$ eV.

Further detailed measurements of the longitudinal cascade development in the energy band $10^{15} - 10^{18}$ eV (preferably from a single experiment if they are to improve on those reported here) would be worthwhile to provide corroboration of the present results. At energies $\gtrsim 10^{17}$ eV a further synchronised-timing experiment with improved measurement

resolution (< 1 ns) could yield even more detailed information on the cascade development. Small differences in the shape of the development profile are predicted from the CKP, high multiplicity and scaling models (see, for example, Kalmykov et al. (1981)). A sufficiently high resolution synchronised-timing experiment could discriminate between these options, and coupled with precise measurements of $\overline{t_{max}}$ and $\sigma(t_{max})$ a more complete picture of the primary composition could be achieved. The value of synchronised-timing measurements has also recently been emphasised by Hillas (1982). Hillas concludes, with the aid of computer simulation predictions, that this technique provides the most unambiguous source of information on the cascade development because of the potential of accurately reconstructing the longitudinal development profile. So far, however, the present experiment and the pilot experiment at Haverah Park have been the only attempts to exploit this valuable direct technique.

Additional measurements in the important region of the 'knee' in the energy spectrum at $\sim 3 \times 10^{15}$ eV, where little data presently exists, could be made by Cerenkov light experiments employing flux collectors (e.g. Gibson et al. (1981b)). At the other extreme, information on the highest energy cosmic rays ($\sim 10^{20}$ eV) may come from the 'Fly's Eye' scintillation light experiment (Bergeson et al. 1977)).

REFERENCES

Aguirre C., Anda R., Trepp A., Kaneko T., Yoshii H., Nishi K., Yamada Y., Tajima N., Nakatani H., Gotoh E., Kakimoto F., Mizumoto Y., Suga K., Izu N., Kamouchi Y., Inoue N., Kawai M., MacKeown P.K., Toyoda Y and Murakami K. (1979), Proc. 16th Int. Conf. on Cosmic Rays, Kyoto, 8, 107.

Aliev N., Alimov T.A., Kaharov M., Makhmudov B.M., Scvirenko S., Kalmykov N.N., Khristiansen G.B. and Prosin V.V. (1981), Proc. 17th Int. Conf. on Cosmic Rays, Paris, 11, 262.

Allen C.W. (1955), 'Astrophysical Quantities' (2nd Edition), The Athlone Press, University of London, 134.

Amaldi U., Cocconi G., Diddens A.N., Dobinson R.W., Dorenbosch J., Dunker W., Gustavson D., Meyer J., Potter K., Wetherell A.M., Baroncelli A., and Bosio C. (1977), Phys. Lett. B., 66, 390.

Andam A., Chantler M.P., Craig M.A.B., Orford K.J., Shearer J.A.L., Turver K.E. and Walley G.M. (1979), Proc. 16th Int. Conf. on Cosmic Rays, Kyoto, 9, 48.

Anderson C.D. (1932), Science, 76, 238.

Antonov R.A., Kuzmin V.A. and Fateeva I.M., (1981), Proc. 17th Int. Conf. on Cosmic Rays, Paris, 6, 229.

Ascoli R. and Balzanelli A. (1953), Nuovo Cim., 10, 1345.

Barclay F.R. and Jelley J.V. (1955), ibid., 2, 27.

Barclay F.R. and Jelley J.V. (1956), Proc. Oxford Conf. EAS, (A.E.R.E. report), 74.

Bell M.C., Kota J. and Wolfendale A.W. (1974), J. Phys. A., 7, 420.

Bergeson H.E., Cassidy G.L., Chiu T.W., Cooper D.A., Elbert J.W., Loh E.C., West W.J., Linsley J. and Mason G.W. (1977), Phys. Rev. Lett., 39, 847.

Blackett P.M.S. (1948), Dep. Gassiot Comm. of the Roy. Soc., 34.

Blake P.R., England C.D., Lapikens J., Nash W.F., Norwood H., O'Connel B., Reid R.J.O., Strutt R.B. and Watson A.A. (1979), Proc. 16th Int. Conf. on Cosmic Rays, Kyoto, 8, 67.

Boley F.I. (1964), Rev. Mod. Phys., 36, 792.

Boley F.I., Baum J.H., Pasledge J.A. and Pereue J.H. (1961), Phys. Rev., 124, 1205.

de Boor C. (1978), 'A Practical Guide to Splines', Applied Mathematical Sciences, vol. 27, Springer-Verlag, New York.

Bosia G., Maringelli M. and Navarra G. (1972), Nuovo Cim., 9B, 201.

Bower A.J., Cunningham G., England C.D., Lloyd-Evans J., Reid R.J.O., Walker R. and Watson A.A. (1981), Proc. 17th Int. Conf. on Cosmic Rays, Paris, 9, 166.

Cerenkov P.A. (1934),Dokl. Akad. Nauk., 2, 451.

Cerenkov P.A. (1937), Phys. Rev., 52, 378.

Chantler M.P., Craig M.A.B., McComb T.J.L., Orford K.J., Turver K.E. and Walley G.M. (1981), Proc. 17th Int. Conf. on Cosmic Rays, Paris, 6, 121.

Chantler M.P., Orford K.J., Shearer J.A.L., Turver K.E. and Walley G.M. (1979a), Proc. 16th Int. Conf. on Cosmic Rays, Kyoto, 9, 42.

Chantler M.P., McComb T.J.L., Orford K.J., Shearer J.A.L., Turver K.E. and Walley G.M. (1979b), ibid, 9, 56.

Cocconi G., Koester L.G. and Perkins D.H. (1961), Lawrence Radiation Lab., High Energy Physics Seminars, No. 28, Part 2, U.C.I.D., 1444.

Cowsik R., Tonwar S.C., Viswanath P.R., Ellsworth R.W., Goodman J.A., Ito A.S., Streitmatter R.E. and Yodh G.B. (1981), Proc. 17th Int. Conf. on Cosmic Rays, Paris, 2, 120.

Cowsik R. and Wilson L.W., (1973), Proc. 13th Int. Conf. on Cosmic Rays, Denver, 1, 500.

Cox M.G. (1972), J. Inst. Math. App., 10, 134.

Coy R.N., Lloyd-Evans J., Patel M., Reid R.J.O. and Watson A.A. (1981a), Proc. 17th Int. Conf. on Cosmic Rays, Paris, 9, 183.

Coy R.N., England C.D., Pearce D., Reid R.J.O. and Watson A.A. (1981b), ibid, 6, 43.

Craig M.A.B., McComb T.J.L. and Turver K.E. (1979), Proc. 16th Int. Conf. on Cosmic Rays, Kyoto, 8, 180.

Dixon H.E. and Turver K.E. (1974), Proc. R. Soc. Lond. A., 339, 171.

Dixon H.E., Turver K.E. and Waddington C.J. (1974), Proc. R. Soc. Lond. A, 339, 157.

Dyakonov M.N., Egorov T.A., Egorova V.P., Ivanov A.A., Knurenko S.P., Kozlov V.I., Kolosov V.A., Krasilnikov A.D., Krasilnikov D.D., Lishchenuk F.F., Pavlov V.N., Sidorov R.G., Sleptsov I.Ye. and Nikolsky S.I. (1981a), Proc. 17th Int. Conf. on Cosmic Rays, Paris, 6, 106.

Dyakonov M.N., Knurenko S.P., Kozlov V.I., Kolosov V.A., Krasilnikov D.D., Lishchenuk F.F., Makarov K.N., Pavlov V.N., Sleptsov I.Ye., Shamsutdinova F.K. and Nikolsky S.I. (1981b), ibid, 6, 110.

Eadie W.T., Drijard D., James F.E., Roos M. and Sadoulet B. (1971), 'Statistical Methods in Experimental Physics', North-Holland, Amsterdam.

Efimov N.N., Krasilnikov D.D., Khristiansen G.B., Shikalov F.V. and Kuzmin A.I. (1973), Proc. 13th Int. Conf. on Cosmic Rays, Denver, 4, 2378.

Egorov T.A., Kolosov V.A., Krasilnikov D.D., Orlov V.A. and Slepstov H.E. (1971), Proc. 12th Int. Conf. on Cosmic Rays, Hobart, 6, 2164.

Elterman L. (1968), Air Force Cambridge Research Labs., Ref. AFC RL-68-0153.

Feynman R.P. (1969), Phys. Rev. Lett., 23, 1415.

Fomin Yu. A. and Khristiansen G.B. (1971), Sov. J. Nucl. Phys., 14, 360.

Frank I.M. and Tamm Ig. (1937), Dokl. Akad. Nauk. SSSR, 14, 109.

Gaisser T.K., Protheroe R.J., Turver K.E. and McComb T.J.L. (1978), Rev. Mod. Phys., 50, 859.

Gaisser T.K. and Stanev T. (1982), Bartol Technical Report, BA-82-1.

Gaisser T.K. and Yodh G.B. (1980), Ann. Rev. Nucl. Part. Sci., 30, 475.

Galbraith W. and Jelley J.V. (1953), Nature, 171, 349.

Galbraith W. and Jelley J.V. (1955), J. Atmos. Terr. Phys., 6, 250.

Garcia-Munoz M., Mason G.M. and Simpson J.A. (1975), Ap. J. Lett., 201, L141.

Gibson A.I., McComb T.J.L. and Turver K.E. (1981a), Proc. 17th Int. Conf. on Cosmic Rays, Paris, 6, 16.

Gibson A.I., Harrison A.B., Kirkman I.W., Lotts A.P., MacRae H., Orford K.J. and Turver K.E. (1981b), ibid, 8, 38.

Giler M., Wdowczyk J. and Wolfendale A.W. (1980), J. Phys. G., 6, 1561.

Glushkov A.V., Grigorev V.M., Efimov N.N., Pravdin M.I., Diminstein O.S. and Sokurov V.F. (1979), Proc. 16th Int. Conf. on Cosmic Rays, Kyoto, 8, 158.

Greisen K. (1966), Phys. Rev. Lett., 16, 748.

Hammond R.T., Protheroe R.J., Orford K.J., Shearer J.A.L., Turver K.E., Waddoup W.D. and Wellby D.W. (1978), Nuovo Cim., 1C, 315.

Hess V.F. (1912), Phys. Z., 13, 1084.

Hillas A.M. (1975), Phys. Rep., 20C, 59.

Hillas A.M. (1979), Proc. 16th Int. Conf. on Cosmic Rays, Kyoto, 8, 7.

Hillas A.M. (1981a), Proc. 17th Int. Conf. on Cosmic Rays, Paris, 13, 69.

Hillas A.M. (1981b), ibid, 2, 125.

Hillas A.M. (1982), preprint.

Hillas A.M., Marsden D.J., Hollows J.D. and Hunter H.W. (1971), Proc. 12th Int. Conf. on Cosmic Rays, Hobart, 3, 1001.

Hillas A.M. and Ouldridge (1975), Nature, 253, 609.

Inoue N., Sugawa N., Tamura T., Kakimoto F., Inaba T., Matsumoto Y., Suga K. and Nishi K. (1981), Proc. 17th Int. Conf. on Cosmic Rays, Paris, 11, 270.

Ivanenko I.P. and Makarov V.V. (1977), Proc. 15th Int. Conf. on Cosmic Rays, Plovdiv, 8, 303.

James M. and Roos M. (1975), Comp. Phys. Comm., 10, 413.

Jelley J.V. (1958), 'Cerenkov Radiation and its Applications', Pergamon Press, London.

Jelley J.V. (1967), Proc. Cosmic Ray Phys., 10, 41.

Jelley J.V. and Galbraith W. (1953), Phil. Mag., 44, 619.

Jelley J.V. and Galbraith W. (1955), J. Atmos. Terr. Phys., 6, 304.

Juliusson E. (1975), Proc. 14th Int. Conf. on Cosmic Rays, Munich, 8, 2689.

Kakimoto F., Inoue N., Sugawa N., Tachi K., Suga K., Mizumoto Y., Hara T., Kaneko T., Yoshii H., Toyoda T., Maeda T., Nishi K., Gotoh E., Nakatani H., Yamada Y., Tajima N., Murakami K., MacKeown P.K., Anda R., Aguirre C., Siles L. and Veramendi D. (1981), Proc. 17th Int. Conf. on Cosmic Rays, Paris, 6, 27.

Kalmykov N.N., Khristiansen G.B., Nechin Yu. A., Prosin V.V., Efimov N.N. and Grigorev V.M. (1976), paper presented at the European Symposium on Air Showers, Leeds.

Kalmykov N.N., Khristiansen G.B., Nechin Yu. A., Prosin V.V., Grigorev V.M. and Efimov N.N. (1977), Proc. 15th Int. Conf. on Cosmic Rays, Plovdiv, 8, 244.

Kalmykov N.N., Nechin Yu.A., Prosin V.V., Efimov N.N., Fomin Yu.A., Khristiansen G.B. and Grigorev V.M. (1981), Proc. 17th Int. Conf. on Cosmic Rays, Paris, 6, 114.

Kalmykov N.N., Nechin Yu.A., Prosin V.V., Fomin Yu.A., Khristiansen G.B. and Berezhko I.A. (1979), Proc. 16th Int. Conf. on Cosmic Rays, Kyoto, 9, 73; and Berezhko I.A., Grigorev V.M., Efimov N.N., Kalmykov N.N., Nechin Yu.A., Prosin V.V., Fomin Yu.A. and Khristiansen G.B. (1979), Sov. J. Nucl. Phys., 30, 215.

Karakula S., Osborne J.L. and Wdowczyk J. (1974), J. Phys. A., 7, 437.

Khristiansen G.B., Makhmudov B.M., Aliev N., Sirodzhev N., Silaev A.A. and Chukanov V.A. (1977), Proc. 15th Int. Conf. on Cosmic Rays, Plovdiv, 8, 504.

Kiraly P., Kota J., Osborne J.L., Stapley N.R. and Wolfendale A.W. (1979), Riv. Nuovo Cim., 2, No. 7, 1.

Krasilnikov D.D. (1979), Proc. 16th Int. Conf. on Cosmic Rays, Kyoto, 8, 26.

Krieger A.S. and Bradt H.V. (1969), Phys. Rev., 185, 1629.

Landau L.D. (1953), Izv. Akad. Nauk. SSSR, 17, 51, translated in 'Collected Papers of L.D. Landau', 1965, edited by D. Ter Haar, Gordon and Breach, New York.

Lapikens J., Walker R. and Watson A.A. (1979), Proc. 16th Int. Conf. on Cosmic Rays, Kyoto, 8, 95.

Lattes C.M.G. et al. (Brazil-Japan collaboration) (1975), Proc. 14th Int. Conf. on Cosmic Rays, Munich, 7, 2393.

Linsley J. and Watson A.A. (1981), Phys. Rev. Lett., 46, 459.

Lloyd-Evans J., Pollock A.M.T. and Watson A.A. (1979), Proc. 16th Int. Conf. on Cosmic Rays, Kyoto, 13, 130.

Malos J.D., Miller D.D. and Wallace C.S. (1962), J. Phys. Soc. Japan, Suppl., A-III, 114.

McComb T.J.L. and Turver K.E. (1981a), Proc. 17th Int. Conf. on Cosmic Rays, Paris, 6, 130.

McComb T.J.L. and Turver K.E. (1981b), ibid, 6, 234.

McComb T.J.L. and Turver K.E. (1982a), Nuovo Cim., in the press.

McComb T.J.L. and Turver K.E. (1982b), accepted for publication in J. Phys. G.

Morrison D.R.O. (1973), Proc. R. Soc. Lond. A., 335, 461.

Nelder J.A. and Mead R. (1967), Comp. J., 7, 308.

Nesterova N.M. and Chudakov A.E. (1955), Zh. Eksp. Teor. Fiz., 28, 384.

Nikolsky S.I., Nikolskaja N.M., Stamenov I.N. and Ushev S.Z. (1981), Proc. 17th Int. Conf. on Cosmic Rays, Paris, 2, 129.

Orford K.J., Stephenson I., Turver K.E. and Walley G.M. (1981), ibid, 6, 118.

Orford K.J., Stubbs R.J. and Waddoup W.D. (1977), Nucl. Inst. and Meth., 146, 389.

Orford K.J. and Turver K.E. (1976), Nature, 264, 727.

Orford K.J. and Turver K.E. (1980), Phys. Rev. Lett., 44, 959.

Orford K.J., Turver K.E. and Waddoup W.D. (1976), unpublished.

Orford K.J., Turver K.E. and Wellby D.W. (1975), Proc. 14th Int. Conf. on Cosmic Rays, Munich, 8, 3019.

Peters B. (1961), Nuovo Cim., 22, 800.

Protheroe R.J. (1977), Ph.D. thesis, University of Durham.

Protheroe R.J., Smith G.J. and Turver K.E. (1975), Proc. 14th Int. Conf. on Cosmic Rays, Munich, 8, 3008.

Protheroe R.J. and Turver K.E. (1977), Proc. 15th Int. Conf. on Cosmic Rays, Plovdiv, 8, 275.

Protheroe R.J. and Turver K.E. (1979), Nuovo Cim., 51A, 277.

Shapiro M.M.,Silberberg R. and Tsaa C.H. (1975), Proc. 14th Int. Conf. on Cosmic Rays, Munich, 2, 532.

Shearer J.A.L. (1978), M.Sc. thesis, University of Durham.

Shearer J.A.L. (1980), Ph.D. thesis, University of Durham.

Smith G.J. and Turver K.E. (1973), J. Phys. A, 6, L121.

Strong A.W., Wdowczyk J. and Wolfendale A.W. (1974), J. Phys. A, 7, 1489.

Stubbs R.J. and Waddoup W.D. (1977), Nucl. Inst. and Meth., 146, 561.

Thornton G.J. and Clay R.W. (1980), Phys. Rev. Lett., 45, 1463.

Thornton G.J., Kuhlmann J.D., Liebing D.F., Clay R.W., Gregory A.G., Paterson J.R. and Prescott J.R. (1979), Proc. 16th Int. Conf. on Cosmic Rays, Kyoto, 9, 103.

Tonwar S.C. (1981), Proc. 17th Int. Conf. on Cosmic Rays, Paris, 13, 325.

Tornabene H. (1979), Proc. 16th Int. Conf. on Cosmic Rays, Kyoto, 9, 99.

Volk H.J. (1981), Proc. 17th Int. Conf. on Cosmic Rays, Paris, 13, 131.

Waddoup W.D. and Stubbs R.J. (1976), Nucl. Inst. and Meth., 137, 603.

Waddoup W.D. and Stubbs R. J. (1977), ibid., 146, 569.

Walker R. and Watson A.A. (1981), J. Phys. G., 7, 1297.

Wellby D.W. (1977), Ph.D. thesis, University of Durham.

Yodh G.B., Yash Pal and Trefil J.S. (1972), Phys. Rev. Lett., 28, 1005.

Zatsepin G.T. and Kuzmin V.A. (1966), Zh. Eksp. Teor. Fiz., 4, 78.

ACKNOWLEDGEMENTS

I wish to thank Professor A.W. Wolfendale and Professor B.H. Bransden for provision of facilities in the Department of Physics, University of Durham. I am also indebted to my supervisor, Dr. K.E. Turver, for his advice and encouragement throughout the course of this work.

I thank all my colleagues in the Extensive Air Shower group for their assistance. In particular I am grateful to Ms. M.A.B. Craig, Dr. T.J.L. McComb, Dr. K.J. Orford and Mr. G.M. Walley for many useful discussions.

The U.S. Army Technical and Evaluation Command is thanked for provision of land and support facilities at Dugway Proving Grounds. The Fly's Eye group of the University of Utah are thanked for their help.

The provision of a Research Studentship by the Science Research Council is gratefully acknowledged.